THÈSE

En vue de l'obtention du

DOCTORAT DE L'UNIVERSITÉ DE TOULOUSE

Délivré par :

Institut National Polytechnique de Toulouse (Toulouse INP)

Discipline ou spécialité :

Dynamique des fluides

Présentée et soutenue par :

M. GLAD CALIN LICSANDRU

le mercredi 18 novembre 2020

Titre :

Evaporative NaCl salt crusts: formation, patterning, displacement and detachment mechanisms

---

Ecole doctorale :

Mécanique, Energétique, Génie civil, Procédés (MEGeP)

Unité de recherche :

Institut de Mécanique des Fluides de Toulouse (IMFT)

Directeur(s) de Thèse :

M. MARC PRAT

MME CATHERINE NOIRIEL

Rapporteurs :

MME NOUSHINE SHAHIDZADEH, UNIVERSITE D'AMSTERDAM

M. NIMA SHOKRI, TECHNISCHE UNIVERSITAT HAMBOURG

Membre(s) du jury :

M. LIONEL MERCURY, UNIVERSITE D'ORLEANS, Président

M. MARC PRAT, CNRS TOULOUSE, Membre

MME ARIANE ABOU-CHAKRA, Laboratoire de Mécanique et Génie Civil, Invité(e)

MME CATHERINE NOIRIEL, CNRS TOULOUSE, Membre

MME SANDRINE GEOFFROY, INSA TOULOUSE, Membre

M. PAUL DURU, TOULOUSE INP, Invité(e)

Résumé

La halite se rencontre souvent dans la nature sous la forme de grands dépôts formant des croûtes de sel à la surface des sols ou plus généralement de milieux poreux. Il a été rapporté que les croûtes de sel peuvent fortement affecter le processus d'évaporation et qu'elles peuvent conduire à des phénomènes intrigants, tels que la formation de dômes de sel ou le détachement de la croûte de l'hôte poreux sous-jacent.

Dans ce contexte, les travaux présentés dans cette thèse ont pour objectif de mieux comprendre la formation des croûtes de sel et leur dynamique à travers une expérience originale de laboratoire combinée à une approche de modélisation simple. Une série d'expériences est menée dans un environnement de laboratoire bien contrôlé (température, humidité, concentration en sel, saturation en eau, etc.), en 2D (cellule Hele Shaw) et en 3D (récipients cylindriques en PTFE) avec un milieu poreux formé par des billes de verre. Les expériences sont analysées à partir d'images à haute définition prises à intervalle régulier accompagnée d'un balayage de la surface par laser 3D et d'une visualisation par rayons X. Ceci permet notamment de quantifier la croissance, l'épaisseur et la vitesse de déplacement de la croute de sel ou encore d'obtenir des motifs originaux de structuration.

Les changements contrôlés de la morphologie, du déplacement et du détachement de la croûte sont présentés en faisant varier certains facteurs environnementaux. En plus des informations détaillées sur le déplacement des croûtes compactes et le processus de détachement de la croûte, les expériences montrent qu'une croûte compacte peut évoluée vers une morphologie ramifiée et vice versa. Les expériences montrent également que deux types différents de motifs cellulaires peuvent être obtenus à la surface d'une croûte de sel dans des conditions de laboratoire bien contrôlées.

Une modélisation simple du transport réactif dans la croute couplant le transport, l'évaporation, la dissolution et la précipitation des solutés a ensuite été développée afin d'aider à analyser les résultats expérimentaux et de développer des modèles prédictifs. En particulier, la modélisation indique que tous les phénomènes mis en évidence dans les expériences peuvent être expliqués par la combinaison de processus couplés d'évaporation, dissolution et recristallisation.

Abstract

Halite (NaCl(s)) is often found in nature as large efflorescence salt crust deposits (salt flats). Reports show that salt crusts can greatly affect the evaporation process and can lead to puzzling phenomena, such as the formation of salt domes or crust detachment from the underlying porous host.

In this context, the present work has the objective to bring forth a better understanding of salt crust formation and its dynamics through original laboratory-based experiments put against a simple modelling approach. A series of experiments are conducted in well controlled laboratory environment (temperature, humidity, salt concentration, water saturation, etc.), in 2D (Hele Shaw cell) and 3D (PTFE cylindrical containers) packed with a glass bead porous medium. The imaging is done with time-lapse high definition photography, while accompanied by 3D laser surface scanning and X-ray based visualization. These allow identifying and quantifying crust behaviors such as growth, size, speed of displacement or even pattern formation.

Controlled changes in crust morphology, displacement and detachment are presented by varying certain environmental factors. In addition to detailed information on the displacement of compact crusts and the crust's detachment process, the experiments show that a uniform compact crust can be changed into a branched morphology and vice versa. Furthermore, there are presented two types of salt crust cellular patterns which can be obtained under well controlled laboratory conditions.

Simple reactive transport modeling coupling solute transport, evaporation, dissolution and precipitation was then developed in order to help analyze the experimental results and develop predictive models. In particular, the modelling indicates that all the phenomena evidenced in the experiments can be explained by the combination of coupled evaporation - dissolution-recrystallization processes.

Acknowledgments

This thesis was done as a multi-laboratory and multi-disciplinary collaboration, the primary laboratory was the IMFT and as secondary there were the GET and LMDC. Although it never felt like that, all these, to me, felt like my laboratories and there was no difference. This has been the case from the beginning as all have been very welcoming, patient and helpful with me. The amount of people that I need to thank is quite large, it has been quite an adventure, and I hope not to miss any of them.

During this thesis there were many hard moments when I felt confused or just wanted to give up, but I never did and this is due to the kind and warm people that were my teachers and supervisors. They all proved to be as good a person as they are in their own fields of research. So they all deserve my thanks and gratitude for all their help and guidance they provided. My most sincere thank you for offering me the opportunity to work on this thesis with you. Marc Prat, Catherine Noiriel, Paul Duru, Ariane Abou Chakra and Sandrine Geoffroy you all have helped me tremendously on every aspect of this thesis and with your help I feel like I have grown both professionally and personally.

Marc Prat offered me so much time while following my progress in the experimental work helping me with the new ideas I had and their interpretation. Always pushing me to improve as not always experiments went well. He was the driving force behind the mathematical modeling part of the present thesis. However, he was very understanding of the time it takes to do a proper experiment and was always there when I had a question or needed some advice. He devoted a lot of his time just to talk with me about my new ideas and supported me in experimenting with them. Due to these long conversations we managed to have the present work. I consider myself lucky to have worked with him.

Catherine Noiriel was one of my previous supervisors, during my internship, and became my thesis co-supervisor. To her I owe the introduction in scientific studies and image processing. Both of which I enjoy tremendously and I will always be thankful to her for introducing me to them. She was the voice of reason and balance during this thesis. Her help truly made me evolve as a student and as a person. There was never a moment when she didn’t have time for me or lost patience during these years of studies. She read so many of my bad drafts and made them pertinent teaching me along the way. Whenever I had a technical problem or just needed some advice I always felt that I could count on her. After all these years I feel that she was not only my supervisor but also a friend.

Paul Duru was the teacher who introduced me to the IMFT laboratory. As such he taught me what experimental setups to use and how to do a proper one myself. He represented the experimental beginnings of my thesis. Due to his experience I was able to fully understand how the setups should be done and why. In the second part of my thesis he also became the help I needed in the X-ray department of the laboratory. So I am very thankful for all his input and help throughout this endeavor.

Ariane Abou Chakra and Sandrine Geoffroy have always been the help I needed in the LMDC laboratory. There I was able to teach and have answers in the mechanical part of my studies. I will always be thankful to them for all the patience and understanding they had with me. Especially Ariane who was always there when I needed to learn or find a mechanical solution even if some of them never made it out of the design stage.

Marc, Catherine, Paul, Ariane, Sandrine I truly feel that I was lucky to meet and work with you.

On the experimental part I would have never been able to do a successful experiment without Ruddy Soeparno, Julien Lefort and Sebastien Cazin.

Ruddy was always a breath of fresh air with his extreme positivity and happiness. He has helped me in the beginning of my thesis so much and made so many things that I can't even count. The saying was if you need something ask Ruddy he will make it appear. He was the back bone of my experimental setup construction in the beginning of this thesis. As such I would like to thank you for all the help.

Julien was the person responsible for the second part of the thesis. He probably spent more time with me in the laboratory than anybody else. The endless overtime hours he lost helping me start experiments before the laboratory closed so that I won't lose them. The patience he had with all the small modifications on my setups so that they were perfect and I could get the best possible results. Even on a personal level he became a good friend that I will always treasure. So thank you Julien for all of your efforts and spent time.

Sebastien was the imaging responsible because of him I always had all the cameras that I needed and the right lenses for them too. Thank you for trusting me with so much equipment and always helping me when I needed it.

I would also like to give a big thank you to the members of my jury for agreeing to evaluate my thesis and especially for the way they looked at my work. Their input was priceless and very encouraging. Their point of view was very helpful in terms of future directions that I should take and where there is a need for a more in depth study. Finally, their comments and approach gave me the final confidence that I needed in order to consider myself a member of the scientific community.

I would like to thank globally the laboratories that took part in this thesis IMFT, GET and LMDC and say that I always felt welcomed in these establishments. The help that they offered was essential for the present thesis and as such I am grateful for their help.

On a personal level I would like to thank my friends and family. My mother and father that supported me unconditionally throughout this complicated period in my life. A special thanks to my brother Erol who helped me move to France and do the initial paperwork (only people that went through the French system can understand) as well as with my initiation as a PhD student.

Finally, I would like to say thank you to everybody involved as this was a wonderful experience. This wouldn't have been the case without each and every one of them!

Table of contents

Introduction **1**

Chapter I Dynamics of salt crust formation in a porous medium **4**

I.1. Evaporation of saline solutions and porous media 4

I.1.1. Wick and drying situations 5

I.1.2. Dynamics of evaporation 7

I.1.3. Solute transport 8

I.1.4. Precipitation of salt 10

I.1.4.1. Chemical conditions for precipitation 10

I.1.4.2. Precipitation patterns in the wick and drying situations 10

a) Subflorescence – efflorescence 10

b) Branched vs compact efflorescence (crust) 11

c) Efflorescence root systems 12

d) Efflorescence distribution and influencing factors 13

e) Efflorescence dynamics 15

f) Evaporation and formation of subflorescence 15

I.2. Impact of efflorescence on drying kinetics 16

I.3. Patterned crusts 18

I.4. Modelling of salt crystallization dynamics 19

I.5. Other salts 20

Chapter II Laboratory induced patterns **27**

II.1. Objective and general description of the study 27

II.2. General description of the experiments 29

II.2.1. Concept 31

II.2.1.1. Design of the saturation and drying conditions of the experiment 31

II.2.1.2. Choice of porous medium 32

II.2.1.3. Choice of brine concentration and initial experimental configuration 32

II.2.2. Driving phenomenon: Influence of steady-state flow in porous media 33

II.2.2.1. Pore invasion and transient flow 33
II.2.2.2. Porous media local and global concentration gradients 35
II.2.2.3. Pretesting the experimental environment conclusions 37
a) Chosen environment and protocol 37
b) Table II.I header disambiguation 38
c) Environment: conclusions 40
II.2.3. Driving phenomenon: Influence of steady-state flow in porous media 42
II.2.3.1. Pore invasion and transient flow 42
II.2.3.2. Porous media local and global concentration gradients 44
II.2.3.3. Pretesting the experimental environment conclusions 46
a) Chosen environment and protocol 46
b) Table II.I header disambiguation 47
c) Environment: conclusions 49
II.2.4. Controlled experiments: reducing the uncertainty of the process 51
II.2.4.1. Controlled boundary conditions 51
II.2.4.2. Solving the deionized water injection inconsistency 52
II.2.4.3. Final sample configuration 54
II.3. Experimental results 55
II.3.1. Successful recipe for GP type patterns 56
II.3.2. Adapting the successful GP recipe to form a RP crust 68
II.4. Discussion 71
II.4.1. GP type crusts 71
II.4.2. RP type patterns 74
II.5. Conclusions 75
Chapter III Dissolution – precipitation driven upward migration of a salt crust 80
III.1. Abstract 80
III.2. Introduction 80
III.3. Experimental set-up 82
III.4. Results 83
III.5. Modeling 84

III.6. Discussion 87

III.7. Conclusions 90

III.8. Appendix A Pre-processing of experimental data 91

III.9. Appendix B Closed – form equations for the crust top and bottom surfaces velocity 93

Chapter IV Air gap formation between an efflorescence salt crust and the porous medium surface under deficit evaporation conditions 97

IV.1. Abstract: 97

IV.2. Absorption 110

IV.3. Evaporation 115

IV.4. Summary 118

IV.5. Discussion-conclusions 119

IV.6. Appendix A 121

Chapter V **Moving salt crust in a Hele-Shaw cell: from compact to branched morphology 126**

V.1. Abstract: 126

V.2. Introduction 126

V.3. Experiment 127

V.4. Results 129

V.4.1. Images 129

V.4.2. Crust thickness 131

V.4.3. Absorption rate –Evaporation rate 133

V.4.4. Absorption rate – Evaporation rate – Crust-thickness – Crust displacement 138

V.4.5. Evaporation rate, Kelvin effect 144

V.4.6. Crust shrinkage 148

V.4.7. Stabilization, destabilization (branched morphology) 149

V.4.8. Crust frozen state – Crust apparent effective diffusion coefficient 151

V.4.9. Crust displacement regimes 153

V.4.10. Conclusion 156

General conclusions and perspectives 160

Introduction

Halite or $NaCl_{(s)}$ is found in abundance naturally, this makes it of high importance for different areas, from use such as a storage site for gas (Drying Rate Measurements in Convection- and Diffusion-Driven Conditions on a Shaly Sandstone Using Nuclear Magnetic Resonance | SpringerLink, n.d.) to being regarded as having high destructive properties such as responsible for porous material degradation, as an example building heritage weathering (Flatt et al., 2017) as well as an ecological and agricultural problem due to the fact that soil salinization is becoming increasingly problematic (Jamil et al., 2011). While when found naturally in large over the ground deposits (salt flats) can form spectacular and regulated polygonal patterns such as the ones in Death Valley – Badwater Basin (Death Valley National Park, California, U.S.A.) or the biggest Salt flat in the world Salar de Uyuni (Daniel Campos Province, Bolivia). Although these patterns are a source of fascination for the scientific community, their formation is still a matter of debate and no laboratory controlled reproduction is available yet.

In nature halite gets solubilized either by water from the ground, rain or as a result of human activity thus forming a brine. Which in term finds its way into porous materials (usually as a result of capillary effects). This porous medium (such as building materials or even the ground itself) then becomes imbibed with brine. As the water in the material starts to evaporate, the ion concentration (Na^+, Cl^-) of the brine starts to increase until its point of supersaturation. Over this point, halite can precipitate (crystallize) thus forming crystalline structures. If these structures are formed on the surface of the porous medium they are called efflorescences, while if they appear inside it they will be called subflorescences. If the type of crystallization is grouped by morphology, two types of crystalline structures can be distinguished: the first is a discrete and well defined one as it only appears in certain spots over the porous medium known as branched or cauliflower (patchy), and the second is an evenly spread one that covers the whole available surface known as a crusty formation. The latter will be mostly the subject of the present work due to the fact that crusty formations are not a fully understood subject. Reports show that once formed, they can be responsible for lowering the evaporation rate by more than one order of magnitude (Eloukabi et al., 2013). In addition, they can form hollow salt domes also referred to as blistering type of phenomenon at the surface of the porous host (Nachshon et al., 2018) or large (order of meters) highly ordered polygonal patterns.

While if one takes into consideration the detachment and displacement mechanics, the reports show that even if the crust forms on the porous medium still there are some root systems into the topside pores (Desarnaud et al., 2015), which once the actual detachment happens, get broken due to the uneven characteristic of the phenomenon.

Since it is known that salt crystallization in pores can generate stresses (Flatt et al., 2007; Fletcher & Merino, 2001; Naillon et al., 2018; Weyl, 1959) and important damages (Noiriel et al., 2010), it is tempting to consider that some of the above mentioned phenomena, such as the blistering phenomenon or the formation of polygonal patterns, is due to mechanical effects. However, the mechanics of salt crusts are not yet fully understood. There are some suppositions as seen in (Lasser et al., 2020), but there are no clear mechanics behind it thus the need for a more in depth analysis. As it will be shown, other mechanisms can actually contribute to these phenomena. The knowledge that would be obtained, in term, could help with the problems associated above and not only those. In the case of patterns, one needs to take into consideration that a multitude of factors control and affect the crystallization process, in order to reproduce it.

In the present thesis, a series of studies are presented to better understand the formation and dynamics of salt crystallization in the presence of a porous medium, with an emphasis on new experimental techniques that allow simple mathematical models to be tested against the new data.

In term of these techniques, the common denominator will be the actual salt crust formation as the porous medium will have different properties and shapes/forms such as glass beads, salt grains or the crust itself, and different configurations of grain size and layering will be varied, as experiments will be presented both in 2D (Hele Shaw cell) and 3D (PTFE cylindrical containers). These variations are necessary in order to reproduce certain effects as briefly discussed earlier.

The first chapter will serve as a general bibliographic study in relation to salt properties as well as terminology and current progress in the area. The purpose of this being to introduce the reader to different concepts and problematics in relation to halite crystallization.

The second chapter explores the patterning properties of salt crusts. Here a laboratory controlled interpretation of the naturally formed polygonal patterns is presented. An experimental point of view of the natural phenomena is explored so that certain control factors can be found. The whole process is described and two different reproducible patterns are obtained and shown.

The third chapter will treat the subject of efflorescent salt crust displacement. There a salt crust grown on a glass bead porous medium in a Hele Shaw cell is purified by removal of the glass bead packing substrate. This in order to obtain a self-propelled porous crust in the presence of pure water vapor. This technique allows for a better understanding of salt transport dynamics in actual salt porous media.

The fourth chapter represents a long experimental study on salt crust growth and detachment from its porous host. The experiment is carried out in a Hele Shaw Cell in the presence of glass bead porous media. The main difference from the previous chapter is that here the salt crust is mechanically detached from the porous medium but not purified of entrapped beads. Thus the crust has a double porous layer structure. The bottom part is glass beads cemented in salt while the top is just a crystalized porous salt layer. This type of experiment allows for data to be collected on salt ion transport in porous media in the presence of dissolution-precipitation-recrystallization processes.

The fifth chapter is based on the concept of creating instabilities in the salt crust growth morphology. This is an experiment carried out in a similar setup as the one in chapter three as the preparation of the crust is purified from the bead porous media in a Hele Shaw Cell. Here the studied phenomenon is the change of crust morphology, due to modifications in the balance between adsorption (condensation) of water at its bottom and its potential evaporation at the liquid-gas interface. This experiment shows how a crust can evolve from a crusty type to a branched (discrete) one and that the process can be reversed.

Chapter I

Dynamics of salt crust formation in a porous medium

I.1. Evaporation of saline solutions and porous media

In a porous medium, crystallization can be the result of either a lowered solubility due to a variation in temperature, brine composition, or to an increase in ion concentration as an effect of evaporation at the liquid-gas interface. The combined action of several phenomena is also possible. In the context of this study, the emphasis will be put on the situation where evaporation is the governing phenomenon that leads to an increase in concentration to the point of crystallization. In the following work, we limit the study to the situation where the crystallization growth can appear both inward and outward of the porous medium as the product of evaporation, and thus the temperature variation is considered negligible. The general goal here is to familiarize with how one can predict and if possible model where the crystallization will take place, i.e. in which pores, on the surface or in depth, at isolated points or uniformly distributed. In addition, it permits to check its impact on evaporation, i.e. does the formation of a salt crust negatively impact the evaporation rate compared to the expected pure water one, or even block it.

Another closely related question that will be briefly discussed concerns the impact of crystallization on the porous structure itself and its effects: cracking, chipping, etc., as well as the possible coupling between these structural alteration phenomena, transport and crystallization. Although the degradation of porous materials has been linked to crystallization and is a very important topic of study, the evaporation of saline solutions in porous media will not be discussed in this chapter. Here the emphasis is therefore on the processes of evaporation - transport – crystallization in the absence of major mechanical effects. Here, we will only discuss a simplified laboratory approach as such a single salt solution (sodium chloride) will be our subject with very few exceptions. Here the assumption is that many generic aspects can be studied with ease. In fact, this chapter will mainly focus on the case of a solution containing only water and sodium chloride, this salt being widely encountered in nature and applications. This gives the case of sodium chlorine solutions an important place and specific interest beyond the generic aspects common to all saline solutions.

With this framework established, the covered main points follow the order of the evaporation - transport - crystallization chain. We will therefore begin by recalling a few basic elements of evaporation in a porous medium. The transport aspect will follow as the factors affecting the spatial and temporal evolution of the ion concentration will be presented in relation to the interior and exterior of the porous medium. As well as discussing the coupling between evaporation - transport and precipitation. Another important factor concerns the scale of analysis and discussion. As for other situations involving a porous medium, the phenomena of interest here can be studied at the scale of a single pore, e.g. (Naillon et al. 2017, 2018, 2019), a pore network e.g. (Sghaier et al. 2014; Veran-Tissoires and Prat 2014; Dashtian et al. 2018) or the classical framework with the continuous porous media approach e.g. (Bear and Bachmat 1990). The favoured approach in this chapter is the latter. However, as this approach is

sometimes ill-suited for some of the mentioned phenomena interpretation or analysis, it will be occasionally abandoned when deemed necessary.

The proposed literature review in this chapter is adapted and modified in order to suit its current purpose from (Prat. 2021).

I.1.1. Wick and drying situations

Despite the numerous situations involving evaporation in porous media, from soil evaporation (e.g. Or et al. 2013), to the drying stages involved in the production of many types of porous materials (e.g. Mujundar 2006). Two generic situations emerge, i.e., wick and drying, where transfers can be expected to be almost one-dimensional along the vertical direction. These are shown schematically in Fig. 1.1. For both of these situations, evaporation occurs at the porous medium upper surface.

In the wick situation (Fig. 1.1 a), the porous medium at its base is in contact with an aqueous solution of fixed ion concentration. Due to the capillary effects resulting from the upper surface curvature of the menisci of the porous medium, this solution is continuously driven through the porous medium up to its surface, where water can evaporate. This corresponds with the case where the capillary effects are sufficiently strong so that the porous medium will be permanently and fully saturated with solution. In some cases, however, the evaporation front is established inside the porous medium and no longer on its upper surface e.g. (Noiriel et al. 2010).

In the wicking situation, the medium is considered completely saturated as long as the liquid at its bottom is in place. While in the drying situation (Fig. 1.1b), the evaporation is not compensated by a fresh supply of liquid water. The walls of the sample are impermeable in both situations and limit the evaporation front to the upper surface. The medium therefore gradually desaturated as a result of evaporation. The main difference being that the liquid lost due to evaporation in the drying situation does not get replaced by new one from a supply at its bottom.

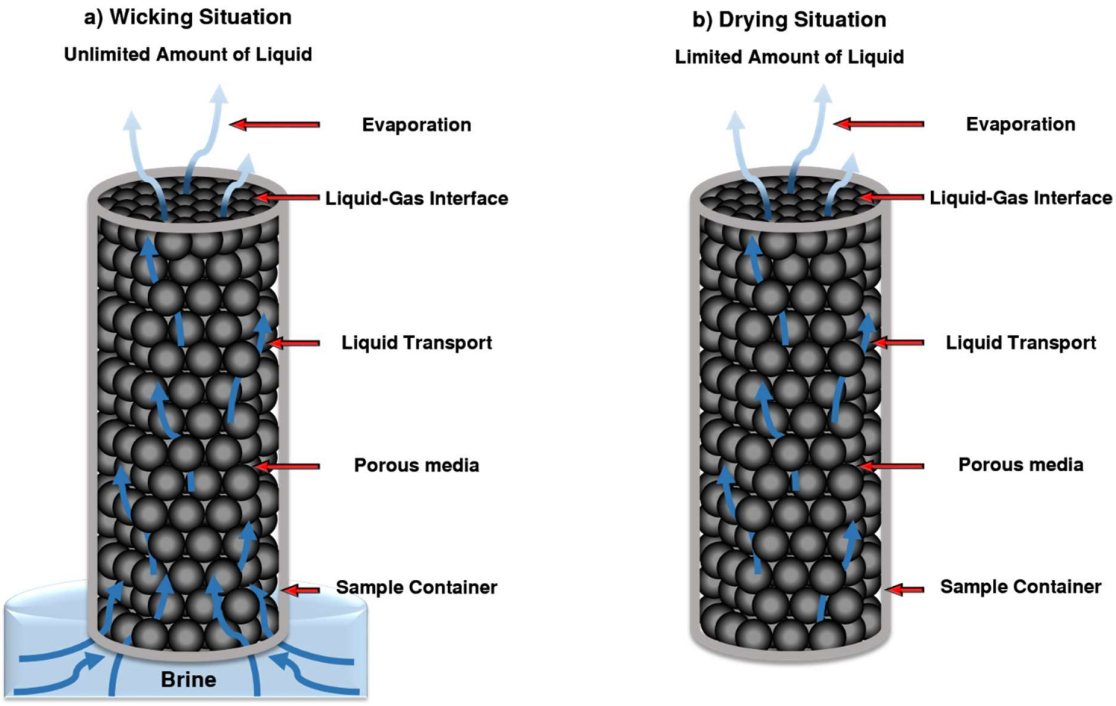


Figure 1.1. The two generic situations of evaporation from a porous medium

The following considerations will be taken in the context of a completely saturated porous medium as it allows for a simpler approach.

Evaporation in the case of drying is usually characterized by the evolution of the evaporation flux j at the surface as a function of the mean saturation $\bar{S}$ of the sample ($\bar{S}$ is the ratio between the total volume of solution in the porous medium and the total volume of available the pore space, for $\bar{S} = 1$ the medium is completely saturated while for $\bar{S} = 0$ the medium is completely dry). The j ($\bar{S}$) curve is called the drying kinetics curve (Van Brakel 1980).

The pore size has a direct impact on the drying kinetics (Van Brakel 1980). Usually, in this context, a distinction is made between a hygroscopic medium that is capable of fixing by physical adsorption a quantity of water which represents a large fraction of the pore volume, from a capillary-porous media in which this fraction is very low. The latter typically corresponds to media with pores larger than about 0.1 - 1 µm while the strongly hygroscopic medium has a pore majority of smaller ones.

In the following, we will only be considering the case of capillary-porous media. These, generally, are characterized by a three period drying kinetics as in (Fig.1.2a). The first period is named constant rate period of evaporation or CRP (“Constant Rate Period”) due to the fact that the evaporation flow remains close to the flow experienced in the beginning of drying. The second period is said to have a decrease in drying rate or FRP ("Falling Rate Period") because the period experiences a net decrease in evaporation rate. Finally, the last period called the RFP ("Receding Front Period") which is characterized by a slow decrease in evaporation rate. The latter corresponds to a period in which evaporation occurs entirely inside the porous medium and thus no longer at its surface. The FRP represents a transition period between the CRP where evaporation takes place mainly at the surface and the RFP where it takes place mainly inside the media. In reality the situation has a more subtle nuance and depends on the competition between the capillary, viscous and gravity effects (Prat 2002). The just described

drying kinetics corresponds to the situation frequently observed in laboratory experiments where capillary effects are predominant, at least over a good part of the drying period. So we call this case the capillary regime and is the only one we take into consideration in this chapter.

Finally, it should be noted that some authors, e.g. (Shokri and Or 2002) distinguish only two periods and not three. The first corresponds to the CRP and the second is a FRP-RFP merge. It should also be noted that in fact the evaporation flow often decreases a little during the CRP and therefore this period should be designated as the 1st drying period as it is more suitable than a constant evaporation rate one.

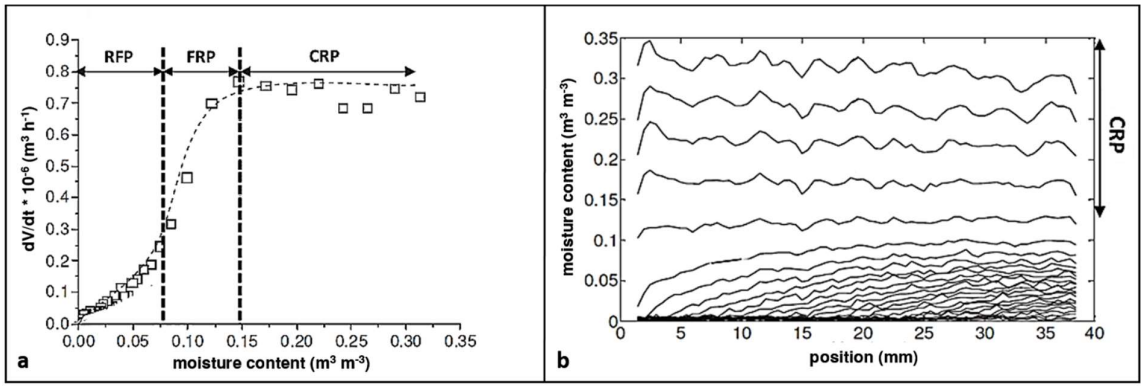


Figure 1.2. a) Typical drying kinetics of a capillary-porous medium at room temperature (figure adapted from Gupta et al. 2014), V designates the volume of water evaporated, b) Saturation profiles for the capillary regime during drying of a capillary-porous medium (figure adapted from Gupta et al. 2014). The water content is equal to εS where S is the water saturation and ε the porosity of the medium.

Despite what can be read in many publications devoted to the porous capillary media drying, there is no completely satisfactory model, that is to say without an adjustment parameter, making it possible to predict the drying kinetics. We can refer, for example, to (Vu and Tsotsas 2018) for a presentation of the most classical model. On the other hand, a well-documented aspect and in agreement with the "theory" of drying is that in the capillary regime and during a good part of the CRP the profiles of saturation are (almost) uniform spatially. This is illustrated in Fig. 1.2 a (Gupta et al. 2014). This property exploit is presented in the following section.

I.1.2. Dynamics of evaporation

The velocity field in a porous medium induced by evaporation of the solution is generally a very important aspect in relation to ion transfer, due to the role it plays regarding the convective effects thus the transport of ions in solution. In the case of the saturated "wick" situation illustrated in Fig. 1.1a, the solution is simple when the medium is homogeneous, that is to say when the porous medium porosity and permeability do not vary spatially. The filtration rate is spatially uniform, directed upwards and its non-zero component is equal in all points as follows:

$$U_z = \frac{j}{\rho} \tag{1.1}$$

where j is the evaporation flux (kg / m2 / s) and ρ is the density of the solution. For the drying configuration of Fig. 1.1b, the speed during CRP varies linearly with position along the vertical, e.g. (Huinink and Michels 2002, Moghaddam et al. 2017):

$$U_z(z) = \frac{j}{\varepsilon S \rho}\frac{z}{H} \tag{1.2}$$

where $z = 0$ at the bottom of the sample and $z = H$ at the top, where H is the dimension to the sample's top surface the place where evaporation occurs, ε is the porosity. S is obtained by simple mass balance (Huinink and Michels 2002):

$$S = 1 - \frac{j}{\varepsilon \rho H} t \tag{1.3}$$

taking advantage of the fact that we limit ourselves here to the period where S is spatially uniform.

I.1.3. Solute transport

The solution is an ionic one and the modelling of ion transport implies an interest in the transfer phenomena occurring for this type of solution. Interesting material on this topic can be found in (del Rio and Whitaker 2016). A simplified approach that consists in reducing transport to a single equation for the dissolved salt is generally adopted, e.g. (Huinink and Michels 2002, Guglielmini et al. 2008; Hidri et al. 2013; Diouf et al. 2018) and not as in (del Rio and Whitaker 2016):

$$\frac{\partial \varepsilon \rho S C}{\partial t} + \nabla.(\rho \mathbf{U} \nabla \mathrm{C}) = \nabla.(\rho \varepsilon S D_S^* \nabla \mathrm{C}) \tag{1.4}$$

where C is the mass fraction of ions. In the most common situation, the Péclet number built on the pore scale is very small so that the mechanical dispersion effects (Dagan 2012) are negligible. D_S^* is therefore the effective ion diffusion coefficient. The latter is a function of saturation, e.g. (Hidri et al. 2013). In that case, the ions (Na^+ and Cl^-) are considered to have the same diffusion coefficient and no electrical interaction between them is assumed.

A transport equation is attributed for each ion, i.e., one for Na^+ and one for Cl^- in our case. In the porous media continuous approach context this amounts to considering the transport equation,

In the case of a saturated wick, Eq. (1.4) applies, with S = 1. By taking as characteristic spatial scale the sample height H and as characteristic speed the evaporation rate j / ρ, Eq. (1.4) can be written as 1D dimensionless form as (the variation of the density with the mass fraction in ion being neglected):

$$Pe\left(\frac{\partial C^*}{\partial t^*} + \frac{\partial C^*}{\partial z^*}\right) = \frac{\partial^2 C^*}{\partial z^{*2}} \tag{1.5}$$

where $Pe = \frac{j\,H}{\varepsilon \rho D_S^*}$ is the Péclet number ($z^* = z / H$, $t^* = t /(H\rho\,\varepsilon / j)$, $C^* = C / C_0$)

In the saturated wick case, using a mass fraction of salt which is spatially uniform and equal to the mass fraction C_0 in solution, an analytical solution giving the concentration evolution profile can be obtained (Pel et al. 2018):

This solution shows a very good agreement with the NMR measured profiles by (Pel et al. 2018). As illustrated in Fig. 1.3, the profile is characterized by the marked gradient zone which develops from the evaporative surface. In this gradient zone, the concentration decreases exponentially with depth. At each instant, the maximum concentration is at the surface where it increases linearly over time. Further inside the medium the concentration gradient becomes very low as the mass fraction of ions is essentially uniform and equal to C_0. This is the profile obtained for the situation where the Péclet number Pe > 1, so that the convective effect combined with the condition that the ions cannot escape from the medium's evaporative layer leads to a preferential accumulation at its surface as shown in Fig.1.3. When $Pe << 1$, convection is negligible by comparison to diffusion, and the concentration distribution is uniform, and equal to ρC_0. As illustrated in Fig. 1.3b, the situation in the case of drying is qualitatively similar to the wicking situation when the Péclet number is large, with the formation of a gradient zone in the upper part of the sample.

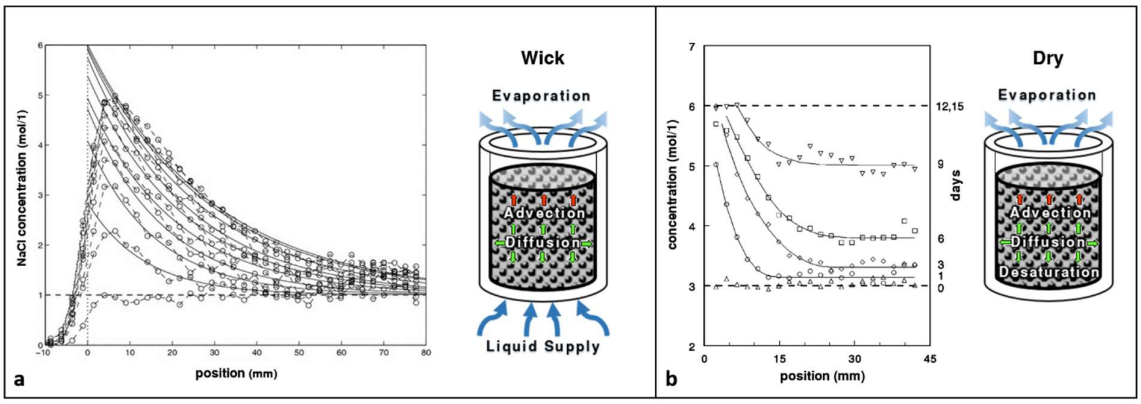


Figure 1.3. Typical profiles of NaCl concentration at moderate Péclet number with 0 as the evaporative surface position. a) Wicking situation (figure adapted from Pel et al. 2018), b) Drying situation (figure adapted from Pel et al. 2002).

However, the variation in concentration in the case of drying does not only result from the convective effect. As during drying the pore saturation decreases, the concentration needs to increase on average due to this effect, since the dissolved salt quantity occupies a volume of liquid which decreases during this time. Thus during the CRP we have $\bar{C}(t) = S^{-1}C_0$ (by neglecting the solution's density variation with the mass fraction in ions). In the $Pe << 1$ case the mass fraction of salt is spatially uniform and equal to $C(t) = S^{-1}C_0$.

For more details in the case of drying, one can refer to (Huinink and Michels 2002; Sghaier et al. 2007; Guglielmini et al. 2008; Hidri et al. 2013, Rad et al. 2013). Unlike in the wick situation, no detailed comparison between experimental profiles and predictions based on Eq. (1.4) appear to have been done. We can however cite (Shokri 2014) where in fact it is concluded that Eq. (1.4) only allows a qualitative prediction. However, the comparison presented in (Shokri 2014) is for a case that only has about ten grains over the height of the sample, which makes doubtful the comparison value, given the lack of scale separation (ten particles correspond to less than a representative elementary volume size (REV)).

I.1.4. Precipitation of salt

I.1.4.1. Chemical conditions for precipitation

Precipitation of salt is driven by the law of mass action. Halite precipitates according to the following $Na^+ + Cl^- \leftrightarrow NaCl_{(s)}$, with the equilibrium constant $Kps = a_{Na+} \times a_{Cl-}$, where a_i denotes for the chemical activity of species *i*.

Later, we will resume activities to concentrations, although the high solubility of $NaCl_{(s)}$ (360 $g.l^{-1}$ or 0.264%w at 25 °C) let us know that deviation to an ideal solution behavior is expected (Burgess, 1978).

A solution is supersaturated with respect to halite when the ion activity product (IAP) is larger than the equilibrium constant, in other words, when the saturation index $\Omega = IAP/Kps > 1$ ($\Omega = 1$ at equilibrium, and < 1 when the solution is undersaturated with respect to the mineral). However, a question is whether crystallization initiates just above the equilibrium or requires a larger supersaturation index ($\Omega > 1$). This point is an important subject especially in direct link with the crystallization pressure concept as presented in (cf. (Correns, 1949; Naillon et al., 2018; Noiriel et al., 2010), the latter being directly dependent on supersaturation. In model systems, such as capillary tubes or single channels (Desarnaud et al. 2014; Naillon et al. 2017, 2018), quite notable supersaturations ($\Omega \sim 1.7 - 1.8$) have been reached before crystallisation stats. On the other hand, the estimates from profiles measured by NMR in porous samples, e.g. (Pel et al. 2018) suggest on the contrary a negligible supersaturation ($\Omega \sim 1$). One can object that the NMR gives a spatially integrated measurement and therefore incapable of following the spatial fluctuations of concentration at the surface, where moreover the measurement is unreliable (the edge effect and the spatial resolution problem). In addition, the crystallization kinetics is very fast in the case of NaCl (Naillon et al. 2017) so that once crystallization has started, the excess ions are very quickly consumed. The fact remains that for the moment this question remains unanswered. In this regard, can we expect that in the case of real media and/or in practice are the supersaturation levels comparable to those measured in model systems?

I.1.4.2. Precipitation patterns in the wick and drying situations

a) Subflorescence – efflorescence

For the wick and drying reference situations presented above, the maximum concentration of solute is at the surface of the porous medium (with the exception of particularly very low Péclet numbers) and crystallization is therefore expected at the surface. We call efflorescence the sets of crystals developing on the evaporative surface. In other circumstances, the crystallization concentration can be reached inside the medium, for example in the wicking situation if the conditions are such that only part of the porous medium is imbibed by the solution (Noiriel et al. 2010). These groups of crystals that develop within the porous medium are called subflorescence. Figure 1.4 illustrates these two types of crystallization formed during a model medium drying experiment (Sghaier et al. 2014).

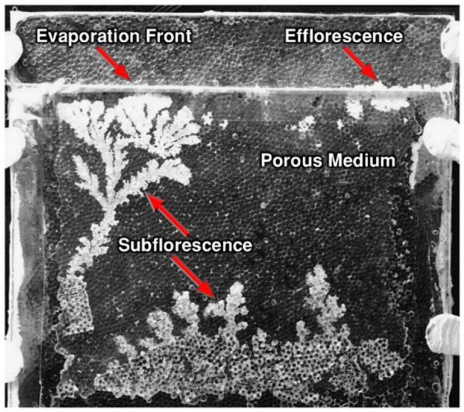


Figure 1.4. Efflorescence and subflorescence in a model porous medium (figure adapted from Sghaier et al. 2014). The salt structures (crystals) formed on the medium top are referred to as efflorescence while the ones formed in the pores as subflorescence.

Another very important point to be taken into account is that these structures are also porous (Sghaier and Prat 2009; Veran-Tissoires and Prat 2014). This being a key element in the analysis of their growth and thus their impact on evaporation.

b) Branched vs compact efflorescence (crust)

An important characteristic of the efflorescence development (and subflorescence) is that their morphology can differ quite significantly depending on the environmental conditions (T°C, relative humidity, etc.)). A rough classification consists in distinguishing two main types (Eloukabi et al. 2013): branched and compact efflorescence (Fig. 1.5). Branched efflorescence, also called cauliflower efflorescence or discrete efflorescence (Veran-Tissoires et al. 2012a) often does not cover entirely the porous medium surface. The glass beads forming the porous medium are, for example, visible between the efflorescence structures in Fig. 1.5a. Compact efflorescence is also called a crust. As shown in Fig. 1.5b, this type of efflorescence tends to develop by covering the entire porous medium surface. Thus the crust-like efflorescence shown in Fig. 1.5b completely covers the upper surface of the porous medium. By comparison with the discrete efflorescence in Fig 1.5a, the underlying porous substrate is not visible in Fig 1.5b.

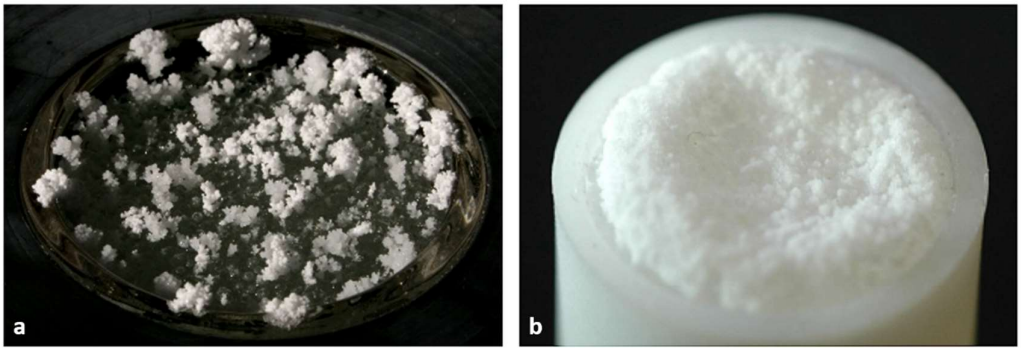


Figure 1.5. (a) Example of discrete efflorescence. (b) Example of compact efflorescence

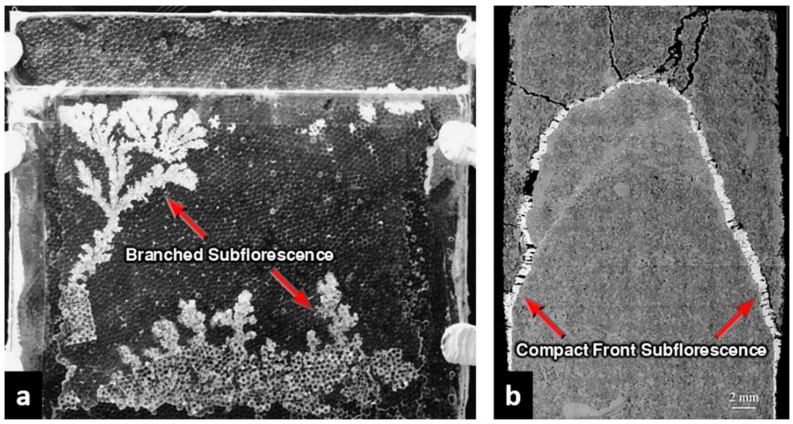


Figure 1.6. a) Branched subflorescence observed in a model system with large pores (order of 100 µm) (figure adapted from Sghaier et al. 2014) b) Image of compact (front) subflorescence in porous rock image obtained by X-ray micro-tomography (figure adapted from Noiriel et al. 2010).

In the case of subflorescence structures, we can observe as with efflorescence, branched or compact subflorescence types depending on the environmental conditions. These types can be seen illustrated in Fig. 1.6. In theory, large pores (100 µm and beyond) and rather low evaporation rate (ambient relative humidity) favors the appearance of discrete structures whereas a smaller porous substrate in the presence of higher evaporation rates (e.g. dry air) promote the formation of a compact structure. Understanding the morphology transition with pore size and/or evaporation conditions, however, remains a completely open subject. We can find some indications on this transition and the beginning of an explanation in the literature, e.g. (Veran-Tissoires and Prat 2014), but finally a lot of studies still need to be done so that these transitions can be fully understood.

c) Efflorescence root systems

As can be seen in Fig. 1.4 and also illustrated in Fig. 1.7, efflorescence is not a strictly superficial structure. The crystallization occurs not only on the porous medium surface but also within its top layer over a distance of a few grain sizes, 1-3 grain sizes in the Fig. 1.7 example. Although the development of efflorescence modelling is for the moment a practically blank subject, see however (Licsandru et al. 2019), this element is certainly one to be considered in the future models, particularly in connection with the impact of efflorescence analysis on drying kinetics as it will be discussed later in this chapter.

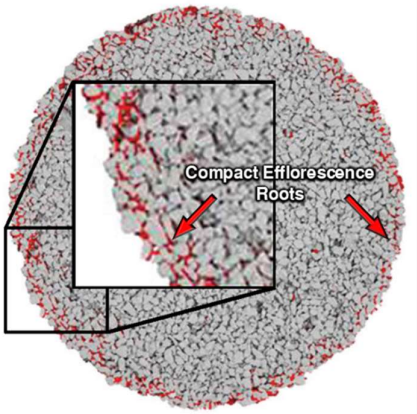


Figure 1.7. Image of compact efflorescence (in red) on a porous rock surface obtained by X-ray micro-tomography (figure adapted from Desarnaud et al. 2015).

d) Efflorescence distribution and influencing factors

Two stages can be distinguished in the formation of efflorescence, the “nucleation” stage (in reality crystals can be generally observed in experiments only after they have reached a detectable size thus larger than the initial first seeds), and the growth stage. One point of interest is to predict where the first crystals will form on the porous medium surface. As shown in Fig. 1.8, this question is not trivial even for simple configurations as mainly considered in this chapter.

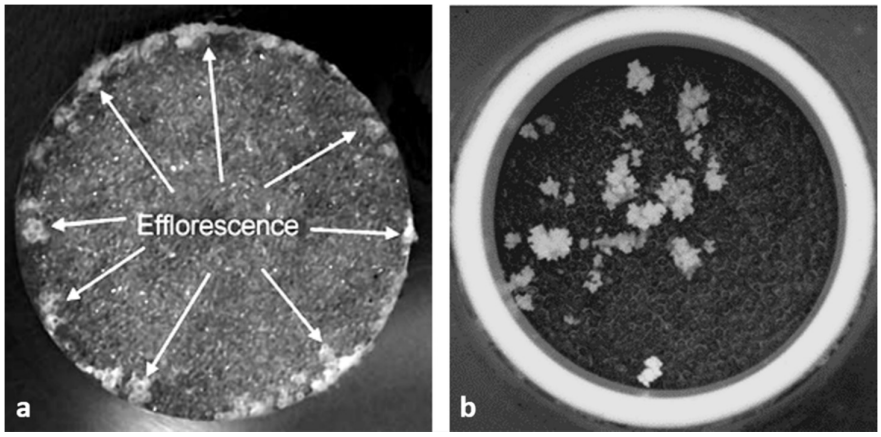


Figure 1.8. a) Fairy ring: discrete efflorescence forming at the sample’s upper surface periphery (figure adapted from Hidri et al. 2013), b) discrete bloom without peripheral effect (figure adapted from Veran-Tissoires and Prat 2014).

As we can see in the Fig. 1.8, the (discrete) efflorescence can form on the periphery (this structure is called fairy ring just through pure visual analogy with the analogous structure, also called witch's ring, that can form mushrooms) or on the contrary, without noticeable peripheral effect. A detailed analysis for the wicking situation can be found in (Veran-Tissoires and Prat 2014) as for the drying situation in (Hidri et al. 2013), the fairy ring effect is a consequence of the higher evaporation flux in periphery of the sample (and according to Eq. (1.1) therefore of a stronger convective transport effect induced at the porous medium periphery). The distribution of the evaporation flux, cf. (Veran-Tissoires et al. 2012a; Veran-Tissoires and Prat 2014), is similar to the one leading to the classical “coffee ring effect” in the case of the droplet evaporation (Deegan et al. 1997) . On the contrary in the case of the experiment illustrated in Fig. 1.8b, the evaporation flux distribution is much more uniform at the

surface and the peripheral effect is then no longer obtained. Thus, a first rule emerges. In the case of a homogeneous medium, the porous medium surface places where the evaporation is strongest are places of preferential efflorescence formation.

The discrete aspect of efflorescence in Fig. 1.8 cannot be analyzed within the continuous approach framework that is to say from Eq. (1.4), because it involves fluctuations in ion concentrations on a scale smaller than that of the REV. As discussed in detail in (Veran-Tissoires and Prat 2014), the two main sources of concentration fluctuations are related to the porous medium disordered nature (the fact that pore sizes are distributed over a certain range). The first is due to the ion convective transport. As the speed varies spatially from pore to pore due to this disorder, thus causing concentration fluctuations throughout the pore network. Another disorder consequence is that the evaporation flow also varies from pore to pore on the surface. These fluctuations cause spatial fluctuations in velocity in the underlying pores which in turn cause fluctuations in ion concentration. The “nucleation” points are then interpreted as the locations of the local maximum concentration on the surface just before crystallization starts. As discussed in (Hidri et al. 2013; Veran-Tissoires and Prat 2014), another effect can also have an impact in the case of granular media, the locally greater porosity near the walls limiting the sample due to the particular grain arrangement in the vicinity of a wall. Thus the surface most likely places of “nucleation" predicting problem can be seen as a problem of predicting the local maxima of ion concentrations just before the crystallization concentration is reached at the surface.

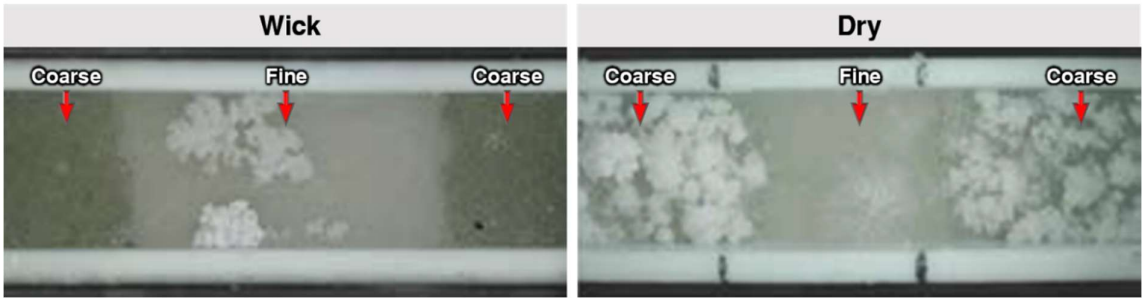


Figure 1.9. The impact of a large-scale heterogeneity on the efflorescence formation site. In the case of a heterogeneous porous medium formed out of a fine bead column placed in between two coarse bead columns (figure adapted from Diouf et al. 2018).

In the case of larger scale heterogeneities (porous media where the porosity and/or the permeability vary spatially), these will generally control the place of crystallization (or at least where the first nuclei will appear). This is illustrated in Fig. 1.9 for the case of columnar heterogeneities (Diouf et al. 2018). As it can be seen in Fig. 1.9 efflorescence develops on the region where the surface has the least permeability (fine porous medium) in the case of wicking, while exactly the opposite can be seen in the case of drying. As explained previously, the concentration evolution is essentially dependent on the velocity field for the wicking situation, while in the drying situation the concentration field depends also on the saturation variation. A consequence of the capillary effects is that in drying, the coarse porous medium will gradually get desaturated while the fine will remain saturated. As analyzed in (Diouf et al. 2018), this preferential desaturation explains the efflorescence development on the coarse medium surface during drying. In the case of wicking, the velocity field structure (the preferential flow in the coarse medium and fine medium redirection towards the top surface) that explains the efflorescence appearance on the fine medium surface. In wicking, this result generalizes to a more complex variation in permeability (Hidri et al. 2019) with a correlation between local concentration surges (picks) and surface velocity field points of stagnation. Further large-scale heterogeneities effect illustrations on the location of crystallization can be

found in (Bechtold et al. 2011; Nachshon et al. 2011a, 2011b; Veran-Tissoires et al. 2012b; Bergstad et al. 2017, 2018).

e) Efflorescence dynamics

The efflorescence dynamics, as in their evolution after the "initial nucleation" stage, is strongly linked to their porous structure. In Fig. 1.10a the phenomenology of growth is illustrated for the case of discrete efflorescence and in Fig. 1.10b the case of compact efflorescence.

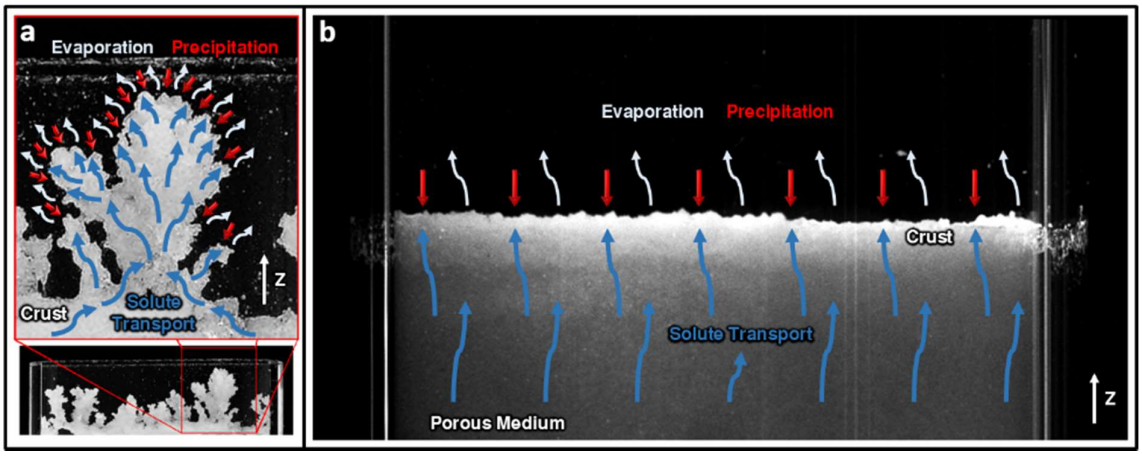


Figure 1.10. Illustration of the main mechanisms involved in the efflorescence growth: a) branched/discrete efflorescence, b) compact/crust efflorescence.

The phenomenology is as follows: due to the porous structure of efflorescence the solution is pumped by capillary action to its periphery where the water evaporates and precipitation contributes to crystal growth. Thus, one would expect a direct link between the efflorescence local growth rate and the local evaporation flux. This correlation has been formally established (Sghaier et al. 2014) in the subflorescence case shown in Fig. 1.6a for which the growth is analyzed in a similar way. Thus for the simple case illustrated in Fig. 1.10b, this suggests a very simple growth law derived from a simple mass balance evaporation flow:

$$\frac{dz_t}{dt} = \frac{C_{sat}\, j}{\rho_{cr}(1-\varepsilon)(1-C_{sat})} \tag{1.7}$$

where z_t is the efflorescence upper surface position (to simplify we consider a surface point where the growth takes place along the vertical), C_{sat} is the equilibrium mass fraction of a saturated solution $C_{sat} = 0.264$), ε is the crust porosity, ρ_{cr} is the crystal density ($\rho_{cr} = 2160\, kg/m^3$). However, we will see in Chapter IV of this manuscript that this law of growth is too simplistic. It is indeed necessary to introduce a correction linked to the transport of ions in the growing crust.

f) Evaporation and formation of subflorescence

Questions similar to that of the efflorescence impact on evaporation rates exist, regarding the impact of subflorescence development. For example, does the development of subflorescence affect evaporation? It seems that this question has been comparatively less studied. Here again, a different impact is expected depending on whether the subflorescence is branched (Fig. 1.6a) or compact (Fig. 1.6b). The experiment on the model medium presented in (Sghaier et al. 2014) with a branched subflorescence (see Fig. 1.6a) indeed leads to a result

similar to the case of branched blooms. That is, a slight increase in the evaporation rate with the development of the subflorescence towards the open surface of the model medium (upper edge in Fig. 1.6a), which is explained by the "wet" nature of the subflorescence. The development of the subflorescence brings the internal evaporation front closer to the surface. Similar results are observed on sand columns (Nachshon and Weisbrod 2015), which is not surprising given the sand grains size used (on the order of 400 μm). The situation where the subflorescence development severely limits the evaporation rate (an analogy to the case of compact efflorescence) has for example been observed in sandstone experiments (pore size ~ 1 - 10 μm) with potassium chloride (Peysson 2012). It can be assumed that a comparable phenomenology must be observed with NaCl if the pores are small enough to lead to a compact subflorescence.

I.2. Impact of efflorescence on drying kinetics

The efflorescence development impact on drying kinetics or on the evaporation flux evolution in the case of the wick situation is dependent on the efflorescence type. When the efflorescence is branched, the evaporation flux is little affected (Elkouabi et al. 2013; Veran-Tissoires and Prat 2014; Shokri-Kuehni et al. 2017a), and can even increase with the efflorescence growth in external air (Sghaier and Prat 2009). The efflorescence can grow several millimetres in height without having a noticeable impact on evaporation. The situation is quite different in the case of crust-like efflorescence covering a significant fraction of the porous medium open surface or even all of it. In this case, the evaporation flux can be considerably reduced from its initial value, when the surface was not covered with efflorescence. As mentioned in section 1.7, a factor affecting the efflorescence type is the initial evaporation rate, i.e. before the efflorescence formation. For a high rate, keeping in place all the other factors, promotes a salt crust formation while a lower rate can lead to branching efflorescence. This can lead to the paradoxical evolution presented in (Gupta et al. 2014). While as in the case of pure water, the drying is faster the lower the relative humidity (RH) in the ambient air is, a reverse situation is reported in (Gupta et al. 2014). Due to the change in efflorescence morphology (crust or branched), drying is slower at low RH than at higher RH in the case of evaporation with NaCl solution for the conditions presented in (Gupta et al. 2014).

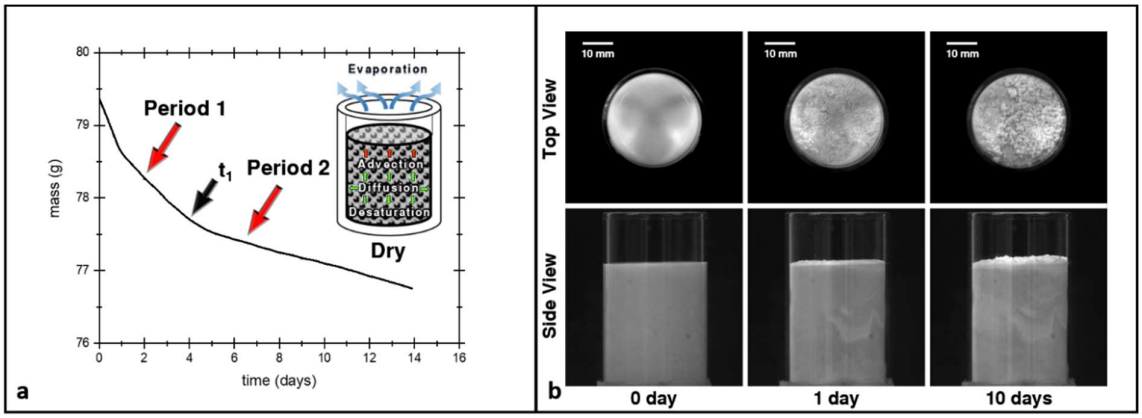


Figure 1.11. a) Mass variation in time of a porous medium cylindrical sample (glass beads with a diameter in the range [1 - 50 μm]) initially saturated with a close to saturation NaCl solution during drying at room temperature (22°C) and RH = 7%, b) Crust completely covering the sample's upper surface (period 2).

Fig. 1.11 shows a typical example of the crust development and its strong impact on the evaporation kinetics as also seen in (Duenas-Velasco 2016). In this example, it can be noted that the crust does not completely block evaporation but reduces it very strongly. Thus the evaporation rate in period 2 is about 5 times lower than in period 1. The latter corresponds to a period when the crust develops without affecting the evaporation rate. In period 2, the crust (Fig. 1.11b) completely covers the porous medium upper surface. A key question is the explanation of this very strong reduction in the evaporation rate. Like many other questions in this research area, it remains unsolved and in fact it is quite an open subject. In (Desarnaud et al. 2015), the crust is considered to be dry during period 2, so that the reduction in evaporation rate is then fully explained by the crust impact translated as a diffusion barrier. Since the crust is assumed to be little to none pores, its vapor effective diffusion coefficient would be sufficiently low to reduce the rate by the proportion observed, despite the small thickness of the crust. However, very often, for example, in the experiment shown in Fig. 1.11, in period 2 when the evaporation rate is very low while the saturation in the underlying porous substrate is still very high. In other words, the crust is theoretically in contact with the solution at its bottom. Also it has been established that the solution wets the halite almost perfectly (Corti and Krieger 2007). Thus for the diffusion barrier explanation to be convincing, it would have to be explained why the crust remains dry under these conditions. On the contrary, it is expected to remain at least partially saturated with solution because of its capillarity. Another view of this effect is to consider that the crust remains wet. The solution is transported through the crust by capillary effect to its upper surface, where the salt precipitates. The diagram in terms of transport and precipitation phenomenon is similar to that illustrated in Fig. 1.10b. One element in favor of this scenario is that the top surface of the crust moves upwards during Period 2 although the low evaporation rate (Duenas-Velasco 2016). If we consider that this displacement is purely related to transport (see some additional discussion points below), the only mechanism that can explain the observed displacement is the precipitation of salt on the crust's upper surface. In this scenario, the precipitation of salt causes progressive pore clogging and therefore changes the pore distribution on the crust upper surface. On the basis of the classical Schlünder model, e.g. (Talbi and Prat 2019), describing evaporation from a perforated surface, it then seems possible to explain the reduction in flux by a crust upper surface reduction in surface porosity (Duenas-Velasco 2016). However, these elements remain to be confirmed. Finally, another argument presented for example in (Nachshon et al. 2018) is based on the observation that the crust can in fact be detached from the surface on a porous medium (see Fig. 1.12). A gap between the crust bottom and the porous substrate surface in the order of a millimeter is for example mentioned in (Nachshon et al. 2018). Under conditions where the deviation is greater or on the order capillary length, the scenario based on the crust see as a vapor barrier for diffusion resumes its interest. One can reasonably imagine that a detached from the surface crust is thus dry. In reality this scenario poses a problem because it is not explained how the crust comes off and we do not know when this crust detachment occurs, i.e. from the point of transition between the two periods (point "t1" in Fig. 1.11a) or much later in Period 2.

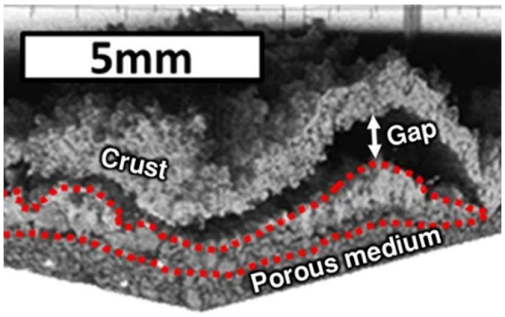


Figure 1.12. Example of a crust detached from the porous substrate on which it is initially developed (figure adapted from Nachshon et al. 2018)).

Two types of mechanisms that can explain the detachment are briefly mentioned in (Nachshon et al. 2018). The first explanation suggests possible mechanical effects in connection with the known fact that crystallization can have mechanical consequences (Naillon et al., 2018; Noiriel et al., 2010). In contrast, another approach consists in neglecting any initial mechanical effect and relating the detachment to a dissolution-precipitation effect. The fact that the displacement of a crust can be entirely explained by the means of dissolution-precipitation mechanisms is clearly established in the rest of this manuscript (see Chapter III) from an experiment involving a salt crust suspended in a Hele-Shaw cell (Licsandru et al. 2019). However, this does not provide a definitive conclusion regarding possible mechanical effects, especially in field situations. It is clear however, as it will be illustrated in this manuscript, that the phenomenon of dissolution-precipitation is a key element for understanding the salt crust's dynamics and more generally the efflorescence and subflorescence. In summary, the elements of the puzzle for explaining and modelling results such as the one shown in Fig. 1.11 now appear to be in place. However, there remains substantial work to be done, particularly in terms of numerical simulations or of characterization (structural properties of crusts), to firmly establish this explanation.

I.3. Patterned crusts

Salt crusts can be a site of very organized structures. A very famous example is the polygonal patterning found on the surface of the Salar de Uyuni in Bolivia (Fig. 1.13a).

Given their resemblance to Bénard cells (Bénard 1901), one could relate this structuring to possible thermosolutal convection effects in the underlying porous layers. Without a clear possible impact of these effects in a natural situation (Lasser et al. 2019), it should be noted however that quite similar structures, but with cells of a different scale centimeter size rather than metric, have been observed in laboratory experiments (Fig. 1.13b). In this experiment, the impact of natural convection within the porous medium is completely negligible. The structuring is then completely linked to the efflorescence growth from "nucleation" points randomly distributed on the surface. This distribution is explained by the analysis of spatial fluctuations in ion concentration at the surface during evaporation. However, how the growth takes place from these seeds is not yet understood. This problem of polygonal patterns is another very open problem example. The same applies to the question of the pattern scale, this being very different between the two images (a few orders of magnitude) in Fig. 1.13. A clear contributing to this issue is also a major objective of this work (see 0).

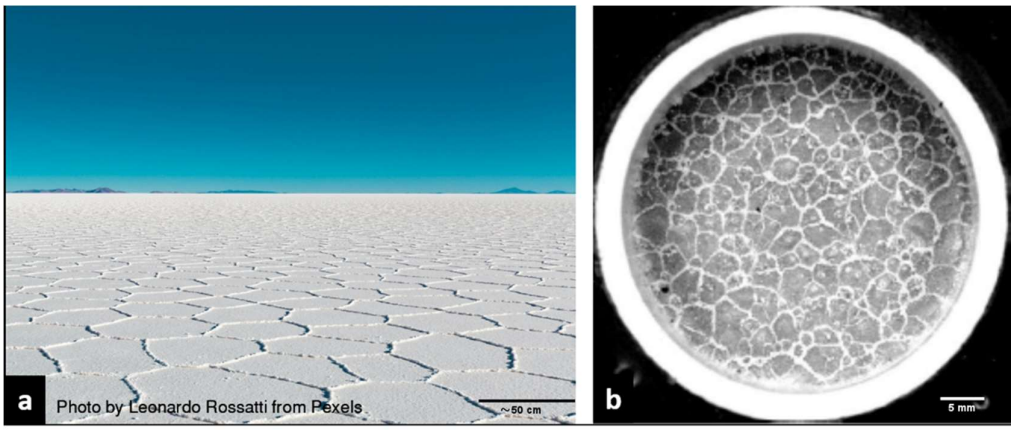


Figure 1.13. a) Polygonal cells observed on the Salar de Uyuni in Bolivia surface. The size of the polygonal cells is at the metric scale; b) Salt crust with cell structure formed in the laboratory (figure adapted from Veran-Tissoires and Prat 2014) by evaporation of an aqueous solution of NaCl saturating the porous medium (the cylinder diameter is ~38 mm).

I.4. Modelling of salt crystallization dynamics

Regarding the modelling aspects, by always limiting ourselves to the continuous approach of porous media, we can first of all distinguish a first category of models for which the objective is to model the ion transport in the presence of evaporation, that this either for drying or wicking situations (Huinink et al. 2002; Sghaier et al. 2007; Guglielmini et al. 2008; Hidri et al. 2013, Diouf et al. 2018). This type of model typically couples Eq. (1.4) to the classical equations allowing to model the drying or the flow in a wick situation. An additional step consists in taking into account the precipitation phenomena (and dissolution if needed), see for example (Xu et al. 2006; Pruess and Müller 2009; Koniorczyk (2012); Jambhekar et al. 2015, 2016; Mejri et al. 2017; Grementieri et al. 2017). It should be noted that these models can be extended to situations where several salts are present in the same solution, e.g. (Mejri et al. 2017). Finally, the most complete models can also take into account poro-mechanical effects, e.g. (Koniorczyk and Gawin 2012; Derluyn et al. 2014). These models take into consideration the precipitation in the porous substrate but generally are not designed to model the efflorescence development, whether branched or compact on the porous medium surface, so that in fact the efflorescence modelling of the drying situation with development of a crust illustrated in Fig. 1.11 remains an open subject. It can be noted that a model for transfer in the crust is proposed in (Licsandru et al. 2019). Coupling this type of model with more classic models describing changes in the porous substrate seems possible. Chapter IV of this manuscript will aim precisely to fill this gap.

I.5. Other salts

As indicated above, we have considered practically only the case of aqueous sodium chloride solutions. Besides the fact that it is very present in practical situations, it is distinguished by a very high solubility compared to most other salts. This explains why the evaporation of NaCl solutions can lead to very significant efflorescence or subflorescence development. Another differentiating element is that under the usual conditions the crystallized sodium chloride is anhydrous (a hydrated form exists only for a sufficiently cold temperature, typically below 0 ° C). This simplifies the modelling compared to the case of hydrated salts such as for example sodium sulphate which can moreover crystallize in various hydrated forms in addition to the non-hydrated form (Rijniers et al. 2005). Some elements of comparison between the case of sodium chloride and sodium sulphate can be found in (Shahidzadeh and Desarnaud 2012; Shahidzadeh-Bonn et al. 2010) while a comparison between the case of sodium chloride, calcium chloride and potassium iodide is presented in (Shokri-Kuehni et al. 2017). Evidence on drying with gypsum formation can be found in (Seck et al. 2015, 2016). We will limit ourselves here to these references. A detailed comparative study of evaporation in porous media for different salts remains also a subject for future work.

Bibliography

Bear, J., Bachmat, Y. (1990). Introduction to Modeling of Transport Phenomena in Porous Media. Springer.

Bechtold, M., Haber-Pohlmeier, S., Vanderborght, J., Pohlmeier, A., Ferré, T. P. A., Vereecken, H. (2011). Near-surface solute redistribution during evaporation. Geophysical Research Letters, 38, L17404.

Bénard, H. (1901). Les tourbillons cellulaires dans une nappe liquide transportant de la chaleur par convection en régime permanent, Annales de chimie et de physique, Série 7 (23), 62-144.

Bergstad, M., Or, D., Withers, P.J., Shokri, N. (2017). The influence of NaCl concentration on salt precipitation in heterogeneous porous media. Water Resour. Res. 53(2), 1702–1712.

Bergstad, M., Or, D., Withers, P.J., Shokri, N. (2018). Evaporation Dynamics and NaCl Precipitation on Capillarity-Coupled Heterogeneous Porous Surfaces. Water Resources Research 54 (6), 3876-3885.

Burgess, J. (1978). Metal Ions in Solution. Prentice Hall Europe.

Correns, C. W. (1949). Growth and dissolution of crystals under linear pressure. Discussions of the Faraday Society, 5, 267. https://doi.org/10.1039/df9490500267

Corti, T., Krieger, U. K. (2007). Improved inverted bubble method for measuring small contact angles at crystal-solution-vapor interfaces. Appl. Opt., 46, 5835-5839.

Dagan, G. (2012). Flow and transport in porous formations. Springer Science & Business Media.

Dashtian, H., Shokri, N., Sahimi, M. (2018). Pore-network model of evaporation-induced salt precipitation in porous media: The effect of correlations and heterogeneity. Adv. in Water Res. 112, 59-71.

Del Río,J.A., Whitaker, S. (2016). Diffusion of charged species in liquids, Scientific Reports 6, 35211.

Derluyn, H., Moonen, P., Carmeliet, J. (2014). Deformation and damage due to drying-induced salt crystallization in porous limestone. J. Mech. Phys. Solids 63, 242–255.

Duenas-Velasco, M. (2016). Evaporation en milieu poreux en présence de sel dissous. Structure et lois de croissance des efflorescences, Thèse Université de Toulouse.

Deegan,R.D., Bakajin, O., Dupont, T. F., Huber, G., Nagel, S.R.,Witten, T.A. (1997). Capillary flow as the cause of ring stains from dried liquid drops. Nature 389, 827.

Desarnaud, J., Derluyn, H., Carmeliet, J., Bonn, D., Shahidzadeh, N. (2014). Metastability limit for the nucleation of NaCl crystals in confinement. J.Phys.Chem.Lett. 5(5) 890–895.

Desarnaud, J., Derluyn, H., Molari, L., de Miranda,S. Cnudde, V., Shahidzadeh, N. (2015). Drying of salt contaminated porous media: Effect of primary and secondary nucleation, Journal of Applied Physics 118 (11) 114901.

Diouf, B., Geoffroy, S., Abou-Chakra, A., Prat, M. (2018). Locus of first crystals on the evaporative surface of a vertically textured porous medium. Eur. Phys. J. Appl. Phys. 81 (1), 11102.

Drying Rate Measurements in Convection- and Diffusion-Driven Conditions on a Shaly Sandstone Using Nuclear Magnetic Resonance | SpringerLink. (n.d.). Retrieved October 5, 2020, from https://link.springer.com/article/10.1007/s11242-011-9829-3

Eloukabi, H., Sghaier, N., Ben Nasrallah, S., Prat, M. (2013). Experimental study of the effect of sodium chloride on drying of porous media: the crusty-patchy efflorescence transition. Int. J. of Heat and Mass Tr. 56, 80–93.

Flatt, R., Aly Mohamed, N., Caruso, F., Derluyn, H., Desarnaud, J., Lubelli, B., Espinosa Marzal, R. M., Pel, L., Rodriguez-Navarro, C., Scherer, G. W., Shahidzadeh, N., & Steiger, M. (2017). Predicting salt damage in practice: A theoretical insight into laboratory tests. RILEM Technical Letters, 2, 108–118. https://doi.org/10.21809/rilemtechlett.2017.41

Flatt, R., Steiger, M., & Scherer, G. (2007). A commented translation of the paper by C.W. Correns and W. Steinborn on crystallization pressure. Environ. Geol., 52, 187–203. https://doi.org/10.1007/s00254-006-0509-5

Fletcher, R. C., & Merino, E. (2001). Mineral growth in rocks: Kinetic-rheological models of replacement, vein formation, and syntectonic crystallization. Geochimica et Cosmochimica Acta, 65(21), 3733–3748. https://doi.org/10.1016/S0016-7037(01)00726-8

Guglielmini, L., Gontcharov, A., Aldykiewicz, A. J., Stone, H. A. (2008). Drying of salt solutions in porous materials: Intermediate-time dynamics and efflorescence. Phys. of Fluids 20, 077101.

Grementieri, L., Molari, L., Derluyn, H., Desarnaud, J., Cnudde, V., Shahidzadeh, N., de Miranda, S. (2017). Numerical simulation of salt transport and crystallization in drying Prague sandstone using an experimentally consistent multiphase model. Building and Environment 123, 289-298.

Gupta, S., Huinink, H.P., Prat, M., Pel,L., Kopinga, K. (2014). Paradoxical drying due to salt crystallization. Chem. Eng. Sci. 109, 204–211.

Hidri, F., Sghaier, N., Eloukabi, H., Prat,M., Ben Nasrallah, S. (2013). Porous medium coffee ring effect and other factors affecting the first crystallization time of sodium chloride at the surface of a drying porous medium. Physics of Fluids 25, 127101.

Hidri, F., Diouf, B., Bouhlila, R., Geoffroy, S., Prat, M. (2019). Stagnation Points as Loci of Solute Concentration Extrema at the Evaporative Surface of a Random Porous Medium Transp. Porous Media 128 (3), 861-879.

Huinink, H.P., Pel, L., Michels, M.A.J. (2002). How ions distribute in a drying porous medium: A simple model. Phys. of Fluids 14 (4), 1389–1395.

Jambhekar, V.A., Helmig, R., Schröder, N., Shokri, N. (2015). Free-flow-porous-media coupling for evaporation driven transport and precipitation of salt. Transp. Porous Media 110, 251–280.

Jambhekar, V.A., Mejri, E., Schröder, N., Helmig, R., Shokri, N. (2016). Kinetic approach to model reactive transport and mixed salt precipitation in a coupled free-flow-porous-media system. Transp. Porous Media 114, 341–369.

Jamil, A., Riaz, S., Ashraf, M., & Foolad, M. R. (2011). Gene Expression Profiling of Plants under Salt Stress. Critical Reviews in Plant Sciences, 30(5), 435–458. https://doi.org/10.1080/07352689.2011.605739

Koniorczyk, M. (2012). Salt precipitation and crystallization in non-isothermal, partially saturated porous materials considering ions interaction model. Int. J. Heat Mass Transf. 55, 665–679.

Koniorczyk, M., Gawin, D. (2012). Modelling of salt crystallization in building materials with microstructure–Poromechanical approach, Construction and Building Materials 36, 860-873.

Lasser, J., Nield, J.M., Ernst, M., Karius, V., Wiggs, G. F. S., Goehring, L. (2019). Salt Polygons are Caused by Convection, preprint.

Lasser, J., Nield, J. M., & Goehring, L. (2020). Surface and subsurface characterisation of salt pans expressing polygonal patterns [Preprint]. Geosciences – Geophysics. https://doi.org/10.5194/essd-2020-86

Licsandru, G., Noiriel, C., Duru, P., Geoffroy, S., Abou-Chakra, A., Prat, M. (2019). Dissolution-precipitation-driven upward migration of a salt crust. Physical Review E 100 (3), 032802.

Mejri, E., Bouhlila, R., Helmig, R. (2017). Heterogeneity effects on evaporation-induced halite and gypsum coprecipitation in porous media. Transp. Porous Media 118(1), 39–64.

Moghaddam, A.A., Kharaghani A., Tsotsas, E., Prat,M. (2017). Kinematics in a slowly drying porous medium: Reconciliation of pore network simulations and continuum modeling, Physics of Fluids 29 (2), 022102.

Mujumdar, A.S. (2006). Handbook of industrial drying, CRC press.

Mullin, J.W. (2001). Crystallization, 4th ed., Butterworth Heinemann, Oxford, UK.

Naillon, A, Joseph, P., Prat, M. (2017). Sodium chloride precipitation reaction coefficient from crystallization experiment in a microfluidic device, J. of Crystal Growth 463, 201-210.

Naillon, A, Joseph, P., Prat, M. (2018). Ion transport and precipitation kinetics as key aspects of the stress generation on pore walls induced by salt crystallization. Phys. Rev. Letters 120, 034502.

Naillon, A, Joseph, P., Prat, M. (2019). Direct observation of pore collapse and tensile stress generation on pore wall due to salt crystallization in a PDMS channel, Soft Matter 15 (22), 4562-4569.

Nachshon, U., Weisbrod, N., Dragila, M., Grader, A. (2011a). Combined evaporation and salt precipitation in homogeneous and heterogeneous porous media. Water Resour. Res. 47, W03513.

Nachshon, U., Shahraeeni, E., Or, D., Dragila, M., Weisbrod, N. (2011b). Infrared thermography of evaporative fluxes and dynamics of salt deposition on heterogeneous porous surfaces. Water Resources Research 47, W12519.

Nachshon, U., Weisbrod, N. (2015). Beyond the salt crust: on combined evaporation and subflorescent salt precipitation in porous media. Transport in Porous Media 110 (2), 295-310.

Nachshon, U., Weisbrod, N., Katzir, R., Nasser, A. (2018). NaCl Crust Architecture and Its Impact on Evaporation: Three□Dimensional Insights, Geophys. Res. Lett. 45, 6100.

Naillon, A., Joseph, P., & Prat, M. (2018). Ion Transport and Precipitation Kinetics as Key Aspects of Stress Generation on Pore Walls Induced by Salt Crystallization. Physical Review Letters, 120(3), 034502. https://doi.org/10.1103/PhysRevLett.120.034502

Noiriel, C., Renard, F., Doan, M.L., Gratier, J.P. (2010). Intense fracturing and fracture sealing induced by mineral growth in porous rocks, Chemical Geology 269, 197-209.

Or, D., Lehmann, P., Shahraeeni, E., Shokri, N. (2013). Advances in soil evaporation physics—A review. Vadose Zone Journal 12 (4).

Pel, L., Huinink, H.P., Kopinga, K. (2002). Ion transport and crystallization in inorganic building materials as studied by nuclear magnetic resonance. Applied Physics Letters 81 (15), 2893-2895.

Pel, L., Pishkari, R., Casti, M. (2018). A simplified model for the combined wicking and evaporation of a NaCl solution in limestone. Materials and Structures 51 (3), 66.

Peysson, Y. (2012). Permeability alteration induced by drying of brines in porous media. The European Physical Journal-Applied Physics 60(2), 24206.

Prat, M. (2002). Recent advances in pore-scale models for drying of porous media. Chem. Eng. J. 86 (1-2), 153-164.

Prat, M. Chap. 3 - Evaporation, transport et cristallisation from Cristallisation de sels en milieu poreux, Edited by H.Derluyin and M. Prat, book project to appear, ISTE Editions (2021)

Pruess, K., Müller, N. (2009). Formation dry□out from CO2 injection into saline aquifers: 1. Effects of solids precipitation and their mitigation. Water Resources Research W03402.

Rad, M.N., Shokri, N., Sahimi,M. (2013). Pore-scale dynamics of salt precipitation in drying porous media. Physical Review E 88 (3), 032404.

Rijniers, L.A., Huinink, H.P., Pel, L., Kopinga, K. (2005). Experimental evidence of crystallization pressure inside porous media. Physical Review Letters 94 (7), 075503.

Seck, M.D., Van Landeghem, M., Faure, P., Rodts, S., Combes, R., Cavalié, P., Keita, E., Coussot, P. (2015). The mechanisms of plaster drying. Journal of Materials Science 50 (6), 2491–2501.

Seck, M.D., Keita, E., Faure, P., Cavalié, P., Van Landeghem, M., Rodts, S., Combes, R., Coussot, P. (2016). Subflorescence and plaster drying dynamics. Chemical Engineering Science 148, 203-211.

Shahidzadeh-Bonn, N., Desarnaud, J., Bertrand, F., Chateau, X., Bonn, D. (2010). Damage in porous media due to salt crystallization. Physical Review E 81 (6), 066110.

Shahidzadeh, N., Desarnaud, J. (2012). Damage in porous media: role of the kinetics of salt (re) crystallization. The European Physical Journal-Applied Physics 60, 24205.

Shokri, N. (2014). Pore-scale dynamics of salt transport and distribution in drying porous media. Physics of Fluids 26 (1), 012106.

Shokri, N., Or, D. (2011). What determines drying rates at the onset of diffusion controlled stage□2 evaporation from porous media? Water Resources Research W09513.

Shokri-Kuehni, S. M. S., Vetter, T., Webb, C., Shokri, N. (2017a). New insights into saline water evaporation from porous media: Complex interaction between evaporation rates, precipitation, and surface temperature. Geophysical Research Letters, 44, 5504–5510.

Shokri-Kuehni, S. M. S., Rad, M.N., Webb, C., Shokri, N. (2017b). Impact of type of salt and ambient conditions on saline water evaporation from porous media. Advances in Water Resources 105, 154–161.

Sghaier, N., Prat, M., Ben Nasrallah, S. (2007). On ions transport during drying in a porous medium. Transport in Porous Media 62, 243-274.

Sghaier, N., Prat, M. (2009). Effect of efflorescence formation on drying kinetics of porous media. Transport in Porous Media 80 (3) 441-454.

Sghaier, N., Geoffroy,S., Prat, M., Eloukabi, H., Ben Nasrallah, S. (2014). Evaporation driven growth of large crystallized salt structures in a porous medium, Phys. Rev. E 90, 042402.

Talbi, M., Prat M. (2019). About Schlünder's model: A numerical study of evaporation from partially wet surfaces. Drying Technology 37 (5), 513-524.

Van Brakel, J. (1980). Mass transfer in convective drying. in Advances in Drying, edited by A. S. Mujumdar, Hemisphere, New York.

Veran-Tissoires, S., Marcoux, M., Prat,M. (2012a). Discrete salt crystallization at the surface of a porous medium. Phys. Rev. Letters 108, 054502.

Veran-Tissoires, S., Marcoux, M., Prat,M. (2012b). Salt crystallization at the surface of a heterogeneous porous medium. Europhysics Letters 98, 34005.

Veran-Tissoires, S., Prat, M. (2014). Evaporation of a sodium chloride solution from a saturated porous medium with efflorescence formation. J. of Fluid Mechanics 749, 701-749.

Vu, H.T., Tsotsas, E. (2018). Mass and heat transport models for analysis of the drying process in porous media: a review and numerical implementation. International Journal of Chemical Engineering ID 9456418.

Weyl, P. K. (1959). Pressure solution and the force of crystallization: A phenomenological theory. Journal of Geophysical Research (1896-1977), 64(11), 2001–2025. https://doi.org/10.1029/JZ064i011p02001

Xu, T., Sonnenthal, E., Spycher, N., Pruess, K. (2006). TOUGHREACT—a simulation program for non-isothermal multiphase reactive geochemical transport in variably saturated geologic media: Applications to geothermal injectivity and CO2 geological sequestration. *Computers & Geosciences* 32 (2) 145-165.

Chapter II

Laboratory induced patterns

II.1. Objective and general description of the study

Naturally formed patterns have always fascinated the scientific world. This fascination led to great progress in both understanding their symmetrical and repetitive tendency as well as the governing equations behind it as one can quote such great findings (e.g., Mandelbrot, 1982; Spry, 1962). These patterns cover a large area of subjects and come in many shapes and sizes. As it can be seen in Figure II.1, there are many examples linked to physical and geological processes, from basaltic columns to precipitation patterns, salts crusts or desiccation mud cracks. This makes them a highly complex problem, due to the fact that each has a vast array of coupled effects that impact the final pattern by different amounts. One needs to understand each of the contributing factors in order to be able to establish its pertinence and contribution towards forming such regulated structures. As one factor can have a large effect on the final pattern while another could have none. Thus, once the driving phenomena have been established the pattern can be analyzed and possibly reproduced. The naturally occurring patterns have a great disadvantage in terms of singling out such defining factors due to their continuous evolution and variation of factors in time (seasonal change, earthquakes, droughts, floods, recharge, etc.). Thus, in order to be able to study factors that can have such important repercussions on the final result, a completely controlled environment needs to be established.

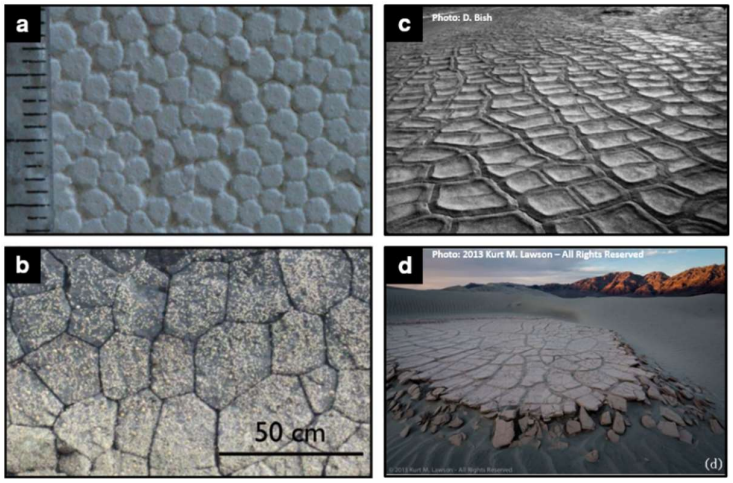


Figure II.1 Different shapes and sizes of patterns found in nature: a) columnar jointing in desiccated corn starch (figure adapted from (L. Goehring et al., 2009)); b) columnar jointing in cooled lava (figure adapted from (L. Goehring et al., 2009); c) Clinoptilolite-rich zeolite tuff, Lake Tecopa, south of Shoshone, CA. Photo: D. Bish. (figure adapted from (Ancient Playa in Glenelg Region, Gale Crater, Mars: Evidence Derived from the Polygonal Flagstone Network in Mudstone Imaged by Curiosity, n.d.)); d) Exposed plates of desiccated interdune sediment in Last Chance Range, Death Valley National Park, CA. Unknown mineralogy, exposure approx. 3 m across. Photo: Kurt M. Lawson. (figure adapted from

(Ancient Playa in Glenelg Region, Gale Crater, Mars: Evidence Derived from the Polygonal Flagstone Network in Mudstone Imaged by Curiosity, n.d.));

Amongst the great patterns that still remain mostly a mystery are the polygonal patterns of salt flats. These patterns can be found from Death Valley – Badwater Basin (Death Valley National Park, California, U.S.A. Figure II.2) to the Salar de Uyuni (Daniel Campos Province, Bolivia). The latter constitutes the largest in the world (>10,000 Km^2) and also presents a remarkably flat surface (Borsa et al., 2002). As discussed in Chapter 1, such a salar is quite a famous example of large (order of meters) highly ordered polygonal patterns. Some assumptions have been made to explain the formation of this tessellation pattern, although controversy remains between different studies. As an example, the geology point of view (Survey (U.S.) & Hunt, 1966) would see this type of pattern as a result of cracking due to desiccation of sediments/mud/salt (mechanical effect) thus the brine would start evaporating on the crust and through the cracks. In term, forming efflorescence crusts and borders give birth to polygonal patterns. In contrast, the fluid mechanics approach as seen in a recent study (Lasser et al., 2020) is based on brine flow in porous media. Here the approach was based on field and laboratory studies related to concentration gradients, which should lead to the formation of convection cells (Pellew & Southwell, 1940) due to density variation of the brine. However, the study's approach is only two-dimensional and although it shows that convection cells can be formed this way no actual three dimensional patterns were obtained.



Figure II.2 Badwater basin: a) salt crust area and b) polygonal salt cracks

Thus, the purpose of this chapter is to bring new insights into the way one can translate naturally occurring environmental conditions in a controlled laboratory series of factors. Thus making the objective of this chapter to study the formation of polygonal salt crust patterns under well-controlled laboratory conditions in order to decipher the different physico-chemical parameters involved in the salt crust formation and their evolution through time.

The sheer complexity of influencing factors makes this task quite complex and hard to study. Due to the fact that chemical and physical interactions combined with material properties work side by side in a non-controlled environment with large variations (e.g., of temperature, humidity, mineral composition, flooding, debris, etc.) that are constantly evolving. A simplified schematic of the coupled interactions can be summarized in Figure II.3. This complexity makes laboratory experiments the ideal way of testing and finding such defining phenomena. As in a laboratory experiment, one can choose and test factors one by one in a precise and reproducible manner.

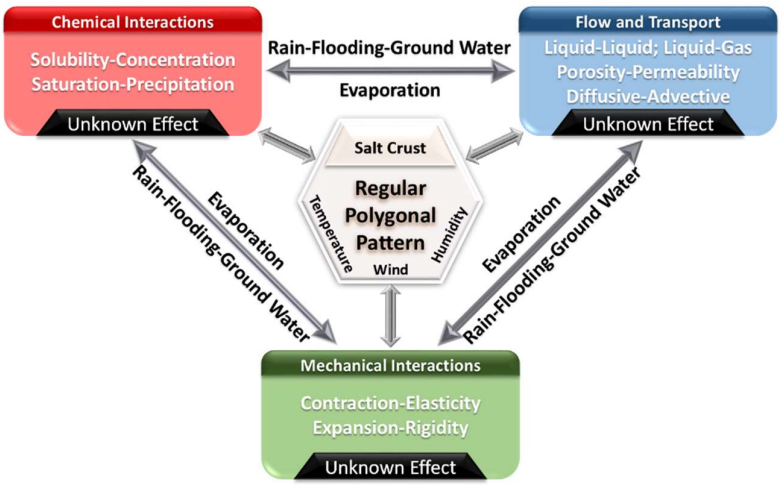


Figure II.3 Simplified schematic of coupled process interactions

Another strong point here is that in a natural setting, there are three types of factors that can be distinguished. First are the factors that are reproducible; e.g. humidity or temperature. Second there are the factors that can be replaced or substituted, e.g. by replacing the multiple salts and debris mixture in the salt flat with a single salt mixture of NaCl (i.e., the majority of salt found in the flats) supposing that it has the most influence in the patterning as for substituting an example would be the naturally formed non-dissolved salt layer with a controlled porous medium (glass beads). Finally, the third type of factors would be the ones that cannot be reproduced, such as the scale of the surface and other unknown or unforeseen influences.

The next step in such an endeavor is being able to establish the driving phenomena inferring in the crust formation. In order to sort through the possible configurations studies on salt flats such as (Chong Díaz et al., 1999; Lasser et al., 2020; Matter & Tucker, 2009) (especially on the topic of Salar de Uyuni), and other naturally formed patterns (Chavdarian & Sumner, 2011; Lucas Goehring et al., 2010) were of great help.

II.2. General description of the experiments

The research on the subject is quite unidirectional as briefly spoken about before. A general trend or direction can be seen in terms of how a pattern the one in (Lasser et al., 2020) can form. Due to the fact that this train of thought did not produce yet any clear reproducible results, this study proposes a different approach to solving this issue. As seen in Figure II.4, two types of patterns are noticeable. The first (Figure II.4 a) resembles an island type of pattern separated by an indented border. The second (Figure II.4 b) is also an island type, which is the opposite of the first in terms of borders, as it has a raised border. One could argue that what we see is a cracking or fissure formation as spoken about earlier or even differential dissolution due to flooding (Figure II.4 a) and once this happens it would favor preferential efflorescence growth in the cracks (Figure II.4 b). The purpose of this study is to reproduce this type of pattern in a laboratory environment. Thus, our approach is more directed towards firstly producing a

series of patterns inspired by the real one as seen in the salt flats, by strictly interpreting and reverse engineering what can be observed in nature.

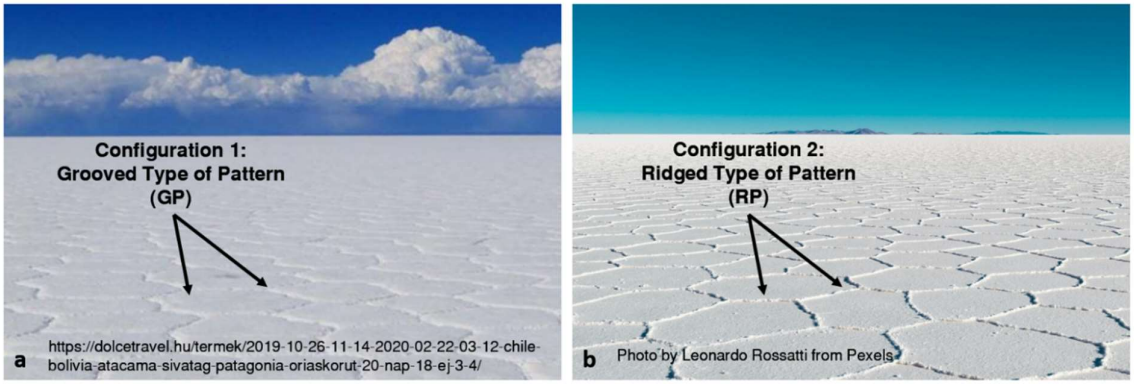


Figure II.4 Naturally formed patterns in Uyuni salt flats, the two proposed configurations for mimicking the phenomenon.

With this interpretation in mind, the first was defined as a series of islands that form due to nucleation spots, leaving a boundary between each other as an area of influence effect and was named a Grooved Pattern (GP). The GP represents the polygonal island part of the natural pattern. The second type was defined as a series of very low permeability macro-crystals formed by a similar effect as the GP. The main difference being that due to the very low permeability of the crystals, the preferred place for the efflorescence to grow, after they form, will be in the least impermeable part of the crust, the crystal boundary, thus leaving a Ridged Pattern (RP). Once these two goals were established the actual design of the experiments can begin.

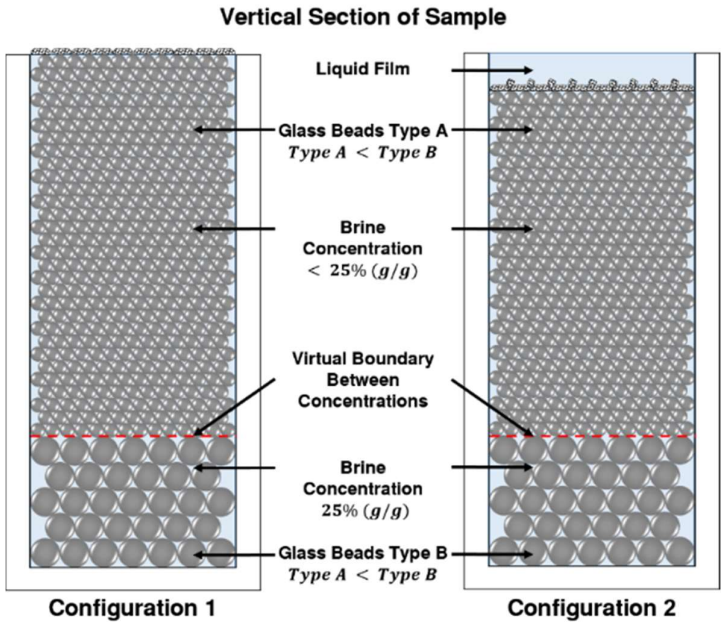


Figure II.5 Vertical sections through the final experimental configurations.

Only by adding a liquid film on top of the porous media in configuration 1 (Figure II.5), we have managed to obtain two different types of patterns Figure II.6, which present similarities with salt flats and are reproducible in the laboratory.

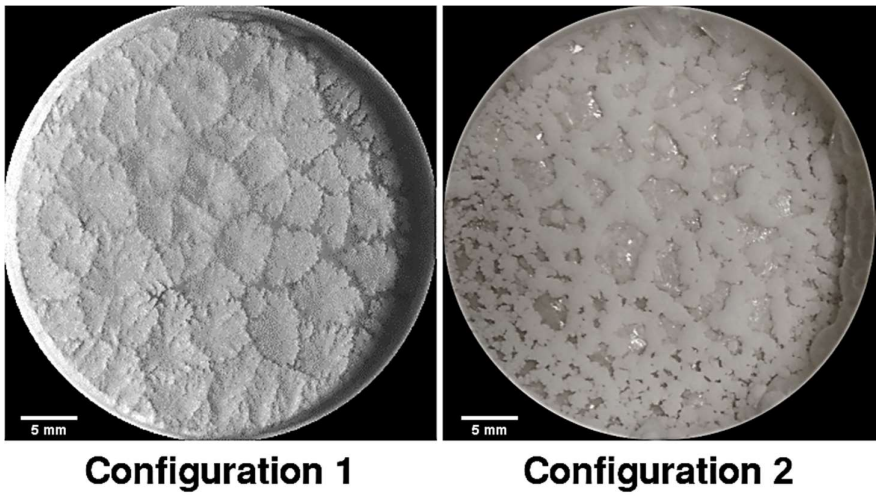


Figure II.6 Examples of patterns obtained for the configurations in Figure II.5

II.2.1. Concept

In this part, the study takes into account two different considerations of the naturally formed pattern.

The first consideration is the actual natural conditions in Salar de Uyuni so that the study will be related to it as much as possible. In the search of the subject most of the data was taken from studies such as (Banks et al., 2005; Fritz et al., 2004; Svendsen, 2003) on the actual Salar de Uyuni and was completed with other sources as (Bobst et al., 2001; Chen, 1992; Risacher & Fritz, 2009) due to the complicated research conditions in the Bolivian area.

While for the second consideration will be that certain factors can be reproduced with difficulty, so that they need to be replaced or equivalents need to be found. This part will be the most difficult in terms of testing. As for example, the size of the actual salt flats and the wind conditions. In terms of sheer size this could be translated into a boundless surface and no edge effects should take place as shown in (Veran-Tissoires et al., 2012). While if we take into consideration wind conditions, it will create areas of higher evaporation depending on speed and direction. So these phenomena will need a separate discussion as we progress in the study.

II.2.1.1. Design of the saturation and drying conditions of the experiment

Out of these, a picture can be set in terms of general natural conditions the climate can be set as a salt desert with according to (Risacher & Fritz, 2009) estimated evaporated amount per year of $1{,}200\ mm/year$ with precipitations estimated at $250-300\ mm/year$ and seasonal flooding from runoff waters or rise of the water table, thus we can consider that the salt planes, while not flooded, have a higher evaporation then its actual rain water intake. With these factors in mind the chosen type of experiment was picked as a classical dry situation (see Evaporation of saline solutions and porous media). One could argue that the natural conditions may allow for groundwater level to rise up to the surface or at least to be brought to the surface by the high wettability and capillarity of the salt layer and fine sediments. To account for a receding groundwater situation as mentioned in (Svendsen, 2003) the height of the samples was chosen

to be sufficiently large (at least 2 times bigger than its diameter) so that the porous media will not be in RFP until a clear Period 2 of salt crust evaporation is reached (as explained in Evaporation of saline solutions and porous media). This series of tests was named as Pattern Dry (PD).

II.2.1.2. Choice of porous medium

Next, the porous medium was chosen with regards to the fact that a certain part of the actual upper layer does not dissolve in totality with the rains or flooding. The only dissolved part being its surface and this happening on an annual basis such as is a new crust forming due to evaporation. Another factor to be taken into consideration is that this upper layer of the salt flat is composed out of cemented salt crystals with quite a high porosity (Dai et al., 2016; Rettig et al., 1980; Risacher & Fritz, 2009) and the fact that the crust is cemented the expected pore size should be smaller than a freshly crystallized one as found in (Dai et al., 2016) with a porosity of about 40% and pore sizes ranging from µm to mm. Thus in terms of porous medium hydrophilic glass beads were chosen with a big range of $1-50\mu m$ which will produce small pores and high porosity due to the fact that a random packing order of beads should produce an average porosity of about 40%.

II.2.1.3. Choice of brine concentration and initial experimental configuration

Different brine concentrations were considered, following two different scenarios.

The first situation would be the presumption that the water table (or any other source of non-salty water such as flooding, rain, etc.) would create a rise in the already existing brine level and mix with it, thus decreasing its salinity. Which in term connects to the existing porous media, as a result of capillary effects. The not yet saturated brine, in our scenario, would be brought to the surface where it evaporates. So that the first chosen configuration would be a concentration gradient from bottom (where the porous cemented salt is) to top (where the unsaturated liquid is brought). In order to achieve this configuration, a double layered porous media was chosen. The bottom layer crystals of pure NaCl salt and the top one $1-50\mu m$ hydrophilic glass beads.

In order to reproduce the rising and mixing of the brine, deionized water would be injected from the bottom through a small inlet (see Figure II.7). The water injection would be stopped once the microbeads in the top layer are visibly saturated and any surplus water removed by adsorption with a syringe.

The second configuration would be a laboratory representation of the salt flat flooding. Here, this will be translated into adding a liquid film on top of the first situation. This factor being of variable thickness and concentration in order to examine its effects on the crust formation (see above Figure II.7).

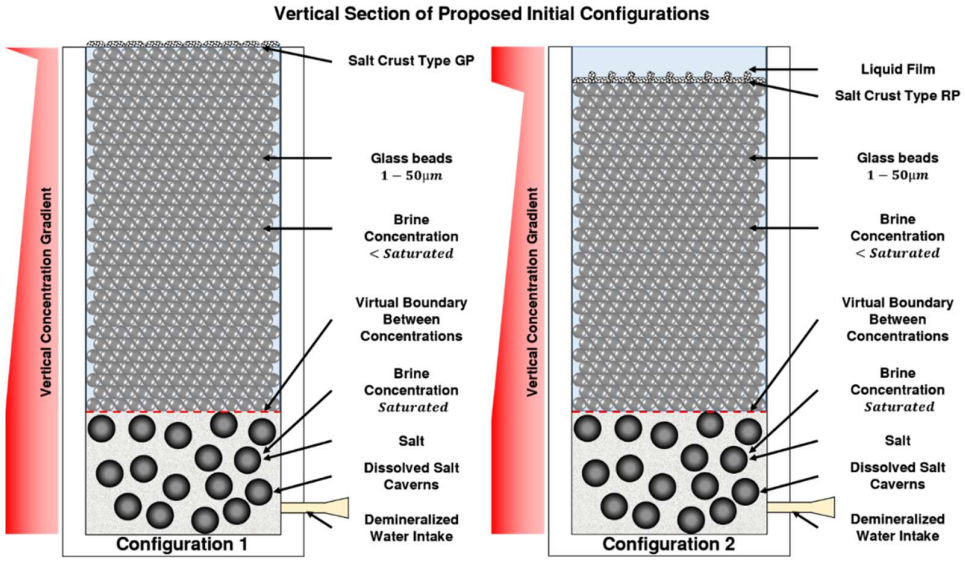


Figure II.7 Vertical section of the two proposed configurations with dissolved NaCl vertical concentration gradients

II.2.2. Driving phenomenon: Influence of steady-state flow in porous media

As spoken briefly in Chapter 1 and will be in more details here, the flow of brine through the media has big repercussions on the concentration fields and thus on the efflorescence growth. So that the objective here will be to have a system that is as much as possible continuous and steady-state in terms of flow.

In this part, the supposed driving phenomenon, in relationship to obtaining patterns in a laboratory environment, will be discussed. As now a configuration has been set for our interpretation on the naturally formed patterns.

Generally speaking, if a phenomenon may produce any kind of repetitive and ordered result, first of all, it will require stability in the developing media. In the present case this stability can be translated in certain factors. Here, the ones taken into account will be related to: (i) flow in porous media (porosity influence and the adjacent capillarity effects, wall effects, evaporation flux) and (ii) concentration gradients in porous media (inside it as well as on top at the opened surface evaporation front).

II.2.2.1. Pore invasion and transient flow

The objective here is to form a system that will allow a full salt crust to form while being continuously and fully supplied with brine from the adjacent porous media. Thus two closely related factors will be taken into consideration.

The first factor is the supply network to the crust. This has been translated into a highly capillary porous medium such as the chosen $1-50\mu m$ glass bead fraction. This type of medium has the benefit of being at the lower limit of micro-porosity, thus its pore size can effectively pull liquid from a big range of pores (Lenormand, 1990). In the case of the proposed setup this small porosity of the top layer ($1-50\mu m$) will play an important role as the salt grains are in the rage of $200-400\mu m$. Thus, after the injection of water. The salt layer pore size should increase due to dissolution effects and the top layer will assure that the liquid gets

pumped first out of the bottom layer and not out of the micro-beads, thus assuring a continuous and uniform brine feed to the top surface (Figure II.8).

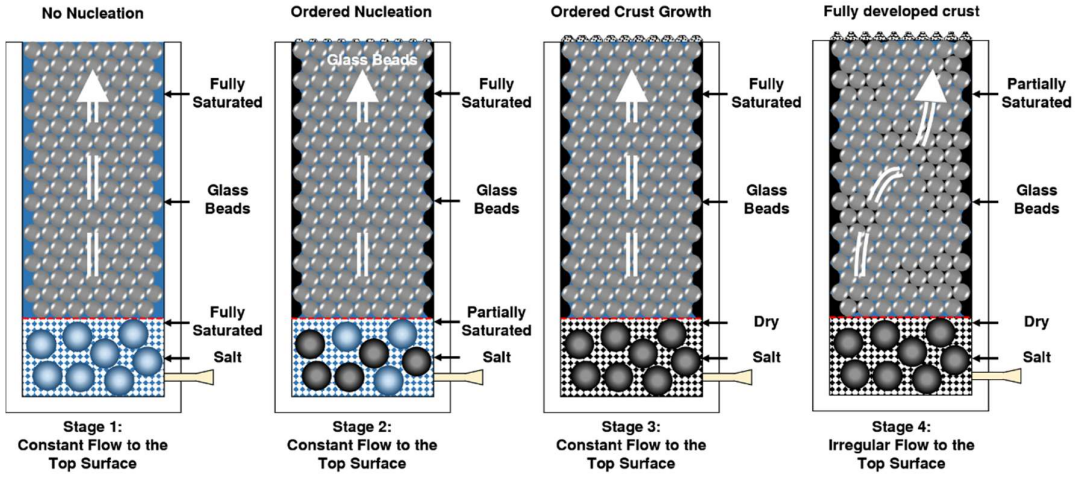


Figure II.8 General depiction of the sample's vertical section while in drying stages.

The second factor would be the pore invasion mechanics which is taken into account due to the fact that once the evaporative processes start. The chosen set up is a dry situation setup and the sample container has a limited amount of liquid in it unlike the wick situation where the porous media has a continuous supply of brine.

Here the same factors are exploited more exactly the pore invasion will preferentially invade the bigger pores first as seen in (Borgman et al., 2017; Lehmann & Or, 2009), which in this situation are situated at the bottom of the sample. This allows for a completely saturated upper layer. By exploiting this phenomenon, the experiment should not have preferential wet and dry zones in the upper layer until the water from the bottom salt layer is completely pulled out and replaced with air (Figure II.8) for evolution of saturation profiles in the pores.

Thus, if there is brine at the bottom of the sample, the top layer should stay fully saturated with a uniform flow of brine. Thus creating a good environment for the formation of crystallization patterns.

In pre-testing, this concept worked only for some of the samples. Some problems were encountered as the crusts formed unevenly. After careful examination, the problem was identified as an uneven dissolution of the bottom layer (salt grains forming sinkholes) and the bead layer became of variable height thus modifying the flow of brine. As seen in Figure II.9, the effect of this local variation in height completely changes the morphology of the crust.

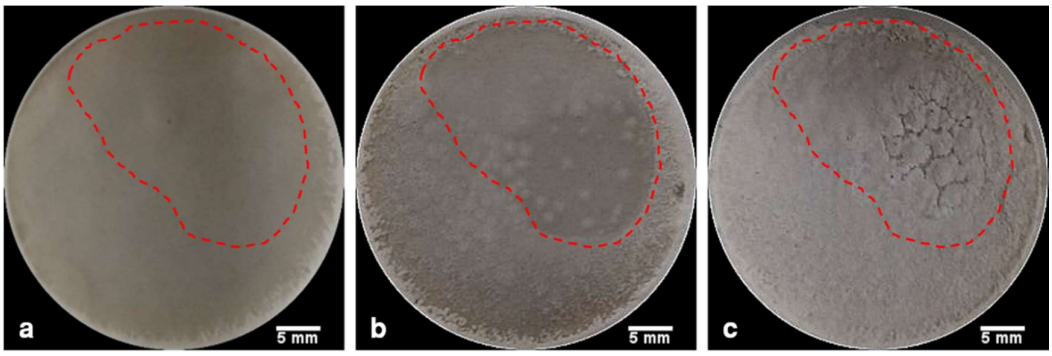


Figure II.9 Salt crust (top view) affected by non-uniform underlying flow (red area): a) Start of experiment, b) First observed nucleation, c) Final crust

II.2.2.2. Porous media local and global concentration gradients

Due to this experiment's configuration, an initial gradient is obtained after the injection of deionized water. This is due to the configuration's salt-bead layers and should insure that this initial gradient will be present for a certain amount of time until diffusive effects render it uniform. Previously, by using the porosity's capillary properties, a constant flow was obtained, while now the focus is on the concentration distribution through the cell. This is an important aspect of the concept, the goal being that a uniformly distributed initial nucleation field needs to form and thus this initial field should control the actual crust formation. The point here being that once the first nucleation takes place it will create preferential growth on the nucleus itself rather than starting a new nucleus (Ganguly, 2000).

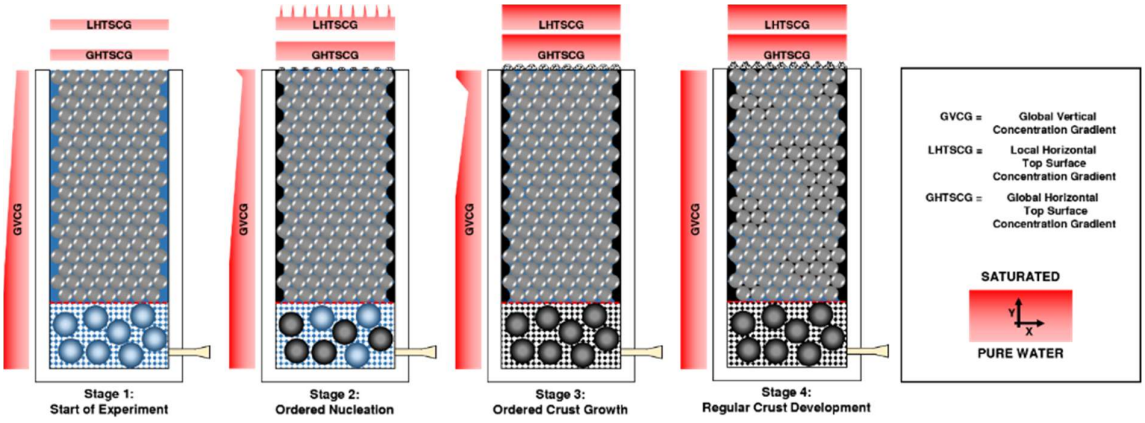


Figure II.10 General depiction of the sample's vertical section while in drying stages with qualitative indications of horizontal top surface concentration gradients (global/local) and vertical section global concentration gradients.

In our experiments, the initial surface concentration needs to be low enough so that the nucleation will take place in a slow and uniformly distributed manner at the liquid-air interface. This phenomenon as spoken briefly in Chapter 1 is related to the local concentration field as discussed in (Guglielmini et al., 2008; Huinink et al., 2002; Sghaier et al., 2007; Veran-Tissoires et al., 2012). The initial nuclei should after serve as growth platforms that incorporate progressively Na^+ and Cl^- ions from solution. This should result in Configuration 1: porous crust islands with some border effect in-between and Configuration 2: non-porous macro crystals with efflorescence borders (the only still porous space) once the liquid film is completely evaporated.

Over the sample's height a concentration gradient is present from low at the top to saturated at the bottom (where the salt grains are), this actually makes sure that all the incoming flow is increasingly concentrated, so that the risk of convection cells forming is reduced. Its secondary role is that the incoming ion concentration increases while the evaporation rate stays almost constant as being CRP (see Chapter 1). This helps fill in faster the new available surface either of the crust islands or the macro-crystals. Thus, a constant supply chain is formed which is tailored for the increasing demand of the new formed crust/crystal layers.

Figure II.11 presents a vertical gradient versus an evaporation rate problem. In (Figure II.11 a) the whole top surface of the sample is covered with a hair thin ($100 < \mu m$) patterned crust. This crust is uniformly grown on top of the sample. Although the island type pattern is visible, it has a great flaw due to its thickness: it is quite fragile and easily grown over by the efflorescence as seen in the final result (Figure II.11 b). Its thickness and the fact that it gets lost in efflorescence growth shows that the balance between the vertical concentration gradient and the horizontal one is not achieved. Here the speed of evaporation is too high compared to the vertical concentration gradient. Thus the surface of the sample is in Stage 2 (GHTSCG Figure II.10) while the vertical gradient is in Stage 4 (GVCG Figure II.10). This experiment shows how delicate the balance is between GHTSCG, LHTSCG and GVCG (see Figure II.10).

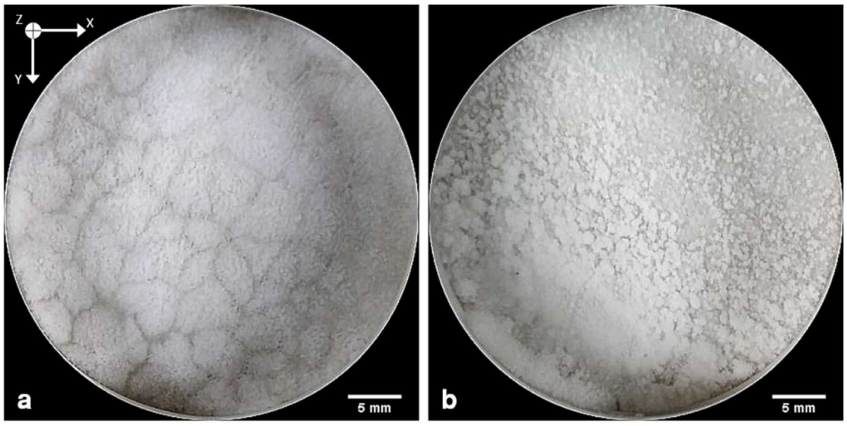


Figure II.11 Salt crust affected by uneven concentration gradient in the XZ and YZ plane: a) First observed patterning, b) Final crust

In theory the obtained concentration gradient on the top of the sample should be quite uniform. However, in practice things get more complex due to external factors such as the interdependency between evaporation rate and the concentration field at the liquid-gas interface. Figure II.11 presents a classical problem that appears when the evaporation rate is not uniform at the surface of the sample. The top part of (Figure II.12 a) shows the nucleation points becoming the island type efflorescence before mentioned while the bottom part has not even started the nucleation stage. In other words, the top part is at the end of Stage 2 or even Stage 3 (Figure II.10) while the bottom is still in Stage 1 (Figure II.10). This type of unbalance affects the whole thin equilibrium of the pattern forming as it can be seen in (Figure II.12 b) by the end of the crust forming process the two halves are so far apart that efflorescence covers the whole surface in an irregular manner. Thus the chosen environment (evaporation rate influencing factors) plays a role of equal importance as the rest of the design stage.

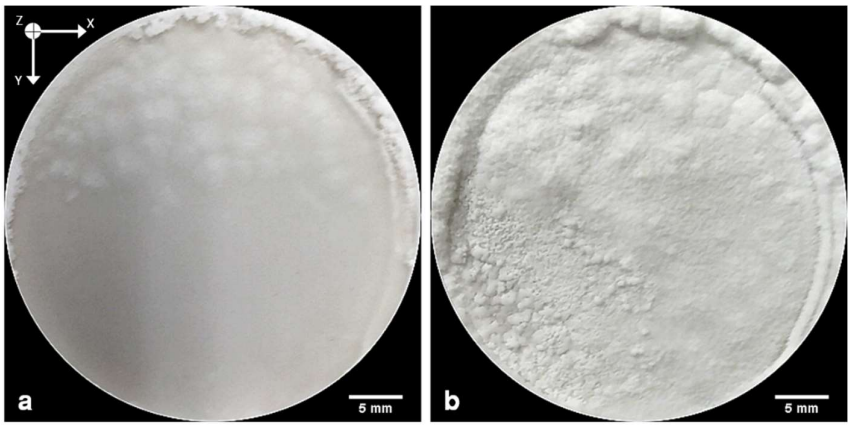


Figure II.12 Salt crust affected by uneven concentration gradient on XY plane: a) First observed island forming, b) Final crust

II.2.2.3. Pretesting the experimental environment conclusions

As discussed previously the coupled effect of flow-concentration-evaporation is of great importance to the formation of the pattern. In order to establish the general environmental conditions and thus the necessary evaporation rate a series of pretests was conducted. These pretests can be seen in Table II.I. The green lines in Table II.I represent successful pretests and thus the starting point for the environmental conditions. The concept here was to test certain factors such as temperature, humidity and wind in different couples as well as the liquid film thickness for Configuration 2 the RP pattern (Figure II.7). This in term allows for a narrowing of the variable field. In the following, we will present the configurations chosen to be pretested.

a) Chosen environment and protocol

The temperature was varied by intervals of about 20 degrees Celsius (22, 40 and 60°C). The 22°C was left in the room conditions as it is kept at constant temperature and humidity (25%) and the rest were in kept two separate ovens one at 40°C and one at 60°C. For the ovens the samples were kept 2 or 4 at a time, so that the humidity will remain about the same (tested from time to time with a hygrometer). However, the contents (salt, water, glass beads and actual containers) of the experiments were not preheated to the desired temperature before being put in the containers. Thus for all the pretests the initial temperature was room temperature (22°C).

The humidity was kept constant by either humidity calibration salts ($7\% \, with \, LiBr$,~$45\% \, with \, K_2CO_3$) in environmental cells, dehumidifier or left as it was in the ovens.

The wind aspect was either in environmental cells as fans (1 or 2 depending on the cell as seen in Table II.I) and also was taken into consideration (due to the climate control) for the samples kept in the experimental room (this is the meaning of “Yes” in Table II.I).

Each experiment was made the same way. A PTFE (Teflon) container was filled with a certain quantity (by mass) of dry salt grains after the dry glass beads were packed on top of it. When they were at the necessary height water was injected through the bottom of the sample. Once the water was visible on the surface of the beads the injecting was stopped. If the beads

were not at the right height after the process more dry beads were added so that the desired height was achieved. Any surplus brine was removed with a syringe. In the case of liquid film on top, deionized water was added slowly by the wall so that the top beads will not be disturbed.

For all the experiments carried out some precautions were taken in order to obtain as much as possible a uniform evaporation at the surface. An example of this irregularity is presented in Figure II.12. This was avoided by rotating each sample 90 degrees every couple of hours in order to avoid any drying irregularity due to the environmental conditions (example: the air movement in the experimental room, uneven heating in the oven, etc.). After the crust completely formed this was deemed unnecessary.

At certain important stages (initial surface, nucleation, fully formed crust) pictures were taken manually and as fast as possible so that there would be little environmental shock (example: taking a sample out from 60°C and shocking it by putting it at 20°C).

b) Table II.I header disambiguation

The pretest number represents the number given by us to the experiment.

PTFE Ø38 refers to a Teflon container with an inner diameter of about 38mm.

T represents temperature and RH relative humidity.

The total media height refers to the height of the salt grains plus the glass beads plus the liquid film if there is any.

The evap. shield (evaporation shield) refers to a border of certain height which is added on top of the sample in order to not have an increased evaporation rate at samples margins for more on this subject see (Veran-Tissoires et al., 2012).

The refill means that water was added on top of the sample after a fully grown crust was formed.

No.	Pretest Number	Sample													Environment			Evap. Shield	Pattern	Refill			General Observations
		Container Type	Porous Media									Liquid Film		Total Media Height	Observations	T	RH	Wind/Fan			Yes/No	Height	Result	
			Type	Bottom layer		Top Layer																		
				Type	Weight	Type	Diameter	Height/ Weight	Yes/No	Type	Height													
					g		µm	mm/g			mm	mm		°C	%	Number	mm			mm		
1	1	PTFE Ø38	Dry	Salt	10	Glass Beads	1-50	-	Yes	Water	5	35	-	22	25	Yes	15	Yes	No	-	-	-
2	3	PTFE Ø38	Dry	Salt	10	Glass Beads	1-50	-	Yes	Water	5	35	-	22	7	2	15	No	No	-	-	-
3	4	PTFE Ø38	Dry	Salt	10	Glass Beads	1-50	-	Yes	Water	10	35	-	22	7	2	15	No	No	-	-	-
4	5	PTFE Ø38	Dry	Salt	10	Glass Beads	1-50	-	Yes	Water	5	35	-	40	20	No	15	No	Yes	5	-	Close to RP after refill
5	6	PTFE Ø38	Dry	Salt	10	Glass Beads	1-50	-	Yes	Water	10	35	-	40	20	No	15	No	Yes	10	-	
6	7	PTFE Ø38	Dry	Salt	10	Glass Beads	1-50	-	Yes	Water	5	35	-	60	~20	No	15	No	Yes	5	Good	Close to RP after refill
7	8	PTFE Ø38	Dry	Salt	10	Glass Beads	1-50	-	Yes	Water	10	35	-	60	~20	No	15	No	Yes	10	-	-
8	9	PTFE Ø38	Dry	Salt	10	Glass Beads	1-50	-	Yes	Water	10	35	Filled from top	22	25	Yes	15	No	Yes	10	-	-
9	10	PTFE Ø38	Wick	Salt	-	Glass Beads	1-50	-	No	-	-	35	-	22	25	Yes	15	No	No	-	-	-
10	11	PTFE Ø38	Wick	Salt	-	Glass Beads	1-50	-	No	-	-	35	-	22	7	2	15	No	No	-	-	-
11	14	PTFE Ø38	Dry	Salt	20	Glass Beads	1-50	-	No	-	-	70	-	40	20	No	No	No	No	-	-	-
12	15	PTFE Ø38	Dry	Salt	20	Glass Beads	1-50	-	No	-	-	85	-	40	20	No	No	Yes	No	-	-	Very ordered GP patern
13	16	PTFE Ø38	Dry	Salt	20	Glass Beads	1-50	-	No	-	-	85	-	60	~20	No	No	No	No	-	-	Tends to pattern
14	17	PTFE Ø38	Dry	Salt	20	Glass Beads	1-50	-	No	-	-	85	-	22	25	Yes	No	Yes	No	-	-	Very ordered GP patern
15	18	PTFE Ø38	Dry	Salt	10	Glass Beads	1-50	-	Yes	Water	1	35	Partial pattern	22	25	Yes	No	No	Yes	1	Pattern	-
16	19	PTFE Ø38	Dry	Salt	10	Glass Beads	1-50	-	Yes	Water	10	35	-	22	25	Yes	No	Yes	No	-	-	Very ordered RP patern
17	20	Petri dish	Dry	Salt	-	Glass Beads	1-50	-	No	-	-	35	-	22	25	Yes	No	No	Yes	-	-	-
18	22	Stainless Steel Tray	Dry	Salt	1105	Glass Beads	1-50	1815 g	No	-	-	-	-	60	45	No	20	No	Yes X3	-	-	-
19	1'	PTFE Ø38	Dry	Salt	10	Glass Beads	1-50	-	Yes	Water	10	35	Partial pattern	22	25	Yes	No	Yes	No	-	-	RP type pattern
20	3'	PTFE Ø38	Dry	Salt	10	Glass Beads	1-50	-	No	-	-	35	-	60	~20	No	15	No	No	-	-	Almost GP pattern
21	4'	PTFE Ø38	Dry	Salt	10	Glass Beads	1-50	-	Yes	Water	2	35	-	22	25	Yes	15	Yes	No	-	-	Very ordered RP patern
22	5'	PTFE Ø38	Dry	Salt	10	Glass Beads	1-50	-	No	-	-	35	Partial pattern	40	20	No	15	No	No	-	-	Almost GP pattern
23	6'	PTFE Ø38	Dry	Salt	10	Glass Beads	1-50	-	Yes	Water	2	35	-	40	20	No	15	Yes	No	-	-	Very ordered RP patern
24	8'	PTFE Ø38	Dry	Salt	10	Glass Beads	1-50	-	Yes	Water	2	35	-	60	~20	No	15	No	No	-	-	-

Table II.I Pretests of environmental conditions

c) Environment: conclusions

As seen in Table II.I out of the 24 performed experiments, 5 experiments were deemed as successful: 2 Configuration 1 GP pattern and 3 Configuration 2 RP pattern.

The environmental conditions that yielded positive results for GP patterns were for experiments 15 and 17. The common characteristic being the height of the porous media which is over two times the containers diameter (85mm in height versus 38mm in diameter), no evaporation and the relative humidity at about 20%. In terms of temperature one was at 22°C and the other at 40°C. As for the wind conditions the 22°C experiment had air flow while the 40°C had none. Thus we can roughly consider that the wind should compensate for the difference in temperature. The final results of the formed crust can be seen in Figure II.13.

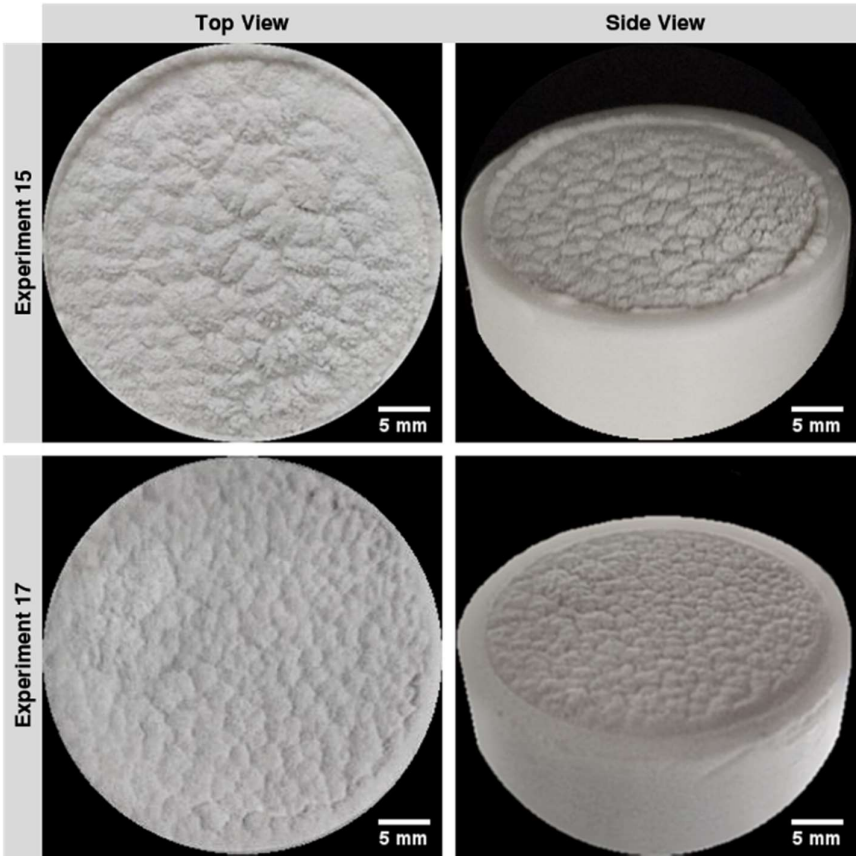


Figure II.13 Top and side views of experiments 15 and 17 with fully developed crusts

While the environmental conditions that yielded positive results for RP patterns were 19, 4' and 6'. The common characteristic here again is the height of the porous media which is about the same as the diameter of the container (35mm in height versus 38 mm in diameter) and the relative humidity at about 20%. In terms of temperature two were at 22°C and the other at 40°C. As for the wind conditions the 22°C experiments had air flow while the 40°C had none as before. However, an interesting conclusion can be taken from the two experiments with 2mm of water film (4' and 6'). That again it seems the air flow compensates for the about 20°C difference between the experiments. The final results of the formed crust can be seen in Figure II.14.

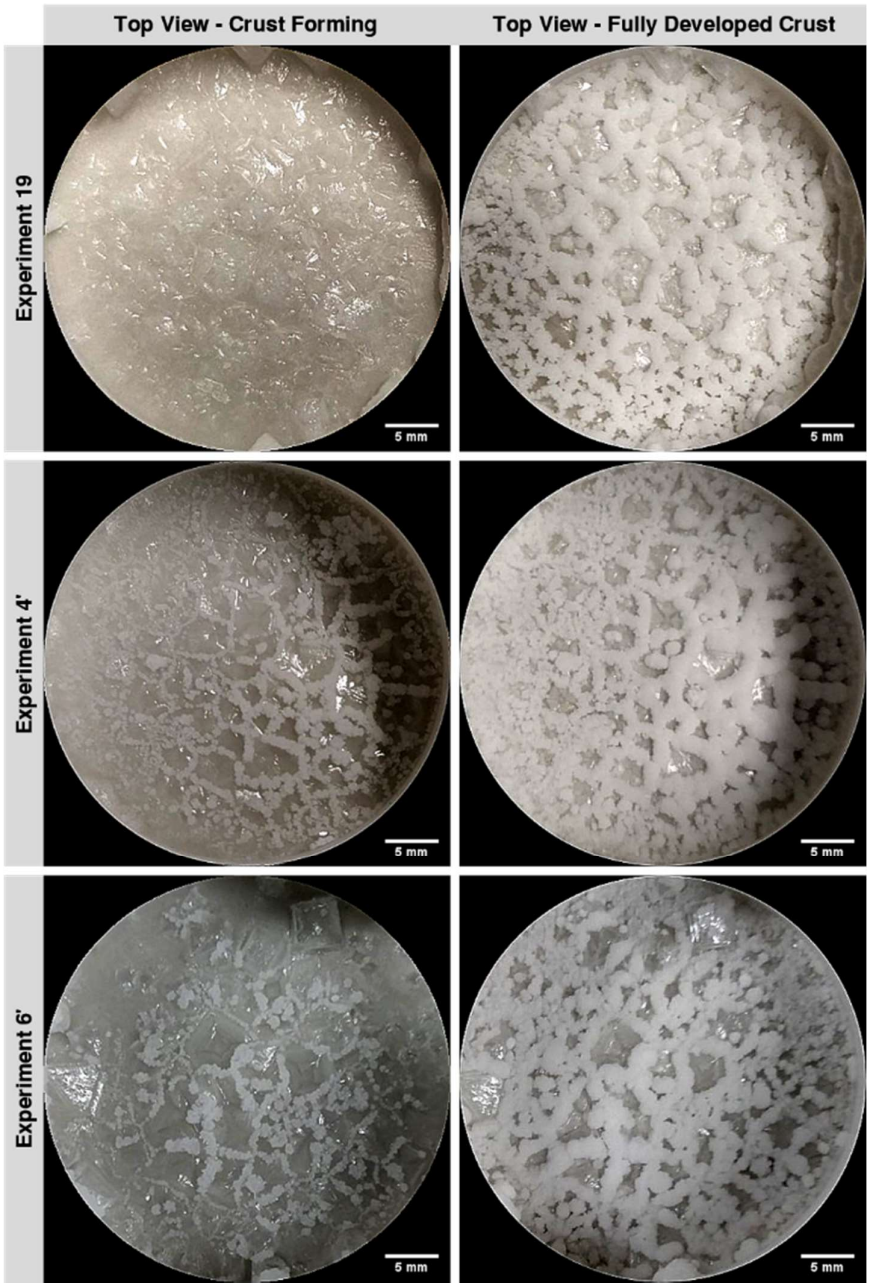


Figure II.14 Top views at different development times of experiments 19, 4' and 6'

For the complete comparison between the successful pattern environments, see Table II.II.

No.	Pretest Number	Sample										Environment			Evap. Shield
		Container Type	Porous Media								Total Media Height	T	RH	Wind/Fan	
			Type	Bottom Layer		Top Layer		Liquid Film							
				Type	Weight	Type	Diameter	Yes/No	Type	Height					
					g		µm			mm	mm	°C	%	Number	mm
GP Pattern															
15	15	PTFE Ø38	Dry	Salt	20	Glass Beads	1-50	No	-	-	85	40	20	No	No
17	17	PTFE Ø38	Dry	Salt	20	Glass Beads	1-50	No	-	-	85	22	25	Yes	No
RP Pattern															
19	19	PTFE Ø38	Dry	Salt	10	Glass Beads	1-50	Yes	Water	10	35	22	25	Yes	No
25	4'	PTFE Ø38	Dry	Salt	10	Glass Beads	1-50	Yes	Water	2	35	22	25	Yes	15
27	6'	PTFE Ø38	Dry	Salt	10	Glass Beads	1-50	Yes	Water	2	35	40	20	No	15

Table II.II Comparison between the successful pretests environmental conditions

In conclusion with the help of the pretests we have established the starting point for the environmental factors and successfully produced two types of regulated patterns. This shows that the suppositions discussed earlier are in the right direction towards producing and controlling salt crust patterns.

II.2.3. Driving phenomenon: Influence of steady-state flow in porous media

As spoken briefly in Chapter 1 and will be in more details here, the flow of brine through the media has big repercussions on the concentration fields and thus on the efflorescence growth. So that the objective here will be to have a system that is as much as possible continuous and steady-state in terms of flow.

In this part, the supposed driving phenomenon, in relationship to obtaining patterns in a laboratory environment, will be discussed. As now a configuration has been set for our interpretation on the naturally formed patterns.

Generally speaking, if a phenomenon may produce any kind of repetitive and ordered result, first of all, it will require stability in the developing media. In the present case this stability can be translated in certain factors. Here, the ones taken into account will be related to: (i) flow in porous media (porosity influence and the adjacent capillarity effects, wall effects, evaporation flux) and (ii) concentration gradients in porous media (inside it as well as on top at the opened surface evaporation front).

II.2.3.1. Pore invasion and transient flow

The objective here is to form a system that will allow a full salt crust to form while being continuously and fully supplied with brine from the adjacent porous media. Thus two closely related factors will be taken into consideration.

The first factor is the supply network to the crust. This has been translated into a highly capillary porous medium such as the chosen $1-50\mu m$ glass bead fraction. This type of medium has the benefit of being at the lower limit of micro-porosity, thus its pore size can effectively pull liquid from a big range of pores (Lenormand, 1990). In the case of the proposed setup this small porosity of the top layer ($1-50\mu m$) will play an important role as the salt grains

are in the rage of $200 - 400\mu m$. Thus, after the injection of water. The salt layer pore size should increase due to dissolution effects and the top layer will assure that the liquid gets pumped first out of the bottom layer and not out of the micro-beads, thus assuring a continuous and uniform brine feed to the top surface (Figure II.8).

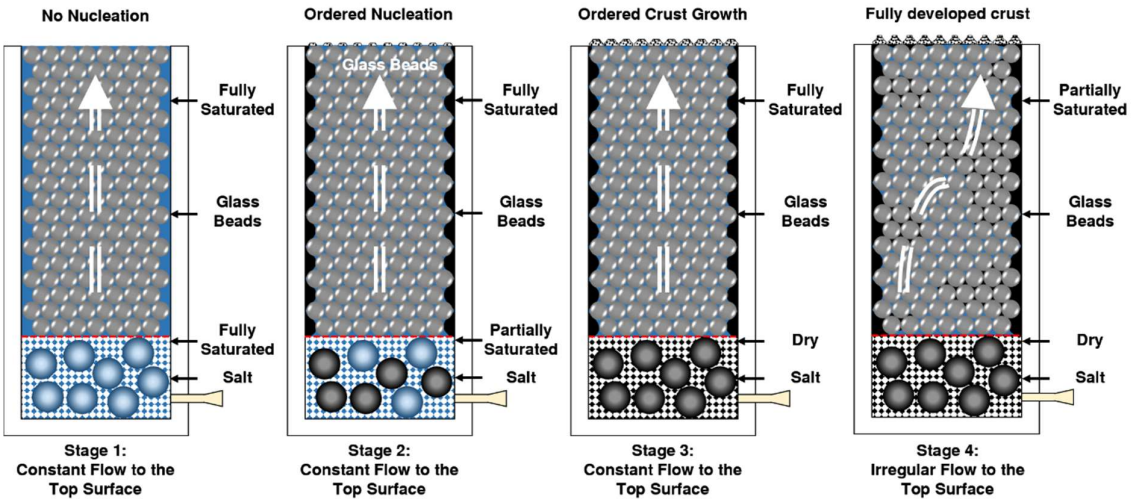


Figure II.8 General depiction of the sample's vertical section while in drying stages.

The second factor would be the pore invasion mechanics which is taken into account due to the fact that once the evaporative processes start. The chosen set up is a dry situation setup and the sample container has a limited amount of liquid in it unlike the wick situation where the porous media has a continuous supply of brine.

Here the same factors are exploited more exactly the pore invasion will preferentially invade the bigger pores first as seen in (Borgman et al., 2017; Lehmann & Or, 2009), which in this situation are situated at the bottom of the sample. This allows for a completely saturated upper layer. By exploiting this phenomenon, the experiment should not have preferential wet and dry zones in the upper layer until the water from the bottom salt layer is completely pulled out and replaced with air (Figure II.8) for evolution of saturation profiles in the pores.

Thus, if there is brine at the bottom of the sample, the top layer should stay fully saturated with a uniform flow of brine. Thus creating a good environment for the formation of crystallization patterns.

In pre-testing, this concept worked only for some of the samples. Some problems were encountered as the crusts formed unevenly. After careful examination, the problem was identified as an uneven dissolution of the bottom layer (salt grains forming sinkholes) and the bead layer became of variable height thus modifying the flow of brine. As seen in Figure II.9, the effect of this local variation in height completely changes the morphology of the crust.

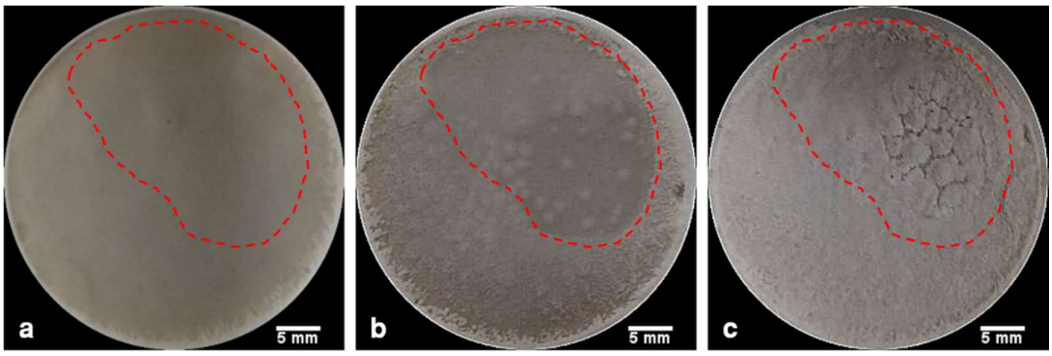


Figure II.9 Salt crust (top view) affected by non-uniform underlying flow (red area): a) Start of experiment, b) First observed nucleation, c) Final crust

II.2.3.2. Porous media local and global concentration gradients

Due to this experiment's configuration, an initial gradient is obtained after the injection of deionized water. This is due to the configuration's salt-bead layers and should insure that this initial gradient will be present for a certain amount of time until diffusive effects render it uniform. Previously, by using the porosity's capillary properties, a constant flow was obtained, while now the focus is on the concentration distribution through the cell. This is an important aspect of the concept, the goal being that a uniformly distributed initial nucleation field needs to form and thus this initial field should control the actual crust formation. The point here being that once the first nucleation takes place it will create preferential growth on the nucleus itself rather than starting a new nucleus (Ganguly, 2000).

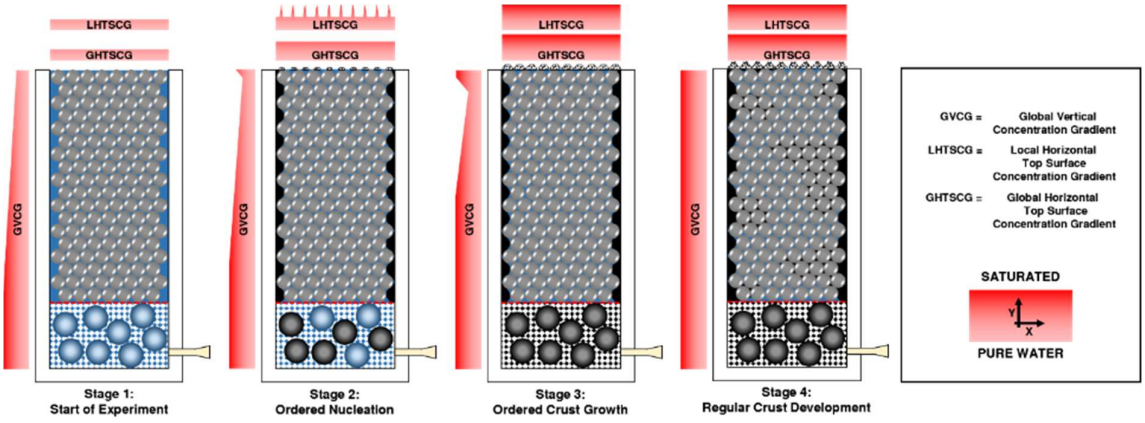


Figure II.10 General depiction of the sample's vertical section while in drying stages with qualitative indications of horizontal top surface concentration gradients (global/local) and vertical section global concentration gradients.

In our experiments, the initial surface concentration needs to be low enough so that the nucleation will take place in a slow and uniformly distributed manner at the liquid-air interface. This phenomenon as spoken briefly in Chapter 1 is related to the local concentration field as discussed in (Guglielmini et al., 2008; Huinink et al., 2002; Sghaier et al., 2007; Veran-Tissoires et al., 2012). The initial nuclei should after serve as growth platforms that incorporate progressively Na^+ and Cl^- ions from solution. This should result in Configuration 1: porous crust islands with some border effect in-between and Configuration 2: non-porous macro crystals with efflorescence borders (the only still porous space) once the liquid film is completely evaporated.

Over the sample's height a concentration gradient is present from low at the top to saturated at the bottom (where the salt grains are), this actually makes sure that all the incoming flow is increasingly concentrated, so that the risk of convection cells forming is reduced. Its secondary role is that the incoming ion concentration increases while the evaporation rate stays almost constant as being CRP (see Chapter 1). This helps fill in faster the new available surface either of the crust islands or the macro-crystals. Thus, a constant supply chain is formed which is tailored for the increasing demand of the new formed crust/crystal layers.

Figure II.11 presents a vertical gradient versus an evaporation rate problem. In (Figure II.11 a) the whole top surface of the sample is covered with a hair thin ($100 < \mu m$) patterned crust. This crust is uniformly grown on top of the sample. Although the island type pattern is visible, it has a great flaw due to its thickness: it is quite fragile and easily grown over by the efflorescence as seen in the final result (Figure II.11 b). Its thickness and the fact that it gets lost in efflorescence growth shows that the balance between the vertical concentration gradient and the horizontal one is not achieved. Here the speed of evaporation is too high compared to the vertical concentration gradient. Thus the surface of the sample is in Stage 2 (GHTSCG Figure II.10) while the vertical gradient is in Stage 4 (GVCG Figure II.10). This experiment shows how delicate the balance is between GHTSCG, LHTSCG and GVCG (see Figure II.10).

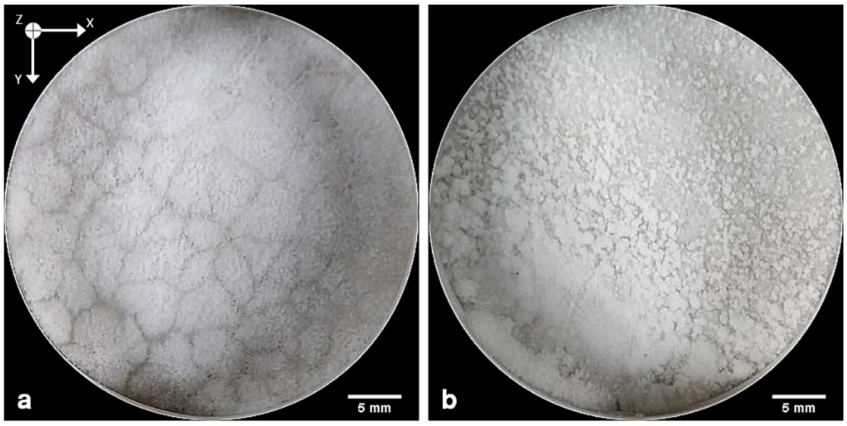


Figure II.11 Salt crust affected by uneven concentration gradient in the XZ and YZ plane: a) First observed patterning, b) Final crust

In theory the obtained concentration gradient on the top of the sample should be quite uniform. However, in practice things get more complex due to external factors such as the interdependency between evaporation rate and the concentration field at the liquid-gas interface. Figure II.11 presents a classical problem that appears when the evaporation rate is not uniform at the surface of the sample. The top part of (Figure II.12 a) shows the nucleation points becoming the island type efflorescence before mentioned while the bottom part has not even started the nucleation stage. In other words, the top part is at the end of Stage 2 or even Stage 3 (Figure II.10) while the bottom is still in Stage 1 (Figure II.10). This type of unbalance affects the whole thin equilibrium of the pattern forming as it can be seen in (Figure II.12 b) by the end of the crust forming process the two halves are so far apart that efflorescence covers the whole surface in an irregular manner. Thus the chosen environment (evaporation rate influencing factors) plays a role of equal importance as the rest of the design stage.

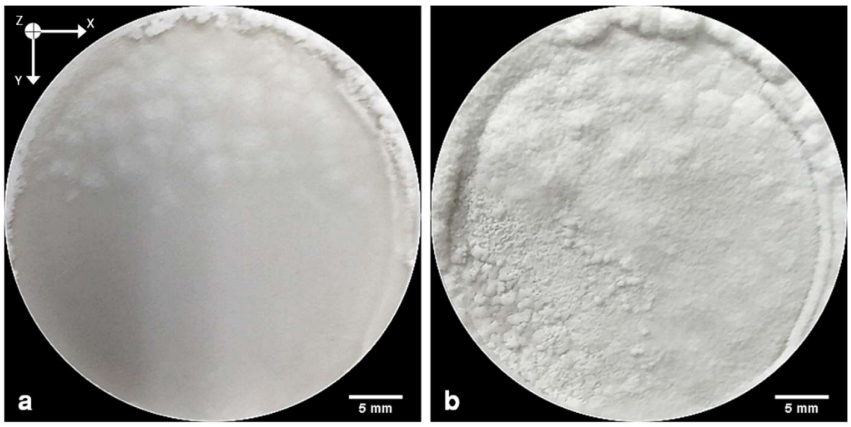


Figure II.12 Salt crust affected by uneven concentration gradient on XY plane: a) First observed island forming, b) Final crust

II.2.3.3. Pretesting the experimental environment conclusions

As discussed previously the coupled effect of flow-concentration-evaporation is of great importance to the formation of the pattern. In order to establish the general environmental conditions and thus the necessary evaporation rate a series of pretests was conducted. These pretests can be seen in Table II.I. The green lines in Table II.I represent successful pretests and thus the starting point for the environmental conditions. The concept here was to test certain factors such as temperature, humidity and wind in different couples as well as the liquid film thickness for Configuration 2 the RP pattern (Figure II.7). This in term allows for a narrowing of the variable field. In the following, we will present the configurations chosen to be pretested.

a) Chosen environment and protocol

The temperature was varied by intervals of about 20 degrees Celsius (22, 40 and 60°C). The 22°C was left in the room conditions as it is kept at constant temperature and humidity (25%) and the rest were in kept two separate ovens one at 40°C and one at 60°C. For the ovens the samples were kept 2 or 4 at a time, so that the humidity will remain about the same (tested from time to time with a hygrometer). However, the contents (salt, water, glass beads and actual containers) of the experiments were not preheated to the desired temperature before being put in the containers. Thus for all the pretests the initial temperature was room temperature (22°C).

The humidity was kept constant by either humidity calibration salts ($7\% \, with \, LiBr$,~$45\% \, with \, K_2CO_3$) in environmental cells, dehumidifier or left as it was in the ovens.

The wind aspect was either in environmental cells as fans (1 or 2 depending on the cell as seen in Table II.I) and also was taken into consideration (due to the climate control) for the samples kept in the experimental room (this is the meaning of “Yes” in Table II.I).

Each experiment was made the same way. A PTFE (Teflon) container was filled with a certain quantity (by mass) of dry salt grains after the dry glass beads were packed on top of it. When they were at the necessary height water was injected through the bottom of the sample. Once the water was visible on the surface of the beads the injecting was stopped. If the beads

were not at the right height after the process more dry beads were added so that the desired height was achieved. Any surplus brine was removed with a syringe. In the case of liquid film on top, deionized water was added slowly by the wall so that the top beads will not be disturbed.

For all the experiments carried out some precautions were taken in order to obtain as much as possible a uniform evaporation at the surface. An example of this irregularity is presented in Figure II.12. This was avoided by rotating each sample 90 degrees every couple of hours in order to avoid any drying irregularity due to the environmental conditions (example: the air movement in the experimental room, uneven heating in the oven, etc.). After the crust completely formed this was deemed unnecessary.

At certain important stages (initial surface, nucleation, fully formed crust) pictures were taken manually and as fast as possible so that there would be little environmental shock (example: taking a sample out from 60°C and shocking it by putting it at 20°C).

b) Table II.I header disambiguation

The pretest number represents the number given by us to the experiment.

PTFE Ø38 refers to a Teflon container with an inner diameter of about 38mm.

T represents temperature and RH relative humidity.

The total media height refers to the height of the salt grains plus the glass beads plus the liquid film if there is any.

The evap. shield (evaporation shield) refers to a border of certain height which is added on top of the sample in order to not have an increased evaporation rate at samples margins for more on this subject see (Veran-Tissoires et al., 2012).

The refill means that water was added on top of the sample after a fully grown crust was formed.

No.	Pretest Number	Sample													Environment			Evap. Shield	Pattern	Refill			General Observations
		Container Type	Porous Media									Liquid Film		Total Media Height	Observations	T	RH	Wind/Fan		Yes/No	Height	Result	
			Type	Bottom layer		Top Layer																	
				Type	Weight	Type	Diameter	Height/ Weight	Yes/No	Type	Height												
					g		µm	mm/g			mm	mm		°C	%	Number	mm			mm		
1	1	PTFE Ø38	Dry	Salt	10	Glass Beads	1-50	-	Yes	Water	5	35	-	22	25	Yes	15	Yes	No	-	-	-
2	3	PTFE Ø38	Dry	Salt	10	Glass Beads	1-50	-	Yes	Water	5	35	-	22	7	2	15	No	No	-	-	-
3	4	PTFE Ø38	Dry	Salt	10	Glass Beads	1-50	-	Yes	Water	10	35	-	22	7	2	15	No	No	-	-	-
4	5	PTFE Ø38	Dry	Salt	10	Glass Beads	1-50	-	Yes	Water	5	35	-	40	20	No	15	No	Yes	5	-	Close to RP after refill
5	6	PTFE Ø38	Dry	Salt	10	Glass Beads	1-50	-	Yes	Water	10	35	-	40	20	No	15	No	Yes	10	-	
6	7	PTFE Ø38	Dry	Salt	10	Glass Beads	1-50	-	Yes	Water	5	35	-	60	~20	No	15	No	Yes	5	Good	Close to RP after refill
7	8	PTFE Ø38	Dry	Salt	10	Glass Beads	1-50	-	Yes	Water	10	35	-	60	~20	No	15	No	Yes	10	-	-
8	9	PTFE Ø38	Dry	Salt	10	Glass Beads	1-50	-	Yes	Water	10	35	Filled from top	22	25	Yes	15	No	Yes	10	-	-
9	10	PTFE Ø38	Wick	Salt	-	Glass Beads	1-50	-	No	-	-	35	-	22	25	Yes	15	No	No	-	-	-
10	11	PTFE Ø38	Wick	Salt	-	Glass Beads	1-50	-	No	-	-	35	-	22	7	2	15	No	No	-	-	-
11	14	PTFE Ø38	Dry	Salt	20	Glass Beads	1-50	-	No	-	-	70	-	40	20	No	No	No	No	-	-	-
12	15	PTFE Ø38	Dry	Salt	20	Glass Beads	1-50	-	No	-	-	85	-	40	20	No	No	Yes	No	-	-	Very ordered GP patern
13	16	PTFE Ø38	Dry	Salt	20	Glass Beads	1-50	-	No	-	-	85	-	60	~20	No	No	No	No	-	-	Tends to pattern
14	17	PTFE Ø38	Dry	Salt	20	Glass Beads	1-50	-	No	-	-	85	-	22	25	Yes	No	Yes	-	-	-	Very ordered GP patern
15	18	PTFE Ø38	Dry	Salt	10	Glass Beads	1-50	-	Yes	Water	1	35	Partial pattern	22	25	Yes	No	No	Yes	1	Pattern	-
16	19	PTFE Ø38	Dry	Salt	10	Glass Beads	1-50	-	Yes	Water	10	35	-	22	25	Yes	No	Yes	No	-	-	Very ordered RP patern
17	20	Petri dish	Dry	Salt	-	Glass Beads	1-50	-	No	-	-	35	-	22	25	Yes	No	No	Yes	-	-	-
18	22	Stainless Steel Tray	Dry	Salt	1105	Glass Beads	1-50	1815 g	No	-	-	-	-	60	45	No	20	No	Yes X3	-	-	-
19	1'	PTFE Ø38	Dry	Salt	10	Glass Beads	1-50	-	Yes	Water	10	35	Partial pattern	22	25	Yes	No	Yes	No	-	-	RP type pattern
20	3'	PTFE Ø38	Dry	Salt	10	Glass Beads	1-50	-	No	-	-	35	-	60	~20	No	15	No	No	-	-	Almost GP pattern
21	4'	PTFE Ø38	Dry	Salt	10	Glass Beads	1-50	-	Yes	Water	2	35	-	22	25	Yes	15	Yes	No	-	-	Very ordered RP patern
22	5'	PTFE Ø38	Dry	Salt	10	Glass Beads	1-50	-	No	-	-	35	Partial pattern	40	20	No	15	No	No	-	-	Almost GP pattern
23	6'	PTFE Ø38	Dry	Salt	10	Glass Beads	1-50	-	Yes	Water	2	35	-	40	20	No	15	Yes	No	-	-	Very ordered RP patern
24	8'	PTFE Ø38	Dry	Salt	10	Glass Beads	1-50	-	Yes	Water	2	35	-	60	~20	No	15	No	No	-	-	-

Table II.I Pretests of environmental conditions

c) Environment: conclusions

As seen in Table II.I out of the 24 performed experiments, 5 experiments were deemed as successful: 2 Configuration 1 GP pattern and 3 Configuration 2 RP pattern.

The environmental conditions that yielded positive results for GP patterns were for experiments 15 and 17. The common characteristic being the height of the porous media which is over two times the containers diameter (85mm in height versus 38mm in diameter), no evaporation and the relative humidity at about 20%. In terms of temperature one was at 22°C and the other at 40°C. As for the wind conditions the 22°C experiment had air flow while the 40°C had none. Thus we can roughly consider that the wind should compensate for the difference in temperature. The final results of the formed crust can be seen in Figure II.13.

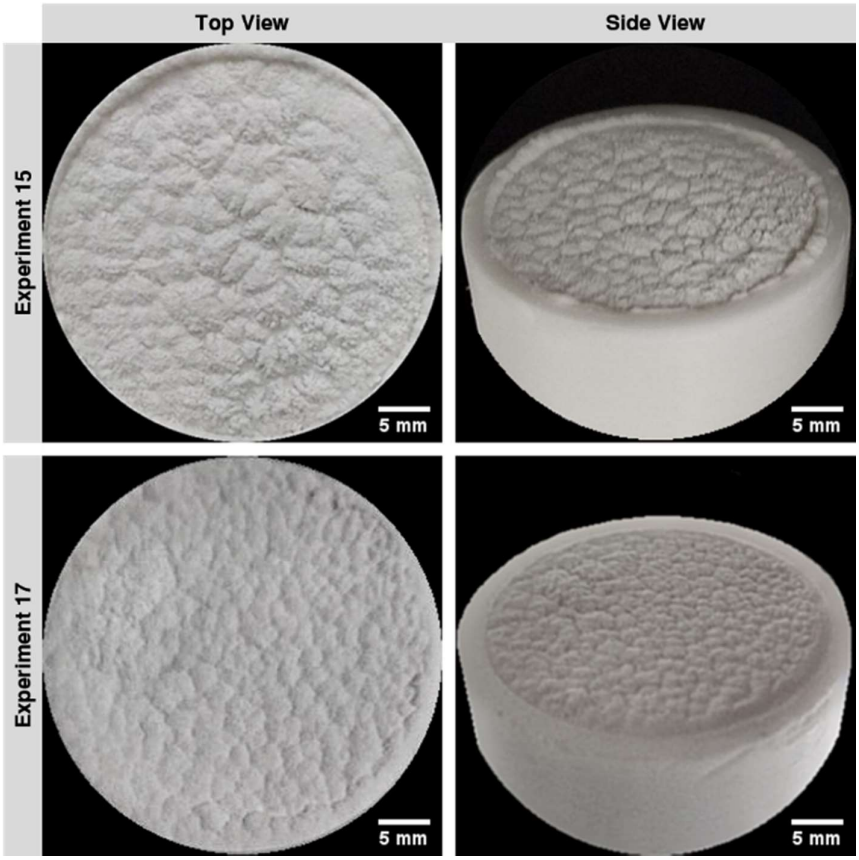


Figure II.13 Top and side views of experiments 15 and 17 with fully developed crusts

While the environmental conditions that yielded positive results for RP patterns were 19, 4' and 6'. The common characteristic here again is the height of the porous media which is about the same as the diameter of the container (35mm in height versus 38 mm in diameter) and the relative humidity at about 20%. In terms of temperature two were at 22°C and the other at 40°C. As for the wind conditions the 22°C experiments had air flow while the 40°C had none as before. However, an interesting conclusion can be taken from the two experiments with 2mm of water film (4' and 6'). That again it seems the air flow compensates for the about 20°C difference between the experiments. The final results of the formed crust can be seen in Figure II.14.

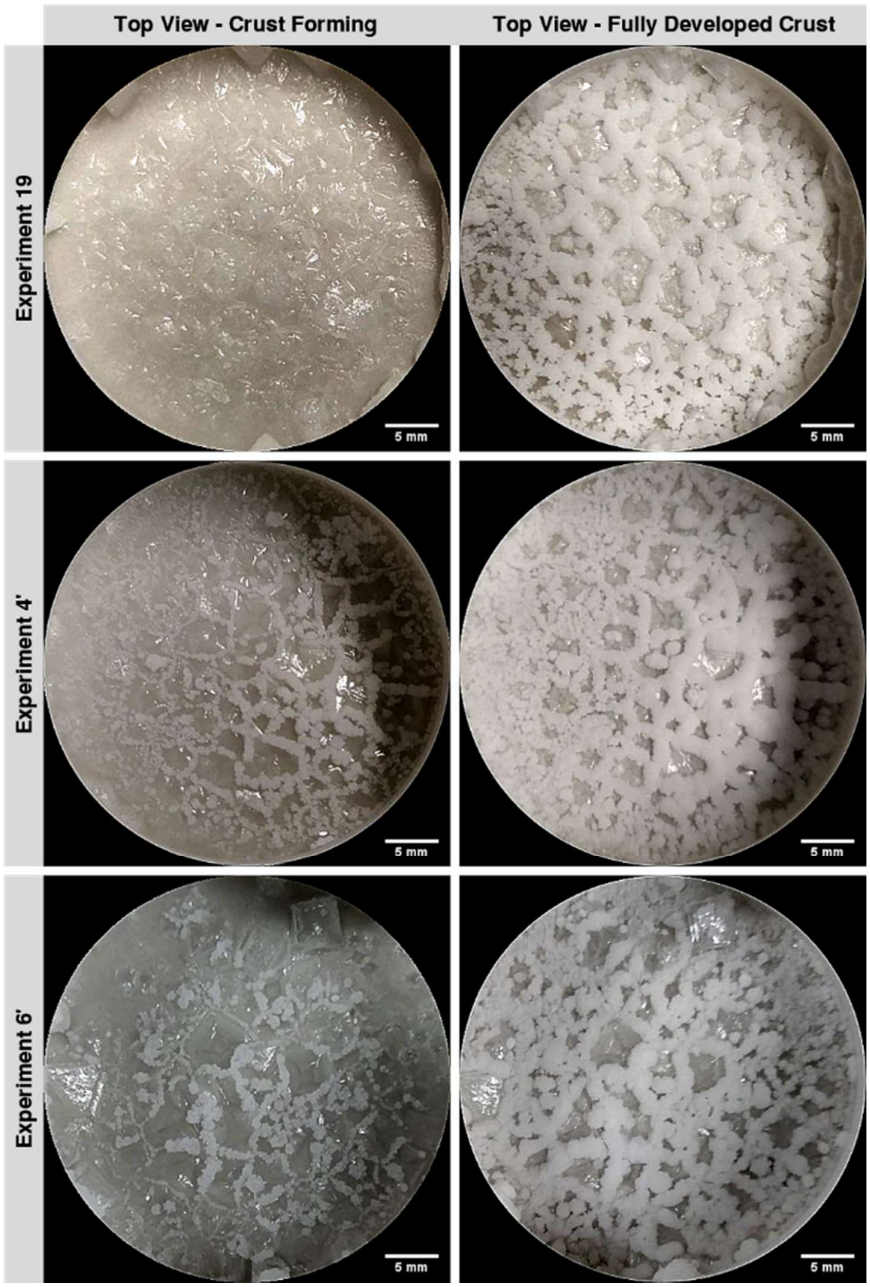


Figure II.14 Top views at different development times of experiments 19, 4' and 6'

For the complete comparison between the successful pattern environments, see Table II.II.

No.	Pretest Number	Sample											Environment			Evap. Shield
		Container Type	Porous Media									Total Media Height	T	RH	Wind/Fan	
			Type	Bottom Layer		Top Layer		Liquid Film								
				Type	Weight	Type	Diameter	Yes/No	Type	Height						
					g		µm			mm	mm		°C	%	Number	mm
GP Pattern																
15	15	PTFE Ø38	Dry	Salt	20	Glass Beads	1-50	No	-	-	85		40	20	No	No
17	17	PTFE Ø38	Dry	Salt	20	Glass Beads	1-50	No	-	-	85		22	25	Yes	No
RP Pattern																
19	19	PTFE Ø38	Dry	Salt	10	Glass Beads	1-50	Yes	Water	10	35		22	25	Yes	No
25	4'	PTFE Ø38	Dry	Salt	10	Glass Beads	1-50	Yes	Water	2	35		22	25	Yes	15
27	6'	PTFE Ø38	Dry	Salt	10	Glass Beads	1-50	Yes	Water	2	35		40	20	No	15

Table II.II Comparison between the successful pretests environmental conditions

In conclusion with the help of the pretests we have established the starting point for the environmental factors and successfully produced two types of regulated patterns. This shows that the suppositions discussed earlier are in the right direction towards producing and controlling salt crust patterns.

II.2.4. Controlled experiments: reducing the uncertainty of the process

As shown previously patterns were obtained in the pretesting stage moreover both patterns were successfully produced. Now the main goal is to not only produce the patterns but also to control precisely the experiments so that certain factor changes can be linked to certain behaviors.

Here we will be discussing what uncertainty is still at play in the previous pretests. As it can be seen in Table II.I, there is still need for improvement as for example experiment 19 produced a RP type pattern while experiment 1' produced only a partial pattern, although they were made the same way. Thus the need for a better and more controlled experimental setup is required.

Once a good reproducibility is achieved, certain factors can be tested in regards to their influence on the patterning. When talking about laboratory controlled experiments, all the influencing factors must be controlled and as such the pretesting gives just an indication of what could yield results. This method helps in reducing the experimental testing stage time. One can use relatively simple tests with high variation just to obtain a starting point for the actual experiments (in this case the environmental factors in relation with the established setups).

In the current stage of our testing there are still quite a lot of variables and as such each needs to be controlled. Due to the uncertainty that it provides with it. As such, in the case of pretests the most problematic would be: air flow, the injecting of deionized water and the vertical brine concentration gradient.

II.2.4.1. Controlled boundary conditions

Previously the boundary conditions were kept relatively controlled as an example the ovens were opened to take pictures or the room climate control creating air currents.

In order to have well controlled conditions, environmental cells were chosen. These in term were placed on precision balances so that mass loss can be recorded at constant intervals as well as relative humidity and temperature sensors were inserted in the cell enclosure with the same purpose. The relative humidity was maintained in the cell with the help of humidity maintaining salts ($7\%\ with\ LiBr$, $\sim 45\%\ with\ K_2CO_3$). While the temperature was controlled by circulating water around the cell at controlled temperature with the help of a heated water bath circulator. In case wind was needed one or two fans were fitted in the cell. The full setup is presented in Figure II.15.

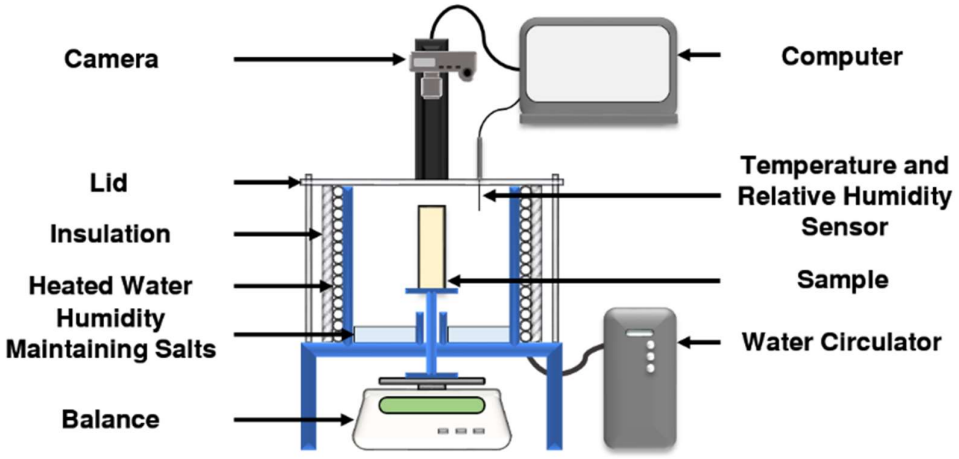


Figure II.15 Environmental cell setup

With this type of setup, the reproduction of the patterns would be in truly controlled conditions. Thus the next step would be to establish the actual boundary conditions.

As seen in **Environment: conclusions** for the GP pattern two successful recipes were obtained one at 22°C, the other at 40°C and both at about 20% RH. The one at 22°C in the presence of wind while the other without. Due to the complications attributed to wind in regards to modeling of the phenomenon it was established to compensate the loss in evaporation rate by using the 40°C temperature. Thus the temperature would be 40°C with no air flow (this helps also in obtaining an even evaporation rate on the surface of the sample. For the RH conditions were changed from the beginning as instead of about 20%, initially 7% would be tested and after the successful reproduction of the pattern a comparison would be made with a 45% one. This in order to establish the RH influence on the morphology of the crust.

As for the RP once the GP will be successful the environment will be tested on it too as the pretest results showed that it is less difficult to obtain. This due to the film on top which helps with its stability and recurrence.

Once these conditions were established the focus falls on the design of the sample in order to solve the rest of the variables.

II.2.4.2. Solving the deionized water injection inconsistency

When thinking about the injection process there are certain inconsistencies at play, for the pretesting these were deemed as non-essential in terms of the global result and as such

ignored. Now that the concept was proven and the contributing factors will be analyzed this technique is deemed as imprecise and thus needs to be redesigned.

The first problem with the injection process is the location or better said the unique location on the side of the sample. Thus forming irregularities when dissolution occurs in the bottom salt layer. Practically dissolving more salt at the inlet opening then in the rest of the salt layer. This has effects on the concentration gradient as well as in the liquid flow in the media (different porosity in the bottom layer) as spoken about in **Pore invasion and transient flow** and **Porous media local and global concentration gradients**.

The second problem is due to the fact that injecting generates overpressure at the bottom of the sample and there is a risk that the porous network will get locally and globally rearranged. Thus, forming preferential pathways, this again affects the concentration gradient and the flow in the media.

The first tested technique was with exactly the same setup in terms of packing composition; the only difference was that the bottom was a multi-hole mount that could be closed after filling it (Figure II.16 a). This, in term being submerged so that instead of injecting the porous media would get filled by capillarity (imbibition). In theory this would allow for a much more uniform dissolution front (as the deionized water would enter uniformly in the media) and filling (without disturbing the beads as the driving force would be the medium's capillarity). However, this has proven as being too slow (between 2 and 4 times slower than injecting) and giving a much too high concentration on the surface of the sample. Thus rendering the new design unusable.

The second tested technique was based on a different approach. Instead of modifying the injection part of the experiment, the bottom layer configuration would be modified. The concept here being, that if the bottom layer has better uniformity then naturally the salt dissolution and flow would be more uniform. Thus, the bottom layer would become from pure salt grains medium a big glass bead (1.2mm diameter) and an exact amount of salt grains medium (Figure II.16 b). Although the technique was promising, the results showed that still there is need for redesign as it did not yield results.

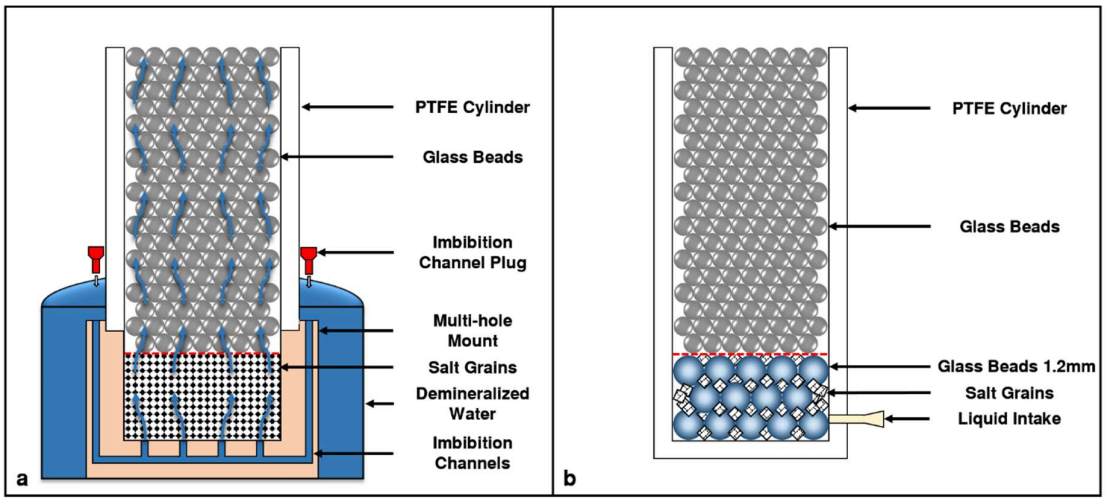


Figure II.16 Sample redesign: a) Multi-hole bottom mount; b) Large beads and salt grains bottom layer;

II.2.4.3. Final sample configuration

Previously, we discussed how the uncertainties in the system were too important in relation to the final goal of successfully understanding the phenomenon. Thus a complete redesign was done to the packing so that there will be no room for the variables presented before to intervene in the final crust forming. Thus the final experiment packing was done as follows.

The salt would be replaced with glass beads saturated with brine at 25% by weight. This allows for replicating the salt effect of high saturation in the bottom layer with the saturated glass beads as a reservoir that would feed the top layer uniformly in terms of concentration and flow.

Their average size, in order to preserve the concept of bigger pores in the bottom layer, would be always bigger than the top layer's. To obtain their impact on the pattern formation they will be varied so that their influence on the pattern formation could be studied.

The top layer would be kept constant in terms of glass bead size ($1 - 50\mu m$). While the porous layer would be filled with varied brine concentrations until a pattern will be obtained. These concentrations were to be varied in 5% steps.

Both the bead layers would be vacuumed separately before being stacked in the container so that no entrapped air would be present.

Looking at the pretests (see Table II.I) it seemed that GP experiment 14 had stability issues at a total height of 70mm while GP experiment 15 had the pattern at 85mm. Due to stability concerns the bottom and top layer height was increased as follows: bottom layer 20mm and top layer 105mm.

The first experiment with the new design was a GP with 25% by weight brine mixed in with $40 - 70\mu m$ glass beads on the bottom layer and on the top a 5% by weight brine mixt in with $1 - 50\mu m$. This experiment did not produce any pattern and was deemed as lacking the concentration needed to form the pattern. Thus the next concentration was tested on the top

layer a 10% brine. This successfully formed a patterned crust. However, it seemed that an increase in the bottom layer would be a better fit in terms of how long the layer could feed constant flow in the crust. The main difference between the GP configuration and the RP is that a certain amount of the top porous layer will be replaced with a liquid film that is put on top of the sample. The final sample configuration can be seen in Figure II.17.

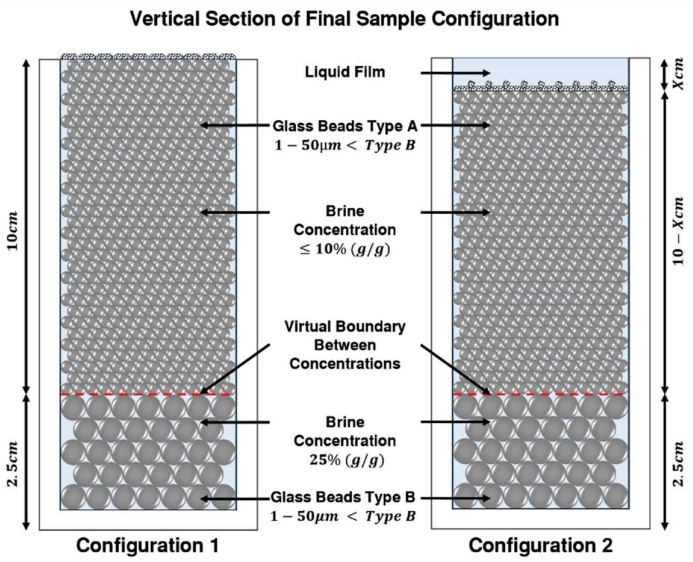


Figure II.17 Final sample configuration

II.3. Experimental results

In this section the final undergone experiments are presented. Here the emphasis was put on the GP patterns due to the fact that they are considered highly complex and hard to obtain with a good recurrence rate. This, in fact, is related to the way the stacked porous medium porous medium is formed in the final design. In theory the pore saturation in the sample should have an important effect towards the GP type pattern formation especially in terms of flow dynamics. The evaporative surface should be constantly supplied by the flow of brine at least as long as there is brine in the bottom layer. This, in term, influences the growth of the islands on the surface. While the RP type pattern should be less or not at all affected by it. This is due to the fact that the evaporative surface is completely covered by a film of liquid and thus as long as the film creates a complete crust the actual morphology should be less influenced. For the RP type crust other factors should affect the final result more, such as film thickness or wind.

As such, the primary goal here will be to obtain a recipe with a high success rate for the GP type and after to apply and adapt to the RP type.

II.3.1. Successful recipe for GP type patterns

As we established previously, the general layering of the samples and the environmental conditions, the last thing to test for a complete successful recipe is the actual bottom bead size and its influence. As in theory this has the potential to affect the final result (Table II.III and Figure II.18 to Figure II.25). A series of experiments were done in order to reach a conclusion on the influence of the bottom layer pore size.

The concept was as follows the experiments will be done in series of three (PD GP 1 to PD GP 16) the variable being only the bottom bead size (1-50μm, 40-70μm, 70-110μm, 100-200μm and 1200μm). The size 1-50μm was taken as a reference for the case of uniformity in pore size over the height of the sample. The 1200μm was taken as an extreme size so that the influence of the other part of the spectrum can be explored. As for the rest they were chosen geometrically, so that in theory the smallest diameter of two neighboring bottom beads (100μm extreme case) does not offer enough space for two of the top layer highest diameters (50μm) to fall through. This forming effect takes place at the border between the two layers (a clogged type space between the bottom and top layers). As such, offering the possibility to study the most possible available situations.

The only bead size with 4 experiments made the same being 40-70μm. This is because after three experiments the results were inconclusive, so that another experiment was needed in order to draw a conclusion.

Three concentration references were also tested in order to see if the concentration has an effect or not, they were as follows: PD GP REF 1: a sample full with 1-50μm beads and 10% brine, PD GP REF 2 a sample full with 1-50μm beads and 10% brine and in the end (when the most successful recipe was established) a PD GP REF 3 a double layer sample was prepared with bottom glass beads of 70-110μm and a top layer of 1-50μm both saturated with 10% brine (all concentrations are referred to by weight).

The temperature and relative humidity will be kept constant at 40°C and 10% RH for two reasons. First the idea here was to avoid as much as possible any kind of diffusion effects thus trying to have an advection based drying of the sample. The second reason was related to the formation of a crust in time, as the higher the evaporation rate the faster the crust will form. With these in mind the following results can be seen Table II.III and Figure II.18 to Figure II.25. For the table heather disambiguation see **Table II.I header disambiguation**.

No.	Experiment	Sample			Porous Media									Environment		Evap. Shield	Result
		Container Type	Type	Bottom layer				Top Layer				Liquid Film	Total Media Height	T	RH		
				Type	Diameter	Height	Brine	Type	Diameter	Height	Brine	Yes/No	mm	°C	%		
					µm	mm	%		µm	mm	%		mm				
1	PD GP REF 1	PTFE Ø38x125	Dry	Glass Beads	1-50	25	10	Glass Beads	1-50	100	10	No	125	40	7-10	-	No Pattern
2	PD GP REF 2	PTFE Ø38x125	Dry	Glass Beads	1-50	25	25	Glass Beads	1-50	100	25	No	125	40	7-10	-	No Pattern
3	PD GP REF 3	PTFE Ø38x125	Dry	Glass Beads	70-110	25	10	Glass Beads	1-50	100	10	No	125	40	7-10	-	Partial pattern
4	PD GP 1	PTFE Ø38x125	Dry	Glass Beads	1-50	25	25	Glass Beads	1-50	100	10	No	125	40	7-10	-	No Pattern
5	PD GP 2	PTFE Ø38x125	Dry	Glass Beads	1-50	25	25	Glass Beads	1-50	100	10	No	125	40	7-10	-	No Pattern
6	PD GP 3	PTFE Ø38x125	Dry	Glass Beads	1-50	25	25	Glass Beads	1-50	100	10	No	125	40	7-10	-	Partial pattern
7	PD GP 4	PTFE Ø38x125	Dry	Glass Beads	40-70	25	25	Glass Beads	1-50	100	10	No	125	40	7-10	-	Full pattern
8	PD GP 5	PTFE Ø38x125	Dry	Glass Beads	40-70	25	25	Glass Beads	1-50	100	10	No	125	40	7-10	-	No Pattern
9	PD GP 6	PTFE Ø38x125	Dry	Glass Beads	40-70	25	25	Glass Beads	1-50	100	10	No	125	40	7-10	-	Partial pattern
10	PD GP 7	PTFE Ø38x125	Dry	Glass Beads	40-70	25	25	Glass Beads	1-50	100	10	No	125	40	7-10	-	No Pattern
11	PD GP 8	PTFE Ø38x125	Dry	Glass Beads	70-110	25	25	Glass Beads	1-50	100	10	No	125	40	7-10	-	Full pattern
12	PD GP 9	PTFE Ø38x125	Dry	Glass Beads	70-110	25	25	Glass Beads	1-50	100	10	No	125	40	7-10	-	Partial pattern
13	PD GP 10	PTFE Ø38x125	Dry	Glass Beads	70-110	25	25	Glass Beads	1-50	100	10	No	125	40	7-10	-	Full pattern
14	PD GP 11	PTFE Ø38x125	Dry	Glass Beads	100-200	25	25	Glass Beads	1-50	100	10	No	125	40	7-10	-	Partial pattern
15	PD GP 12	PTFE Ø38x125	Dry	Glass Beads	100-200	25	25	Glass Beads	1-50	100	10	No	125	40	7-10	-	Partial pattern
16	PD GP 13	PTFE Ø38x125	Dry	Glass Beads	100-200	25	25	Glass Beads	1-50	100	10	No	125	40	7-10	-	Full Pattern
17	PD GP 14	PTFE Ø38x125	Dry	Glass Beads	1200	25	25	Glass Beads	1-50	100	10	No	125	40	7-10	-	No Pattern
18	PD GP 15	PTFE Ø38x125	Dry	Glass Beads	1200	25	25	Glass Beads	1-50	100	10	No	125	40	7-10	-	Full Pattern
19	PD GP 16	PTFE Ø38x125	Dry	Glass Beads	1200	25	25	Glass Beads	1-50	100	10	No	125	40	7-10	-	Full pattern
20	PD GP 17	PTFE Ø38x125	Dry	Glass Beads	40-70	25	25	Glass Beads	1-50	100	10	No	125	40	7-10	15	Partial pattern*
21	PD GP 18	PTFE Ø38x125	Dry	Glass Beads	40-70	25	25	Glass Beads	1-50	100	10	No	125	40	7-10	15	Partial Pattern*
22	PD GP 19	PTFE Ø38x125	Dry	Glass Beads	40-70	25	25	Glass Beads	1-50	100	10	No	125	40	45-50	-	Full Pattern
23	PD GP 20	PTFE Ø38x125	Dry	Glass Beads	40-70	25	25	Glass Beads	1-50	100	10	No	125	40	45-50	15	Partial Pattern*

Table II.III GP experiment sets on the influence of bottom layer porosity (* will be discussed separately)

As it can be seen in Table II.III, another four experiments were done in order to establish the possible creation of the pattern in different environmental conditions.

Two experiments were conducted at the same temperature and relative humidity but with evaporation shields on top of them PD GP 17 and PD GP 18. The bottom layer bead size is 40-70μm due to the fact that this was the first formulation to create patterns and as such the most variations were done with it in the beginning.

As another two were conducted PD GP 19 and PD GP 20 at different relative humidity 45-50% in order to establish a baseline of how it will be affecting the patterns. The only difference between the two samples is that one has an evaporation shield and one does not.

For all the experiments mass (Figure II.28 and Figure II.29), temperature (Figure II.30), relative humidity (Figure II.30) and pictures were recorded. Mass and pictures were taken at 100s intervals, as for temperature and relative humidity at 1000 second intervals.

During the data acquisition of experiments PD GP REF 2, PD GP 3 and PD GP 19 the temperature and relative humidity data was lost due to a software error. These are clearly marked in the legends of the graphs (Figure II.30) in red. However due to the very well controlled environment they were not discarded.

Due to the low contrast of the white crust patterns the last picture taken was light from the side so that the pattern is more visible. This technique was applied after the first batch of experiments was done and as such not all the experiments benefit from this increased visibility. The experimental pictures can be seen in direct comparison in Figure II.18 to Figure II.25.

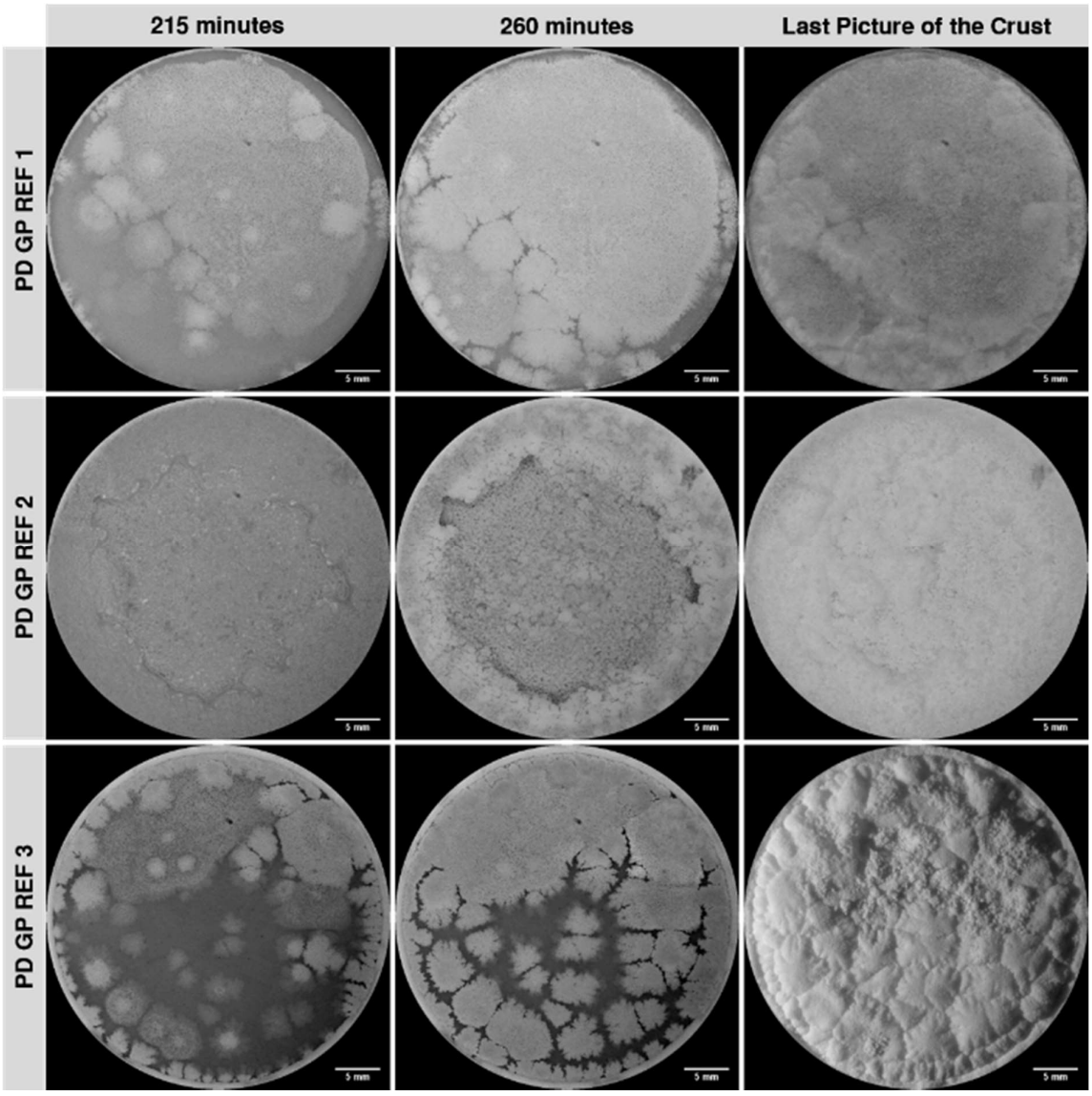


Figure II.18 Key aspects of crust formation (reference group)

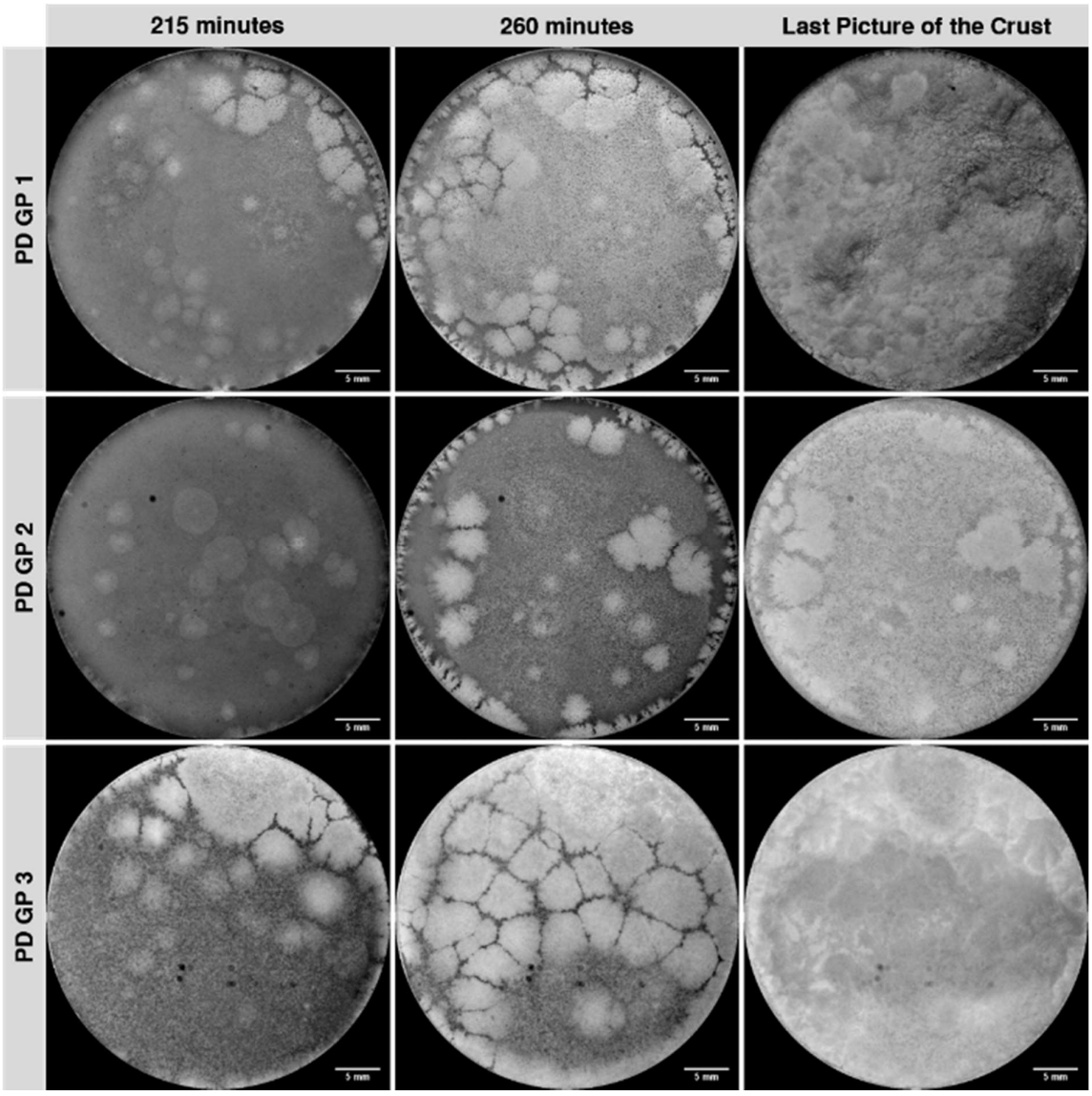


Figure II.19 Key aspects of crust formation (1-50µm group)

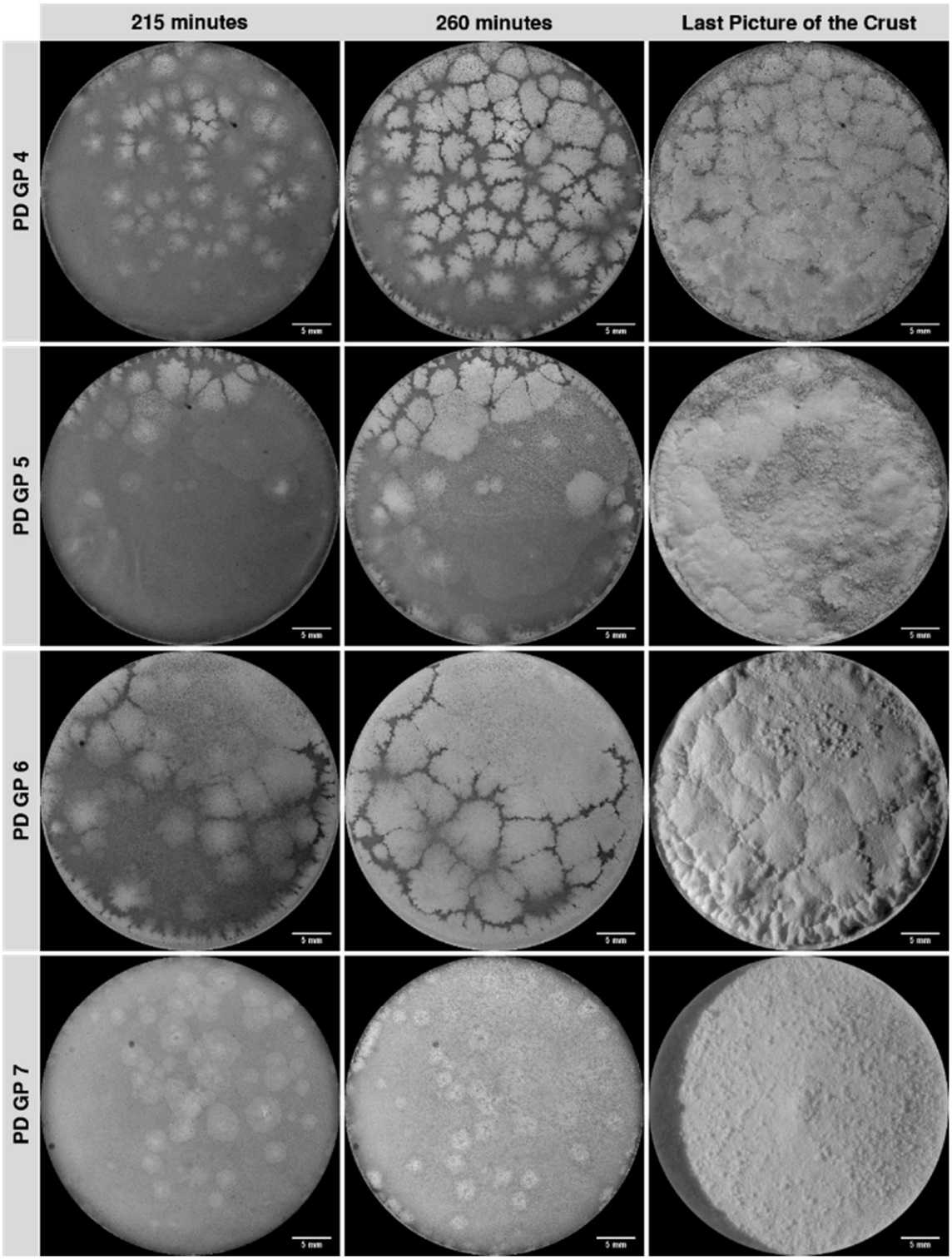


Figure II.20 Key aspects of crust formation (40-70µm group)

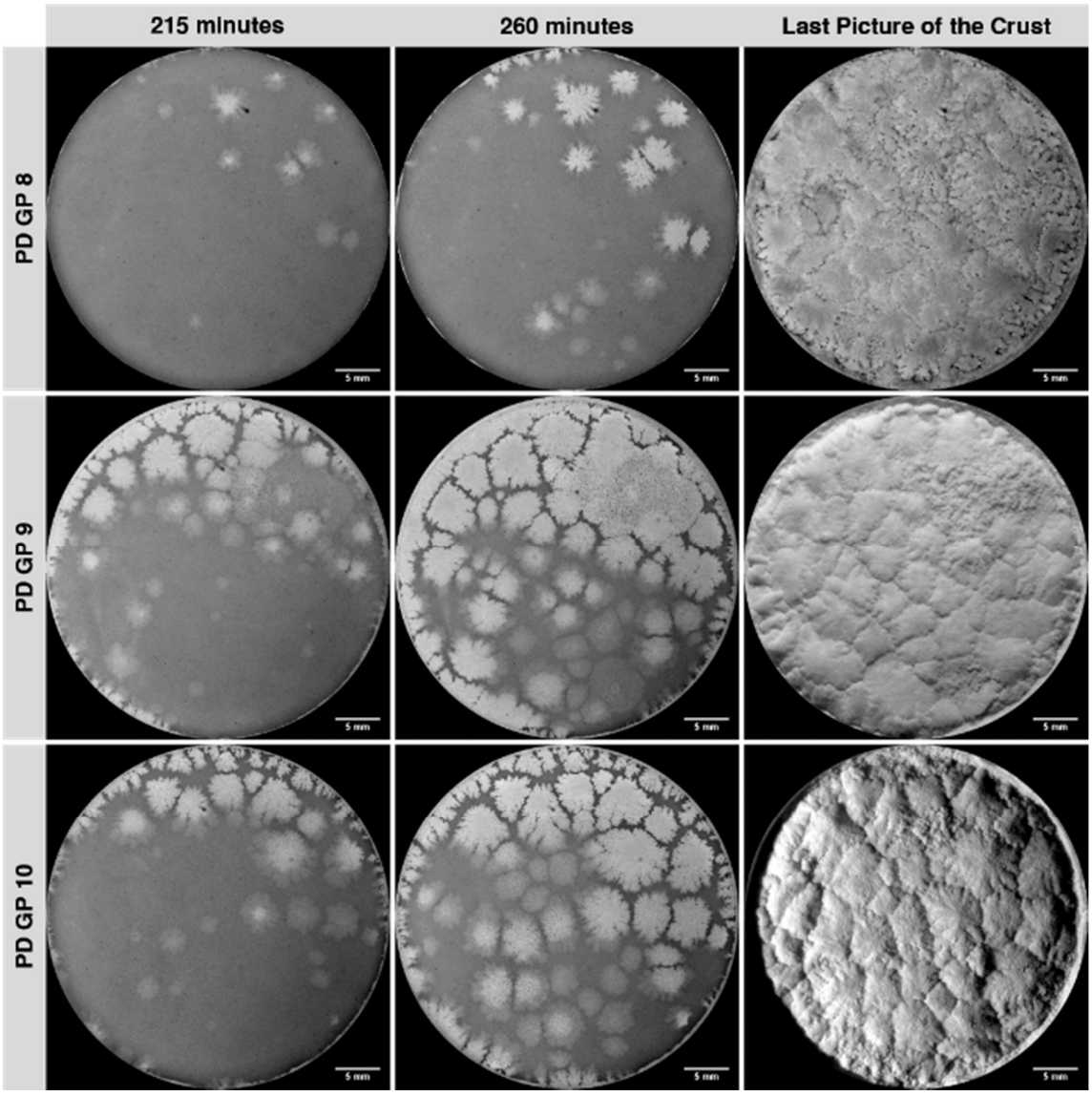


Figure II.21 Key aspects of crust formation (70-110µm group)

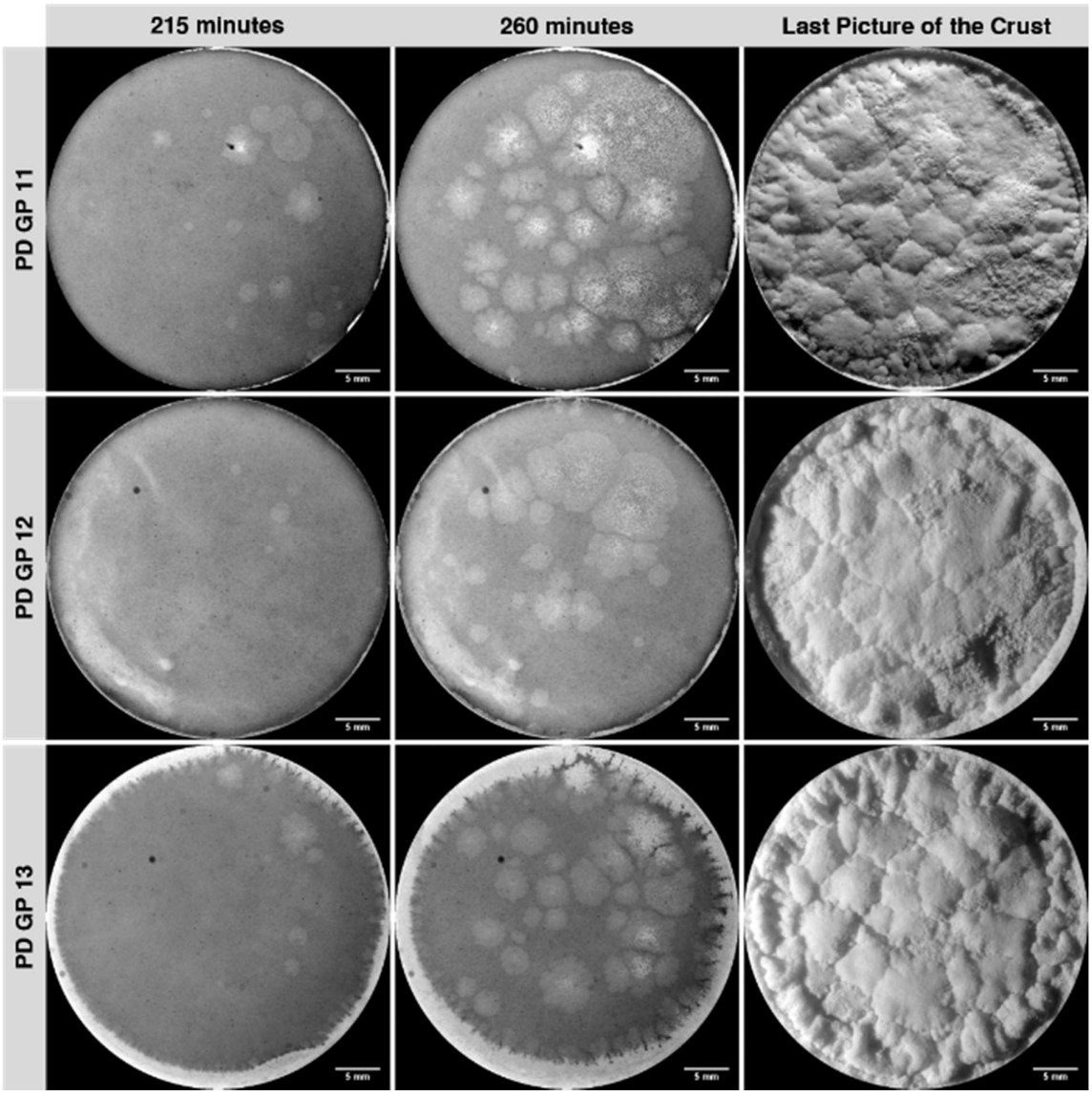


Figure II.22 Key aspects of crust formation (100-200µm group)

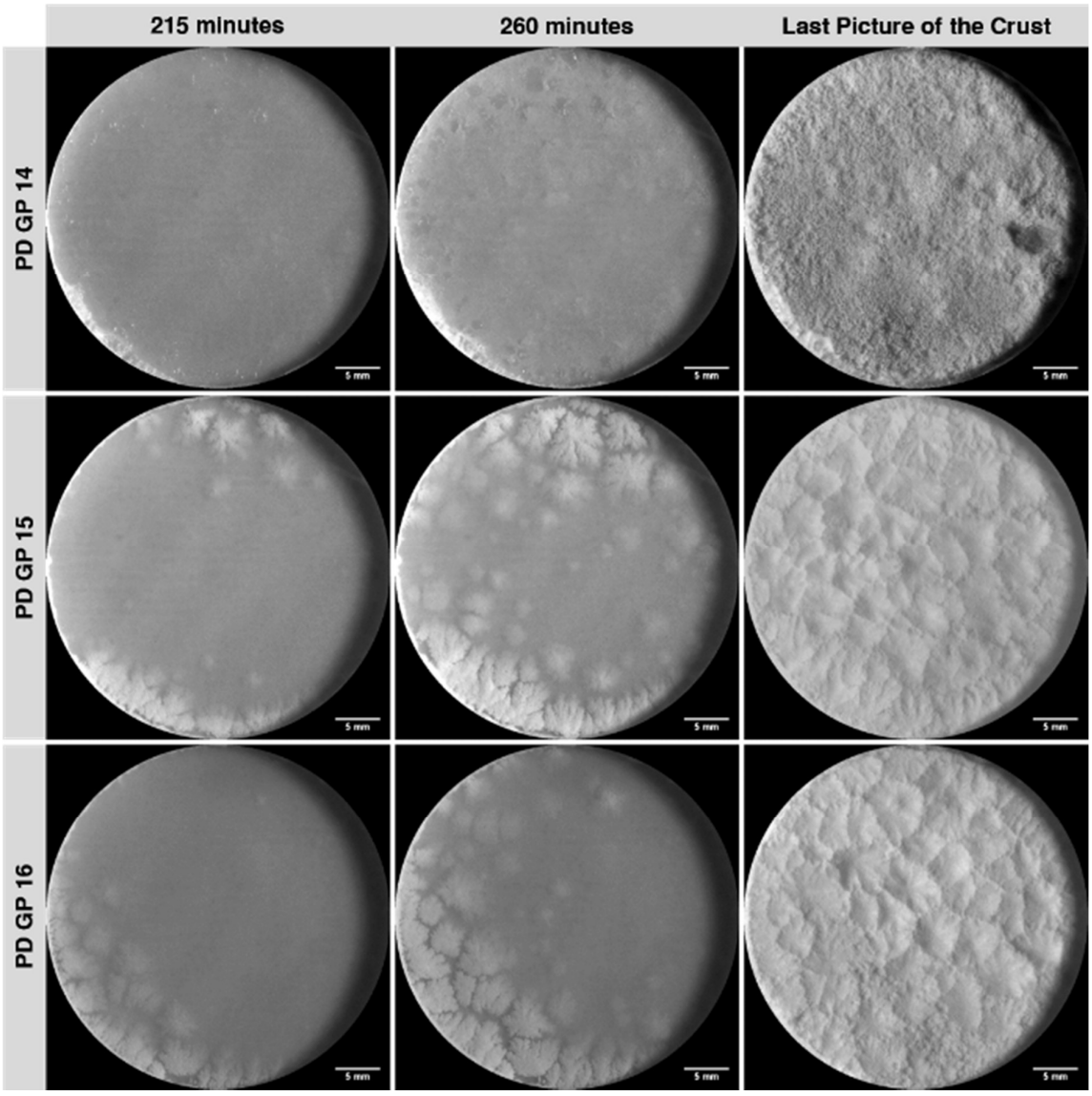


Figure II.23 Key aspects of crust formation (1200µm group)

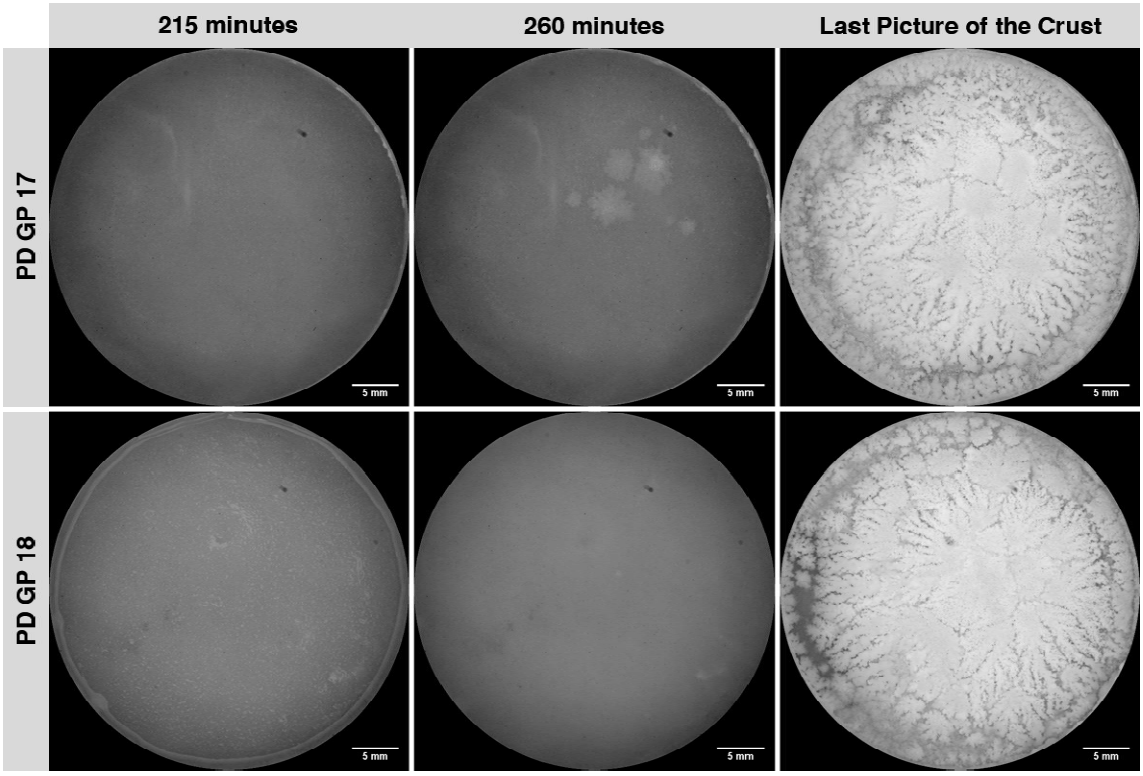


Figure II.24 Key aspects of crust formation (Evaporation shield at 7-10% RH Group)

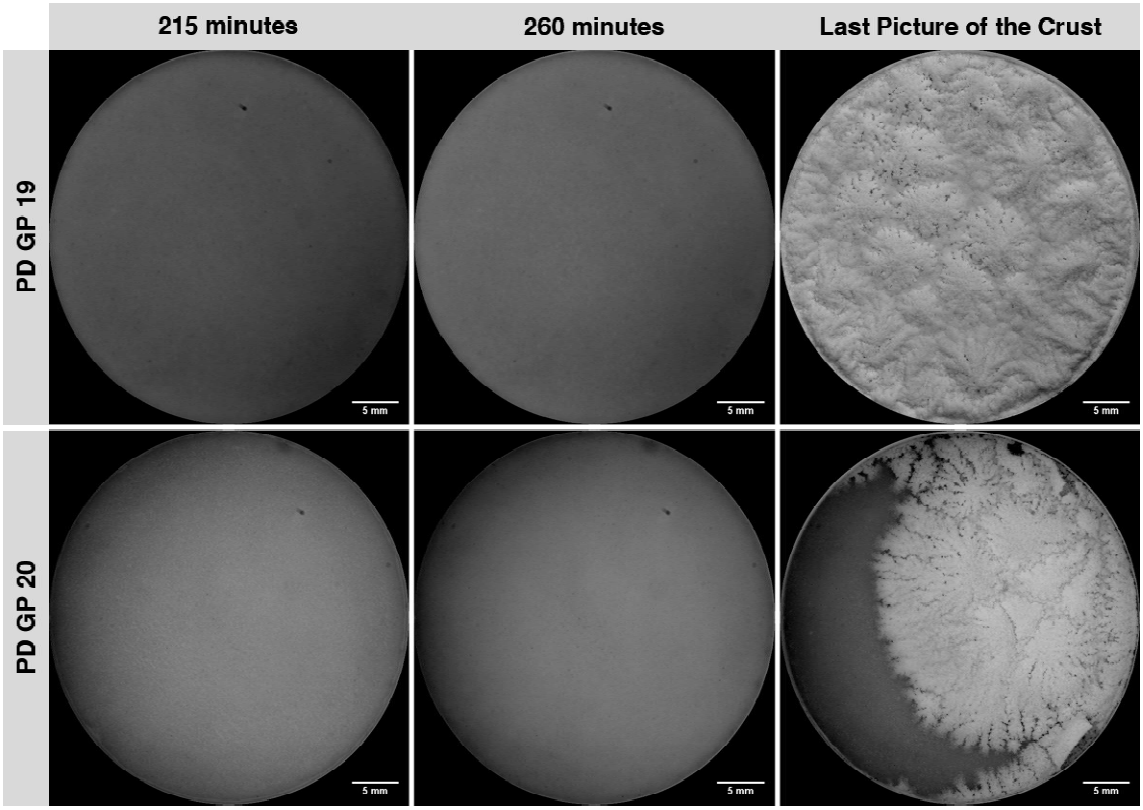


Figure II.25 Key aspects of crust formation (45-50% RH group)

In order to quantify the aspect of a successful pattern two procedures were applied as follows.

The first is the successful forming of a GP crust and was defined as follows. If a crust has all of its surface covered by a regulated pattern then it is deemed “Full pattern or GP crust”, if it is covered by the pattern on more than 50% of the crust then it is deemed a “Partial pattern or a Partial GP crust” and if it is covered over less than 50% of the total crust it is considered as a “No pattern or No GP crust” (Figure II.26).

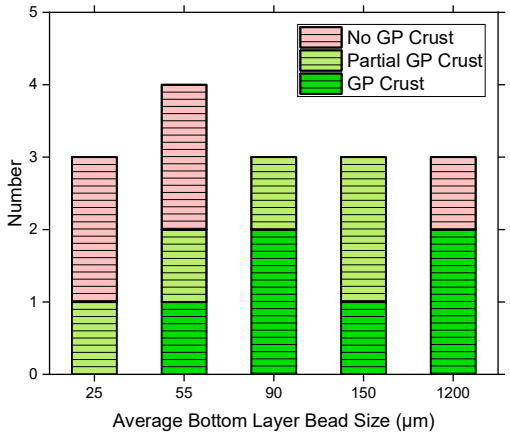


Figure II.26 PD GP 1 to PD GP 16 crust results obtained for varied bottom layer bead sizes

The second type of success it is the success rate (S_x) of a nucleation to transition into an island and thus form the GP crust. Here this was calculated as $S_x = \frac{\sum_i^1 s_i}{i}$ where s_i is the individual success rate of a series experiment thus $s_i = \frac{N_N}{N_I} * 100$ and N_N, N_I are number of nuclei per sample respectively number of formed islands in the final crust. N_N, N_I both are taken only for the nuclei that are found on the porous media. Thus, all the nuclei that appear on the border between the container and the porous medium are removed from calculations. For the success rates see Figure II.27.

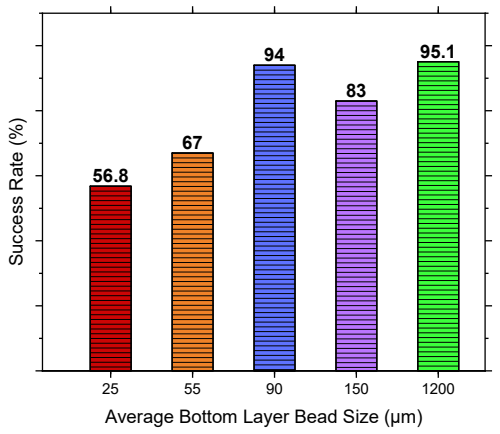


Figure II.27 PD GP 1 to PD GP 16 Nucleation to island success rate for the varied bottom layer bead sizes

In order to be sure that the experiments were as much as possible the same a direct comparison was done between the mass losses in the same group (Figure II.28).

Due to a big discrepancy in the evaporation curve of PD GP 14, it was considered null and was not taken into account as reliable in calculations such as success rate (Figure II.27). After a close inspection of the pictures it seems that the top layer collapsed into the bottom layer after the experiment started. Thus, it pumped all the brine out forming a large film of brine on the sample top. The rest of the experiments were considered reliable.

For all the formulations at least one experiment was kept longer than the rest in order to establish the stability of the pattern and the general evaporation curve.

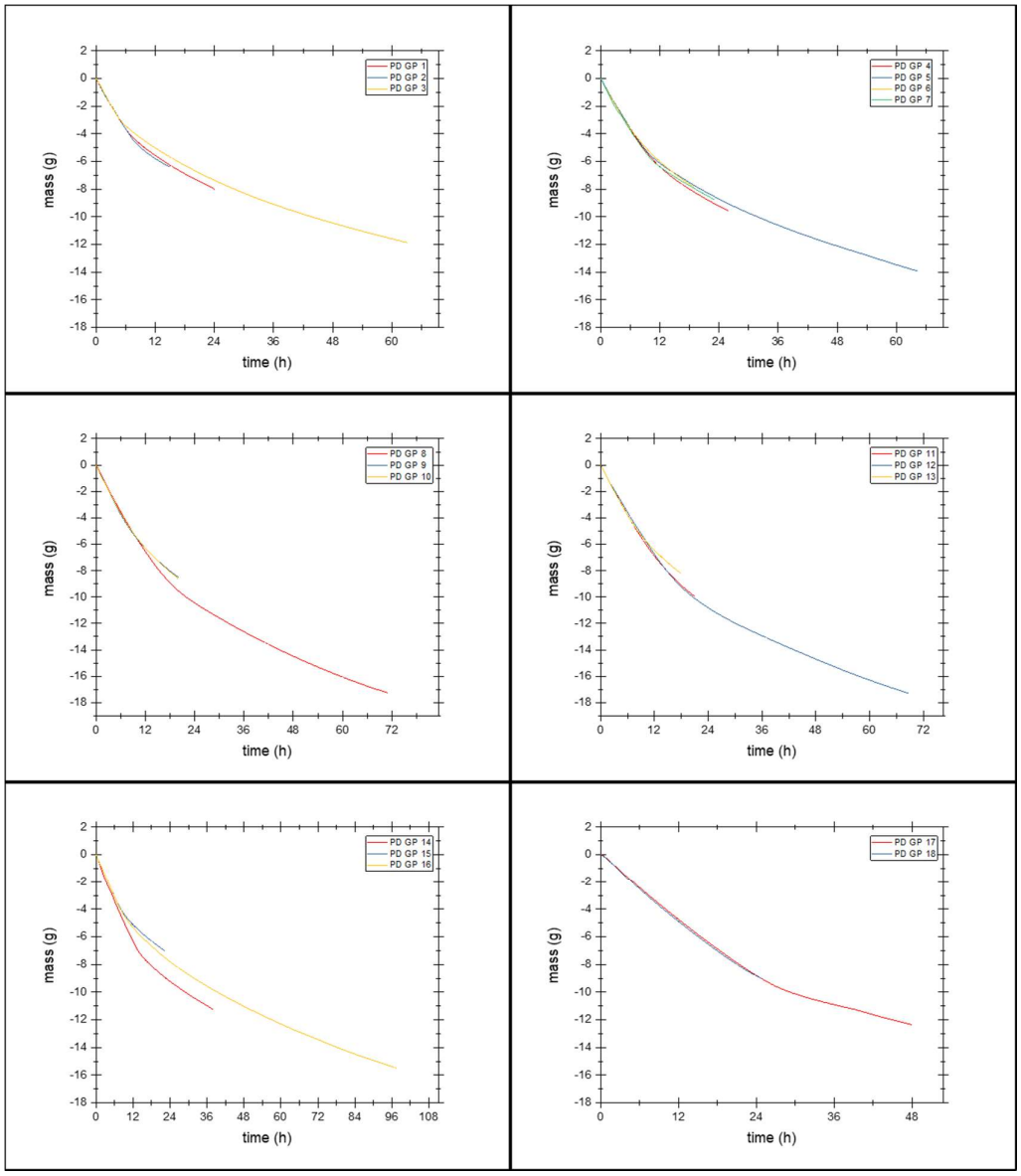


Figure II.28 Direct comparisons between mass losses (7-10% RH)

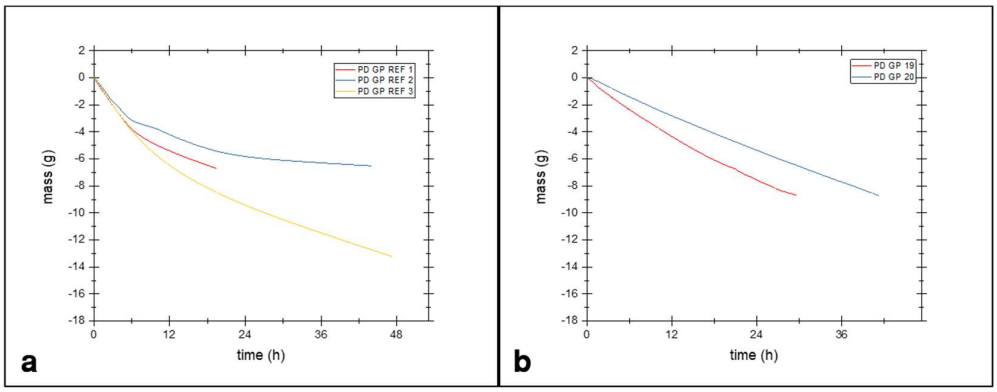


Figure II.29 Direct comparisons between: a) reference mass losses; b) Direct comparison between 45-50% RH experiments

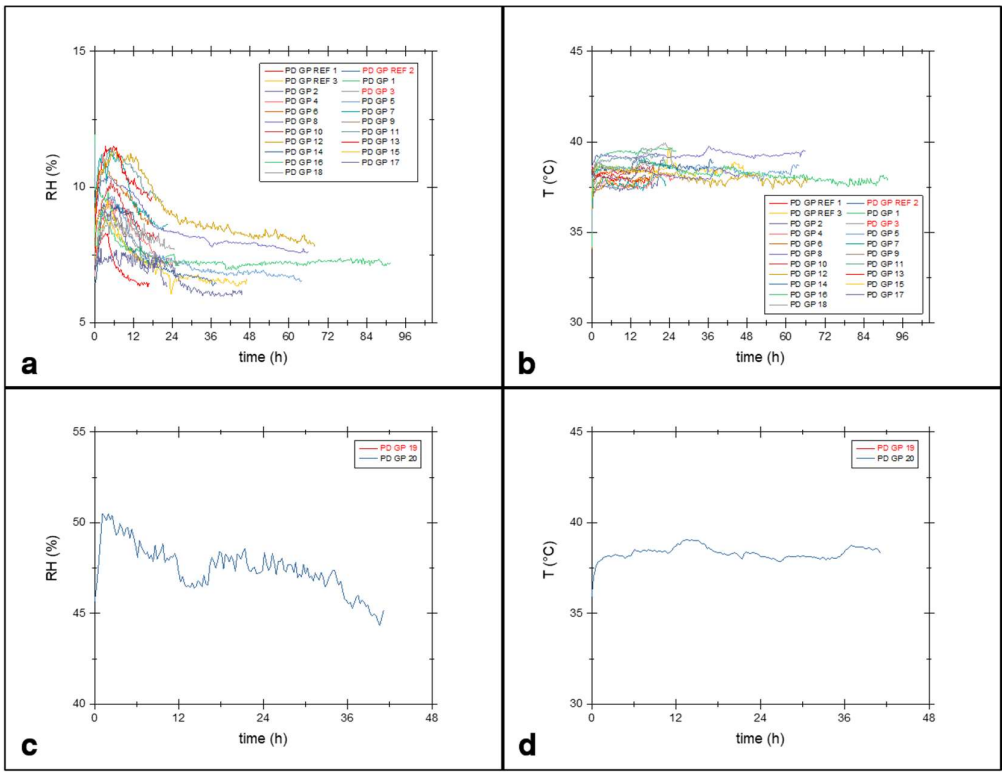


Figure II.30 Recorded relative humidity and temperature: a); b) RH and T for 7-10% RH sets, c); d) RH and T for 45-50% RH set

II.3.2. Adapting the successful GP recipe to form a RP crust

As discussed previously the RP type crust will be produced on the same under layers as the most successful GP type patterns. Here the major difference will be the top layer height. This will be shortened as seen in Figure II.17 configuration 2 and will vary depending on the amount of liquid on top of the sample.

The proposed experiments can be seen in Table IV as well as in Figure II.31 and Figure II.32. This series of experiments was done in limited numbers due to time concerns and as such serves as proof of concept.

The focus on the RP type crust will fall on the actual film and environment influence rather than on the porous media itself. Here the film thickness and the environment are varied in a double set of "brother and sister" experiments. In other words, two identical experiments are submitted to one variation and the results directly compared. In this case the first set was done with a film thickness of 10 mm, the two experiments were submitted to the two situations seen in Table II.II experiments 4' and 6'. However, a change has been made in order to have less variation on the surface on the samples, the film was of 10% saline solution by weight. In order to have more control on the air flow fans were used.

The second set was done in the same conditions but with a variation of film thickness (4mm) and bottom bead size (1200µm). The change in bottom bead size was adopted so that it can be shown that both of the most successful recipes of GP can be used in order to create RP crusts.

No.	Experiment	Sample											Environment			Film		Result
		Container Type	Porous Media										T	RH	Fan	Height	Concentration	
			Type	Bottom layer				Top Layer				Liquid Film	Total Media Height					
				Type	Diameter	Height	Brine	Type	Diameter	Height	Brine	Yes / No							
					µm	mm	%		µm	mm	%		mm	°C	%		mm	%	
1	PD RP 1	PTFE Ø38x125	Dry	Glass Beads	70-110	25	25	Glass Beads	1-50	90	10	Yes	125	40	9-13	No	10	10	Partial Pattern*
2	PD RP 2	PTFE Ø38x125	Dry	Glass Beads	70-110	25	25	Glass Beads	1-50	90	10	Yes	125	~22	6-7	Yes	10	10	Full Pattern
3	PD RP 3	PTFE Ø38x125	Dry	Glass Beads	1200	25	25	Glass Beads	1-50	96	10	Yes	125	40	9-13	No	4	10	Partial Pattern*
4	PD RP 4	PTFE Ø38x125	Dry	Glass Beads	1200	25	25	Glass Beads	1-50	96	10	Yes	125	~22	6-7	Yes	4	10	Full Pattern

Table IV RP experiment sets on the influence of film thickness and environment

Here the same data was recorded as before in Successful recipe for GP type patterns. The mass loss can be seen in Figure II.34 as for the relative humidity and temperature in Figure II.35. As for the success of the patterns the same procedure as before was applied and the results can be seen in Figure II.33.

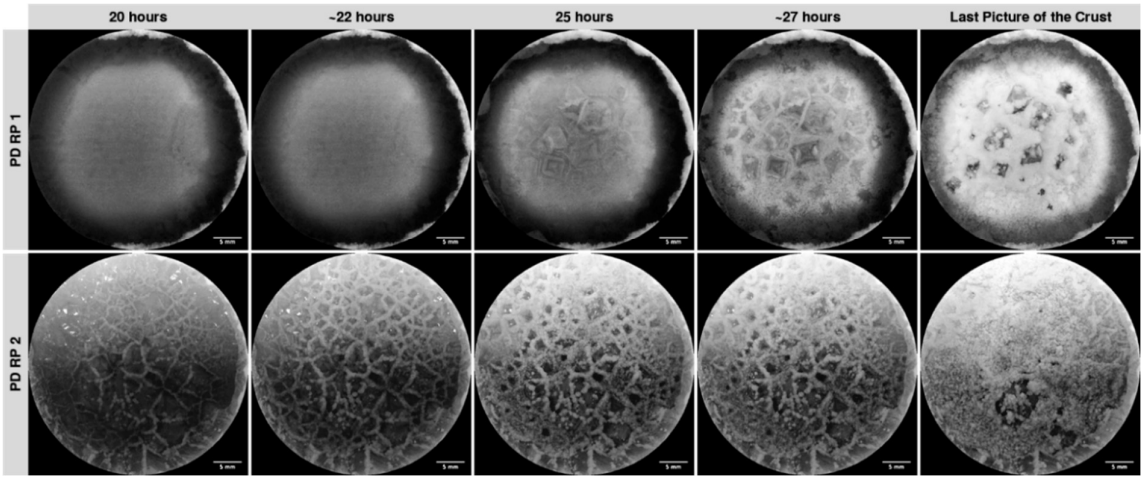


Figure II.31 Key aspects of crust formation PD RP 1 and PD RP 2

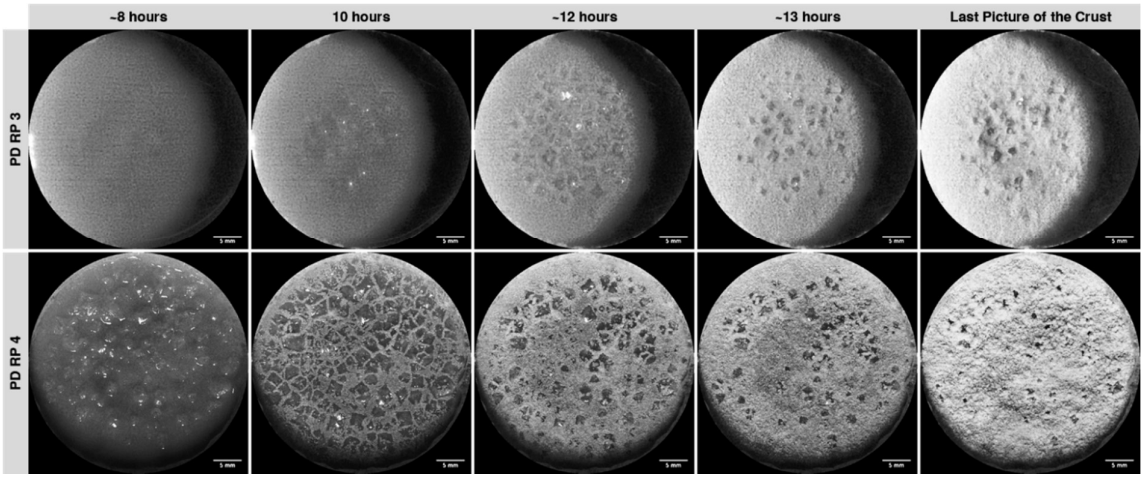


Figure II.32 Key aspects of crust formation PD RP 3 and PD RP 4

The success rate of transforming a nucleation in a macro-crystal was not calculated due to the fact that the nuclei cannot be seen well under the liquid. Moreover, the floating halite crystals are in continuous motion until they sink so that with pictures it is not possible to get a reliable result.

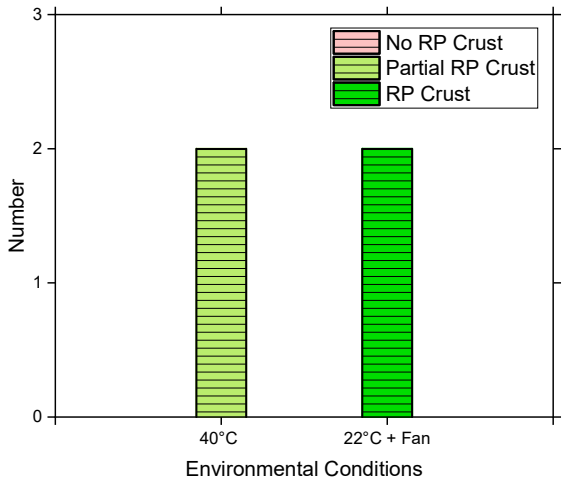


Figure II.33 PD RP 1 to PD RP 16 crust results obtained

After a careful inspection of the pictures and the samples, two issues were identified in terms of stability of the crusts.

The first would be that the macro-crystals are highly susceptible to creeping, this phenomenon happens once the whole surface of the sample is covered with crystalline tiles and no liquid is left on top of the crystals. This can be seen affecting more the smaller macro-crystals then the bigger see Figure II.31 in comparison with Figure II.32.

The second would be that the crusts actually detach from the porous substrate in the middle, this kind of behavior is known and discussed in (Chapter IV). After this happens they go through a dissolution-precipitation-recrystallization process that further affects their stability in time. However, again the same thing can be said here, that the small crystals are affected more by this behavior than the bigger ones. Due to these observations the RP crust can be improved on in future work.

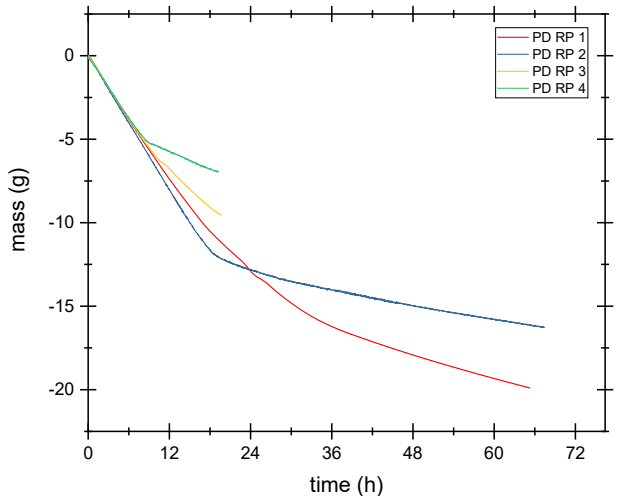


Figure II.34 Direct comparisons between mass losses of the experiments

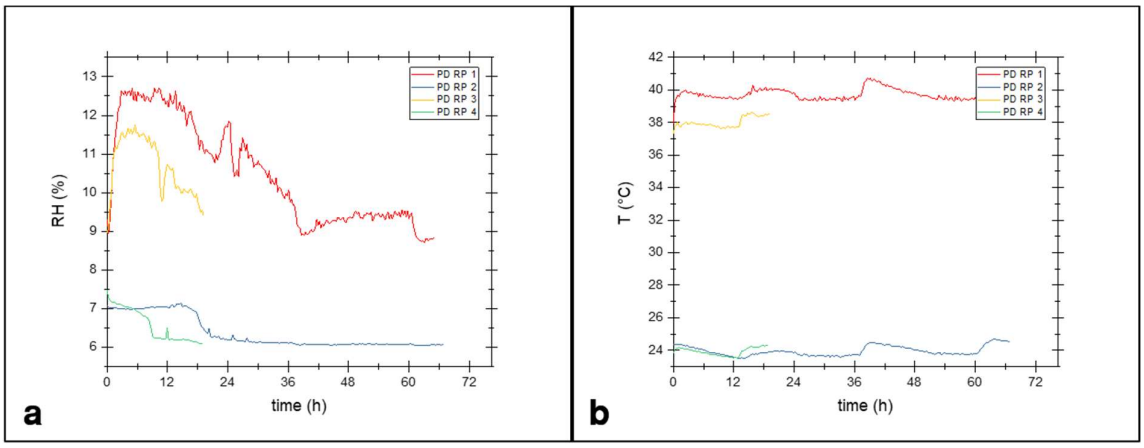


Figure II.35 Recorded relative humidity and temperature during the experiments: a) relative humidity and b) temperature

II.4. Discussion

In this part we will explore the different results obtained so far in our studies. This will be split into sections due to the fact that the experimental part is split into two types of patterns.

II.4.1. GP type crusts

The successful reproduction of the GP type crusts has been presented and as explained the reproducibility of them is quite hard to properly quantify. Thus, in our approach we have defined this as the successful transformation of a nucleus into an island and as such

this approach allows to us conclude where are the best chances to obtain such a pattern (Figure II.36).

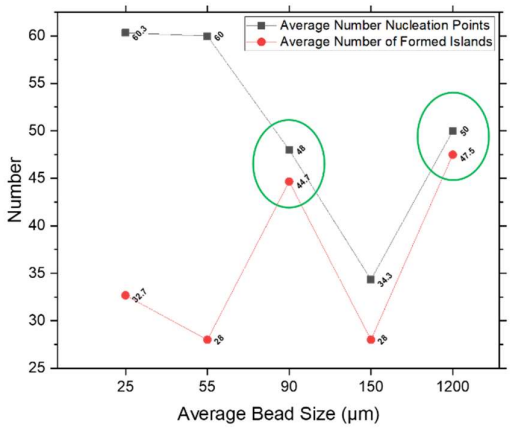


Figure II.36 Direct comparison of nuclei vs islands by averaged bottom bead layer grain size

As it can be seen in Figure II.36 (green circles represent the best chance of conversion) the chances of obtaining a positive result while trying to obtain a GP crust increases with the bottom glass bead size. This however, is only valid for the environmental conditions that have been explored in this study. The two formulations that were found most successful are the 70-110µm and the 1200µm. Thus the question is why particularly these two were the most successful.

For the 70-110µm bottom layer it can be quite understandable as the biggest bead size is 110µm. As discussed in **Successful recipe for GP type patterns** it is related to the geometrical aspect and the chances of a "clogged by small beads" border to form in-between the two layers are high enough. While the bottom pore size stays intact (the top layer beads have less chances of falling through the big pores). However, this is not the case for the 100-200µm bottom layer, this layer being at the upper geometrical limit for this to happen with its smallest bead size 100µm not as the 70-110µm which is under this limit with almost all of its size spectrum. As such the reservoir maintains its integrity and thus the uniform flow through the medium is maintained the longest. In support of this phenomenon come the averaged evaporation rates of each formulation (Figure II.37).

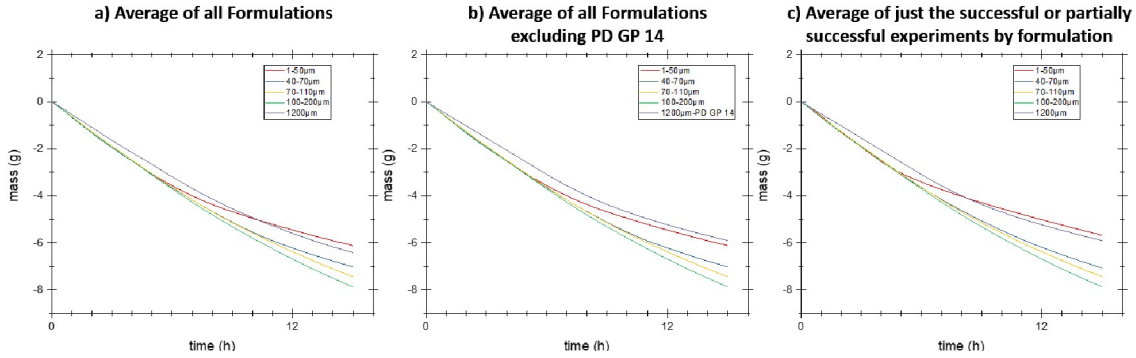


Figure II.37 Average mass loss of all formulations (PD GP 1 to PD GP 16) by bead size

In Figure II.37 the evaporation curves show a clear trend regarding their influence on the mass loss of the samples. In (Figure II.37 a) the arithmetical average of all the GP

experiments is shown by bottom bead layer range, (Figure II.37 b) shows the impact of discarding the experiment which was deemed null and in the (Figure II.37 c) the average was done only on the successful and partially successful GP crusts.

Out of these results it can be clear that the bottom porosity impacts the evaporation rate, and that the patterning can be reproduced with better chances in certain evaporative conditions.

This clear trend shows that the higher the bottom porosity the higher evaporation rate or if seen from a different perspective, this bottom bead reservoir affects directly the point of transition from the Period 1 evaporative regime to Period 2. However, this can be stated only up to the 100-200µm diameters, once the geometrical condition (as the situation of 1200µm) is not met the opposite effect takes place and the transition comes faster into play. This was related to the fact that the smaller top layer collapses into the bottom layer and thus evacuates the liquid in its pores. This creates a smaller pore size in the bottom layer as a result having the opposite behavior then desired (reversing the capillary flow towards the bottom of the sample). This was also the case while examining the samples after the experiments were finished. At a close inspection the bottom layer was full of small top layer beads and visibly wetter than the top layer.

A question still remains: why do the 1200µm beads form GP crusts with such a high success rate (the highest found in the study). In all actuality, this is due to a secondary effect of the reduced evaporation rate. When the crust enters the period (Period 2) of low evaporation the islands still form. Thus, the nucleation points have time to form into islands and they don't get overrun by efflorescence or by neighboring nuclei, as such, the process gives good rates of formation.

The big problem with this type of formulation is its crust stability. The outcome of forming a GP type crust like this is that the actual crust is extremely thin and quite feeble. The crusts suffered from very quick detachment effects in the middle as seen in Figure II.38 (pictures taken after two weeks in the experimental room). In the side view it can be seen a complete detachment (especially the middle dome) of the crust, while in the top view the crust is actually see-through as the black background is visible through it.

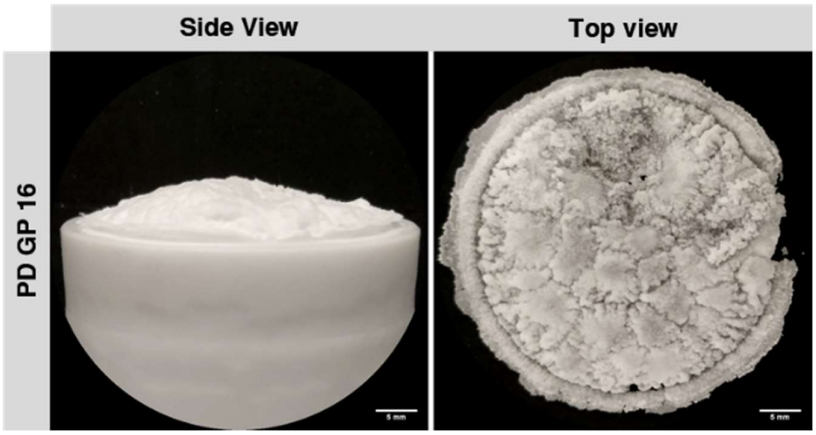


Figure II.38 Side and top views of experiment PD GP 16

Another observation refers to the curves presented in (Figure II.37 c) here the average is only done for the experiments that produced GP crusts and partial GP crusts. Here the single 1-50µm bottom layer experiment that produced a partial crust is shown as having an even

lower evaporation rate than the average evaporation curve of the 1200μm samples. As such it seems that the patterns appear for this evaporation rate too, but again they seem to be very feeble thus not the stable patterned ones that the bigger porosities produce. A preliminary analysis on the number of islands that form give the following result. On the only variation of relative humidity experiment PD GP 19 there are a $N_{I45\%} = 20$ (**Successful recipe for GP type patterns** for disambiguation) in comparison with the average of the same formulation for 7-10% RH which presents a $N_{AVG,I7\%} = 28$ while $I_{R=} N_{AVG,I7\%}/N_{i45\%} = 1.4$. If we do the same calculation with the mass loss over 12 hours for both PD GP 19 $m_{45\%} = 4.34g$ and for 40-70μm samples at 7-10% RH $m_{AVG,7\%} = 6.221g$ then $M_R = m_{7\%}/m_{45\%} = 1.43$. Here we can see a promising $I_{R\approx}M_R$ which is a good indication of a directly proportional relationship between the islands that form and the evaporation rates, thus giving the direction of future studies.

The series of GP crusts (*PD GP 17, *PD GP 18 and *PD GP 20) done with evaporation shields on top have shown that the islands form in the middle of the sample but they get very large due to the low evaporation regime (Figure II.28, Figure II.29 b) and cover the surface with a few islands losing stability. Although technically the sample was covered more than 50% with a pattern they were not taken into consideration due to their unstable behavior.

II.4.2. RP type patterns

Due to the fact that the goal in this study was to have reproducible patterns and that the main focus was put on the GP type patterns. The part of RP types was less examined as only 4 experiments were performed. These even though small in numbers compared to the GP analysis have shown a quite good rate of reproduction. All samples have at least formed a partial RP crust. In this case some factors can be directly discussed based on the “brother and sister protocol”.

In **Environment: conclusions** one of the questions was if the temperature difference between the samples could be compensated by the wind conditions. With this series of experiments, it seems that the situation is quite complex. When looking at the mass loss in time (Figure II.39) the first about 6 hours have an almost identical behavior. Here one could say that indeed the temperature difference is compensated by the air flow conditions. However, after this time period the curves start to have very different behaviors. The two 22°C have a very obvious and sharp transition to Period 2 as the ones in 40°C have a later and smoother transition. This shows that the crusts done at 40°C (PD RP 1 and PD RP 2) are still in formation and not covering perfectly the sample surface. This tendency actually helps in destabilizing the patterns. Due to the still high evaporation rate the crusts continue to grow even after the surface macro-crystal covering and thus the pattern starts to disappear while the 22°C crusts have a much better stability in time (Figure II.31, Figure II.32).

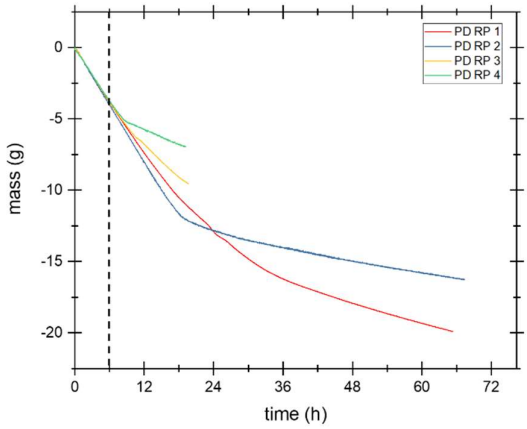


Figure II.39 Direct comparisons between mass losses of the experiments

Looking at Figure II.31 and Figure II.32 a clear morphological difference can be made between the two environmental conditions. The PD RP 1 and PD RP 3 have a tendency of creating well ordered (square shaped) macro-crystals in the middle of the sample with large space for efflorescence to grow. While the PD RP 2 and PD RP 4 macro-crystals shape is more irregular and form uniformly on the sample leaving just their borders as a place for efflorescence to grow. This actually can be related to the evaporation curves as the uniform distribution of the crystals has a direct effect on the evaporation rate.

When further analyzed this type of behavior is normal as the well-ordered samples have basically an evaporation shield on top once the brine evaporates. However, this evaporation shield effect is not present on the 22°C with wind present samples. This is due to the fact that the air is in continuous movement and does not allow for a preferential evaporation in the middle of the sample once the brine is evaporated.

As a general observation these crusts seem to be influenced, as expected, by the environmental conditions, air currents give it a uniform crystallization and film thickness as well as concentration have a direct impact on the stability of the crystals and their size (direct comparison between PD RP 1 and PD RP 3 and the same can be said for PD RP 2 and PD RP 4)

II.5. Conclusions

In the present study, we have managed to obtain a series of laboratory designed patterns which are reproducible. These have been split into two types of patterns, i.e., Grooved Patterns and Ridge Patterns, and are in direct contrast with each other as one has grooved characteristics on the island borders and the other has ridged ones. The data collected allowed for a protocol to be put in place in order to grade such patterns and obtain by statistics the best recipe for a good reproducibility out of the studied situations.

The GP, in depth studied crusts, have shown good stability. Thus, the recipe can be called of great success this being the first time anybody managed to produce such ordered structures to the best of our knowledge. Although the control is not fully obtained for this type

of crust the preliminary testing shows that the island size could be proportional to the evaporation rate. As for the evaporation rate and more exactly the transition between Period 1 and Period 2. It was clearly shown that it is dependent on the flow in the medium and as such can be controlled in terms of when it will appear.

For the RP crusts we have shown that just by modifying one parameter a completely different pattern can be obtained quite successfully. Although the patterns are not yet completely stable. The island size of the RP seems to be related to the thickness of the liquid film (Figure II.31 and Figure II.32) and as such it should be directly proportional to the concentration of such film. Air movement is an important factor in this case and it gives stability and uniformity to the pattern. The competition between air movement and temperature although it can give the same evaporation rates in the end will not give the same result in terms of crust behavior/morphology. As it also affects the way the transition to Period 2 is done as well as when this phenomenon happens. The stability of the RP needs great improvement but the ground work and clear directions have been set.

Due to the size of the samples certain situations were not explored as an example the samples with evaporation shields (*PD GP 17, *PD GP 18 and *PD GP 20) these show great potential in creating large islands. Thus there is a great need for upscaling the experiments.

As no other sample heights were explored in a controlled manner this could be another key aspect to be later on tested. Thus, downscaling or upscaling of the sample height could prove quite interesting.

Amongst the most needed aspects of the study is the actual mathematical modeling of the phenomenon and as such the data collected could be truly capitalized upon.

Bibliography

Ancient playa in Glenelg Region, Gale Crater, Mars: Evidence derived from the polygonal flagstone network in mudstone imaged by Curiosity. (n.d.). 70.

Banks, D., Markland, H., Smith, P. V., Mendez, C., Rodriguez, J., Huerta, A., & Sæther, O. M. (2005). The effect of filtration on analyses of surface water samples. A study from the Salars of Coipasa and Uyuni, Bolivian Altiplano. Journal of Geochemical Exploration, 86(2), 104–118. https://doi.org/10.1016/j.gexplo.2005.04.003.

Bobst, A. L., Lowenstein, T. K., Jordan, T. E., Godfrey, L. V., Ku, T.-L., & Luo, S. (2001). A 106ka paleoclimate record from drill core of the Salar de Atacama, northern Chile. Palaeogeography, Palaeoclimatology, Palaeoecology, 173(1), 21–42. https://doi.org/10.1016/S0031-0182(01)00308-X.

Borgman, O., Fantinel, P., Lühder, W., Goehring, L., & Holtzman, R. (2017). Impact of spatially correlated pore-scale heterogeneity on drying porous media. Water Resources Research, 53(7), 5645–5658. https://doi.org/10.1002/2016WR020260.

Borsa, A. A., Fricker, H. A., Bills, B. G., Carabajal, C. C., Quinn, K., Minster, J. B., & Schutz, B. (2002). GPS Survey of the salar de Uyuni, Bolivia, for Satellite Altimeter Calibration. AGU Fall Meeting Abstracts, 52, OS52A-0193..

Chavdarian, G. V., & Sumner, D. Y. (2011). Origin and evolution of polygonal cracks in hydrous sulphate sands, White Sands National Monument, New Mexico. Sedimentology, 58(2), 407–423. https://doi.org/10.1111/j.1365-3091.2010.01169.x.

Chen, X. Y. (1992). Evaporation from a salt encrusted sediment surface—Field and laboratory studies. Soil Research, 30(4), 429–442. https://doi.org/10.1071/sr9920429.

Chong Díaz, G., Mendoza, M., García-Veigas, J., Pueyo, J. J., & Turner, P. (1999). Evolution and geochemical signatures in a Neogene forearc evaporitic basin: The Salar Grande (Central Andes of Chile). Palaeogeography, Palaeoclimatology, Palaeoecology, 151(1), 39–54. https://doi.org/10.1016/S0031-0182(99)00014-0.

Dai, S., Shin, H., & Santamarina, J. C. (2016). Formation and development of salt crusts on soil surfaces. Acta Geotechnica, 11(5), 1103–1109. https://doi.org/10.1007/s11440-015-0421-9.

Fritz, S. C., Baker, P. A., Lowenstein, T. K., Seltzer, G. O., Rigsby, C. A., Dwyer, G. S., Tapia, P. M., Arnold, K. K., Ku, T.-L., & Luo, S. (2004). Hydrologic variation during the last 170,000 years in the southern hemisphere tropics of South America. Quaternary Research, 61(1), 95–104. https://doi.org/10.1016/j.yqres.2003.08.007.

Ganguly, J. (2000). LASAGA, A. C. 1998. Kinetic Theory in the Earth Sciences. Princeton Series in Geochemistry. x+811 pp. Princeton, Chichester: Princeton University Press. Price £65.00 (hard covers). ISBN 0 691 03748 5. https://doi.org/10.1017/S0016756800234614.

Goehring, L., Mahadevan, L., & Morris, S. W. (2009). Nonequilibrium scale selection mechanism for columnar jointing. Proceedings of the National Academy of Sciences, 106(2), 387–392. https://doi.org/10.1073/pnas.0805132106.

Goehring, Lucas, Conroy, R., Akhter, A., Clegg, W. J., & Routh, A. F. (2010). Evolution of mud-crack patterns during repeated drying cycles. Soft Matter, 6(15), 3562. https://doi.org/10.1039/b922206e.

Guglielmini, L., Gontcharov, A., Aldykiewicz, A. J., & Stone, H. A. (2008). Drying of salt solutions in porous materials: Intermediate-time dynamics and efflorescence. Physics of Fluids, 20(7), 077101. https://doi.org/10.1063/1.2954037.

Huinink, H. P., Pel, L., & Michels, M. A. J. (2002). How ions distribute in a drying porous medium: A simple model. Physics of Fluids, 14(4), 1389–1395. https://doi.org/10.1063/1.1451081.

Lasser, J., Nield, J. M., & Goehring, L. (2020). Surface and subsurface characterisation of salt pans expressing polygonal patterns [Preprint]. Geosciences – Geophysics. https://doi.org/10.5194/essd-2020-86.

Lehmann, P., & Or, D. (2009). Evaporation and capillary coupling across vertical textural contrasts in porous media. Physical Review E, 80(4), 046318. https://doi.org/10.1103/PhysRevE.80.046318.

Lenormand, R. (1990). Liquids in porous media. Journal of Physics: Condensed Matter, 2(S), SA79–SA88. https://doi.org/10.1088/0953-8984/2/S/008

Mandelbrot, B. B. (1982). The Fractal Geometry of. Nature, 394–397.

Matter, A., & Tucker, M. E. (2009). Modern and Ancient Lake Sediments. John Wiley & Sons.

Pellew, A., & Southwell, R. V. (1940). On maintained convective motion in a fluid heated from below. Proceedings of the Royal Society of London. Series A. Mathematical and Physical Sciences, 176(966), 312–343. https://doi.org/10.1098/rspa.1940.0092.

Rettig, S. L., Jones, B. F., & Risacher, F. (1980). Geochemical evolution of brines in the Salar of Uyuni, Bolivia. Chemical Geology, 30(1), 57–79. https://doi.org/10.1016/0009-2541(80)90116-3.

Risacher, F., & Fritz, B. (2009). Origin of Salts and Brine Evolution of Bolivian and Chilean Salars. Aquatic Geochemistry, 15(1), 123–157. https://doi.org/10.1007/s10498-008-9056-x.

Sghaier, N., Prat, M., & Nasrallah, S. Ben. (2007). On Ions Transport during Drying in a Porous Medium. Transport in Porous Media, 67(2), 243–274. https://doi.org/10.1007/s11242-006-9007-1.

Spry, A. (1962). The origin of columnar jointing, particularly in basalt flows. Journal of the Geological Society of Australia, 8(2), 191–216. https://doi.org/10.1080/14400956208527873.

Survey (U.S.), G., & Hunt, C. B. (1966). Hydrologic Basin, Death Valley, California. U.S. Government Printing Office.

Svendsen, J. B. (2003). Parabolic halite dunes on the Salar de Uyuni, Bolivia. Sedimentary Geology, 155(1), 147–156. https://doi.org/10.1016/S0037-0738(02)00206-3.

Veran-Tissoires, S., Marcoux, M., & Prat, M. (2012). Discrete Salt Crystallization at the Surface of a Porous Medium. Physical Review Letters, 108, 054502-p1–p4. https://doi.org/10.1103/PhysRevLett.108.05450

Chapter III

Dissolution – precipitation driven upward migration of a salt crust

III.1. Abstract

Salt crusts forming at the surface of a porous medium can dynamically evolve with crust displacements leading to the formations of domes, blisters or simply to the upward migration of the crust. However, the mechanisms explaining the displacements are unclear. It has been conjectured that they could be related to dissolution – precipitation phenomena and/or to mechanical effects associated with the concept of crystallization pressure. We present a simple experiment where the crust upward migration is significant and can be entirely explained from the consideration of dissolution – precipitation phenomena. Equations governing the crust displacement are derived, leading to a quite good agreement with the experimental results.

III.2. Introduction

Salt precipitation in porous media is a phenomenon of great importance in various applications such as soil sciences and hydrology [1, 2], archelogy and monument preservation [3-5], concrete science [6] and geotechnical engineering [7]. When the precipitation occurs at the surface of a drying porous medium, this process can lead to the formation of a porous salt crust covering the surface [8-12]. The impact of the later can be quite significant with a reduction of the evaporation rate by more than one order of magnitude [8]. The effect is tentatively explained by considering that the crust acts as a vapor diffusion barrier reducing the vapor transfer rate to the atmosphere [10, 13]. However, since this reduction in the evaporation rate can occur when liquid saturation in the medium is quite high and the salt water solution is almost perfectly wetting the crystals [14], it is difficult to explain why the crust would be dry and not wetted by the solution rising into the crust by capillary forces. Interestingly, it has also been shown [15, 16] that blistering phenomena could occur. This corresponds to zones where the salt crust is actually not in contact with the porous medium surface anymore with some air trapped between the crust and the porous medium surface. The formation of the air layer, which can be on the order of a few mm, i.e. on the order of the capillary length, or much greater under field conditions [15] could locally prevent the solution from rising into the crust by capillarity and might be instrumental in the diffusion barrier scenario. Then, the air layer formation must be explained. This point is very briefly discussed in [15] with the qualitative evocation of the possible role of dissolution – precipitation mechanisms and / or mechanical effects. The latter being suspected in relation with the well-known fact that crystallization in

Adapted from: Licsandru, G., Noiriel, C., Duru, P., Geoffroy, S., Abou-Chakra, A., Prat, M. (2019). Dissolution-precipitation-driven upward migration of a salt crust. Physical Review E 100 (3), 032802.

pores can lead to stress generation [4,5,7,17]. Actually, one must realize that the physics of salt crusts is an unexplored area. There is no paper going beyond speculative discussions and proposing a model of what happens in a moving salt crust. In this context, the objective of the present paper is to start filling this gap. More specifically, we present an experiment showing unambiguously that a salt crust can migrate upward as a result of dissolution – precipitation phenomena and that this motion can be modelled without consideration of mechanical effects (i.e. stress generation), at least in the conditions of our experiment.

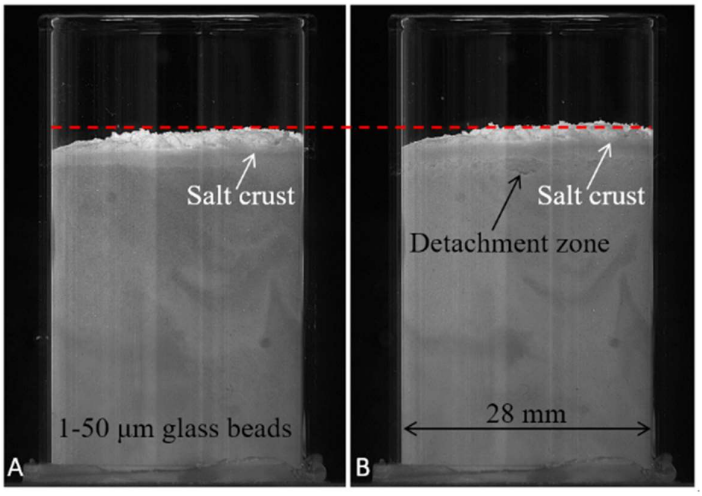


FIG.1. Illustration of the upward migration of salt crust in a basic drying experiment performed in a cylindrical container filled with glass beads. The elapsed time between the two images is 18 days. An elongated gap is visible in the detachment zone (at the end of the black arrow).

Before going into the details of this experiment, we show in Fig.1 an illustration of the crust upward migration phenomenon in a drying laboratory experiment. In this experiment, a random packing of glass beads (of diameters in the range 1- 50µm) saturated with a NaCl aqueous solution of salt mass fraction 0.25 was put in a cylindrical container open on top and exposed to drying at room temperature (T ~22°C). As a result of evaporation, a salt crust formed on top of the porous medium. After a while, the phenomenon of interest for the present paper occurred. The crust moved upward and a detachment zone became visible, as illustrated by the gap which can be seen in Fig.1. In other words, the crust slightly detached from the porous medium. Further analysis of this drying experiment is out of the scope of the present paper. The focus is on the explanation of the phenomenon illustrated in Fig.1. Actually, the region indicated as the crust in Fig.1 can be decomposed itself into an upper crust where few glass beads, if any, are present and a lower crust where precipitated salts and glass beads are both present. This will be discussed in details in a future publication.

The paper is organized as follows. In Sec. II the experimental set-up is described. Equations governing the crust displacement are derived in Sec. III. In Sec. IV, the results obtained with the model are compared to the experimental results and a discussion is presented. Conclusions are drawn in Sec. V.

Adapted from: Licsandru, G., Noiriel, C., Duru, P., Geoffroy, S., Abou-Chakra, A., Prat, M. (2019). Dissolution-precipitation-driven upward migration of a salt crust. Physical Review E 100 (3), 032802.

III.3. Experimental set-up

As sketched in Fig. 2, a salt crust was “suspended” in a transparent Hele-Shaw cell. The cell was filled with pure liquid water up to a certain height at the bottom of the cell. The liquid water was not in contact with the crust but located at distance h_b (~ 9 mm) from the crust bottom surface. The cell was positioned in a transparent enclosure at controlled temperature (T ~ 22°C) and relative humidity (RH_{inf} ~ 40 – 50 %), which were both recorded all along the experiment using a Rotronic HigroFlex HTS22X with a Rotronic Hygroclip IC05 probe. The mass evolution of this system was measured by placing it on a Mettler-Toledo AX205 precision scale. The solution mass loss was measured at 1 second intervals with data automatically recorded on a computer. A Nikon D800E camera with a resolution of 7360 pixels x 4912 pixels was set to take side view pictures of the cell. Images of the crust and water level in the cell were recorded using as acquisition software Nikon Camera Control Pro 2.26.0 at 1000 second intervals. The pictures were exploited thanks to the ImageJ© software to analyze the crust motion by tracking the bottom and top crust-gas interfaces.

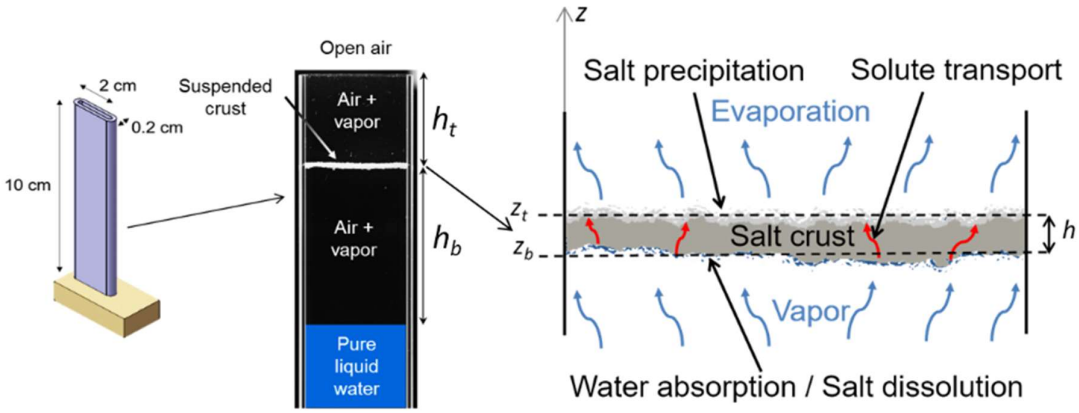


FIG. 2. (Color online) Schematic of the suspended crust experiment.

The suspended crust was obtained during a drying experiment at room temperature. The cell was filled up to a certain height with glass beads (of diameters in the range 1 - 50 μm) saturated with a NaCl aqueous solution of salt mass fraction ~ 0.25. As a result of drying, a crust formed on top of the glass bead packing. After about 4 days, the drying was stopped and the beads were carefully removed from the cell bottom so as to obtain the suspended crust. The crust shown in Fig.2 actually corresponds to the upper half of the crust so obtained. The lower part where beads are trapped has been removed. So there are little to none beads present in the crust shown in Fig. 2.

Note that the cell is rendered hydrophobic by salinization in order to avoid as much as possible the salt creeping phenomenon, e.g. [18], along the inner wall of the cell. In what follows the mechanical equilibrium of the suspended crust within the cell, especially why the crust sticks to the cell wall, will not be discussed. It is an interesting topic which certainly deserves to be investigated. However, it is our belief that this is not necessary to explain and predict the crust migration within the cell.

As explained in Appendix A, the direct exploitation of measured mass loss and relative humidity RH_{inf} led to some inconsistencies between the evaporation rate computed from the measured mass loss and the evaporation rate computed from the position of the crust limiting

Adapted from: Licsandru, G., Noiriel, C., Duru, P., Geoffroy, S., Abou-Chakra, A., Prat, M. (2019). Dissolution-precipitation-driven upward migration of a salt crust. Physical Review E 100 (3), 032802.

surfaces within the cell. This led to determine a parasitic mass loss and to introduce a correction on $RH_{inf}(t)$ (details are given in Appendix A).

III.4. Results

The major result is illustrated in Fig. 3. The crust moves upward during the experiment. The migration is quite noticeable, on the order of 1.5 mm, thus comparable here to the capillary length ($l_c = \sqrt{\frac{\gamma}{\rho g}} \approx 2.6\ mm$ for a NaCl saturated solution, and about twice as much as the initial thickness h_0 of the crust (h_0 ~ 0.8 mm, as show in the inset in Fig. 4)). Also, the shape of the crust does not change appreciably during the displacement (see the supplemental movie [19]). As a result, this crust displacement regime is qualified as compact. We can now focus on the mechanisms controlling the displacement and the derivation of equations able to predict the observed displacement.

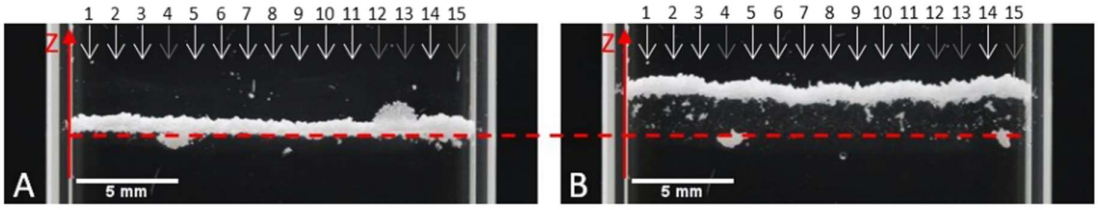
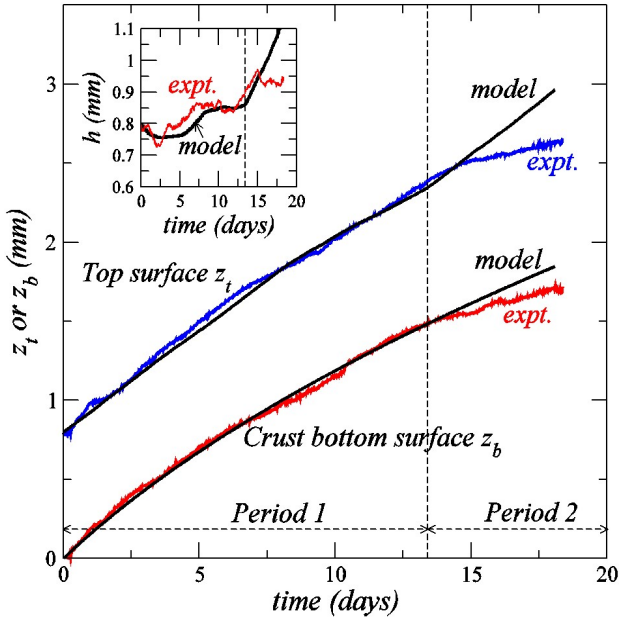


FIG. 3. (Color online) Comparison between the initial position of the crust in the cell (A) and its final position (B). The red line approximately corresponds to the initial position of the lower surface of the crust. The elapsed time between the two images is about 18 days. The white arrows indicate approximately the position of the vertical pixel lines considered to extract the data shown in Fig. 4.



Adapted from: Licsandru, G., Noiriel, C., Duru, P., Geoffroy, S., Abou-Chakra, A., Prat, M. (2019). Dissolution-precipitation-driven upward migration of a salt crust. Physical Review E 100 (3), 032802.

FIG. 4. (Color online) Crust top and bottom surface positions as a function of time. The inset shows the changes in crust thickness as a function of time. The vertical dashed line corresponds to the end of period 1 (see text).

More details on the crust upward displacement are shown in Fig. 4 together with the results of a model which is presented below. The experimental data shown in Fig. 4 are the arithmetic average of the data extracted from eleven out of fifteen vertical pixel lines evenly distributed over the crust image width at 100 pixel intervals. These lines correspond to the arrows shown in Fig.3. Lines 4, 15 were excluded due to the presence of residual beads, visible in Fig.3, initially in contact with the crust bottom; also lines 12 and 13 due to a creeping spot, visible in Fig.4A, thus rendering them unusable. As indicated in Fig. 4, one can distinguish two main periods. During the first period of about 13 days, the thickness of the crust fluctuates around the value ~ 0.85 mm. In the second period (day 13 to day 18), there is first a noticeable increase in the crust thickness. Then the crust top surface motion noticeably slows down and the crust thickness stabilizes around 0.95 mm.

III.5. Modeling

The mechanisms at play are discussed in what follows from a simple 1D model considering that the crust is porous [13] and assuming that the crust pores are filled by a NaCl saturated solution (due to the absorption of water vapor resulting from the evaporation of liquid water at the cell bottom). Since the equilibrium vapor pressure of a NaCl saturated solution is $0.75p_{vs0}$ where p_{vs0} is the saturation vapor pressure for pure water, then there is a water vapor transport by diffusion in the gas phase between the liquid water at the bottom and the lower surface of the crust together with evaporation driven by diffusion at the top surface of the crust. Under the classical quasi-steady assumption, the corresponding mass fluxes j_b (vapor absorption flux at the crust bottom surface) and j_t (evaporation flux from crust top) can be expressed as

$$j_b = D_v \frac{M_v}{RT} p_{vs0} \frac{(1-RH_s)}{h_b} \tag{1}$$

$$j_t = D_v \frac{M_v}{RT} p_{vs0} \frac{(RH_s-RH_{inf})}{h_t} \tag{2}$$

where D_v is the binary diffusion coefficient of the vapor in gas phase, R is the universal gas constant, M_v is the vapor molecular weight, RH_s is the relative humidity at the surface of NaCl saturated solution (RH_s = 0.75), RH_{inf} is the relative humidity at the top of the cell. One can refer to Fig. 2 for the definition of the lengths h_b and h_t indicated in Eqs. (1-2). These fluxes induce a flow in the pore space of the crust and thus the transport of ions from the crust bottom surface where dissolution must occur owing to the absorption of pure water to the crust top surface where evaporation and thus precipitation take place (as schematically illustrated in Fig. 2). Within the framework of the classical continuum approach to porous media [20], the convection-diffusion equation governing the ions transport within the crust is

$$\varepsilon\rho \frac{\partial C}{\partial t} + \rho V \frac{\partial C}{\partial z} = \frac{\partial}{\partial z}\left(\rho\varepsilon D_s^* \frac{\partial C}{\partial z}\right) - (1-C)a_v\rho k_r(C - C_{sat}) \tag{3}$$

Adapted from: Licsandru, G., Noiriel, C., Duru, P., Geoffroy, S., Abou-Chakra, A., Prat, M. (2019). Dissolution-precipitation-driven upward migration of a salt crust. Physical Review E 100 (3), 032802.

where ρ is the density of the solution, C is the ion mass fraction in the solution, C_{sat} is the equilibrium ion mass fraction in a saturated solution (C_{sat} =0.264), ε is the crust porosity, V is the filtration velocity, D_s^* is the effective diffusion of the ions, a_v is the pore wall surface area per unit volume, k_r is the reaction (dissolution or precipitation) coefficient.

Then we express the mass balance on the crust moving top surface for the solution as [21]

$$\rho V = (\rho\varepsilon + \rho_{cr}(1-\varepsilon) - \rho_v)\frac{dz_t}{dt} + j_t \qquad \textit{at } z = z_t \tag{4}$$

where ρ_{cr} is the crystal density and ρ_v is the vapor concentration.

Similarly, the mass balance for the ions at the crust top surface reads,

$$\rho CV - \rho\varepsilon D_s^*\frac{\partial C}{\partial z} = (\rho C\varepsilon + \rho_{cr}(1-\varepsilon))\frac{dz_t}{dt} \qquad \textit{at } z = z_t \tag{5}$$

Similarly, the mass balance equations on the crust moving bottom surface for the solution and the ions are expressed respectively as

$$\rho V = j_b + (\rho\varepsilon + \rho_{cr}(1-\varepsilon) - \rho_v)\frac{dz_b}{dt} \qquad at\ z = zb \tag{6}$$

$$\rho CV - \rho\varepsilon D_s^*\frac{\partial C}{\partial z} = (\rho C\varepsilon + \rho_{cr}(1-\varepsilon))\frac{dz_b}{dt} \qquad \textit{at } z = z_b \tag{7}$$

Multiplying Eq.(4) by C and subtracting Eq.(5) leads to (where ρ_v has been neglected since $\rho_v << \rho_{cr}$ and $\rho_v << \rho$),

$$\frac{dz_t}{dt} = \frac{C_{sat}j_t - \rho\varepsilon D_s^*\frac{\partial C}{\partial z}}{\rho_{cr}(1-\varepsilon)(1-C_{sat})} \tag{8}$$

Similarly,

$$\frac{dz_b}{dt} = \frac{C_{sat}j_b - \rho\varepsilon D_s^*\frac{\partial C}{\partial z}}{\rho_{cr}(1-\varepsilon)(1-C_{sat})} \tag{9}$$

where we have assumed $C \sim C_{sat}$ at $z = z_t$ or z_b.

The ion mass fraction gradients in Eqs. (8) and (9) are the gradient at the crust top surface (Eq. (8)) and bottom surface (Eq. (9)), respectively. The displacement rates are also expressed using a macroscopic version [22] of the relationship modelling the precipitation – dissolution reaction within the framework of the diffusion reaction theory [23], namely

$$\frac{dz_t}{dt} = \frac{\rho}{\rho_{cr}}k_r\left(C_{top} - C_{sat}\right) \tag{10}$$

$$\frac{dz_b}{dt} = \frac{\rho}{\rho_{cr}}k_r(C_{sat} - C_{bot}) \tag{11}$$

where C_{top} and C_{bot} are the ion mass fraction at the top and bottom surfaces of the crust, respectively. Then it can be argued that the convective term in Eq. (3) can be neglected from the estimate of the Peclet number Pe characterizing the competition between the convective and diffusive transports of the ions within the crust: $Pe = \frac{j_t h}{\rho\varepsilon D_s^*}$ [24]. The evaporation velocity $V_{ev} = \frac{j_t}{\rho}$, as can be computed from Eq. (1), is on the order of 10^{-8} m/s (as indicated by Eq.(4),

Adapted from: Licsandru, G., Noiriel, C., Duru, P., Geoffroy, S., Abou-Chakra, A., Prat, M. (2019). Dissolution-precipitation-driven upward migration of a salt crust. Physical Review E 100 (3), 032802.

the filtration velocity induced in the crust is actually higher than the evaporation velocity but of comparable order of magnitude). With $h \sim 0.7\ mm$ and for simplicity $\varepsilon D_s^* \sim D_s$ where $D_s \approx 1.3 \times 10^{-9}$ m²/s is the molecular diffusion of ions in solution, one obtains $Pe \sim 0.006$. As expected ***Pe*** <<1. Then, it can be argued that the ion distribution within the crust is quasi-steady since the characteristic time for diffusion $t_D \approx \frac{h^2}{D_s} \approx 490\ s$ is quite short compared to the characteristic time of the crust displacement (about two weeks according to Fig. 4). As a result, Eq. (3) can be simplified as

$$\frac{\partial}{\partial z}\left(\rho \varepsilon D_s^* \frac{\partial C}{\partial z}\right) = (1 - C) a_v \rho k_r (C - C_{sat}) \tag{12}$$

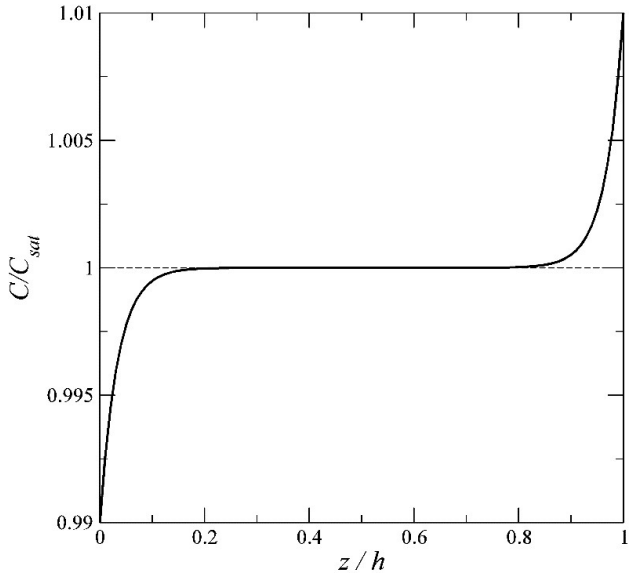


FIG. 5. Typical computed ion mass fraction profile along the crust thickness. The crust bottom and top surfaces correspond to $z = 0$ and $z/h = 1$, respectively.

Assuming that the porosity of the crust is spatially uniform within the crust and varies little during the displacement (consistently with the fact, as we shall see, that the ion mass fraction is very close to the equilibrium ion mass fraction over most of the crust), Eq. (12) can be solved analytically (details are given in Appendix B).

A typical profile so obtained is shown in Fig. 5. The ion mass fraction is different from the equilibrium ion mass fraction C_{sat} only in the vicinity of the crust top and bottom surfaces. The ion mass fraction is lower than C_{sat} near the crust bottom surface consistently with the occurrence of a dissolution process whereas C is greater than C_{sat} near the crust top surface consistently with the occurrence of a precipitation process. The fact that C is close to C_{sat} even in the regions where precipitation or dissolution occurs is a consequence of the high value of the reaction coefficient $k_r \approx 2.3 \times 10^{-3}$ m/s [25]. The most important point, however, is the existence of a noticeable ion mass gradient at the crust top and bottom surface. As we shall see, this gradient is sufficiently high for the term $\varepsilon D_s^* \frac{\partial C}{\partial z}$ in Eqs (8, 9) to have an impact on the displacement velocity of each surface. In other words, the crust displacement velocity does depend on the ion distribution within the crust. By exploiting the analytical solution to Eq. (12) closed form expressions for the crust surface displacement velocities can be derived (see Appendix B),

Adapted from: Licsandru, G., Noiriel, C., Duru, P., Geoffroy, S., Abou-Chakra, A., Prat, M. (2019). Dissolution-precipitation-driven upward migration of a salt crust. Physical Review E 100 (3), 032802.

$$\frac{dz_t}{dt} = \frac{C_{sat} j_t}{\rho_{cr}(1-\varepsilon)(1-C_{sat})}\left[\frac{Da}{1+Da}\right] \quad (13)$$

$$\frac{dz_b}{dt} = \frac{C_{sat} j_b}{\rho_{cr}(1-\varepsilon)(1-C_{sat})}\left[\frac{Da}{1+Da}\right] \quad (14)$$

where $Da = \frac{(1-\varepsilon)(1-C_{sat})\lambda k_r}{\varepsilon D_S^*} = \sqrt{\frac{(1-\varepsilon)^2(1-C_{sat})k_r}{\varepsilon D_S^* a_v}}$ is a Damkhöler number characterizing the competition between the precipitation – dissolution reaction and the diffusive ion transport [23]; $\lambda = \sqrt{\frac{\varepsilon D_S^*}{(1-C_{sat})a_v k_r}}$ is a length characterizing the extent of the gradient edge zones illustrated in Fig. 5 (see Appendix B).

III.6. Discussion

Eqs. (13) and (14) make clear that the crust displacement velocity depends on the competition between the precipitation – dissolution reaction and the diffusive ion transport. In order to use Eqs. (13-14), some properties of the crust (i.e. ε, a_v, D_S^*) must be specified. However, crusts are thin and fragile porous media for which conventional characterization methods are difficult to use. The result is that these properties are actually not known. From the SEM image of the crust surface shown in [13], it is reasonable to assume that the porosity of the crust is low. We have taken $\varepsilon = 0.1$. Then we have checked whether the above model led to good results by fitting the value of the Damkhöler number *Da*. The value *Da* = 4.07 leads to the quite good results shown in Fig. 4 (obtained from the numerical solution of Eqs. (13) and (14) using a first order temporal scheme and after correction of the measured relative humidity RH_{inf} and consideration of a parasitic leakage as explained in the Appendix A), at least during the first period. The crust thickness predicted by the model and shown in the inset of Fig. 4 is simply obtained from the relationship $h = z_t - z_b$. Such a value of *Da* is obtained for instance for the following values of parameters estimated from classical relationships for packing of monodisperse spheres: a mean "grain" radius r_b = 0.6 μm corresponding to small pores on the order of 1μm or less (consistently again with the SEM image of salt crust in [13]), ε = 0.05, $a_v = \frac{3(1-\varepsilon)}{r_b}$ [26], $D_S^*/D_S = \varepsilon^{0.4}$ [27]. Such a value of the Damkhöler number can be also obtained with $r_b \approx$ 1.5 μm and ε = 0.1. Although the crust is different from a random packing of spherical particles, we surmise that the corresponding values are consistent with a low porosity compact crust with sub-micronic to micronic pores.

Also, it is interesting to comment the value of the Damkhöler number *Da* in our simulations. The crust displacement velocity becomes independent of *Da* for sufficiently large *Da*. This corresponds for instance to the situation where the precipitation - dissolution reaction would be quite fast compared to the diffusive transport. In this limit, the crust displacement velocity is independent of the reaction parameter k_r. On the contrary, for lower *Da* the crust velocity displacement depends on the reaction kinetics as in the case of our experiments. The fact that the model leads to less good results in the second period can be explained as follows.

As depicted in Fig. 6, the first period of about 13 days corresponds to a period in which the evaporation flux j_t from the crust top surface is about the same as the water absorption flux j_b on the crust bottom surface. Since the crust moves upward, i.e. gets closer to the cell top, the evaporation flux is expected to increase whereas the absorption flux is expected to decrease.

Adapted from: Licsandru, G., Noiriel, C., Duru, P., Geoffroy, S., Abou-Chakra, A., Prat, M. (2019). Dissolution-precipitation-driven upward migration of a salt crust. Physical Review E 100 (3), 032802.

However, the impact of the distance variation is offset by the increase in the relative humidity RH_{inf} at the cell top during the first period (the variation of RH_{inf} is depicted in the inset of Fig. 6). This relative humidity increase explains the relatively long period when the two fluxes are comparable. In the second period, the evaporation rate becomes greater than the absorption rate and this introduces a change in the crust migration regime. It is likely that the crust starts drying, which makes the modelling of the second period much more challenging. This is also an indication that various regimes of crust migration must exist. Identifying and studying these regimes is an open interesting question.

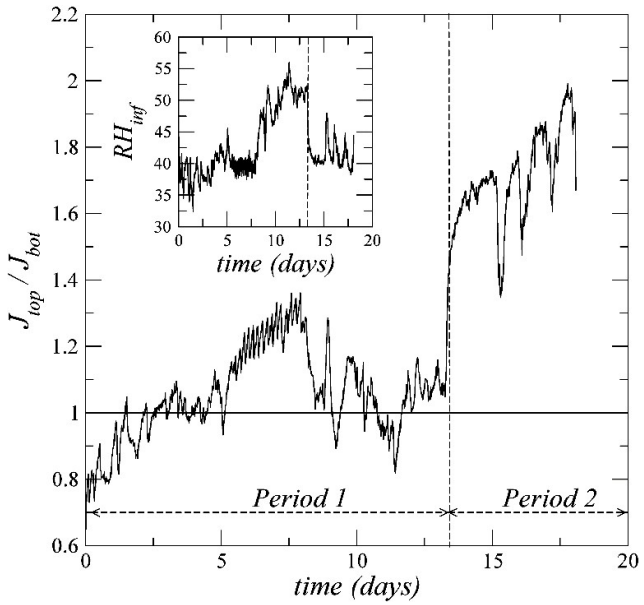


FIG. 6. Ratio between the evaporation rate from the crust top surface and the water absorption rate on the crust bottom surface. The inset shows the variation of the relative humidity at the cell top. As it can be seen the relative humidity is not constant in the experiment due to variations in the room humidity conditions affecting the humidity in the enclosure in which the cell is positioned.

Finally, the model can be used not only to predict the crust displacement but also to compute the variation of the liquid level at the bottom of the cell, and thus the variation of the distance $h_b(t)$ between the crust lower surface and the liquid level as well as the total mass loss of the system. This is performed taking into account the parasitic mass loss and the corrected RH_{inf} (see Appendix A). As shown in Fig.7, the variation of the system mass is well reproduced (Fig.7b) whereas the distance between the liquid level and the crust bottom surface is a bit underestimated (Fig.7a) by the model. The trend is however quite good, which can be seen as an additional validation of the model.

Adapted from: Licsandru, G., Noiriel, C., Duru, P., Geoffroy, S., Abou-Chakra, A., Prat, M. (2019). Dissolution-precipitation-driven upward migration of a salt crust. Physical Review E 100 (3), 032802.

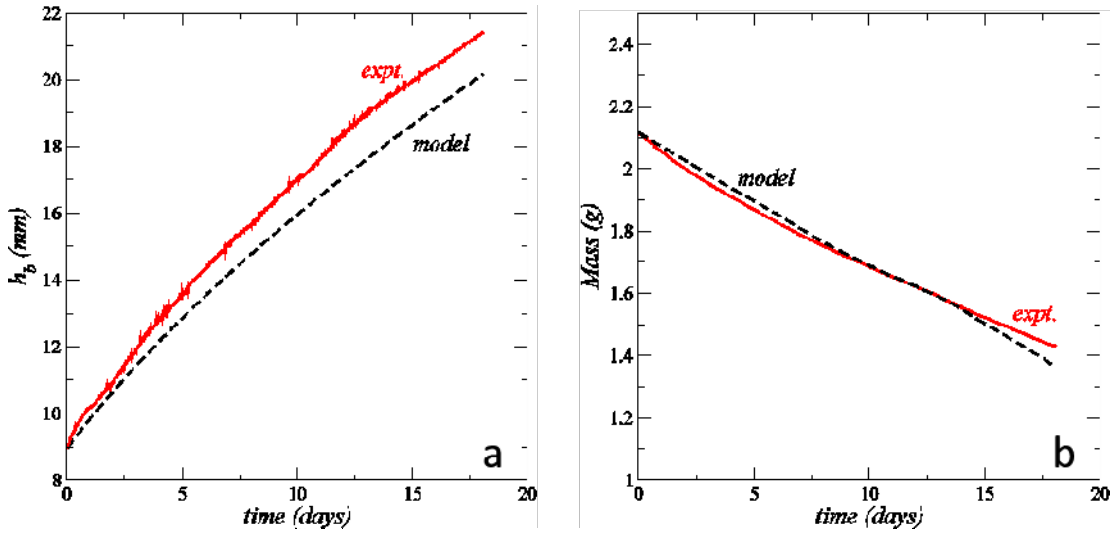


FIG. 7. Comparison between model and experiment: a) distance $h_b(t)$ between crust bottom surface and liquid level in the cell as a function of time, b) total mass loss $m(t)$ as a function of time.

Then, we have to discuss further the link between the suspended crust experiment and the situations, as illustrated in Fig.1, motivating the present study, i.e. the phenomena occurring in the crust on top of a porous medium exposed to evaporation.

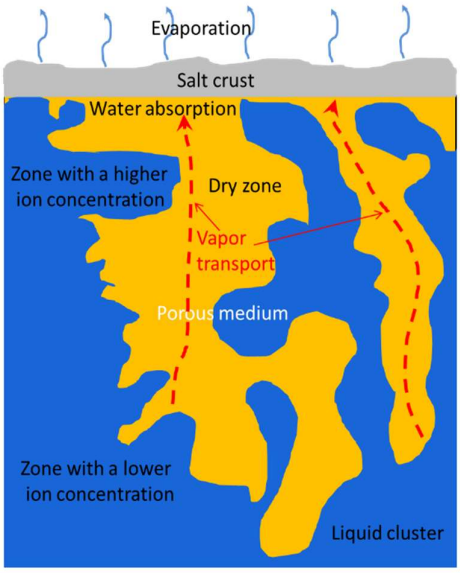


FIG.8. Tentative sketch of a drying porous medium leading to a situation similar to that of the suspended crust experiment. The decrease in the ion mass faction along the height of the porous medium induced a water vapor diffusive transport in the direction of the crust located on top of the porous medium where the dissolution – precipitation mechanism can take place, possibly leading to the crust upward migration and detachment.

This link is pictorially illustrated in Fig.8. Referring to the situation of a salt crust on top of a drying porous medium, it is expected that a vapor pressure gradient forms in the medium as a result of the ion preferential transport towards the top [24] where they feed the crust. Since

Adapted from: Licsandru, G., Noiriel, C., Duru, P., Geoffroy, S., Abou-Chakra, A., Prat, M. (2019). Dissolution-precipitation-driven upward migration of a salt crust. Physical Review E 100 (3), 032802.

the lower the ion concentration, the greater is the vapor pressure, this should induce a water vapor flux within the porous medium in the direction of the crust, leading to water absorption at the crust bottom. The situation would be then comparable to the situation in our experiment with water vapor absorption coupled with dissolution at the crust bottom and evaporation - precipitation on the top. Confirming this scenario is one interesting topic for future research. A temperature inside the porous medium higher than at the surface can also contribute to the occurrence of the internal vapor flux toward the crust bottom.

III.7. Conclusions

In summary, we have shown that dissolution – precipitation processes combined with transport phenomena can entirely explain the migration of salt crusts. This is made clear by the presented model which does not rely on any poro-mechanical property of the crust. To the best of our knowledge, our model is the first proposing closed form equations enabling one to compute quantitatively the crust displacement or the growth of a porous crust surface resulting from evaporation, internal transport and precipitation. It was shown in previous works, e.g. [28], that the growth of a porous salt structure was proportional to the evaporation flux. This is fully consistent with Eq. (13) which furthermore makes clear the dependence with other factors, such as the ones related to the transport of ions within the salt structure and the precipitation kinetics. It can be argued that we have presented only one experiment, thus without varying the parameters, i.e. the mean evaporation rate for instance, and use the Damkhöler number *Da* as an adjustable parameter. Nevertheless, the value of *Da* leading to a good agreement between the model and the experiment is quite consistent with the properties expected for the crust in the current state of the art. In this respect, more work on crust characteristics is desirable since little is actually known on the crust microstructure. Also, the suspended crust experiment is relatively delicate. This, coupled with the fact that this experiment is the very first of this type, explains why we have not tried to explore a large range of parameters. We hope that the present work will stimulate further works in this direction.

Finally, it can be also noted that patterned salt crusts can form, the most famous being the salar de Uyuni with its polygonal patterns. Explaining this pattern formation is an open problem [29]. The dissolution –precipitation mechanisms described in the present paper might also play a role in the formation of this particular pattern as well as in other crust patterns observed in nature such as blisters and domes [29].

ACKNOWLEDGEMENT

The help of J. Lefort in the development of the experiment is gratefully acknowledged.

Adapted from: Licsandru, G., Noiriel, C., Duru, P., Geoffroy, S., Abou-Chakra, A., Prat, M. (2019). Dissolution-precipitation-driven upward migration of a salt crust. Physical Review E 100 (3), 032802.

III.8. Appendix A Pre-processing of experimental data

To run the model predicting the crust motion presented in Section IV, we only need the initial position of the crust in the cell $h_t(0)$, the initial crust thickness $h(0)$, the level of the liquid at the cell bottom $z_l(0)$ and the relative humidity $RH_{inf}(t)$ at the cell top. However, the direct use of the data measured in our experiment does not lead to very good results. For this reason, we have checked the consistency of the experimental data. As discussed in this Appendix, this led to take into account a parasitic mass loss and to introduce a correction on $RH_{inf}(t)$. The experimental data available either from direct measurements or image processing are the following:

- mass of the system as a function of time $m(t)$ measured with a balance
- distance between top cell and crust upper surface $h_t(t)$
- distance between top cell and crust lower surface $h_t(t)+h(t)$
- thickness of the crust $h(t)$
- distance between crust lower surface and free liquid level in the cell $h_b(t)$
- relative humidity $RH_{inf}(t)$ in the ambient air next to the cell top
- temperature T in the ambient air (T ~21°C)

First we establish that the variation of the mass $m(t)$ measured by the balance corresponds to the variation of the free liquid level (the corresponding mass computed from the variation of the liquid level is denoted by $m_l(t)$). Both masses are compared in Fig.9. As can be seen both curves are very close which is an indication that the amount of water in the crust does not increase or perhaps very little during its displacement.

We have also plotted in Fig.9a, the variation of mass m_b corresponding to the mass transferred between the liquid level and the crust lower surface computed assuming quasi-steady vapor diffusion between the two surfaces, i.e. using Eq. (1) of the main text,

$$m_b(t) = m(0) - AD_v \frac{M_v}{RT} p_{vs0}(T)(1 - RH_s) \int_0^t \frac{dt}{h_b(t)} \tag{A.1}$$

where $RH_s = 0.75$, which corresponds to a NaCl saturated solution.

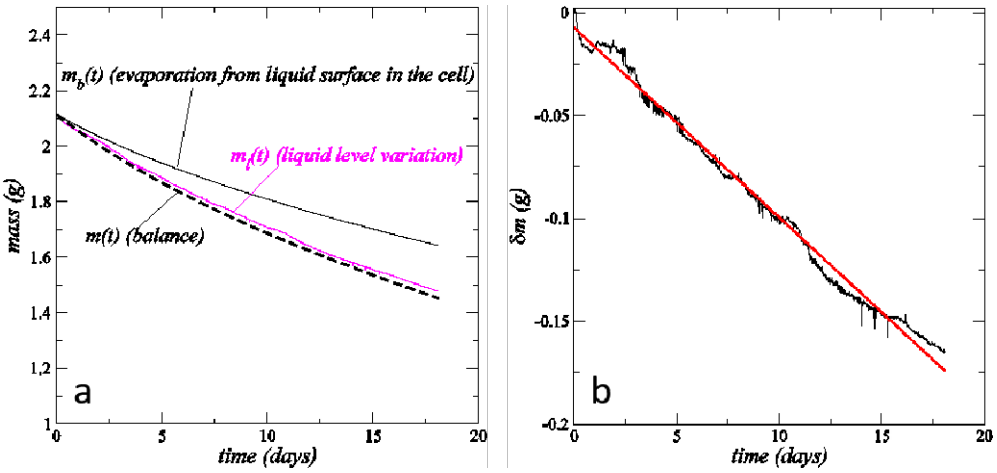


FIG. 9. a) Mass variation as a function of time; b) parasitic mass loss as a function of time.

As can be seen, $m_b(t) > m_l(t)$, which means that the mass loss due to evaporation from the liquid surface in the cell is less than the mass loss measured by the balance. A first option

is that RH_s in Eq.(A.1) is less than 0.75. However, this seems quite unlikely since the crust is made of crystallized salt. Another option is to assume some liquid leak (at the bottom of the cell where tightness can be imperfect). Thus we define this parasitic mass loss δm as

$$\delta m(t) = m(t) - m_b(t) \tag{A.2}$$

As can be seen from Fig.9b, δm varies linearly, indicating a constant leak rate J_{par}. From a linear fit (red curve in Fig.9b), one obtains $J_{par} \approx 0.00922$ g/day.

Then, if there is no liquid water mass variation in the crust, the mass loss measured by the balance should also correspond to the sum of the loss by evaporation from the crust upper surface and the parasitic loss,

$$m(t) = m_t(t) + |\delta m(t)| \tag{A.3}$$

where

$$m_t = m(0) - AD_v \frac{M_v}{RT} p_{vs0}(T) \int_0^t \frac{(RH_s - RH_{inf}(t))}{h_t(t)} dt \tag{A.4}$$

As can be seen from Fig.10, $m(t) < m_t(t)$ as expected meaning that the mass loss due to evaporation from the crust top surface is less than the mass loss measured with the balance. It can be also seen that adding the parasitic loss leads to more consistent results. Finally, assuming a systematic measurement error on the relative humidity $RH_{inf}(t)$ (shown in Fig.10b) with $RH_{infc}(t) = RH_{inf}(t) + 0.03$ leads to the most consistent results between the available experimental data.

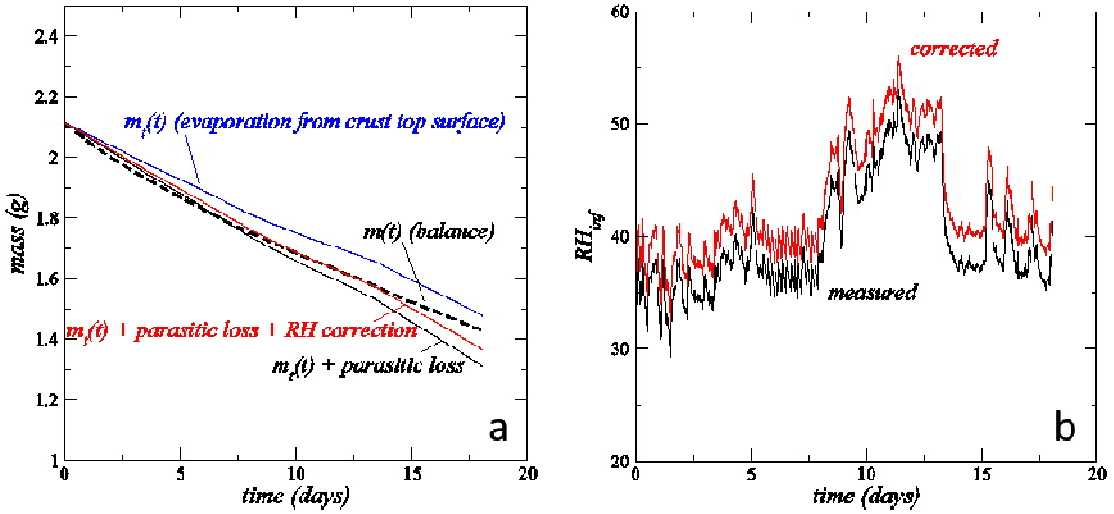


FIG. 10. a) Mass variation as a function of time; b) measured relative humidity variations with and without correction.

Adapted from: Licsandru, G., Noiriel, C., Duru, P., Geoffroy, S., Abou-Chakra, A., Prat, M. (2019). Dissolution-precipitation-driven upward migration of a salt crust. Physical Review E 100 (3), 032802.

III.9. Appendix B Closed – form equations for the crust top and bottom surfaces velocity

The ion transport within the crust is governed by the following equation,

$$\varepsilon\rho\frac{\partial C}{\partial t}+\rho V\frac{\partial C}{\partial z}=\frac{\partial}{\partial z}\left(\rho\varepsilon D_s^*\frac{\partial SC}{\partial z}\right)-(1-C)a_v\rho k_r(C-C_{sat}) \quad \text{(B1)}$$

Under the assumptions of quasi-steady transport and low Peclet number (see main text), Eq.(B1) is simplified as

$$\frac{\partial}{\partial z}\left(\rho\varepsilon D_s^*\frac{\partial C}{\partial z}\right)-(1-C)a_v\rho k_r(C-C_{sat})=0 \quad \text{(B2)}$$

Neglecting the variation of density ($C \sim C_{sat}$) and porosity Eq.(B2) is expressed as,

$$\frac{\partial^2 C}{\partial z^2}-\frac{1}{\lambda^2}(C-C_{sat})=0 \quad \text{(B3)}$$

where

$$\lambda^2=\frac{\varepsilon D_s^*}{(1-C_{sat})a_v k_r} \quad \text{(B4)}$$

The boundary conditions are expressed as,

$C = C_{top}$ at $z = z_t$ (B5)

$C = C_{bot}$ at $z = z_b$ (B6)

The solution of Eqs. (B3, B5, B6) then reads,

$$C=C_{sat}+\left(C_{top}-C_{sat}\right)\frac{\exp\left(\frac{z}{\lambda}\right)-\exp\left(-\frac{z}{\lambda}\right)}{\exp\left(\frac{h}{\lambda}\right)-\exp\left(-\frac{h}{\lambda}\right)}+(C_{bot}-C_{sat})\frac{\exp\left(\frac{h-z}{\lambda}\right)-\exp\left(-\frac{h-z}{\lambda}\right)}{\exp\left(\frac{h}{\lambda}\right)-\exp\left(-\frac{h}{\lambda}\right)} \quad \text{(B7)}$$

$$\frac{\partial C}{\partial z}=\frac{(C_{top}-C_{sat})}{\lambda}\frac{\exp\left(\frac{z}{\lambda}\right)+\exp\left(-\frac{z}{\lambda}\right)}{\exp\left(\frac{h}{\lambda}\right)-\exp\left(-\frac{h}{\lambda}\right)}-\frac{(C_{bot}-C_{sat})}{\lambda}\frac{\left(\exp\left(\frac{h-z}{\lambda}\right)+\exp\left(-\frac{h-z}{\lambda}\right)\right)}{\exp\left(\frac{h}{\lambda}\right)-\exp\left(-\frac{h}{\lambda}\right)} \quad \text{(B8)}$$

Then noting that $\exp\left(\frac{h}{\lambda}\right)\gg\exp\left(-\frac{h}{\lambda}\right)$ when $\lambda < h$, the above equations are expressed as

$$C=C_{sat}+\left(C_{top}-C_{sat}\right)\left(\exp\left(-\frac{h-z}{\lambda}\right)-\exp\left(-\frac{h+z}{\lambda}\right)\right)+(C_{bot}-C_{sat})\left(\exp\left(-\frac{z}{\lambda}\right)-\exp\left(-\frac{2h-}{\lambda}\right)\right) \quad \text{(B9)}$$

$$\rho\varepsilon D_s^*\frac{\partial C}{\partial z}\Big|_{z=h}\approx\rho\varepsilon D_s^*\frac{(C_{top}-C_{sat})}{\lambda} \quad \text{(B10)}$$

Adapted from: Licsandru, G., Noiriel, C., Duru, P., Geoffroy, S., Abou-Chakra, A., Prat, M. (2019). Dissolution-precipitation-driven upward migration of a salt crust. Physical Review E 100 (3), 032802.

$$\rho\varepsilon D_S^* \left.\frac{\partial C}{\partial z}\right|_{z=0} \approx \rho\varepsilon D_S^* \frac{(C_{sat}-C_{bot})}{\lambda} \tag{B11}$$

In this limit, Eqs. (8) and (9) in the main text can be expressed as,

$$\frac{dz_t}{dt} \approx \frac{C_{sat} j_t - \rho\varepsilon D_S^* \frac{(C_{top}-C_{sat})}{\lambda}}{\rho_{cr}(1-\varepsilon)(1-C_{sat})} \approx \frac{\rho}{\rho_{cr}}\, k_r\left(C_{top}-C_{sat}\right) \tag{B12}$$

$$\frac{dz_b}{dt} \approx \frac{C_{sat} j_b - \rho\varepsilon S D_S^* \frac{(C_{sat}-C_{bot})}{\lambda}}{\rho_{cr}(1-\varepsilon)(1-C_{sat})} \approx \frac{\rho}{\rho_{cr}}\, k_r(C_{sat}-C_{bot}) \tag{B13}$$

which give estimate of the ion mass fraction at the bottom and the top,

$$\left(C_{top}-C_{sat}\right) \approx \frac{C_{sat} j_t}{\rho(1-\varepsilon)(1-C_{sat})k_r + \frac{\rho\varepsilon D_S^*}{\lambda}} \tag{B14}$$

$$(C_{sat}-C_{bot}) \approx \frac{C_{sat} j_b}{\rho(1-\varepsilon)(1-C_{sat})k_r + \frac{\rho\varepsilon\ {}^*_S}{\lambda}} \tag{B15}$$

Using Eqs. (B14-B15) and taking into account Eq.(B4) lead to express Eqs. (B12) and (B13) as

$$\frac{dz_t}{dt} \approx \frac{C_{sat} j_t}{\rho_{cr}(1-\varepsilon)(1-C_{sat})}\left(\frac{(1-\varepsilon)(1-C_{sat})\lambda k_r}{(1-\varepsilon)(1-C_{sat})\lambda k_r + \varepsilon D_S^*}\right) \tag{B16}$$

$$\frac{dz_b}{dt} \approx \frac{C_{sat} j_b}{\rho_{cr}(1-\varepsilon)(1-C_{sat})}\left(\frac{(1-\varepsilon)(1-C_{sat})\lambda k_r}{(1-\varepsilon)(1-C_{sat})\lambda k_r + \varepsilon D_S^*}\right) \tag{B17}$$

which after introduction of the Damkhöler number $Da = \frac{(1-\varepsilon)(1-C_{sat})\lambda k_r}{\varepsilon D_S^*}$ lead to Eqs (13-14) in the main text.

Bibliography

1. X. Y. Chen, Aust. J. Soil Res., **30**, 429 (1992).
2. U. Nachshon, N. Weisbrod, M.I. Dragila and A. Grader, Water Resour. Res., **47**, W03513 (2011).
3. A. S. Goudies and H. A. Viles, *Salt Weathering Hazards* (Wiley, Chichester, 1997).
4. R. J. Flatt, F. Caruso, A. M. A. Sanchez, and G. W. Scherer, Nat. Commun.**5**, 4823 (2014).
5. M. Schiro, E. Ruiz-Agudo, and C. Rodriguez-Navarro, Phys. Rev. Lett. **109**, 265503 (2012).
6. G. W. Scherer, Cem. Concr. Res.**34**, 1613 (2004).
7. E. E. Alonso and A. Ramon, Géotechnique **63**, 857 (2013).
8. H. Eloukabi, N. Sghaier, S. Ben Nasrallah, and M. Prat, M. (2013). Int. J. of Heat and Mass Transf., **56**, 80 (2013).
9. S. Gupta, H. Huinink, M. Prat, L. Pel, and K. Kopinga, Chem. Eng. Sci. **109**, 204 (2014).
10. H. Fujimaki, T. Shimano, M. Inoue, and K. Nakane, Vadose Zone J., **5**, 1246 (2006).
11. S. Veran-Tissoires, and M. Prat, J. of Fluid Mech. **749**, 701 (2014).
12. S. Shokri-Kuehni, T. Vetter, C. Webb, and N. Shokri, Geophys. Res. Lett. **44**, 5504 (2017).
13. J. Desarnaud, H. Derluyn, L. Molari, S. de Miranda, V. Cnudde, and N. Shahidzadeh J. of Appl. Phys. **118**, 114901 (2015).
14. T. Corti, and U. K. Krieger, Applied Optics, **46**, 5835 (2007).
15. U. Nachshon, N. Weisbrod, R. Katzir, and A. Nasser, Geophys. Res. Lett., **45**, 6100 (2018).
16. S. Dai, H.Shin, and J. C. Santamarina, Acta Geotechnica, **11**, 1103 (2016).
17. A. Naillon, P. Joseph, and M. Prat, Phys. Rev. Lett., **120**, 034502 (2018).
18. W.J.P. Van Enckevort, and J.H.Los, Crystal Growth and Design, **13**, 1838 (2013).
19. See Supplemental Movie at [https://journals.aps.org/pre/abstract/10.1103/PhysRevE.100.032802].
20. J. Bear, *Dynamics of fluids in porous media*, (Dover Publication New-York 1972).
21. J.C. Slattery, *Momentum, Energy and Mass Transfer in Continua*, (McGraw-Hill, New-York, 1972).
22. F. J.Valdés-Parada, B. Goyeau, and J. A.Ochoa-Tapia, Chem. Eng. Sci., **61**, 1692 (2006).
23. J. W. Mullin, *Crystallization*, (Butterworth Heinemann, Oxford, 2001), 4th edition.
24. H. P. Huinink, L. Pel, and M. A. J.Michels, Physics of Fluids, **14**, 1389 (2002).
25. A. Naillon, P. Joseph, and M. Prat, J. Cryst. Growth **463**, 201 (2017).
26. F. A. L; Dullien, Porous *media: fluid transport and pore structure*, (Academic Press, San Diego 1992) 2nd edition.
27. J.-H. Kim, Ochoa J.A., and Whitaker S., Transport in Porous Media, **2**, 327 (1987)
28. N.Sghaier, S.Geoffroy, M.Prat, H.Eloukabi and S. Ben Nasrallah, Phys. Rev. E 90, 042402 (2014).
29. T. M. Goodall, C. P. North, K.W. Glennie, Sedimentology, **47**, 99 (2000)

Adapted from: Licsandru, G., Noiriel, C., Duru, P., Geoffroy, S., Abou-Chakra, A., Prat, M. (2019). Dissolution-precipitation-driven upward migration of a salt crust. Physical Review E 100 (3), 032802.

Chapter IV

Air gap formation between an efflorescence salt crust and the porous medium surface under deficit evaporation conditions

IV.1. Abstract:

Salt efflorescence growth on a porous medium can severely reduce the evaporation rate in comparison with a non-precipitated porous surface, thereby affecting the soil-atmosphere exchanges and the transfers in the underlying porous medium. As it has been reported efflorescence salt crusts can present local detachment areas of the porous surface. It is therefore tempting to relate the two observations. However, we first present a simple experiment where the strong reduction in the evaporation rate is clearly not due to the detachment, i.e. to the formation of an air gap between the crust and the porous medium substrate. In such an experiment, the strong evaporation rate reduction is attributed to pore clogging. After which a second experiment is performed in order to obtain quite a significant and accurate representation of the phenomenon. Such an air gap formation is clearly shown to result from the upward migration of the salt and actually leading to a complete detachment of the crust from the top region of the porous substrate. The event's formation is entirely explained as the result of salt dissolution – precipitation mechanisms coupled with water absorption and evaporation at the bottom and top surface of the crust. Also, the study shows that the evaporation rate from a wet salt crust can be much lower than the crust potential evaporation. More generally, the study shows that salt structures in an appropriate water vapor concentration gradient can be a self-propelled system also being able to carry small objects such as soil particles for instance.

Soil salinization plays a major role in land degradation that decreases soil fertility and it is a significant component in the world desertification processes (Vengosh 2003). It has been estimated that more than 50% of the arable land would be salinized by the year 2050 (Jamil et al. 2011). Therefore, it is of high importance to much better understand such processes. This phenomenon is often associated with the soil surface being covered with salt crusts due to evaporation of water rich in dissolved salts. Such a salt crust is referred to as an efflorescence salt crust (ESC), in what follows since it forms at the porous medium surface. The ESC formation modifies the evaporation as well as other surface properties, such as the albedo for example. Thus the soil–atmosphere exchanges (Nield et al. 2016), which in turn, affect the solute transfer in soil and salinization processes. Laboratory experiments have shown that the salt crust formation can reduce the evaporation rate by more than one order

of magnitude compared to the pre-crust evaporation rate, e.g. (Eloukabi et al. 2013). Although the effect is extreme, a detailed understanding of the mechanisms leading to such a severe impact on evaporation is lacking. It has also been reported that ESC development could be associated with intriguing phenomena such as the formation of an air gap between the crust and the porous medium surface (Nachshon et al. 2018) or the formation of salt domes and blisters (Dai et al., 2016). These blisters are salt shells locally detached from the surface of the underlying porous medium. Here again, the phenomena are spectacular but they are lacking a detailed analysis. It is tempting to directly attribute the strong evaporation reduction to the ESC air gap formation. However, it will be shown that this is not as simple. In other words, the physics of salt crusts remains largely an open area of research. The objective of the present paper is therefore to clearly establish ESC as an object of high interest associated with rich physics. This being carried out through laboratory experimenting and thus showing how an air gap can form between the salt crust and the porous medium surface. Before going into the paper details, it is worth mentioning that ESC are of importance also in other contexts than soil physics. Salt weathering related issues are just another area of very active research in civil engineering and monument preservation, e.g. (Goudies and Viles, 1997, Flatt et al. 2014, Shiro et al. 2012) since it has been established that salt crystallization in pores could lead to severe damages (Noiriel et al. 2010). ESC are frequently observed in these contexts and as in soil physics, their formation greatly affects the evaporation rate from the porous materials, e.g. (Desarnaud et al. 2015), which in turn affect the evolution of the solute concentration field in the porous building materials and thereby the risk of salt damages. Since it is well known that salt crystallization can generate stresses (Becker and Day 1905), one might wonder whether the air gap formation or the dome/blister formation result from a mechanical effect. However, the analysis presented in the present paper considers completely different lines of thought. The main idea is to consider dissolution-precipitation mechanisms as responsible for the air gap formation and more generally for the other phenomena associated with the ESC dynamics. This viewpoint is supported by the experiment reported in (Licsandru et al. 2019) showing that a crust can move in a Hele-Shaw cell as a result of dissolution – precipitation mechanism. Here, we report results on air gap formation obtained with a similar set-up. The main and important difference is that the present experiment reveals how an air gap can be formed. In (Licsandru et al. 2019), only the detached crust was considered and the porous substrate was completely removed in the beginning of the experiment. Also, the present experiment provides important information on the crust structure. In particular, the experiment makes clear that the crust should not be considered, at least when it forms, as a salt layer simply set on top of the porous medium. It should be considered as a partially embedded layer in the porous medium. There also are other important differences compared to the experiment reported in (Licsandru et al. 2019). First this is a much longer experiment, 138 days (not taking into account the period of crust formation) compared to 18 days in (Licsandru et al. 2019). Another would be that in (Licsandru et al. 2019) the evaporation rate at the surface of the crust corresponded to the potential evaporation rate, i.e. the expected evaporation rate from a surface covered by a NaCl saturated liquid film. The situation discussed in the following experiment is that when the evaporation is lower than the actual potential one. For this reason, the situation is referred to as a deficit evaporation situation. This is of great difference as an important outcome of the present article is to show that the evaporation from a wet salt crust can be substantially lower than the potential evaporation. In addition, this leads to the identification of different salt crust migration regimes.

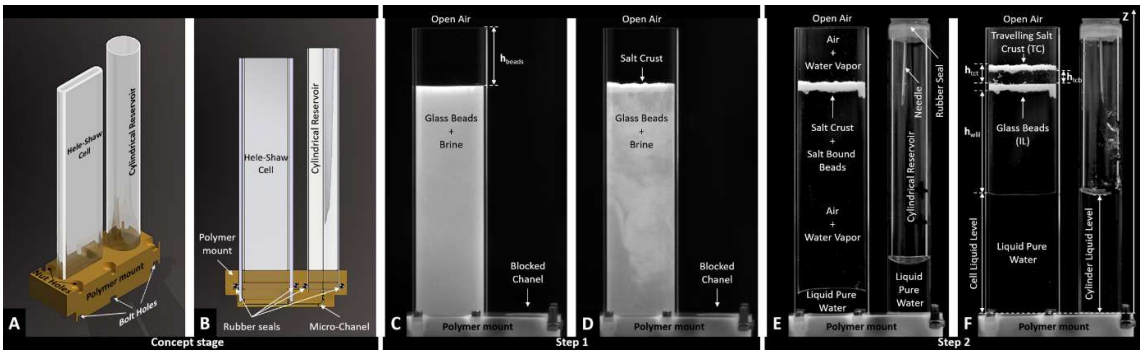


Figure 1. The two step experiment: (A,B) Concept stage of the experimental setup, (A) 3D isometric view of setup, (B) Vertical section of setup ; (C,D) Step 1 porous medium drying in a Hele-Shaw cell: (A) beginning and (B) end of experiment (experiment of about 130 days); (E,F) Step 2 suspended crust experiment: (E) Stage 1 Crust still linked to porous medium, (F) Stage 2 Crust is completely detached from the porous medium (experiment of about 138 days). At the end of Step 1, most of the glass beads are removed from the cell thus a suspended and partially embedded in glass beads salt crust is obtained. Then water is injected at the cell bottom and Step 2 starts. The crust starts to move upward and after a while detaches from the glass bead layer.

The experiment is performed in controlled environmental conditions: room temperature ($T \approx$ 22-23°C) and relative humidity around the cell at $H_{r,inf} \approx$ 39 %. The set-up is set on a balance (not shown) so as to follow the mass variation, i.e. the evaporation from the cell, during the experiment. This mass loss is recorded every 100 s. As exemplified in Fig.1, pictures of the experiment are taken at 1000 s intervals in portrait mode as follows: Step 1 a PCO SensiCam records pictures at a resolution of 1280X1024 pixels, Step 2 a Nikon D800E records pictures at a resolution of 7360X4912 pixels. An important aspect of the experiment is the associated sheer volume of image data required for processing (in .tif format 1 Step 2 picture weighs at ~100MB thus the ~12000 pictures of Step 2 give a total of ~ 1.2TB). This data enables one to determine the evolutions of various points of interest (liquid levels, salt crust top and bottom surface positions, etc.). Another very important aspect is that once an experiment has such a long running time period (~130days and ~138 days) the camera alignment will start to deteriorate and as such giving a lateral drift which in term needs correcting for precision purposes. Here the ImageJ Fiji plugin developed by (Preibisch et al. 2010) has proven very powerful, as all the pictures have been realigned with an average displacement of 0.4072 pixels and a total number of corresponding detections of 4.085.356.

The actual image processing was done completely with ImageJ Fiji using already established techniques such as filtering and general binary operations applied either globally or locally. The only issues encountered were at the detection of the dissolution front in the porous medium, where due to lack of uniformity in contrast a small amount of manual linking was applied (this was the case in the first ~1500 pictures). After processing, all the data was verified for accuracy both by eye and by curve plotting in order to check for inconsistency in trends. All data will be available at request.

The experiment can be split into two main steps. First, a classical drying experiment of a glass bead packing was performed with bead diameters in the range of [1 – 50 µm]. The packing was saturated by a NaCl aqueous solution of ion mass fraction 25 % initially and confined in a Hele-Shaw cell. The cell was rendered hydrophobic by silanization in order to avoid as much as possible the salt creeping phenomenon, e.g. (Van Enckevort, and Los, 2013), along the inner wall of the cell. The experiment Step 1 is illustrated in Fig. 1 (A). As a result of the drying process, a crust formed at the surface of the packing within the cell. This

first step lasted about 130 days.

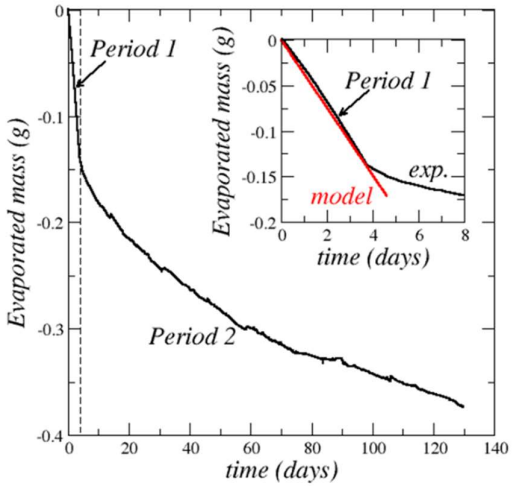


Figure.2. Evaporated mass as a function of time during experiment Step 1. The inset shows a zoom of Period 1 with a comparison with the evaporated mass computed from Eq. (1) (Red curve).

As it can be seen from Fig.2, the crust formation leads to a severe drop in the evaporation rate. The rate in Period 2 is about 40 times lower than in Period 1 (see Fig. 2 for the definition of Periods 1 and 2). The evaporated mass during Period 1 was also estimated assuming that the evaporation rate during the first period of Step 1, resulted from the pure diffusive water vapor transport between the top of the beads and the cell top, namely,

$$J_{perio} = A\, D_v \frac{M_v}{RT} p_{vsat} \frac{\left(0.75 - H_{r,inf}\right)}{h_{bead}} \quad (1)$$

where A is the cross-section surface area of the cell, D_v is the binary diffusion coefficient of the vapor in gas phase, R is the universal gas constant, M_v is the vapor molecular weight, h_{bead} is the distance between the top of the beads and the cell top (Fig.1 Step 1), p_{vsat} is the saturation vapor pressure. Note that 0.75 in Eq. (1) corresponds to the activity of a NaCl saturated aqueous solution. As can be seen from the inset in Fig. 2, using Eq. (1) leads to a quite good agreement with the experimental measurements in Period 1.

Interestingly, it can be noted that the liquid saturation of the porous substrate was quite high ($S \sim 0.7$; where S is the volume fraction of the pore space occupied by the solution) when it was decided that Step 1 was over, i.e. when the evaporation rate was quite low. However, the detailed analysis of the results during Step 1 is left for future work. The focus of the current article is on what happens during Step 2.

At the end of Step 1, the beads were gently removed from the cell and the object (salt crust) was left suspended as illustrated in Fig.1 (E). After which Step 2 was started by feeding some pure water in the mounted cylinder which in term, has a link to the cell through a small channel in the polymeric base. During the experiment actually, the water level was modified twice as shown in Fig.3 (A) and also illustrated in Fig.1 (E, F). First, the level was set to $h_{wl\text{-}from\text{-}bottom} \approx 13$ mm for about 8 days (distance measured from the position of the cell's polymeric base top, see Fig.1 (E). If the level in the cylinder is set initially too high the gas pressurization effect in the region between the water level and the suspended object can be damaging. For this reason, the water level in the cell is left quite low initially. Over this period, the suspended

object absorbs water as a result of water vapor transport between the pure liquid water at the bottom and the object. As it will be discussed in more details later, this induces the upward migration of the crystal phase within the cell. Then the level is gradually raised in about 10 hours so that $h_{wl} \approx 43$ mm in the cell.

Once this level is reached a long period of 130 days starts without any further addition of liquid water. As it can be seen from Fig.3 (A), the water level in the cell does not change in the first time span of about eleven days from this long period whereas evaporation does occur as shown in Fig.3 (B). This is a consequence of the cell wall hydrophobization. In the beginning, the level in the adjacent feeding cylinder is higher than the one in the cell (as illustrated in Fig.1(E, F) on the left side). During this time the water level in the cell is stagnating while the one in the cylinder decreases until the two are leveled. Then both levels recede at approximately the same pace. The estimate of the maximum difference between the level in the cell and the level in the cylinder, based on the equilibrium between the capillary forces and the gravity forces, i.e. $\delta h = -\gamma cos\theta / r / \rho g \approx 3$ mm, where θ is the contact angle in the cell resulting from the silanization, i.e. $\theta \sim$ 110-120°, and $r \approx 1$ mm the cell aperture half, is consistent with the observations. As it can be seen from Fig.3 (A), the liquid level dynamics in the cell and the adjacent cylinder is however more complex than one could assume based on the simplicity of the system. For instance, consider the long period after detachment in Fig.3 (A). Initially the cylinder level is higher than the one in the cell, which, as explained before, is consistent with the cell's hydrophobic treatment. After a while, the cylinder level is less than in the one in the cell. It should be noted that we have chosen to consider the lowest point of the transition region between the liquid and the gas phase, as an indicator of the liquid level in the cylinder images. Because of the rising meniscus along the cylinder wall, the "equivalent" position (the point corresponding to the measured position and added the equivalent liquid thickness corresponding to the mass in the region delimited by the wall meniscus) is actually closer to the liquid level in the cell. Nevertheless, the liquid level variations in the cell and cylinder, i.e. the slopes in Fig.3 (A), are slightly different. This is not an artefact due to the image processing for instance. The visual inspection of the movie (see Supplemental material) also shows the difference in the level dynamics. This might be due to variations in the cell local wettability properties. In this respect, it can be noted that the contact line in the cell is first advancing (before the detachment in Fig.3 (A)), followed by a standstill and then recedes.

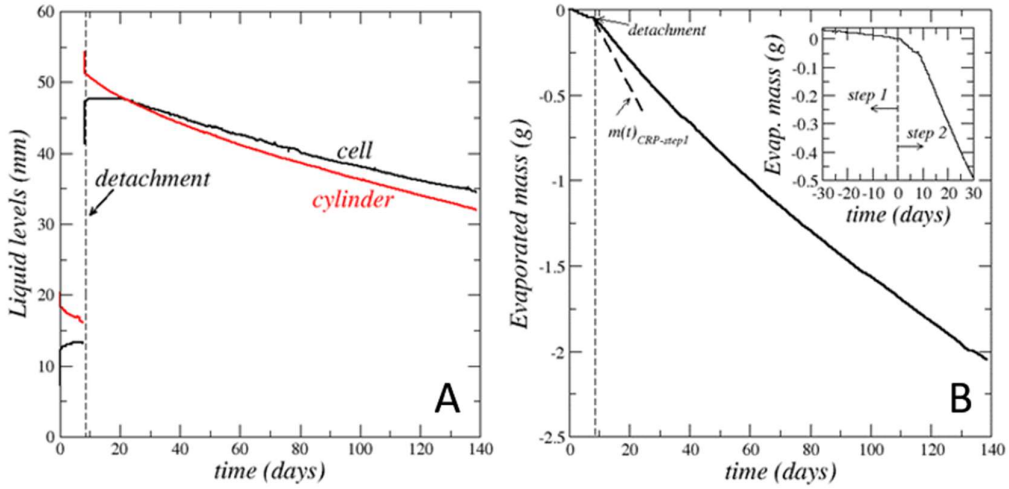


Figure 3. A) Variations of water level in the cell (black) and the adjacent cylinder (red) during Step 2. Levels are measured from the cell bottom (top of polymeric base, see Fig.1(B)), (B) evaporated mass as a function of time during Step 2. The evaporated mass variation at the beginning of Step 1 is also indicated for comparison (straight line indicated by "$m(t)_{CRP\text{-}step1}$" where CRP stands for Constant Rate Period since the evaporation rate is constant in the first period of Step 1). The inset shows that the evaporation rate at the end of Step 1 (slope of the mass vs time curve) is lower than the evaporation rate in Step 2.

Also, it can be noted from Fig.3(B) that: i) the evaporation rate in Step 2 is greater than the evaporation rate at the end of Step 1 (see inset in Fig.3(B)). Also, it can be noted that the maximum evaporation rate during Step 1 (which corresponds to the tilted dashed line in Fig.3(B) indicated by "$m(t)_{CRP\text{-}step1}$") is greater than the maximum evaporation rate during Step 2. It can be also noted that the duration of Step 2 is ~138 days, thus comparable with the duration of Step 1 at ~130 days. This makes the overall experiment duration (Step 1 + Step 2) of about 268 days.

The major event (detachment of the crust) happens in Step 2 and it is illustrated in Fig.4 (E, F) and also in Fig.1(F) (and best seen in the Supplemental Material movie). The most salient feature depicted in Fig.4 is that the suspended object in the Hele-Shaw cell evolves dynamically starting from a seemingly relatively compact object and ending up as a two object system with different bottom and top layer evolutions. As illustrated in Fig.4, the top layer upward displacement is quite significant, on the order of 7 mm. This leads to the formation of a gas gap between the two layers. In contrast, the lower layer does not move within the cell, except for a few local rearrangements. As a result, the system is considered to be formed from an immobile layer (IL) and a mobile layer, also referred to as the travelling crust (TC).

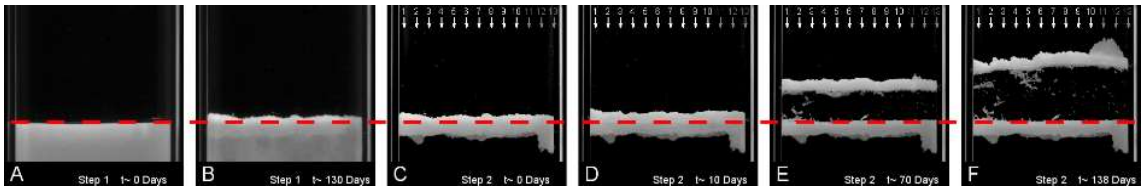


Figure 4. Evolution of the suspended object during Step1 and Step 2 with the pixel line measurement positions (the (A) image on the left shows the glass beads in the cell at the beginning of Step 1 for comparison with respect to the beads top surface position). The (D) image for *t ~ 10 days* corresponds to the time when the mobile layer is about to detach from the immobile layer.

Illustrated in Fig.5 (A), post-mortem SEM images of the immobile layer, i.e. long after the detachment of the mobile layer, indicates that the immobile layer is essentially made of glass beads, i.e. the glass beads forming the porous substrate in the beginning of Step 1. In contrast, the SEM image of the travelling layer in Fig.5 (B) indicates that only a very few beads are present in the mobile layer. The solid component in the mobile layer is essentially halite, i.e. NaCl crystals.

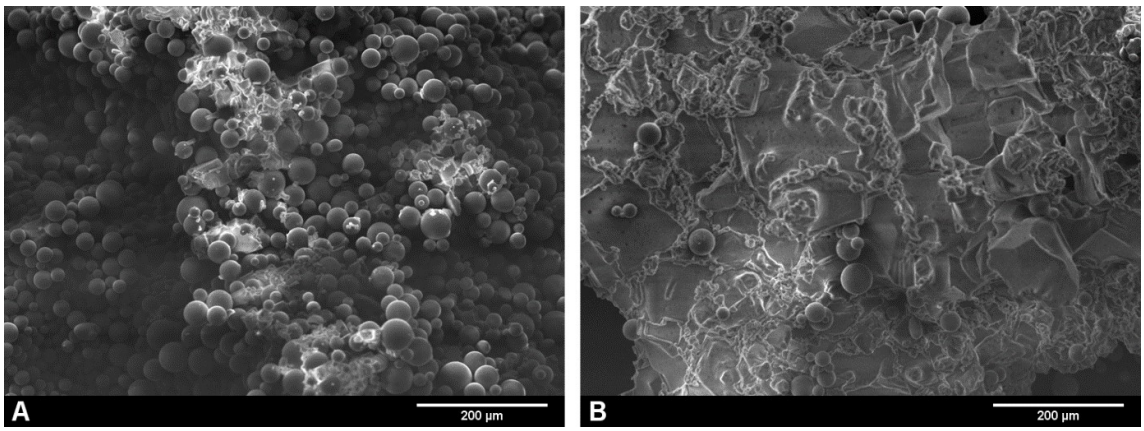


Figure 5. SEM images of (A) the immobile layer and (B) the mobile layer after complete detachment. These images have been obtained about four months after the end of the experiment when both layers were deemed dry. (These samples are from a similar experiment of an overall shorter duration: Step 1 ~27 days and Step 2 ~21 days in total ~48 days. The high vacuum SEM analysis has been done after proper treatment of the samples (drying), at same conditions as during the experiment, this giving a necessary technical time between the end of the experiment and analysis of about 4 months).

Another valuable piece of information on the suspended object comes from Fig.4. The dashed line in Fig.4 corresponds to the position of the porous substrate (glass beads) surface before the formation of the crust in Step 1. This line corresponds to the boundary where the mobile and immobile layers separate. In other words, the top surface of the immobile layer coincides with the top surface of the beads in Step 1. It is clear from Fig.4 that the surface area of the mobile layer region located above the dashed line increases with time until detachment between the two layers occurs. If one assumes little change in the microstructure of the travelling crust, this implies that the growth of this surface area results from salt migration from the immobile layer. From these first insights, a simple picture emerges. The salt crust forming on top of a porous medium is partially embedded in the underlying porous substrate. The crust's lower layer corresponds to the crust region embedded in the porous substrate, i.e. the immobile layer in the experiment, whereas the crust upper layer

corresponds to the crust region located above the surface of the porous substrate.

Based on these observations, a first observation can be made in regards to the mechanisms at play in the experiment. Since the crystals disappear from the bottom layer and the surface of the top layer moves upward, the lower layer crystals should dissolve and the salt should precipitate on top of the upper layer. The displacement of the upper surface is thus interpreted as the result of salt precipitation on top forming successive crystal layers. This scenario is supported by the careful inspection of the time-lapse at different points, clearly showing a front moving upward within the immobile layer (see the Supplemental Material corresponding movie). This front is illustrated in Fig.6 by black dots.

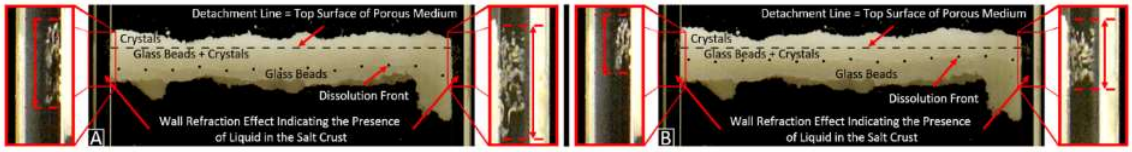


Figure 6. Step 2 Stage 1: The dissolution front upward migration in time (A) about 3 days, (B) about 8 days (indicated by the black dot markers) within the glass bead immobile layer. The vertical red double arrows on the sides indicate the wet zone (see text).

Another piece of information can be seen in the images as exemplified in Fig. 6. A refraction effect on the Hele-Shaw cell wall (Hobeika et al. 2017). This shows a difference in the zone located between the dissolution front and the mobile layer top surface in comparison with the glass bead zone located underneath. The refraction effect results in a greyish cluster on both cell wall sides visible in the images. This effect is illustrated in Fig.6. The “magnified clusters” are indicated by the red vertical double arrows and roughly bounded by two red rectangles in Fig.6. These “clusters” are interpreted as the signature of liquid water presence. It can be noted that they are not present in the first images of the experimental Step 2 but rapidly appear when the suspended object is exposed to vapor coming from the liquid water surface located at the cell bottom. Another mention is that it can be seen following the mobile layer in its displacement throughout the movie. The conclusion is therefore, that the zone between the dissolution front and the mobile layer top surface is wet. As in previous considerations on salt structures, e.g. (Sghaier and Prat 2009, Sghaier et al. 2014, Veran-Tissoires et al. 2012, Veran-Tissoires and Prat 2014, Licsandru et al. 2019), the crust must therefore be considered as a porous medium with a liquid saline solution occupying totally or partially its pores while the crust is moving. Since the refraction effect is not seen below the dissolution front, the corresponding zone of glass beads is considered as mostly dry, not completely however, as explained later in the paper. Since the solution almost perfectly wets the crystal (Corti and Krieger 2007) this is an indication that the capillary pressure in the region above the dissolution front is greater than in the beads region below. In other words, the pores are greater in the bead regions in comparison with the region above the dissolution front. Thus the pores in the travelling crust are smaller than in the porous substrate. Also, the attached movie shows clearly (see the Supplementary Material movie) that very little changes, if any, occur in the immobile layer below the dissolution front.

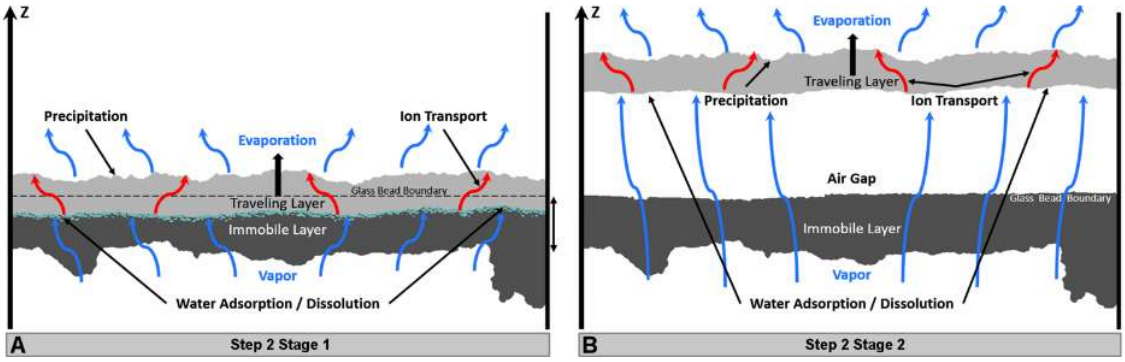


Figure 7. Schematic of the system with the travelling and immobile layers during Step 2 Stage 1 (A) and Stage 2 (B). In Stage 1, the travelling crust is partially embedded in the immobile layer (whose thickness is indicated by a double arrow on the right side of Fig. (A)), which is made of glass beads. Stage 2 starts when the travelling crust is about to detach from the immobile bead layer. Except at the very beginning, the travelling crust is therefore detached from the glass bead immobile layer during Stage 2. As discussed, the immobile layer is actually slightly wet.

The above observations and considerations lead to a relatively simple phenomenology which is sketched in Fig.7. The initial suspended object is decomposed into a two-layer system, in which one layer is mobile and travels upward whereas the other one below is immobile. The mobile layer is a porous layer made of salt crystals with only a very few entrapped glass beads whereas the immobile layer (IL) is essentially made of glass beads. The immobile layer thus corresponds to an upper region fraction of the initial porous medium (glass beads) set in the cell at the beginning of Step 1.

Since the Step 2 experiment leads to a complete detachment of the mobile layer from the initial immobile layer, two main stages are distinguished in Step 2. Stage 1 corresponds to the period in which the mobile salt crust is partially embedded in the immobile glass bead layer. In this stage, the bottom of the mobile layer travels through the immobile layer of the porous substrate and can occasionally disturb/transport a few beads in its upward migration. This explains the sporadic presence of glass beads in the mobile layer. Stage 2 starting from the moment the crust detaches from the immobile layer. At this point the mobile layer releases some of the entrapped beads in its upward migration. This phenomenon is highly visible in the movie (see the Supplementary Material movie). The detachment mark, i.e. the end of Stage 1, is observed ~10 days into the Step 2 experiment and is indicated in Fig.3 and Fig.4. This takes place shortly after the cell is refilled with additional water.

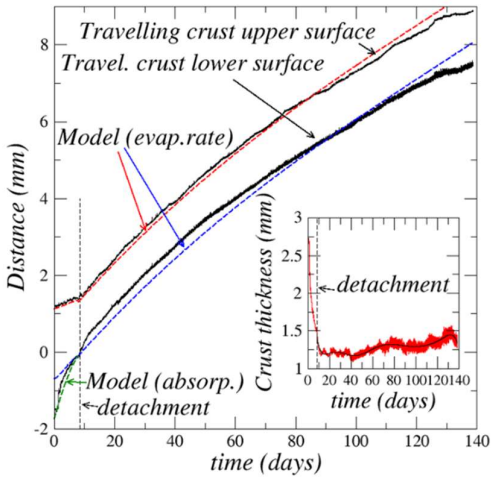


Figure 8. Travelling crust top and bottom surface mean positions as a function of time. Positions obtained from Eqs. (3) and (4) are the plots indicated by "model" (see text). The inset shows the changes in crust thickness as a function of time (the red plot in the inset corresponds to the raw data obtained by image processing, the black line is obtained by regression from the raw data). The vertical dashed lines correspond to the detachment.

A known characteristic of sodium chloride crystals is hygroscopicity. This means that they can absorb water from the water vapor present in the air. Since the equilibrium water vapor pressure of a saline solution is less than that of pure water (for a saturated NaCl solution the equilibrium water vapor pressure is 25% less than for pure water), there is a net flux between the liquid water free surface at the cell bottom and the travelling layer's bottom surface. This induces some salt crystal dissolution, a process also referred to as deliquescence. The salt solution is then transported through the travelling layer's pore network up to the top surface where it precipitates to form a new crystal deposit. The ion transport is in part due to advection since the evaporation on top of the travelling layer induces a flow in the pore space of the travelling crust. The fact that evaporation occurs is illustrated in Fig.3(B), which shows the mass variation of the system as a function of time.

Further information is gained from Fig.8 where the travelling crust's upper and lower surface mean positions are plotted as well as its thickness (inset), which represents the difference between the travelling crust top and bottom mean positions. This data is obtained by image processing using a similar method as described in (Licsandru *et al.* 2019) where an arithmetic average is calculated from up to thirteen vertical pixel lines evenly distributed over the crust width.

Fig.8 first illustrates that the upward migration of the travelling crust is quite significant, with a total displacement of about 6.5 times its average thickness, over the duration of the experiment. Then, two stages can be distinguished: Stage 1 the travelling crust is partially embedded in the IL, Stage 2 after the TC detachment. As can be seen from Fig.8 (inset), the thickness of the travelling layer is greater during Stage 1. The crust thickness decreases over Stage 1 and then varies relatively little over Stage 2, i.e. after the detachment. This is consistent with the fact that glass beads are present in the embedded region of the crust during Stage 1. Assuming that the porosity of the crystal phase, defined as the porous phase forming the travelling crust, does not change appreciably during the travelling crust displacement, a simple mass conservation argument leads to, the salt cannot escape from the system,

$$\frac{h_{det}}{h_{emb}} \approx \frac{h_1+\varepsilon h_2}{h_1+h_2} \quad (2)$$

where h_{det} is the thickness of the traveling layer after detachment, h_{emb} is the thickness of the travelling layer at *t* =0 (Step 2), i.e. when embedded in the immobile layer, h_1 is the height of the travelling crust above the bead surface level at the beginning of Step 2 ($h_1 \approx 1.13$ mm), h_2 is the height of the embedded part of the travelling crust at the beginning of Step 2 ($h_2 \approx$ 1.6 mm) and ε is the porosity of the immobile layer (in the absence of crystals). Assuming a standard value of 0.36 for ε, Eq. (1) leads to $\frac{h_{det}}{h_{emb}} \approx 0.6$ while the corresponding ratio from the data shown in Fig.8 is 0.53. The simple estimate from Eq. (2) is therefore reasonably consistent with the change in the thickness of the travelling layer that can be measured from the images. Accordingly, this can be also seen as an indication that the porosity of the crystal phase does not change appreciably during the travelling layer displacement.

It can also be observed that the crust thickness does not present large variations after the detachment. However, it tends to slightly increase with the elapsed time from about 1.2 mm to about 1.4 mm (see inset in Fig.8).

Further details are provided in Fig.9 showing the displacements of 10 points at the travelling crust (TC) crust top surface (corresponding to the intersections of the surface with 10 vertical pixel lines distributed over the TC width. As mentioned before 13 pixel lines were actually considered but due to some local salt creeping by the wall toward the end of the experiments and crust inconsistency on the right side of the cell, 3 lines were excluded (lines 11, 12 and 13 see Fig.4 (C, D, E, F) in the plots shown in Fig.9). This allows for distinguishing three main regimes. First, the stable regime before detachment in the period where the liquid level is low in the cell (see Fig.3(A)). In this regime, the TC top surface does not noticeably change during its upward displacement. The second regime starts at about the time when the liquid level is raised in the cell. During this regime which lasts about 60 days, the TC top surface tends to become flatter. For this reason, this regime is referred to as stabilizing. The last regime in Fig.9 is the destabilizing regime. The TC top surface becomes increasingly wavier during this regime, which lasts about 38 days. These regimes will be further discussed in a later paper.

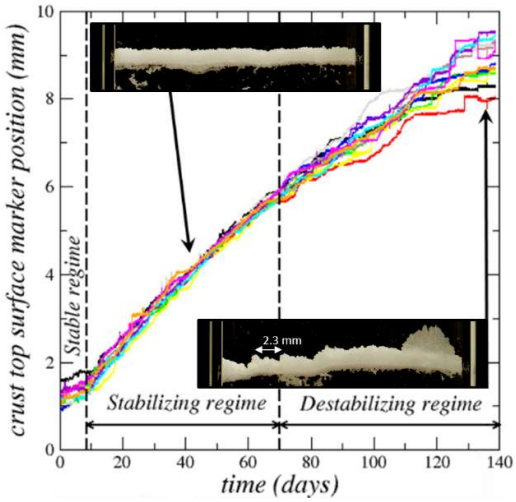


Figure 9. Variation of the travelling crust top surface during Step 2 Stage 2. Images of travelling crust in compact/stabilizing regime and at the end of destabilizing regime. The travelling crust becomes wavier as it gets closer to the cell top in the destabilizing regime.

We first return to the average displacements depicted in Fig.8. We have tested the relationships derived in (Licsandru et al. 2019) relating the displacements of the travelling crust top and bottom surfaces with the evaporation flux (top surface) or the absorption flux (bottom surface). These expressions read,

$$\frac{dz_{tct}}{dt} = \frac{C_{sat} j_t}{\rho_{cr}(1-\varepsilon_c)(1-C_{sat})}\left[\frac{Da}{1+Da}\right] \quad (3)$$

$$\frac{dz_{tcb}}{dt} = \frac{C_{sat} j_b}{\rho_{cr}\varepsilon(1-\varepsilon_c)(1-C_{sat})}\left[\frac{Da}{1+Da}\right] \quad (4)$$

where z_{tct} is the mean position of the travelling crust top surface, z_{tcb} is the mean position of the travelling crust bottom surface, j_t is the evaporation flux at the travelling crust top surface, , j_b is the absorption flux at the travelling crust top surface, ε_c is the crust porosity, ρ_{cr} is the crystal density (2160 kg/m^3) and *Da* is the Damkhöler number characterizing the competition between the precipitation – dissolution reaction and the transport of the ions within the crust. The only difference with the relationships derived in (Licsandru *et al.* 2019) is the presence of the porosity ε in Eq. (4). ε is the porosity of the immobile bead layer when the travelling crust is partially embedded in the beads immobile layer. After the detachment, Eq. (4) is used with ε=1. The evolution of the travelling crust top and bottom surface position have been computed within the cell during Step 2 Stage 2 with Eqs.(3) and (4) using the evaporation flux determined from the mass loss experimental data and the absorption flux from the liquid level variations in the cell and the adjacent cylinder. Details on how these two crucial fluxes have been determined are given just after the discussion on the results obtained from Eqs. (3) and (4). The evolutions computed from Eqs. (4) and (4) are shown in red and blue in Fig.8 (red and blue dashed lines labelled "Model" in Fig.8). As can be seen from Fig.8, Eq. (3) leads to quite consistent results. As in (Licsandru et al. 2019) we have considered a low porosity crust (ε_c =0.1) and adjusted *Da.* The dashed lines in Fig.8 are for *Da* = 7, a value of the same order of magnitude as considered in (Licsandru et al. 2019) where *Da* = 4. As explained in (Licsandru et al. 2019), *Da* requires information such as the crust interfacial area per unit volume or the crust effective diffusion coefficient to be determined directly, i.e. not through a fitting procedure. This information is currently lacking in the literature. However, as discussed in (Licsandru et al. 2019), such a value of the Damkhöler number is consistent with a low porosity crust with sub-micronic pores. Whereas the displacements of the crust top and bottom surfaces are similar after detachment, it can be seen that the bottom surface displacement is faster than the top one before the detachment. This was expected because the available space for the displacement is less when the bottom surface is moving in the immobile layer (this corresponds to the factor ε is Eq.(4)). However, the consideration of this effect is not sufficient to explain the faster displacement of the crust bottom surface before detachment. The main factor lies in the absorption flux j_t which is greater in this period than the evaporation rate. This is shown by the data depicted in the inset on the left in Fig.10. The mass variation computed from the liquid level variation in the adjacent cylinder and the cell is greater than the mass loss measured by weighting. Thus, the crust absorbs more water than it loses by evaporation in this period. For this reason, the period before detachment, where the absorption rate is greater than the evaporation rate, is also referred to as a declogging period. This period corresponds to the stable regime in Fig.9.

Now more details on how the mass variation depicted in Fig.10 is obtained. This data is important since it is used to determine the evaporation and absorption fluxes. The mass variations measured by weighting can be straightforwardly used to determine the evaporation flux as

$$j_{evap.} = -\frac{1}{A}\frac{dm_{weightin}}{dt} \quad (5)$$

whereas the absorption flux is determined from the liquid level variations in the cell and the adjacent cylinder as

$$j_{absorp.} = -\frac{1}{A}\frac{dm_{level}}{dt} = -\frac{\rho}{A}\frac{d}{dt}\left(Ah_{llc} + A_{cyl}h_{llcyl.}\right) \quad (6)$$

where h_{llcell} is the liquid level in the cell, $h_{llcyl.}$ is the liquid level in the adjacent cylinder (visible in Fig.1b), A_{cyl} is the cylinder cross-section surface area, ρ is the liquid water density. The liquid levels h_{llcell} and $h_{llcyl.}$ are obtained every 1000 s by image processing from the experiment pictures (as exemplified in Fig.1).

As it can be seen from Fig.10, $m_{weightin} \approx m_{level}$ during Step 2 Stage 2 , i.e. during the long period after the detachment. This result can be first seen as a verification that no noticeable leakage occurred during the experiment. Second, it shows that $j_{absorp.} \approx j_{evap.}$. The latter were actually determined from polynomial fits of the curves shown in Fig.10. The variation of the ratio $j_{evap.}/j_{absorp.}$ obtained from these fits is shown in the top right inset in Fig.10. The plot of this ratio suggests that $j_{absorp.} > j_{evap.}$ in a first period of about 60 days and that $j_{absorp.} < j_{evap.}$ during the rest of the experiment.

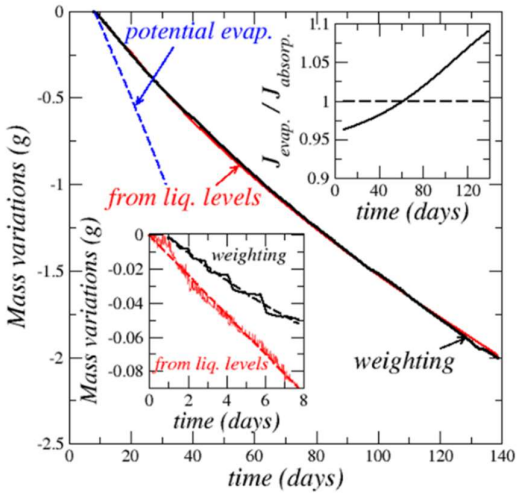


Figure 10. Mass loss as a function of time during Step 2 Stage 2, i.e. after detachment. Comparison between the mass loss measured by weighting and the mass variation computed from the liquid level variations in the cell and the adjacent cylinder. The latter correspond to the red curves. The inset on the left shows the mass loss measured by weighting and the mass variation computed from the liquid level variation in the adjacent cylinder in the period before detachment (the data corresponds to the solid lines, the dashed lines are fits showing the main trends). The inset on the right shows the ratio between the evaporation rate and the absorption rate over Step 2 Stage 2 (see text).

Naturally, the plot shown in this inset cannot be considered as fully reliable since the variations of $m_{weightin}$ and m_{level} in the main plot in Fig.10 are quite close. However, as it will be shown, the variation of the ratio $j_{evap.}/j_{absorp.}$ depicted in the Fig.10 top right inset is quite consistent with other results discussed later in the paper.

IV.2. Absorption

A priori, one can expect to estimate the absorption flux from the consideration of the water vapor diffusive mass transfer between the liquid surface in the cell bottom and the TC bottom surface. For simplicity, the focus will be on Stage 2, i.e. after detachment. According to our phenomenological description the immobile layer is supposed to be dried or with a very low liquid content. An interesting issue is precisely to determine whether the immobile layer is fully dried or a bit wet. The first consideration that the immobile crust is fully dry. Taking into account that vapor diffusion in the immobile layer is reduced compared to a free gas, the mass flux between the liquid water level and the travelling crust bottom is then expressed as

$$j_b = \left(\frac{h_{wlil}}{D_v} + \frac{h_{il}}{\varepsilon D_{eff}} + \frac{h_{tcb}}{D_v}\right)^{-1} \frac{M_v}{RT} p_{vsat}\left(1 - H_{r,cb}\right) \tag{7}$$

where h_{wlil} is the distance between the liquid level and the immobile layer bottom surface, h_{il} is the thickness of the immobile layer ($h_{il} \approx 2.15$ mm), h_{tcb} is the distance between the immobile layer top surface and the travelling crust bottom surface, D_{eff} is the effective diffusion coefficient of the immobile glass bead layer ($D_{eff} \approx \varepsilon^{0.4} D_v$). In Eq.(7), $H_{r,cb}$ is the relative humidity at the travelling crust bottom surface. The variation of $H_{r,cb}$ can then be determined by expressing that the flux given by Eq.(7) should be equal to the absorption flux determined from the liquid level variations in the cell and the adjacent cylinder, namely Eq.(6).

The variation of $H_{r,tcb}$ so obtained is shown in Fig.11 (red curve). As can be seen, this leads to values significantly lower than the relative humidity at the surface of a saturated NaCl solution (~0.75). However, since dissolution occurs at this surface, the ion mass fraction at this surface can be expected to be close to the solubility. Hence, $H_{r,tcb}$ is expected to be close to 0.75. Since assuming a fully dry immobile layer leads to significantly lower values for $H_{r,tcb}$, the conclusion is therefore that the immobile layer is not fully dry. Also, the SEM image of the immobile layer in Fig.5a indicates the presence of salt crystals, notably in the contact regions between beads. Thus, it is reasonable to assume that some leftover crystals are present in the immobile layer.

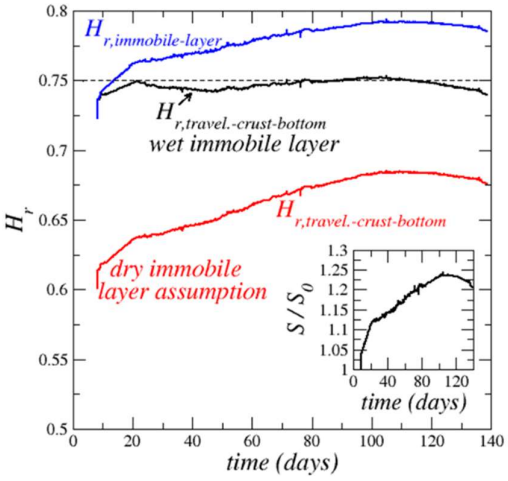


Figure 11. Variation of the relative humidity as a function of time when the immobile layer (IL) is considered as fully dry (red curve) or partially wet (black curve). The inset shows the saturation variation in the immobile layer when the IL is supposed to be wet (see text).

As a result, the immobile layer can absorb some water due to the presence of trapped crystals. This should lead to dissolution of the crystals and the formation of liquid phase in the immobile layer. The liquid phase could also be present as residual liquid after the displacement of the dissolution front. Then, it is hypothesized that this liquid content is small within the immobile layer. The hypothesis that the liquid content should be small is supported by the fact that the sidewall liquid phase indicator index is not visible on the walls adjacent to the immobile layer. An additional argument in favor of a low liquid content is presented later in the paper. Because of the presence of salt in the immobile layer, the liquid phase is an aqueous NaCl solution and not pure water. As a result, the activity of the solution in the immobile layer $H_{r,il}$ is less than 1. Furthermore, it is considered that this activity is uniform over the immobile layer. This assumption is supported in part by some direct simulations of a model porous medium as explained later in the paper. For the moment, it's simply assumed that $H_{r,il}$ is spatially uniform over the immobile layer. Then the absorption flux is given by,

$$j_{absorp.} = j_b = D_v \frac{M_v}{RT} p_{vsat} \frac{(H_{r,il} - H_{r,tcb})}{h_{tcb}} \tag{8}$$

which is the vapor flux between the top of the immobile layer and the TC bottom surface. Then since the process is quite slow, it is reasonable to consider a quasi-steady situation in which the absorption rate is also equal to the mass transfer rate between the pure liquid water at the cell bottom and the bottom surface of the immobile layer, namely

$$j_{absor\ .} = D_v \frac{M_v}{RT} p_{vsat} \frac{(1 - H_{r,il})}{h_{wlil}} \tag{9}$$

Combining Eqs.(8) and (9) with Eq.(6) enables us to compute $H_{r,il}$ and $H_{r,tcb}$ which are the only unknowns since the variations of m_{level}, h_{wlil} and h_{tcb} are obtained by image processing the experimental pictures. It can be noted that this leads to a simple relationship between the activity in the immobile layer and the activity at the crust bottom surface, namely,

$$\left(1 + \frac{h_{wlil}}{h_{tcb}}\right) H_{r,il} = 1 + \frac{h_{wlil}}{h_{tcb}} H_{r,tcb} \tag{10}$$

This gives the results plotted in Fig. 11 (black curve). As can be seen, $H_{r,tcb}$ is now much closer to the expected value for a NaCl saturated solution (0.75). Also, it can be seen that the activity in the immobile layer $H_{r,il}$, slightly increases over a first period of about 100 days, reaches a plateau and then tends to decrease. The variations of $H_{r,il}$ can be expressed in terms of liquid content variations. Suppose that the liquid saturation is S_0 when the detachment occurs (it is recalled that we consider only the period after detachment in this section of the paper). Then salt mass conservation implies $S(t) = S_0 \frac{\rho\,(C(H_{r,il}(0))\,C(H_{r,il}(0))}{\rho\,(C(H_{r,il}(t))\,C(H_{r,il}(t))}$ where time t =0 corresponds to the time when the detachment occurs. $C(H_{r,il})$ is the relationship giving the equilibrium ion mass fraction in the solution as a function of the activity, thus the inverse of the function giving the activity as a function of C. In this way, the variations of S shown in the Fig.11 inset are obtained from the variations of $H_{r,il}$ (black curve) depicted as the main curve in Fig.11. According to these results, the saturation would first increase in the immobile layer and then decrease. The overall variation is small, on the order of 25% at most, thus consistent with a low liquid content all over the experiment.

In summary, considering the immobile layer as slightly wet leads to consistent results. The presence of saline solution the immobile layer acts as a short-cut for the transport of the vapor from the pure liquid water at the cell bottom and the TC bottom surface. This short-cut effect can be illustrated from a few direct simulations in a model porous medium as explained here.

The computational domain is sketched in Fig.12 (A). As it can be seen, the equation governing the water vapor partial pressure under steady – state conditions is solved. The saturation vapor pressure is imposed on the boundary corresponding to the pure liquid water interface at the cell bottom whereas the vapor pressure at the TC bottom surface is supposed to be the vapor pressure for a saturated NaCl solution. The equilibrium vapor pressure p_{veq} at the surface of the menisci inside the immobile layer is unknown in this problem. The latter is supposed to vary only slightly over the IL thickness. For simplicity, p_{veq} is supposed to be the same at each meniscus in the direct simulation. The constraint to be satisfied for determining p_{veq} is that the mass flux $-D_v \frac{M_v}{RT} \nabla p_v . \mathbf{n}$, where $\mathbf{n}$ is a normal unit vector, computed at the pure liquid water surface and equal to the absorption flux computed at the TC bottom surface. This is achieved through an iterative procedure by varying p_{veq} until the difference between the two fluxes is judged sufficiently small. The inputs are the distance h_{wlil}, h_{il}, h_{tcb} obtained by image processing the experimental pictures and the bead size *d*. Two bead sizes have been considered, *d* = 250 µm (bigger than in the experiment for illustration purpose as shown in Fig.12 (B) and *d* = 25 µm (roughly corresponding to the mean bead size in the experiment). The latter corresponds to 100 beads over the immobile layer thickness.

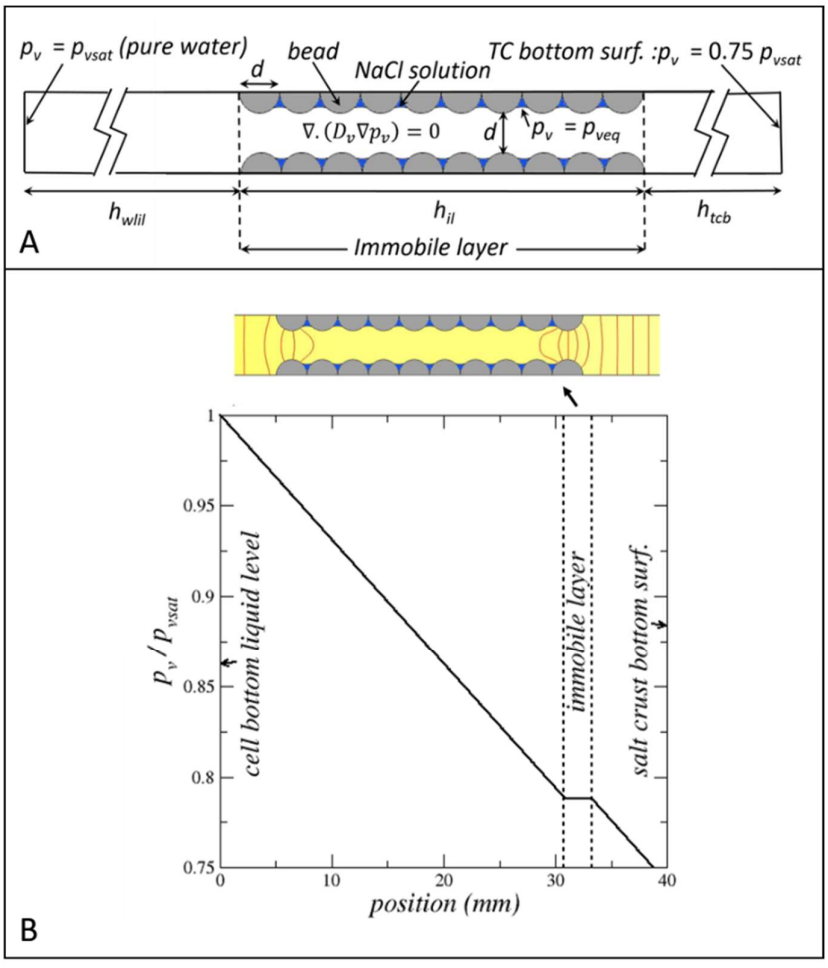


Figure 12. A) Immobile layer model porous medium, governing equation, boundary conditions and computational domain considered in the numerical simulations, a zero flux condition is imposed on the computational domain boundaries for which no indication is given in the figure; B) example of computed water partial pressure isolines (normalized by the saturation vapor pressure) in the model immobile layer and typical variation of the vapor pressure.

Results of the simulation are depicted in Fig.13. As it can be seen, the variation of the immobile layer activity $H_{r,il}$ so obtained is quite consistent with the variations obtained from Eqs. (8) and (9) and the measured absorption mass rate (this corresponds to the analytical solution in Fig.13). The evolution of the computed absorption flux, i.e. the mass transfer flux through the computational domain, is also quite consistent with the evolution of the experiment. The short-cut effect is illustrated in Fig.12 (B). As the vapor pressure gradient is zero in the gas phase inside the immobile layer compared to the gradient in the adjacent gas regions as a result of the solution presence in the immobile layer.

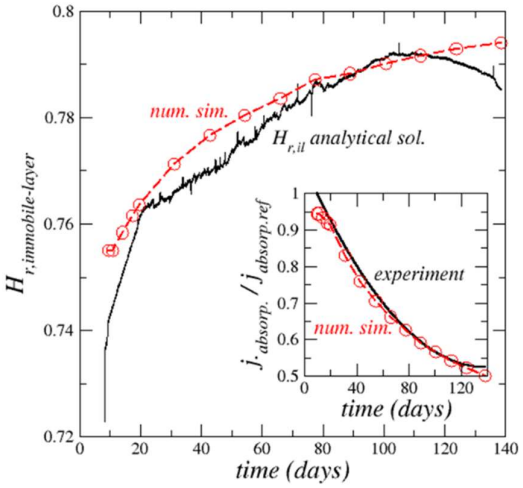


Figure 13. Activity in the immobile layer as a function of time. Comparison between the results obtained from the model depicted in Fig.12 (A) and the analytical prediction (Eq. (9)). The inset shows the variation of the absorption flux. The reference flux is the mass flux in the experiment (6.45 10^{-6} kg/m^2/s) at t = 9.6222338 days (first time considered in the numerical simulations).

Since only diffusion in the gas phase cannot explain the water transfer within the immobile layer, another mechanism is at play. This efficient mechanism is condensation-evaporation and the transport in liquid phase through the immobile layer. A simple option is to consider that liquid phase percolating paths are present through the IL. Then, water vapor would condense on the menisci at the immobile layer (IL) bottom surface and re-forms by evaporation at the IL top surface. However, an argument now developed suggests that this option is unlikely. To this end, the startup equation governing the ion transport in a partially saturated medium, (considering a quasi-steady situation and a quasi-uniform saturation over the layer),

$$\rho U \frac{\partial C}{\partial z} = \rho S \varepsilon D_s^* \frac{\partial^2 C}{\partial z^2} \tag{11}$$

where U is the liquid filtration velocity, D_s^* is the effective ion diffusion coefficient, which can be computed as $D_s^* = \varepsilon^{0.4} \left(\frac{S-S_c}{1-S_c}\right)^{1.5} D_s$, where D_s (~ 1.3 10-9 m2/s) is the ion molecular diffusion coefficient, and Sc is the irreducible saturation (Sc =0.1). Since the ions cannot leave the IL (after detachment), the solution to Eq. (11) can be expressed as,

$$\frac{C}{C_{bil}} = \exp\left(Pe \frac{z}{h_{il}}\right) \tag{12}$$

where C_{bil} is the ion mass fraction at the bottom of the immobile layer and $Pe = \frac{U h_{il}}{\varepsilon S D_s^*}$, which

is the Peclet number characterizing the competition between the ion advection and diffusion transports (Huinink et al. 2002). A careful inspection of the movie does not indicate crystallization on the top surface of the IL. Thus, the ion mass fraction C should be lower than the solubility ion mass fraction Csat. In other words, the saturation in the IL should be compatible with the constraint $\frac{C_{til}}{C_{bil}} = \exp(P_e) < \frac{C_{sat}}{C_{bil}}$ where C_{til} is the ion mass fraction at the IL top surface and C_{bil} can be estimated from the activity in the IL (depicted in Fig. 13). This leads to an estimate of the critical Peclet number in the immobile layer $Pe_{crit.} \approx \log\left(\frac{C_{sat}}{C_{bil}}\right)$ corresponding to the crystallization onset at the IL top surface. For the computed activity in the IL depicted in Fig.13, this leads to a low critical Peclet number on the order of 0.01 – 0.04. The next step is to determine the level of saturation compatible with such low values of the Peclet number. Thus, we define as S_{min}, the IL layer saturation such that Pe =$Pe_{crit.}$. S_{min} is given by the equation $\frac{Uh_{il}}{\varepsilon SD_S^*} = Pe_{crit.}$ where $U = j_{absorp.}/\rho$. To obtain the corresponding range of saturation, one can for instance consider the value $Pe_{crit.} = 0.04$ obtained at t = 100 days for which U = 3.04 10-9 m/s. This leads to $S_{min} \approx 0.83$ (for $\varepsilon = 0.36$, h_{il} =2.5 mm). In other words, the assumption of a connected liquid phase across the immobile layer is here compatible with the observation only for a high saturation in the IL. Also, for earlier times, for instance ~20- 30 days, the absorption rate is greater (see inset in Fig.13) and thus also the filtration velocity. The computed Peclet number is then greater than the critical Peclet number corresponding to the onset of crystallization even for a fully saturated immobile layer. Accordingly, considering the liquid phase connected across the IL leads to the conclusion that salt precipitation should be observed at the IL top surface. Since this is not the case, it is concluded that the liquid phase is not connected but distributed in the form of small liquid clusters within the IL. It can be noted that this assumption is also consistent with the fact that no refraction effect is visible on the side walls of the cell. As discussed previously, this refraction effect (illustrated in Fig.6) is an indication of a strong liquid presence (as in the travelling layer). Thus, we finally reach the conclusion that the IL contains solution of liquid water and dissolved NaCl since this is necessary to obtain the activity depicted in Fig.13 but that the liquid content is low and corresponds to a distribution in the form of small liquid clusters. The liquid clusters are also necessary for the short-cut effect associated with the condensation–evaporation phenomena inside the IL. Condensation would occur on a fraction of the cluster boundary and evaporation on the complementary fraction. The small size of the clusters is consistent with a low Peclet number at the scale of the cluster (since the size of a cluster would be small compared to the IL thickness), thus a quasi-uniform ion mass fraction within a cluster (this would prevent a possible crystallization contrary to the case of the percolating clusters considered above). The water transport within the IL would result from a combination of transport in liquid phase driven by capillarity within the clusters and vapor diffusion between clusters (over a total effective distance much lower than the IL thickness). This would also imply that the activity slightly decreases from one cluster to another over the IL thickness. Of course, all these considerations would require to be supported by a detailed study. However, this is left for future work. As discussed previously (see inset in Fig.11), the saturation in the immobile layer should increase over a long period. The saturation variation is small, thus compatible with a pendular state all along the experiment (the pendular state corresponds to a liquid distribution in the form of small disconnected clusters as hypothesized whereas the funicular state refers to the situation where the liquid phase forms at least one percolating cluster).

IV.3. Evaporation

Since the classical expression of the evaporation flux corresponding to a mass transport by diffusion in gas phase, i.e. Eq. (1), led to excellent results for Step 1 Period 1 , a similar expression must be valid in Step 2 . Hence, it is expected that

$$j_{evap.} = j_t = D_v \frac{M_v}{RT} p_{vsat} \frac{(H_{r,tct} - H_{r,inf})}{h_t} \tag{13}$$

where $H_{r,tct}$ is the relative humidity at the crust top surface, h_t is the distance between the travelling layer top surface and the cell top. This distance as a function of time is obtained by image processing. Since the liquid water content in the crust must be high for the ions to be transported from the crust bottom to its top, an obvious first choice is to consider that $H_{r,tct} \approx 0.75$, which corresponds to the water activity of a NaCl saturated solution. The mass variation corresponding to the evaporation flux obtained from Eq.(13) for $H_{r,tct} \approx 0.75$ is shown in Fig.14 and referred to as the potential evaporation since it corresponds to the maximum flux that can be expected from a NaCl saturated solution. As shown in Fig.14, the potential evaporation, i.e. the mass loss estimates from Eq.(7) with $H_{r,tct} \approx 0.75$ is significantly greater than the measured mass loss. Furthermore, the evaporation rate should increase with time according to Eq.(13) if one assumes $H_{r,tct}$ = constant since h_t decreases with time. This is not what is observed since the slope of the curve $m_{weighting}(t)$ in Fig.14 corresponding to the experimental measurements tends to decrease and not to increase with the elapsed time.

Since the estimate of the evaporation rate from Eq.(1) during Period 1 of Step 1 led to quite good results (as shown in the inset of Fig.2), the conclusion is therefore that $H_{r,tct} < 0.75$. Values of $H_{r,tct}$ leading to a good agreement with the experimental measurements can be determined from the equation,

$$\frac{dm_{weighting}}{dt} = -A\, D_v \frac{M_v}{RT} p_{vsat} \frac{(H_{r,tct} - H_{r,inf})}{h_t} \tag{14}$$

where $m_{weighting}$ is as before the mass measured by weighting. For the long period after the detachment, this leads to the results depicted in Fig. 14.

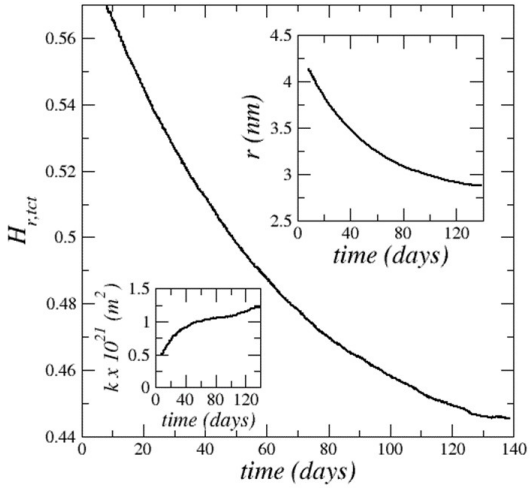


Figure 14. Computed apparent relative humidity at the travelling crust top surface during Step 2 Stage 2. The inset on the right shows the variation of the menisci curvature radius at the crust top surface compatible with the evaporation rate variation observed in the experiments according to Kelvin law (Eq. (15)). The inset on the left shows the crust permeability determined from Eq. (18) (see text).

As it can be seen, the average relative humidity at the travelling crust (TC) top surface must be significantly lower than the equilibrium relative humidity (0.75) for the evaporation rate at the TC top surface to be consistent with the measured mass loss. Several mechanisms can lead to such a reduction of the vapor pressure at the porous top surface. This happens for instance in drying (Attari Moghaddam et al. 2018) when the porous medium is partially saturated. However, the displacement of the crust is remarkably stable, the top surface does not change its shape significantly over a long period (this is further illustrated later in the paper). Thus, it is likely that the TC top surface is on average wet and not partially dry. Then the question is how the porous wet surface evaporation rate can be significantly lower than the potential evaporation, i.e. the evaporation that would be obtained if the surface was covered by a liquid film of NaCl saturated solution. According to the literature, a first option is when the pores are sufficiently spaced from each other at the surface. This option is explored in Appendix A where the corresponding effect is referred to as the Schlünder effect (Schlünder 1988). As it can be seen in Appendix A, this option would lead to the desired evaporation rates only for a surface porosity in the range [10^{-7} -10^{-6}]. Such low values seem unlikely, given the relatively uniform displacement of the travelling crust. Also, a tricky question is understanding how the crust structure would adapt for the evaporation rate so that it would be equal to the maximum possible rate, which here is the absorption rate.

A simpler mechanism is therefore quite likely. Then, a simpler view is to invoke the Kelvin effect (Adamson 1990). The Kelvin effect refers to the modification of equilibrium vapor pressure $p_{vequ.}$ due to the curvature of liquid-gas interface and can be computed from the relationship,

$$H_{r,eq} = \frac{p_{vequ.}}{p_{vs}} = \exp\left(-\frac{M_v}{RT}\frac{2\gamma cos\theta}{\rho_\ell r}\right) \quad (15)$$

where p_{vs} is the saturation vapor pressure corresponding to a flat liquid – vapor interface (thus p_{vs} = 0.75 p_{vsat} for saturated NaCl aqueous solution), γ is the surface tension, θ the contact angle, ρ_ℓ the liquid density; r is the liquid –gas interface curvature radius considering a spherical shape at the entrance of a cylindrical pore. For the values of $H_{r,eq}$ indicated in

Fig.14, Eq.(15) leads to the meniscus curvature radii depicted in the inset of Fig.14. As can it be seen, the curvature radius would be in the range [3-4 nm]. Then an estimate of the crust permeability required to reach such levels of curvature can be determined. Consider that the crust is wet with its pores saturated with solution, which is consistent with the observed liquid presence indicator on the cell's sides. Then the corresponding viscous pressure drop, across the crust, required to reach the desired meniscus curvature levels at the top surface would be,

$$\delta p = \frac{2\gamma cos}{r} \tag{16}$$

assuming that the meniscus curvature radius is much larger at the travelling crust bottom surface (since liquid water forms there one can assume a negligible capillary pressure jump at the bottom surface).

As shown in (Licsandru et al. 2019), the velocity induced in the crust can be estimated as a function of the evaporation flux as

$$\rho V = (1 + \alpha) j_t \tag{17}$$

where $\alpha = \frac{C_{sat}(\rho\varepsilon_c + \rho_{cr}(1-\varepsilon_c))}{\rho_{cr}(1-\varepsilon_c)(1-C_{sat})}\left[\frac{Da}{1+Da}\right]$ (thus α =0.33 for *Da* =7 and ε_c =0.1). Applying Darcy's law, one obtains an estimate of the crust permeability *k* as,

$$k = \frac{\mu\,(1+\alpha) j_t\, h_{tc}\, r}{\rho\; 2\gamma cos\theta} \tag{18}$$

where h_{tc} is the travelling crust thickness and μ is the solution dynamic viscosity. Applying Eq.(18) for θ = 0 (Corti and Krieger 2007), the values of *r* depicted in Fig.14 and the corresponding values of the evaporation flux in the experiments one obtains *k* in the range [0.5 $\times 10^{-21}$- 1.2$\times 10^{-21}$] m^2 (as also depicted in the left inset in Fig.14). This is a quite low permeability. However, if one uses the classical Kozeny-Carman relationship $k = \frac{\varepsilon_c^3 d_p^2}{180(1-\varepsilon_c)^2}$ where d_p represents a typical "grain" size and ε_c is the crust porosity, such low permeability value is obtained for $d_p \approx$ [9 - 13] nm with ε_c =0.1. This "grain" size is consistent with the pore size required to obtain the needed Kelvin effect (since the pore diameter is a fraction of the "grain" size). In other words, the low evaporation rates on top of the travelling crust is compatible with a crust with very small pores on the order of a few nanometers with a reduced solution activity due to the menisci curvature at the travelling crust top surface. The curvature of the menisci would adapt during the crust migration so as to obtain an evaporation rate equal to the maximum possible evaporation rate, the latter corresponding to the absorption rate at the crust bottom surface. Also, as depicted in Fig.14, these considerations suggest that the mean permeability would first increase in the salt crust as the crust moves upward, then reach a plateau and then would increase again. The first increase period is consistent with a slightly greater absorption compared to evaporation and the plateau with the existence of the compact regime (see below). The second increase in the permeability is less obvious to interpret. It roughly corresponds to the destabilizing regime (Fig.9). Since the permeability estimate is based on a 1D model, it is probably more reasonable to simply consider that the salt crust permeability does not vary appreciably during its displacement.

A possible refinement is to invoke the possible impact of thin liquid films since it is known from the studies on the crystallization pressures, e.g. (Naillon et al. 2018) and references therein, that a thin liquid film is sufficient for NaCl crystal to grow. The key concept in the analysis of these thin films is the concept of disjoining pressure (Adamson 1990), denoted in

what follows by p_d. It has been argued, e.g. (Potash and Wayner 1972), that the disjoining pressure could be incorporated in the extended version of the Kelvin equation to take into account the interactions between the liquid molecules in the thin film and the solid substrate impact (here the NaCl crystals forming the solid phase of the crust) on the equilibrium vapor pressure at the film surface,

$$\frac{p_{vequ.}}{p_{vs}} = \exp\left(\frac{M_v}{RT\rho}\left(p_d - \frac{2\gamma cos\theta}{r}\right)\right) \tag{19}$$

where p_d is negative. Thus thin films in the crust top surface pores and possibly over the crystal surface in between the pores might also explain the reduced evaporation rate in the presence of bigger pores than the ones required from the consideration of Eq. (10). In this case, the film thickness would vary in response to the variations in the absorption rates at the traveling crust bottom surface during the crust upward migration. Naturally, the real situation might be a combination of the various effects discussed above, namely the “Schlünder” effect and the Kelvin effect associated with capillarity and or thin film effects. Nevertheless, we note that an explanation via the Kelvin effect is compatible with a crust whose microstructure varies little during its migration since only an adjustment of the menisci curvature radius on the crust top surface is necessary.

IV.4. Summary

The above considerations lead to the following main results. The mechanisms leading to the travelling crust (TC) displacement are basically the same in Stage 1 (TC partially embedded in the immobile bead layer) and Stage 2 (TC detached from immobile bead layer). Deliquescence (dissolution) occurs at the TC bottom surface, the excess ions are transported by advection toward the TC top surface where precipitation leads to the formation of a new layer of crystals and so on. The change in the TC thickness during Stage 1 up to the detachment is consistent with the greater absorption flux compared to the evaporation flux and the fact that the porous crystal phase cannot access the volume corresponding to the glass beads. According to our analysis, the crust gains water during a first period (declogging period). Thus, the crust is essentially dry at the beginning of Step 2 with perhaps some liquid confined in isolated clusters. This is indicated by the fact that the lateral wall refraction effect due to the presence of liquid is not visible at the beginning of the Step 2 experiment. When liquid water is set at the bottom of the cell, the crust starts absorbing water. This induces a dissolution process which should open/create new pores and probably enlarges already existing pores. Since the evaporation rate from the cell is relatively lower during this initial period (as shown in Fig.3), we believe that the solution gradually fills the pores of the region where crystals are present. This is indicated by the occurrence of the lateral wall refraction effect, which becomes visible a short while after the beginning of Step 2. Then, after the rise in the liquid level at the cell bottom, a steady state regime occurs during which the crust is saturated by the solution and the evaporation rate is significantly greater. In the long period that follows, after detachment, the absorption and evaporation rates are very close.

As illustrated in Fig. 9, this leads to a long period of about 60 days where the travelling crust top surface is remarkably stable. Then the top surface tends to get gradually wavier with time. This corresponds to the destabilizing regime in Fig.9. Since according to Eq. (3) the crust local growth rate is proportional to the evaporation flux, the waviness can be seen as the result of a spatial variation in the evaporation flux at the crust top surface. The evaporation flux variation could be due to the fact that the menisci eventually recede into the crust in some pores. As illustrated in Fig.14, the meniscus curvature increases as the crust top surface gets

closer to the cell top. Thus, the curvature could reach in some pores the maximum possible curvature radius which for a cylindrical pore and a perfectly wetting liquid for instance is the pore radius r_p. The region where comparatively more menisci recede would move slower than the region where there are less receding menisci. Such an evolution is also consistent with the ratio of the evaporation flux to the absorption flux depicted in the inset of Fig.10. Although the evolution of this ratio cannot be considered as fully reliable as discussed previously, it can be observed that the transition from the stabilizing regime to the destabilizing regime in Fig. 9 occurs at about t = 70 days. This time is close to the time when the evaporation flux becomes greater than the absorption flux (see inset in Fig.10). Hence, the destabilizing regime would start when the crust cannot be sufficiently fed by the water at its bottom via the absorption mechanism for staying fully saturated. Also, a characteristic size can be seen in the crust waviness (as indicated by an arrow in Fig.9). The emergence of this characteristic size remains to be explained.

IV.5. Discussion-conclusions

Efflorescence salt crusts forming on a porous medium can have a severe impact on the evaporation rate compared to the same situation in the absence of crystallization (pure water). This can significantly modify the soil – atmosphere exchanges and thereby the solute and water transfers in the underlying porous medium. Salt crusts can evolve dynamically. Some previous studies have reported that the crust can separate from the porous medium surface in some places forming salt shells or salt domes. However, the mechanisms explaining the separation were still to be unraveled. It was also tempting to directly correlate the severe reduction in the evaporation rate in the presence of a salt crust and the crust separation from the porous substrate. In this context, the results reported in this article shed lights on several mechanisms associated with the formation, development and impact of efflorescence salt crusts on a porous medium due to evaporation. First, the severe reduction in the evaporation rate is observed when the crust is partially embedded in the porous medium without air gap formation. In other words, the strong reduction in the evaporation rate cannot be attributed here to the detachment of the crust from the porous medium upper surface. It can be noted that the liquid saturation in the porous medium is still quite high when this strong reduction is observed. Thus the crust is in contact with the solution at its bottom. Because of the precipitation phenomena significance in the illustrated crust dynamics of the suspended crust experiment, the severe reduction of the evaporation rate is attributed to pore clogging in the crust due to salt precipitation. A dedicated study is however necessary to analyze in detail this strong evaporation reduction effect. As mentioned before, this is left for a future study.

The efflorescence salt crust should not be considered as a simple accumulation of crystals on top of the porous substrate when it forms. This experiment makes clear that salt precipitation occurs both within the top region and above the porous substrate surface. The efflorescence salt crust is then partially embedded in the porous substrate and not solely growing externally from its surface.

A remarkable aspect is that the travelling crust fully detaches from the porous medium top surface, leading to a quite significant air gap formation between the salt crust and porous medium surface. In part, the crust initially travels in the porous substrate then detaches and continues to migrate upward fully detached from it. The maximum size of the air gap in the experiment is on the order of 7 mm, which corresponds to about 6 times the average crust thickness. Such a quite noticeable air gap is consistent with field observations, e.g. (Nachshon et al. 2018). In relation with the field conditions, the situation studied can be seen as one where the efflorescence salt crust is initially in place at the surface of dry soil. The injection of

liquid water at the cell bottom would then correspond to a rise in the soil water table. The experiment makes clear that dissolution–precipitation phenomena combined with water absorption and evaporation can lead to quite a significant air gap formation. Naturally, associated additional phenomena, for instance temperature variations, should play a role under field conditions. Nevertheless, it is worth mentioning that no consideration of mechanical effects was found necessary to analyze the experiment, which was analyzed consistently only considering transport phenomena, precipitation–dissolution mechanisms in the presence of evaporation-absorption processes.

The analysis also indicates that brine can be present in the top region of the porous medium, i.e. the experiment's immobile layer, even in the absence of liquid pathways between deep porous medium water and its top region. Our analysis strongly suggests that such liquid content is quite small, below the corresponding liquid percolation limit.

The two main factors controlling the crust displacement are the evaporation rate from the travelling crust top surface and the absorption rate at its bottom. In the experiment, the absorption rate was significantly lower than the potential evaporation, i.e. the maximum evaporation that can be expected from a NaCl covered surface saturated with liquid film. For this reason, the regime considered in the article is referred to as a deficit evaporation one. The result is that the absorption rate controls the salt crust displacement. A remarkable result is that the absorption rate actually imposes the evaporation rate. Such a low evaporation rate would correspond to the formation of sub-micronic pores in the crust associated with a noticeable Kelvin-effect. An important result is therefore that the evaporation rate from a wet salt crust can be much lower than its potential evaporation. This provides an alternative view to the low evaporation rate explanation based on the consideration of the (dry) crust as a water vapor diffusion barrier, e.g. (Desarnaud et al. 2015). As a result, the absorption and evaporation rates are essentially equal during the crust displacement. However, two main observations suggest that the evaporation rate tends to become slightly greater than the absorption rate as the crust moves upward. First, the immobile layer saturation is assessed from the estimated crust mean activity presenting a decrease after a long period of steady increase. Second, the detached travelling crust remains remarkably compact over quite a long period of about 60 days, this corresponding to an also significant displacement. Then, the crust tends to become wavy. This change is attributed to a partial drying of the crust starting after the long compact regime period. The occurrence of the waviness can be loosely related to field observations showing the more complex detached crust structure formations, such as domes or blisters for example, than simply a flat slab crust parallel to the porous medium surface. In this respect, it is surmised that various regimes can be expected based on the ratio absorption rate / potential evaporation. Here, we have explored the regime where the absorption rate is lower than the potential evaporation. In (Licsandru et al. 2019), a compact regime was observed when the absorption rate is about equal to the potential evaporation. A preliminary experiment shows that a non-limiting absorption rate leads to a strongly unstable regime, with salt finger like formations. This will be presented in a future work. Here, we just wish to put forth the existence of various regimes depending on the ratio between potential evaporation/potential absorption that might explain in part the diversity of salt crust shapes observed in nature.

More generally, this experiment indicates that porous salt structures in water vapor concentration gradients can move and possibly carry objects, such as glass beads in our experiments, over macroscopic distances during their displacement. In other words, a porous salt structure in an appropriate water vapor concentration gradient can be regarded as a self – propelled system.

IV.6. Appendix A

A wet porous surface, i.e. a porous surface with a meniscus in every pore, can lead to a reduced evaporation rate if the pore size and the mean distance between the pores is sufficiently large compared to the height of the diffusion region (distance between the TC top surface and cell top in this case). Formulas are available to compute the impact of the discrete nature of the surface pore distribution or equivalently the possible co-existence of wet and dry patches at the surface, e.g. (Schlünder 1988). The formula derived by Schlünder can be expressed as

$$\frac{J}{J_{ref}} \approx \frac{1}{1+\frac{d^2}{2\pi r_p h_t}} \tag{A1}$$

where *d* is the mean distance between the pores, r_p is the pore mean diameter at the surface and h_t is the distance between the travelling crust top surface and the cell top. J_{ref} is the evaporation flux when the vapor partial pressure is everywhere equal to the equilibrium vapor pressure for a saturated solution, $J_{ref} = AD_v \frac{M_v}{RT} p_{vsat} \frac{(0.75-H_{r,inf})}{h_t}$.

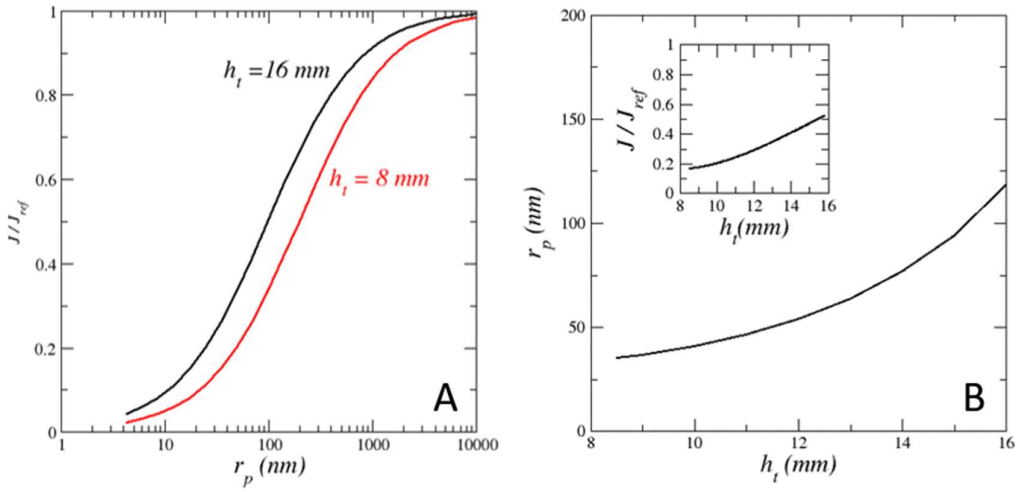


Figure 15. a) Examples of variation of $\frac{J}{J_{ref}}$ as a function of the pore size at the surface predicted by Eq.(A1) for two values of the distance h_t between the travelling crust top surface and the cell top assuming a mean distance between pores of 100 µm; b) Variation of mean pore size at the surface as a function of h_t according to Eq.(15). The inset shows the variation of $\frac{J}{J_{ref}}$ as a function of h_t in the experiment determined from the mass loss data (Step 2 after detachment)

As an example, we have plotted in Fig.15a the variation of $\frac{J}{J_{ref}}$ as a function of the pore size predicted by Eq.(A1) when the mean distance between pores at the surface is 100 µm. The inset in Fig.15b shows the variation of $\frac{J}{J_{ref}}$ with h_t in the experiment where $\frac{J}{J_{ref}}$ is determined from the mass loss data measured by weighting and h_t by image processing. From this data, one can determine from Eq.(A1) the surface pore size variation r_p assuming that the

mean distance between pores at the surface does not vary with h_t (as before this distance is arbitrarily set at d = 100 μm).

The corresponding results are shown in Fig.15b. As it can be seen, the evaporation rate measured in the experiment could correspond to surface pore sizes in the range [30 – 120 nm] according to Eq.(A1) for a mean distance between pores of 100 μm. Thus, the surface pore size would decrease during Step 2. Another option is that the pore size does not change very much and the evaporation flux variation is due to a variation in the distance between pores in addition to h_t. For instance, if we assume a constant pore size of 30 nm, then d would vary between 50 and 92 µm during the experiment. Naturally, it is possible that both d and r_p vary during the travelling crust migration. Thus, the above results could indicate that the lower evaporation rate could be due to the discrete distributions of the pores at the surface. However, these results would correspond to a surface porosity ≈ $4r_p^2/d^2$ in the range [10^{-7} -10^{-6}]. Such low values seem unlikely, given the relatively uniform displacement of the travelling crust. Also, a tricky question is to understand how the crust structure would adapt so that the evaporation rate would be equal to the maximum possible evaporation rate, which is here the absorption rate.

Bibliography

Adamson, A.W., Physical chemistry of surfaces, 5th ed., Wiley (1990).

A. Attari Moghaddam, A. Kharaghani , E. Tsotsas, M. Prat, A pore network study of evaporation from the surface of a drying non-hygroscopic porous medium, AIChE J. 64 (4), 1435-1447 (2018).

G. F. Becker and A. L. Day, The linear force of growing crystals. Proc. Wash. Acad. Sci. 7, 283 (1905).

Corti, T., Krieger, U. K. (2007). Improved inverted bubble method for measuring small contact angles at crystal-solution-vapor interfaces. Appl. Opt., 46, 5835-5839.

S. Dai, H. Shin, and J. C. Santamarina, Formation and development of salt crusts on soil surfaces, Acta Geotech. 11, 1103 (2016).

Desarnaud, J., Derluyn, H., Molari, L., de Miranda,S. Cnudde, V., Shahidzadeh, N. (2015). Drying of salt contaminated porous media: Effect of primary and secondary nucleation, Journal of Applied Physics 118 (11) 114901.

Eloukabi, H., Sghaier, N., Ben Nasrallah, S., Prat, M. (2013). Experimental study of the effect of sodium chloride on drying of porous media: the crusty-patchy efflorescence transition. Int. J. of Heat and Mass Tr. 56, 80–93.

A. S. Goudies and H. A. Viles, Salt Weathering Hazards (Wiley, Chichester, 1997).

N.Hobeika, P.Bouriat, A.Touil, D.Broseta, R. Brown, J. Dubessy, Help from a Hindrance: Using Astigmatism in Round Capillaries To Study Contact Angles and Wetting Layers, Langmuir, 33, 5179−5187 (2017).

Huinink, H.P., Pel, L., Michels, M.A.J. (2002). How ions distribute in a drying porous medium: A simple model. Phys. of Fluids 14 (4), 1389–1395.

Jamil A., Riaz S., Ashraf M., Foolad M.R. Gene expression profiling of plants under salt stress. Crit. Rev. Plant Sci. 2011; 30(5):435–458.

Licsandru, G., Noiriel, C., Duru, P., Geoffroy, S., Abou-Chakra, A., Prat, M. (2019). Dissolution-precipitation-driven upward migration of a salt crust. Physical Review E 100 (3), 032802.

U. Nachshon, N. Weisbrod, R. Katzir and A. Nasser, NaCl Crust Architecture and Its Impact on Evaporation: Three-Dimensional Insights, Geophys. Res. Lett. 45, 6100 (2018).

Naillon, A, Joseph, P., Prat, M. (2018). Ion transport and precipitation kinetics as key aspects of the stress generation on pore walls induced by salt crystallization. Phys. Rev. Letters 120, 034502.

J. M. Nield, G. F. S. Wiggs, J. King, R. G. Bryant,3 Frank D. Eckardt,4 David S. G. Thomas2,4,5 and Richard Washington2,Climate–surface–pore-water interactions on a salt crusted playa: implications for crust pattern and surface roughness development measured using terrestrial laser scanning, Earth Surf. Process. Landforms 41, 738–753 (2016).

Noiriel, C., Renard, F., Doan, M.L., Gratier, J.P. (2010). Intense fracturing and fracture sealing induced by mineral growth in porous rocks, Chemical Geology 269, 197-209.

Potash, Jr., M., and Wayner, Jr., P. C., 1972, ‘‘Evaporation From a Two-Dimensional Extended Meniscus,’’ Int. J. Heat Mass Transfer, 15, pp. 1851–1863.

S. Preibisch, S. Saalfeld, J. Schindelin, P. Tomancak Software for bead-based registration of selective plane illumination microscopy data, Nature Methods 7, 418–419 (2010).

G.W. Scherer, R.J. Flatt, F. Caruso and A.M. Aguilar Sanchez, Chemomechanics of salt damage in stone, Nature Communications 5, 1 (2014).

M. Schiro, E. Ruiz-Agudo, and C. Rodriguez-Navarro, Phys. Rev. Lett. 109, 265503 (2012).

Schlünder, E. U. On the mechanism of the constant drying rate period and its relevance to diffusion controlled catalytic gas phase reactions, Chem. Eng. Sci. 1988, 43(10), 2685–2688.

Sghaier, N., Prat, M. (2009). Effect of efflorescence formation on drying kinetics of porous media. Transport in Porous Media 80 (3) 441-454.

Sghaier, N., Geoffroy,S., Prat, M., Eloukabi, H., Ben Nasrallah, S. (2014). Evaporation driven growth of large crystallized salt structures in a porous medium, Phys. Rev. E 90, 042402.

W.J.P. Van Enckevort, and J.H.Los, Crystal Growth and Design, 13, 1838 (2013).

A.Vengosh, Salinization and Saline Environments, in Treatise on Geochemistry,Volume 9, 2003, Pages 1-35, Edited by H. D. Holland and K. K. Turekian, Elsevier Science (2003).

Veran-Tissoires, S., Marcoux, M., Prat,M. (2012a). Discrete salt crystallization at the surface of a porous medium. Phys. Rev. Letters 108, 054502.

Veran-Tissoires, S., Prat, M. (2014). Evaporation of a sodium chloride solution from a saturated porous medium with efflorescence formation. J. of Fluid Mechanics 749, 701-749.

Chapter V

Moving salt crust in a Hele-Shaw cell: from compact to branched morphology

V.1. Abstract:

This study reports on three experiments in which a salt crust set in a Hele-Shaw cell is exposed to evaporation at its upper surface and water vapor absorption at its bottom surface. The process leads to the upward displacement of the crust within the cell as the result of precipitation mechanisms at the crust top surface and dissolution mechanisms at the crust bottom surface. The study leads to identify two main displacement regimes: compact and branched. The development of the branched regime is observed in a period where the conditions are such that the evaporation rate is comparable to the potential evaporation. This corresponds to a regime where the destabilization of the crust top surface leads to the branched morphology whereas the crust bottom surface remains essentially flat. The destabilization is attributed to the dependence of the crust local growth on the local evaporation flux whereas the precipitation mechanisms are analyzed as stabilizing since it leads to the decrease in the pore openings at the crust top surface and the reduction in the local evaporation flux via the Kelvin effect.

V.2. Introduction

Salt crusts are frequently observed at the soil surface or at the surface of building walls and many elements of our cultural heritage, such as frescos or wall paintings for example. It has been reported that the formation of a salt crust could have a great impact on the evaporation rate [1]. The latter can be reduced by more than one order of magnitude compared to the situation in the absence of crust. Also, it has been reported that puzzling phenomena could take place in the crust [2]. The latter notably include the formation of an air gap under the crust, i.e. the between the crust and the underlying porous medium [2]. Also, the shape of the crust seen from above can be relatively homogeneous under certain circumstances and much more heterogeneous under other circumstances with the formations of local bumps for instance. A major issue in this context is to explain the formation of the air gap and the various shapes, such as for example the domes mentioned in the literature [3], visible at the surface of salt crusts. Since the crusts can be submitted to relatively harsh conditions, such as high temperature variations and intense solar radiations, it is tempting to consider that the evolution of the crust at the surface of a soil is due to mechanical effects such as the generation of a gas pressure or thermal contraction and expansion effects for instance. Although these effects might play a role under field conditions, it has been shown that significant crust displacements could be induced under isothermal conditions as a result of dissolution (deliquescence) – precipitation phenomena [4, 5]. In the latter references, dissolution took place at the crust bottom surface as the result of water vapor absorption

whereas precipitation occurred at the top surface exposed to evaporation. The ions forming at the crust bottom as a result of the dissolution process were transported upward through the crust pore network to the evaporative surface where they precipitated. More precisely, it was shown in [4] that this dissolution-precipitation mechanism could lead to the upward migration of a salt crust whereas it was shown in [5] that this mechanism could also explain the formation of an air gap, i.e. the detachment of the crust from the surface of the underlying porous medium and that this mechanism was comparable with the very low evaporation rates often associated with the crust presence. However, the crust displacements reported and analyzed in [4, 5] were relatively compact, i.e. without very significant deformations of the crust top and bottom surfaces. In the present study, we report an experiment in which the shape of the crust strongly varies from a relatively compact crust to a branched structure. To identify the factor controlling the destabilization, two additional experiments have been performed so as to explore the impact of the ratio between the evaporation rate on top of the crust and the water absorption rate at its bottom.

The paper is organized as follows. In Sec. II the experimental set-up is briefly described. Main results are presented in Sec. III. Conclusions are drawn in Sec. IV.

V.3. Experiment

The experimental set-up is similar to the ones presented in [4, 5] and is sketched in Fig.1. A salt crust is suspended in a Hele-Shaw cell. As described in [4], the procedure to obtain a suspended crust is as follows. The Hele-Shaw is filled with glass beads (1-50 μm in diameter) up to a certain level, saturated with a NaCl aqueous solution (of salt mass fraction equal to 25%) and submitted to evaporation. As a result of evaporation a salt crust forms within the Hele-Shaw cell on top of the beads. After some time, the beads are gently removed from the Hele-Shaw cell and a suspended layer is obtained. As detailed in [5], this layer is actually a composite system formed by the assembly of two layers. The top layer is essentially formed by NaCl crystals whereas the bottom layer is a mixture of glass beads and NaCl crystals. Note that both layers are porous. Then liquid water is introduced at the bottom of the cell and the cell is exposed again to evaporation. As analyzed in [5], this leads to the upward migration of the NaCl up to the detachment of an essentially crystalline layer from the remaining glass bead layer. Then the remaining glass beads are again removed from the Hele-Shaw cell, which therefore now contains a salt crust, i.e. a porous layer whose matrix is essentially formed by NaCl crystals (a few small beads can, however, be still trapped in this layer). Such a salt crust is visible in Fig.1. Liquid water was injected at the cell bottom and the cell containing the salt crust and liquid water in the region below the crust was exposed to evaporation. The parameter which was varied was the distance between the initial liquid water level in the cell and the crust bottom surface. The experiment started with the water level set at 6mm from the crust bottom surface and was run for a little bit more than 4 days. This corresponds to the experiment referred to as the “6 mm first experiment”. Then, the liquid level was raised again at a distance of 6mm from the crust bottom surface and the experiment was run for a little bit more than 2 days. This corresponds to the experiment referred to as the “6 mm second experiment”. Then, the liquid level was raised at a distance of 3 mm from the crust bottom surface and the experiment was run during 18 days. This corresponds to the experiment referred to as the “3 mm experiment”.

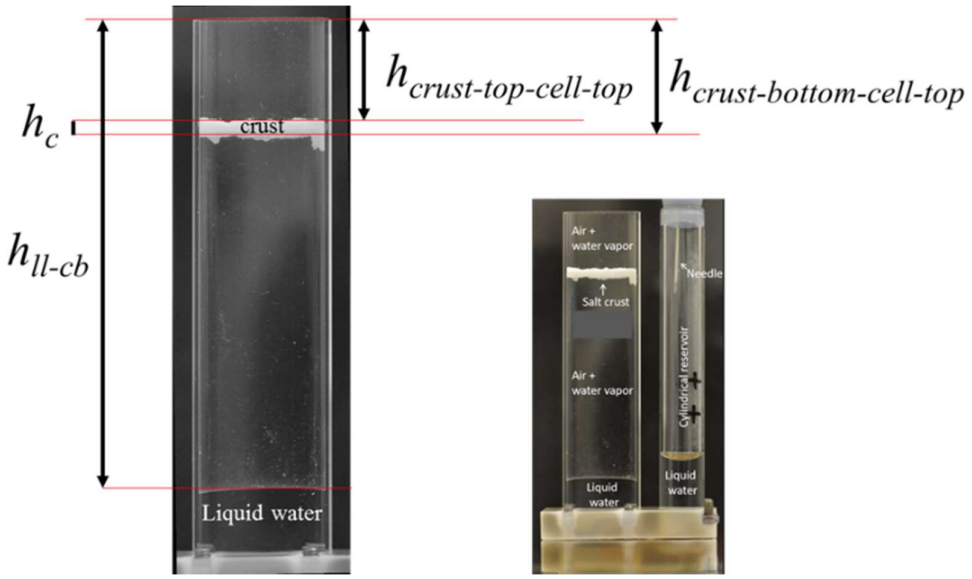


FIG.1. Experimental set-up and distance definition. A crust is suspended in a Hele-Shaw cell. Liquid water is injected at the cell bottom whereas the cell is open at the top to a relatively dry air, which induces evaporation. As shown in the image on the right, the cell is connected to a cylinder containing liquid water. In the considered experiments, the liquid level in the cell is much closer to the crust bottom surface than illustrated here.

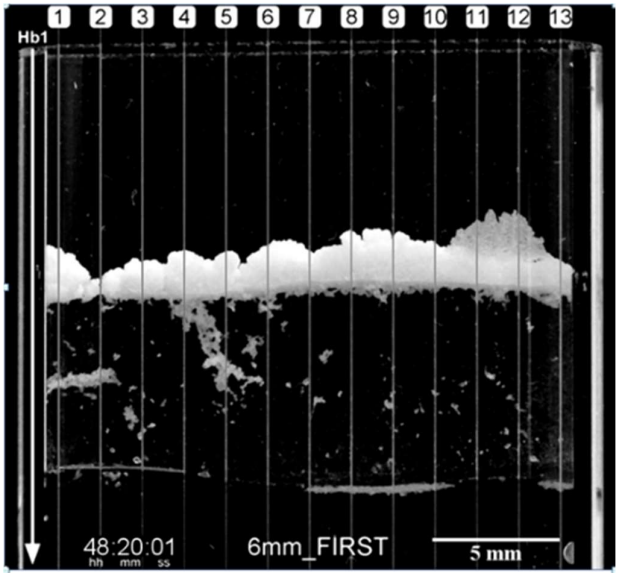


FIG.2. The vertical pixel lines used to determine the distances and crust thickness indicated in Fig.1. Some parasitic wall creeping is visible in this example (top crust - lines 11 and 12).

The following data were obtained with this set-up: the mass of the set-up was measured every 100 s, the relative humidity and temperature in the enclosure inside which the experimental set-up was were measured every 1000s, images of the set-up (such as the ones depicted in Fig.1) were taken every 1000 s. Then image processing techniques were used to obtained the distances and crust thickness indicated in Fig.1. The distance measurements

were typically averages over the 13 lines of pixels depicted in Fig.2. The lines affected by the wall creeping phenomenon (as illustrated in Fig.2) was excluded from the evaluation of the distance between the crust top surface and the cell top. A similar set of vertical pixel lines was considered to determine the liquid water level in the adjacent cylinder.

V.4. Results

V.4.1. Images

The evolution of the salt crust in the three experiments is compared in Fig.3. As expected from previous works [4, 5], the crust moves upward in the cell. The most striking feature is the change in the crust shape obtained in the 3 mm experiment. Contrary to the two other experiments where the crust shape remains relatively compact, significant change in the crust shape can be observed in the 3 mm experiment. Thick salt fingers develop during the upward displacement of the crust and a branched morphology is eventually obtained. It can be observed that the bottom surface of the crust in the 3 mm experiment remains relatively flat. The fingering phenomenon thus essentially affects the top region of the crust. Also, the images in Fig.3 show that the fingering phenomenon eventually stops after a while. This can be seen by comparing “the last image” and the very last image taken about 8 days after the “last image”, the cell continues to lose mass (as can be seen from the position of the liquid water level in the cell) whereas no significant change in the crust branched morphology is observed.

Additional phenomena can be also seen in Fig.3. In the case of the 6 mm first experiment, the crust in the middle image is less compact and a destabilization process of the crust top surface seems to have started. However, contrary to the 3 mm experiment, the final shape is compact. In other words, the fingering phenomenon could not eventually develop in this case in spite of the tendency of destabilization that can be seen in the middle image. A somewhat similar trend can be seen with the 6 mm second experiment. The crust top surface in the middle image is “rougher” than in the first and last pictures.

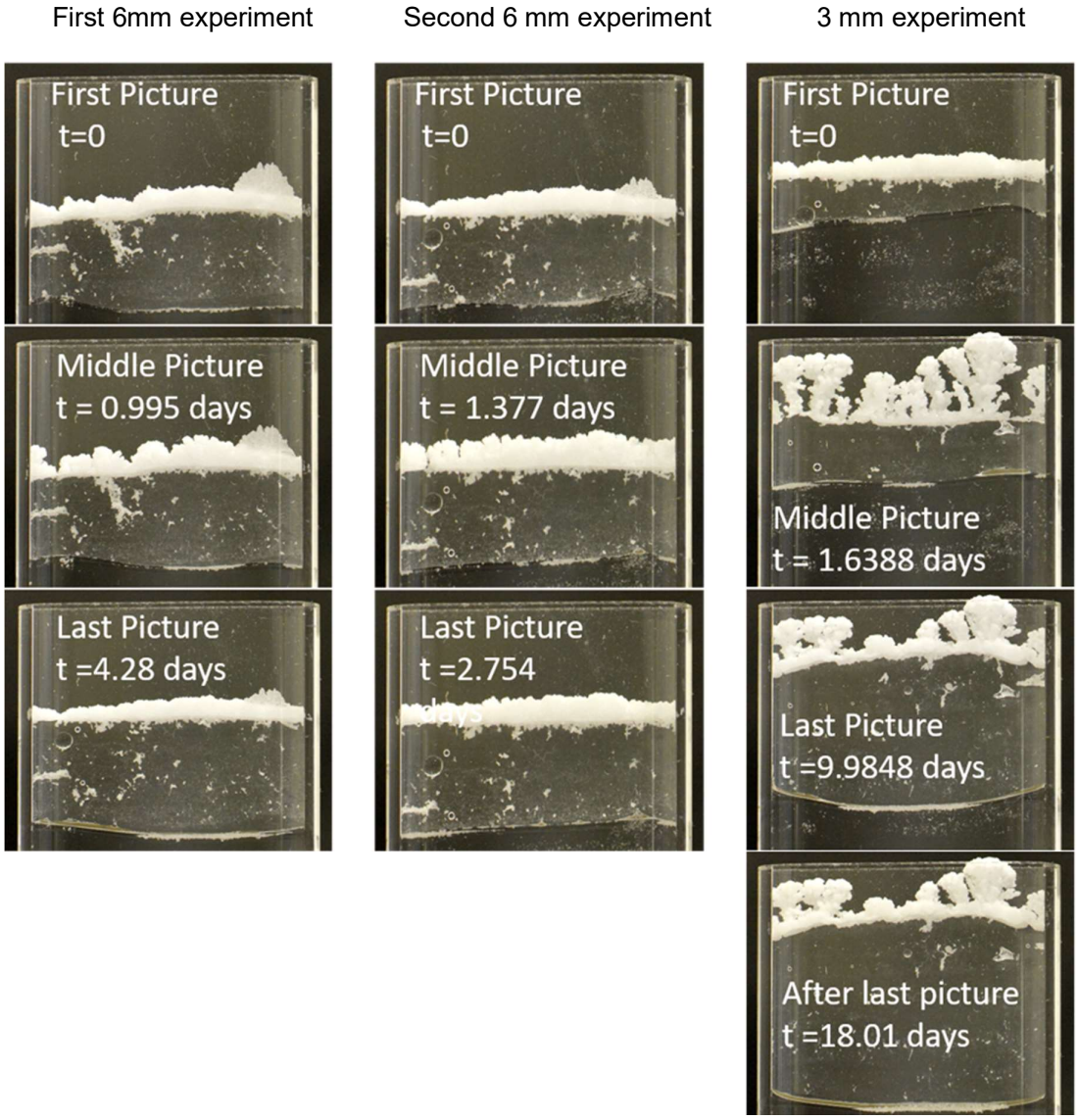


FIG.3. Images of the salt crust in the Hele-Shaw cell for the three experiments. The first image is the image at the beginning of the experiment; the "last" image is the image when the experiment was stopped or when the shape of the crust stopped changing (3 mm experiment).

A more detailed sequence of images is presented in Fig.4 for each experiment. Although relatively minor in the case of the 6mm second experiment, the change in the top crust surface morphology is visible for the 6mm first and second experiments. The images for the 3 mm experiment illustrate that the destabilization, i.e. the transition from compact to branched morphology occurs over a relatively short period of about 1.6 day. Then the crust top surface does not change anymore over the longer period that follows (about 8 days). In this period, the change in the crust morphology takes place mainly in the region of the upwardly moving crust bottom surface. As mentioned previously, no significant change in the crust morphology is visible in the last period of about 8 days, whereas the evaporation process continues as indicated by the downward displacement of the liquid water in the cell. It can be also noted again that the crust bottom surface is flat in the three experiments.

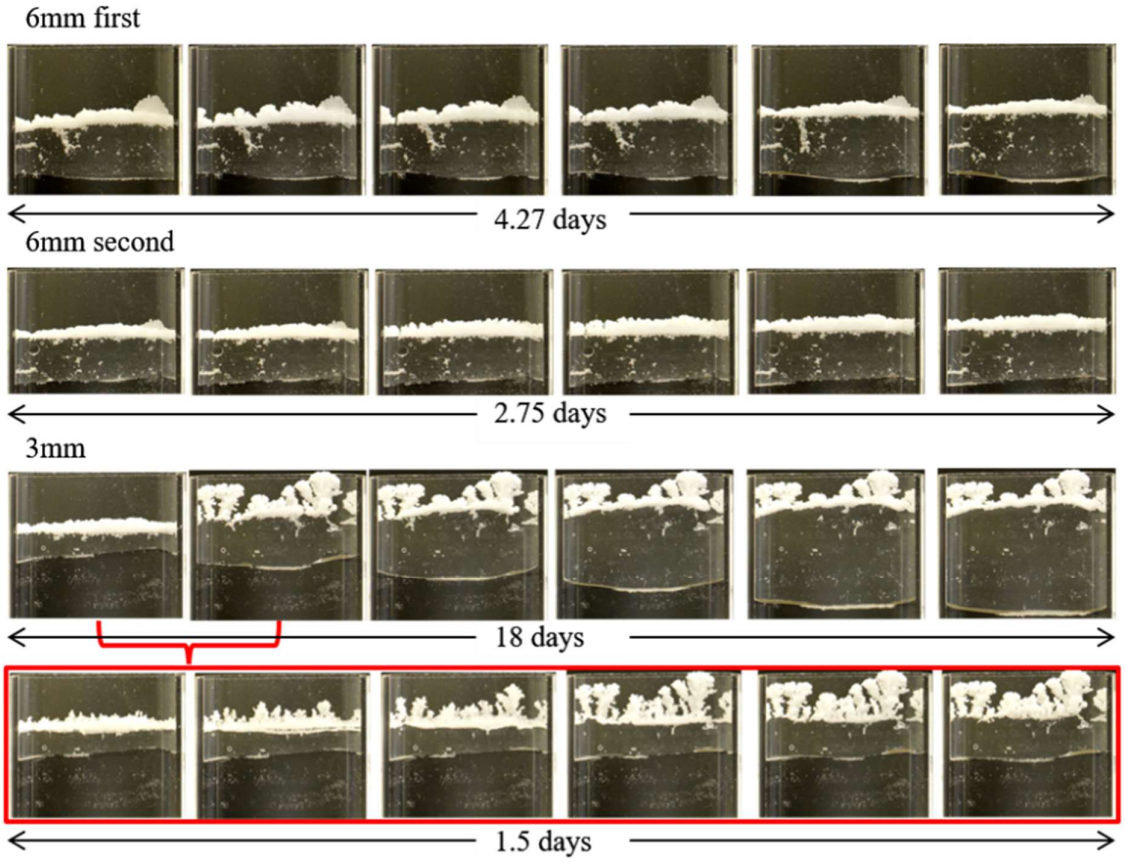


FIG.4. Images of the salt crust in the Hele-Shaw cell for the three experiments.

As discussed in detail in the related previous works [4, 5], the upward displacement of the crust results from a dissolution – precipitation process. The relative humidity at the surface of pure water is 1 whereas the relative humidity at the surface of a NaCl saturated solution is 0.75. This difference induces a water vapor transport by diffusion between the top surface of the liquid water region in the cell and the crust bottom surface. In other words, the crust absorbs water at its bottom surface leading to crystal dissolution. The ions forming as a result of the dissolution process are transported upward through the crust pore network considered as fully saturated by a NaCl solution (in which the ion concentration is the solubility except in the crust top region where the ion concentration is slightly greater than the solubility and in the crust bottom region where the concentration is slightly less than the solubility [4]). As a result of the precipitation on top of the crust where evaporation occurs, a new layer of crystal forms on top of the crust whereas older crystals dissolve at the crust bottom at the same time. Accordingly, it is our belief that the crust top surface morphology change shown in Fig.3 and Fig.4 are due to a combination of precipitation – dissolution mechanisms.

V.4.2. Crust thickness

The evolution of the crust thickness, determined as explained in section II, is plotted in Fig.5 for the three experiments

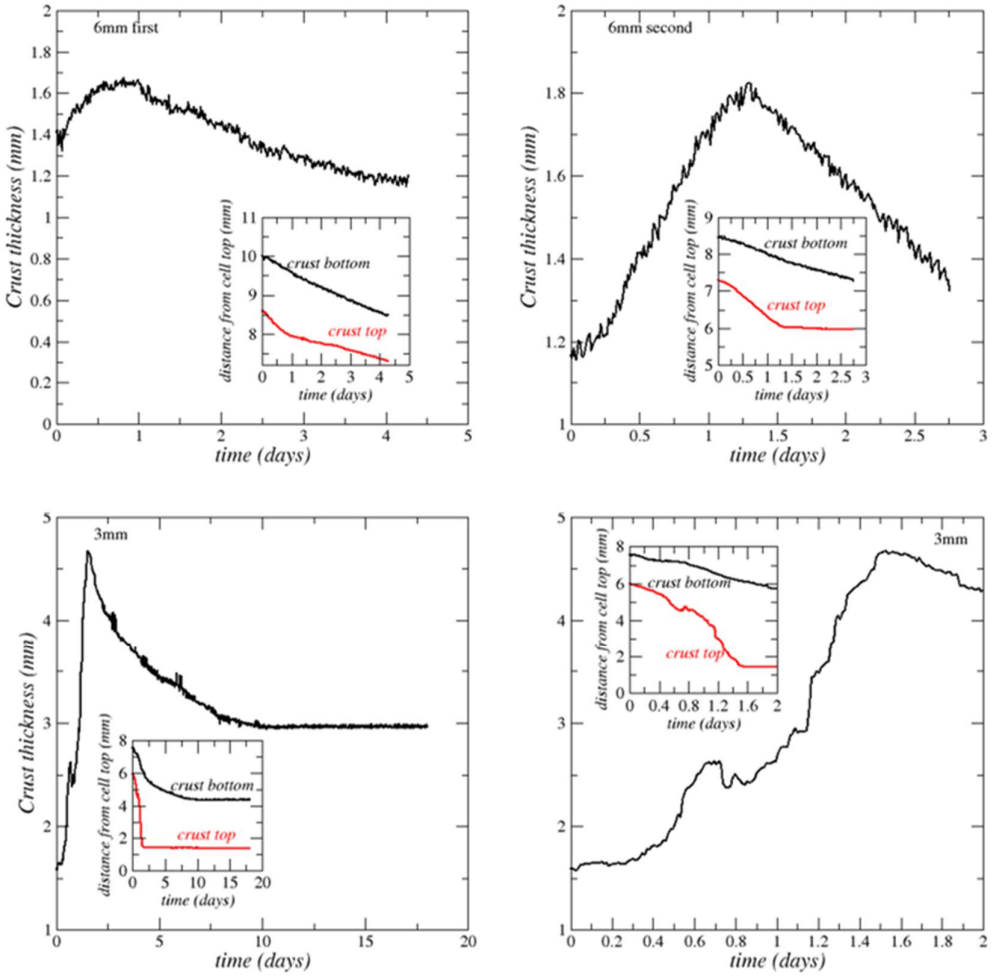


FIG.5. Variation of crust thickness as a function of time for the three experiments. The inset shows the variation of salt crust top and bottom surfaces position in the Hele-Shaw cell as a function of time. The image on the bottom right is a zoom for the 3mm experiment over the first two days.

First, consistently with the images, it can be seen that the crust thickness variation is less for the 6 mm experiments compared to the 3 mm experiment, noting that the period duration over which the crust thickness increases is comparable in the three experiments (1-1.6 days). Second, it can be seen that the crust thickness first increases, then reaches a maximum and then decreases in the three experiments. As reported in Table 1 and visible in Fig. 3, the upward displacement of the crust bottom and top surfaces is significantly greater (~3 – 5mm) in the 3 mm experiment compared to the 6mm experiments (~1-1.5 mm).

For instance, the crust thickness increases between the first image and the intermediate image in the 6 mm experiments and then decreases between the intermediate image and the last image so that the crust thickness in the last image and the first image is roughly comparable.

TABLE 1. Crust maximum and minimum thickness and crust displacement amplitude for the three experiments.

Experiment	6mm first	6mm second	3mm
Crust top surface total upward displacement (mm)	1.29	1.34	4.57
Crust bottom surface total upward displacement (mm)	1.49	1.18	3.24
Crust maximum thickness (mm)	1.676	1.82	4.67
Crust thickness at t =0 (mm)	1.41	1.17	1.58
Crust minimum thickness (mm)	1.20	1.17	1.58

Also, it can be seen from Fig. 5 that the crust thickness increase corresponds to a faster displacement of the crust top surface compared to its bottom surface in the three experiments whereas the decrease in the crust thickness after the maximum thickness is reached corresponds to a displacement of the bottom surface faster than the top surface displacement. The latter is actually immobile (or moving very slowly) in the corresponding period in the 6mm second and 3mm experiments. In the case of the 3mm experiment, there is neither further crust displacement nor noticeable change in the crust thickness after day 10 consistently with the images.

V.4.3. Absorption rate –Evaporation rate

Based on our previous works, i.e. [4, 5], the water absorption rate at the crust bottom and the evaporation rate at the crust top are expected to be key factors in the crust dynamics. Absorption refers to the water mass transfer rate between the liquid water at the cell bottom and the crust bottom surface. The transport between the two surfaces in the cell is by diffusion in the gaseous region separating the two surfaces under consideration. From Fick's law, the absorption rate is expressed as

$$J_{abs.Fick} = A\, D_v \frac{M_v}{RT} p_{vsat} \frac{(1.-0.75)}{h_{ll-cb}} \quad (1)$$

where A is the cell cross-section surface area (A = 0.004 m^2), D_v is the binary diffusion coefficient of the vapor in gas phase, R is the universal gas constant, M_v is the vapor molecular weight, h_{ll-cb} is the distance between the liquid water in the cell and crust bottom surface (Fig.1), p_{vsat} is the saturation vapor pressure. Note that 0.75 in Eq. (1) corresponds to the activity of a NaCl saturated aqueous solution, which is the situation assumed at the crust bottom, "1." corresponds to the activity of pure water (at the top of the liquid region). h_{ll-} is obtained from the cell pictures by image processing as briefly indicated in Sect. II.

The mass transfer rate between the cell bottom liquid zone and the crust bottom surface must also correspond to the variations in the liquid levels and the adjacent cylinder (Fig.1). The correspond mass of liquid is expressed as

$$m_{level} = \rho(Ah_{llcel} + A_{cyl}h_{llcyl.}) \tag{2}$$

where ρ is the liquid water density, h_{llcel} is the height of the liquid water region in the cell, A_{cyl} is the adjacent cylinder cross section surface area (A_{cyl} = 7.7 × 10^{-5} m^2), $h_{llcyl.}$ is the height of the liquid water region in the cylinder. The absorption rate should correspond to

$$J_{abs.level} = \frac{dm_{level}}{dt} = \rho\left(A\frac{dh_{llcel}}{dt} + A_{cyl}\frac{dh_{llcyl.}}{dt}\right) \tag{3}$$

Here two main techniques are generally considered to determine $\frac{dh_{llcel}}{dt}$ and $\frac{dh_{llcyl.}}{dt}$ from the discrete data h_{llcel} and $h_{llcyl.}$(h_{llcel} and $h_{llcyl.}$ are obtained every 1000s ($\Delta t = 1000\ s$) from the pictures by image processing). A first option is to proceed by curve fitting on the plots of h_{llcel} and $h_{llcyl.}$ as a function of time and to derive the obtained (polynomial) fits with respect to time. A second option is to compute $\frac{dh_{llcel}}{dt}$ and $\frac{dh_{llcyl.}}{dt}$ from a simple finite difference,

$$\frac{dh_{llcel}}{dt} \approx \frac{h_{llcel}(t+\Delta t) - h_{llcel}(t)}{\Delta t} \tag{4}$$

and similar an expression for $\frac{dh_{llcyl.}}{dt}$. Tests have shown that both methods lead to comparable results. For this reason, only the results with the finite difference method are presented. The results obtained with this method are shown in Fig.6. The results obtained from Eq. (3) and Eq.(4) are shown in grey and indicated as “Absorption-1”. As can be seen, these results are noisy, which is usual in this type of approach. To smooth out the results and obtained more representative results, running averages of the Absorption-1 data were performed. For instance, the curve labelled “Average-10” in the figures corresponds to arithmetic averages over 10 successive points of the Absorption-1 data set:

$$J_{abs.level-10}(t + 0.5(10-1)\Delta t) = \frac{1}{10}\sum_{i=1}^{i=10} J_{abs.level-1}(t + i\Delta t) \tag{5}$$

The results obtained from Eq. (1) are also shown in Fig.5. As can be seen a fair agreement is generally obtained between the prediction obtained from Fick’s law (Eq. (1)) and the finite difference approach. However, one can observe that the Fick’s law approach predicts a slightly lower absorption rate than the one obtained from the finite difference approach in the case of the 6 mm second experiment. As illustrated in Fig.7, some droplets and glass bead clusters are present in the cell region between the liquid water at the bottom and the crust. This should slightly enhance the water vapor transport between the liquid water at the bottom and the crust compared to the diffusive transport in a purely gaseous region.

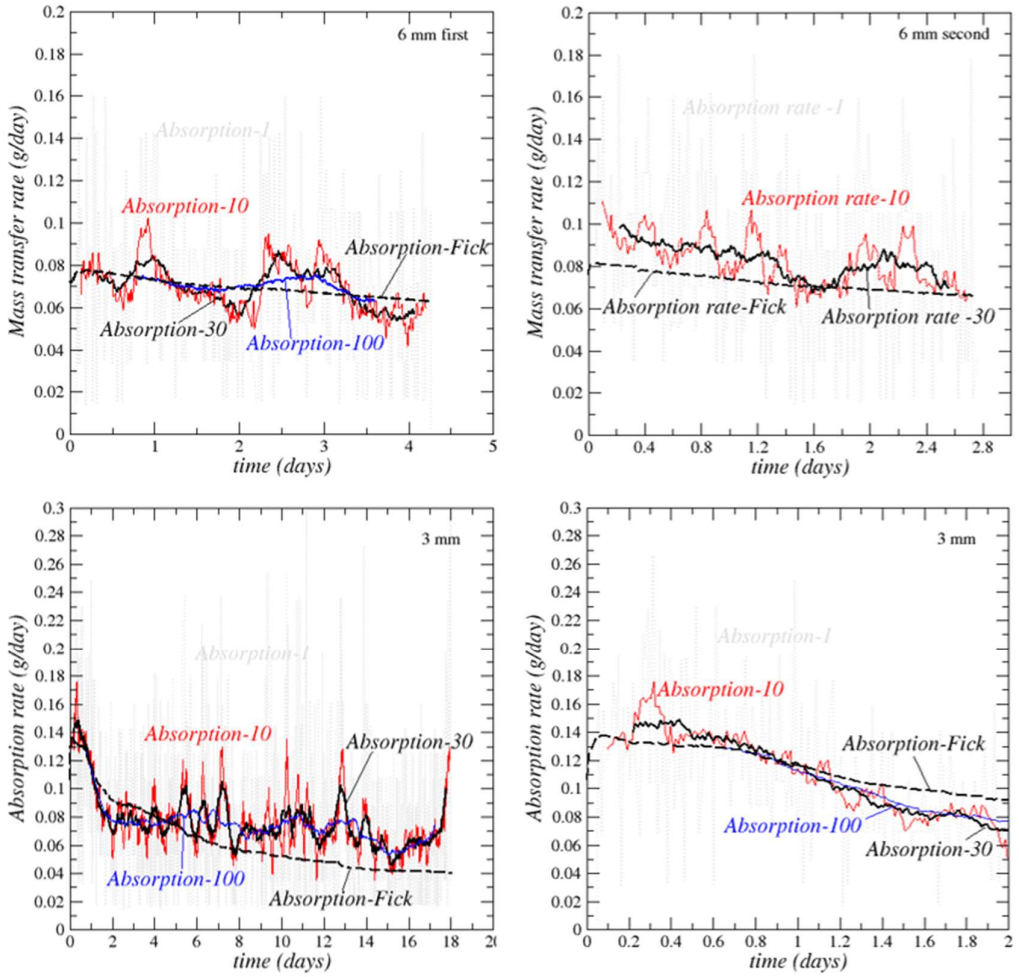


FIG.6. Evolution of absorption rate for the three experiments. Absorption-1 corresponds to the absorption rate determined from a simple first order finite difference scheme whereas Absorption-10 (30 and 100) corresponds to the curves obtained by running averages (see text). The dashed line corresponds to the results from Eq. (1) (Fick's law). The figure on the bottom right is a zoom for the 3mm experiment over the first two days.

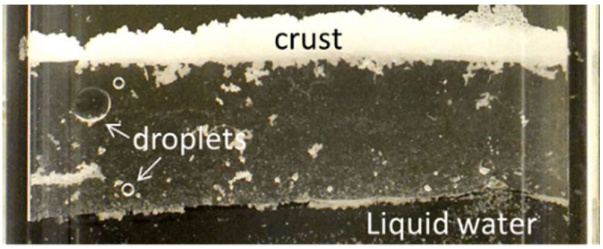


FIG.7. 6mm second experiment. Detailed view of the mainly gaseous region separating the liquid region at the cell bottom and the crust. Droplets and glass bead clusters are visible in this region.

Like the absorption rate, the evaporation rate can be determined using Fick's law and from a finite difference scheme. In the case of the evaporation rate, the finite difference scheme is applied to the measured mass data ($m_{weighting}$),

$$J_{evap-mas} = -\frac{dm_{weighting}}{dt} \approx -\frac{(m_{weighting}(t+\Delta t) - m_{weightin}(t))}{\Delta t} \quad (6)$$

Note that here Δt = 100 s since the mass is measured every 100 s, thus with a time step 10 times shorter than for the images.

The evaporation rate is estimated from Fick's law by combining Eqs. (7) and (8)

$$J_{evap-Fick} = A\, D_v \frac{M_v}{RT} p_{vsat} \frac{(0.75 - RH_{cell-top})}{h_{crust-top-cell-t}} \quad (7)$$

$$J_{evap-Fick} = A\, D_v \frac{M_v}{RT} p_{vsat} \frac{(RH_{cell-top} - R_{inf})}{\delta} \quad (8)$$

Eq.(7) corresponds to the water vapor diffusive transport between the crust top surface (where the solution is assumed to be at saturation, hence the value 0.75 in Eq.(7)) and the cell top where the relative humidity is denoted by $RH_{cell-top}$. In Eq.(7), $h_{crust-top-cell-top}$ is the distance between the crust top surface and the cell top (Fig.1). Eq. (8) corresponds to the water vapor diffusive transport between the cell top and the binary gas (air + water vapor) in the enclosure in which the cell is set. The relative humidity in the enclosure is measured (Fig.8) and denoted by RH_{inf}. The mass transfer at the cell top is obviously three-dimensional. A simplified approach consists in introducing a mass transfer coefficient at the cell top. In Eq.(8), the mass transfer coefficient is expressed as the equivalent thickness δ of an additional layer of cross-section area A.

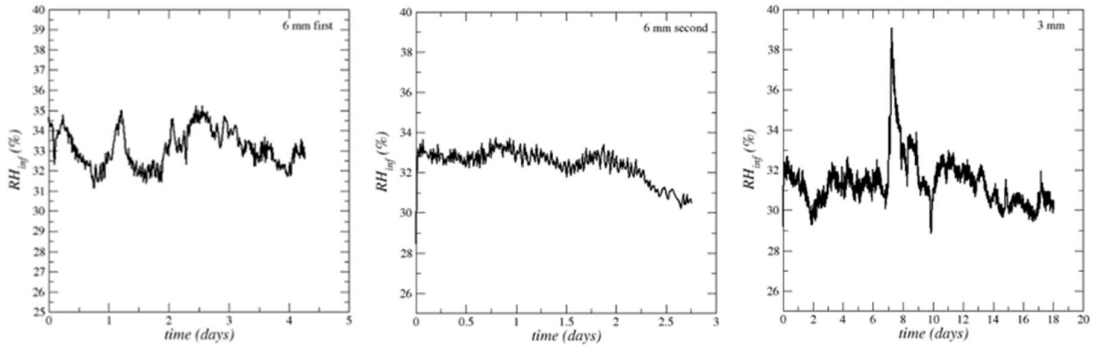


FIG. 8. Measured relative humidity in the enclosure for the three experiments.

Combining Eqs.(8) and (9) leads to express the evaporation rate as

$$J_{evap-Fick} = A\, D_v \frac{M_v}{RT} p_{vsat} \frac{(0.75 - R_{inf})}{(h_{crust-top-cell-top} + \delta)} \quad (9)$$

To make use of Eq.(9), δ must be identified. From comparison with $J_{evap-mass}$ in the first period of each experiment when the crust thickness is increasing (Fig.5), it was found that δ = 3 mm led to consistent results. This value is consistent with the value for tubes [6] indicating that δ is on the order of the tube aperture (it is recalled that the cell aperture is 2 mm).

The evolution of the evaporation rate is shown in Fig. 9 for the three experiments. As for the absorption rate, the evaporation rate obtained from the simple finite difference scheme (Eq. (6)) is noisy (grey data in Fig.9). Smoother results are again obtained by performing running averages. The procedure is the same as for the absorption rate data.

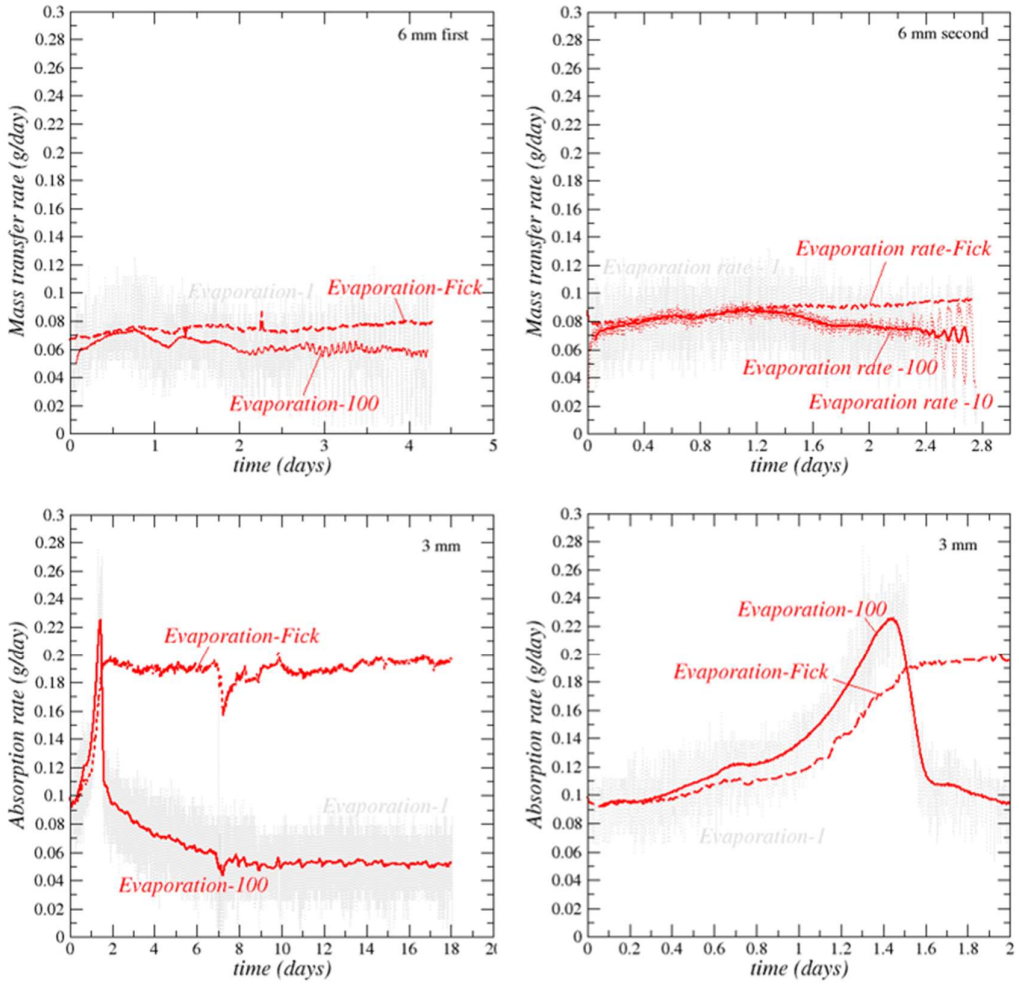


FIG. 9. Evolution of evaporation rate for the three experiments. Evaporation-1 corresponds to the evaporation rate determined from a simple first order finite difference scheme whereas Evaporation-100 (or 10) corresponds to the curves obtained by running averages (see text). The dashed line corresponds to the results from Eq. (9) (Fick's law). The figure on the bottom right is a zoom for the 3mm experiment over the first two days.

Several interesting points can be noticed. First, the evaporation rate determined from Fick's law (Eq. (9)) is as expected in good agreement with the values obtained from the finite difference scheme only in the first period for the three experiments. Then, Eq. (9) (Fick's law) overestimates the evaporation rate. The overestimation is visible for the three experiments but most important for the 3mm experiment. It must be noted that Eq. (9) actually gives the "potential evaporation", i.e. the maximum evaporation rate, since the relative humidity at the crust top surface is assumed to correspond at the equilibrium relative humidity at the surface of a saturated NaCl solution ($RH_{eq.-sat}$ = 0.75). Consequently, the fact that Eq. (9) over predicts the evaporation rate outside the first period is an indication that the effective relative humidity at the top surface of the crust is less than $RH_{eq.-sat}$. This situation can correspond either to the fact that the crust top surface is dry or partially dry or to the fact that the pores are sufficiently small for the Kelvin effect to have an impact [5]. This issue is addressed later in the study. Second, it can be seen that the evaporation rate does not vary very much in the 6 mm experiments whereas a quite significant increase in the evaporation rate occurs over the first 1.5 day in the 3 mm experiment. Then the evaporation rate decreases sharply in a few hours

(between about day 1.4 and day 1.6 in Fig.9 right bottom). The decrease in the evaporation rate is then much less sharp until a long period (between day 10 and the end of the experiment in day 18) is reached where the evaporation is quasi-constant.

V.4.4. Absorption rate – Evaporation rate – Crust-thickness – Crust displacement

The next step consists in comparing the absorption rate and the evaporation rate for the three experiments. This comparison is actually more insightful in relation with the crust thickness variations and the crust top and bottom surfaces displacement. These comparisons are presented in Fig.10 (6mm experiments) and Fig.11 (3mm experiment).

For the three experiments, it can be first noticed that each experiment starts with a period during which the crust thickness increases. Since the crust gains water when $J_{abs} > J_{evap.}$ and loses water when $J_{abs} < J_{evap.}$ a somewhat naïve view would be to consider that the crust thickness should increase when $J_{abs} > J_{evap.}$ and should decrease when $J_{abs} < J_{evap.}$ This simple approach is in agreement with the results reported in Fig.10 for the 6mm second experiment where the time when the crust thickness stops growing approximately coincides with the time when the absorption rate stops being greater than the evaporation rate. It seems that this is also the case for the 6mm first experiment (Fig.10) but the absorption rate is actually too close to the evaporation rate in this experiment for leading to a firm conclusion. By contrast, this simple view is contradicted by the results for the 3mm experiments (Fig.11 right column). For this experiment, the crust thickness growth period can be actually decomposed into two sub-periods. In the first sub-period, the absorption rate is indeed greater than the evaporation rate, i.e. $J_{abs} > J_{evap.}$. However in the second sub-period (between about $t \approx 0.9$ days and $t \approx 1.5$ days) the crust thickness continues growing whereas $J_{abs} < J_{evap.}$ The results reported in [4,5] also correspond to situations where the crust thickness increases when $J_{evap.} > J_{abs.}$ In other words, the information on the ratio $J_{abs}/J_{evap.}$ is not sufficient to predict whether the crust thickness is increasing or decreasing. In order to develop a more refined analysis, one can begin with simple mass conservation considerations. Assuming the crust fully saturated by the solution (all pores in the crust are “liquid”, i.e. fully saturated by the solution) and flat crust top and bottom surfaces, the liquid water mass in the crust can be expressed as

$$m_{water} \approx \int_{z_b}^{z_t} A\varepsilon\rho_\ell(1 - C_{sat})\, dz \tag{10}$$

where ρ_ℓ is the solution density, C_{sat} is the ion (NaCl) mass fraction in the solution assumed everywhere closed to the solubility (C_{sat} =0.264), ε is the crust porosity, z_b is the crust bottom surface position in the cell (assuming a vertical axis z with z directed upward), z_t is the crust top surface position in the cell. Deriving Eq. (10) with respect to time leads to

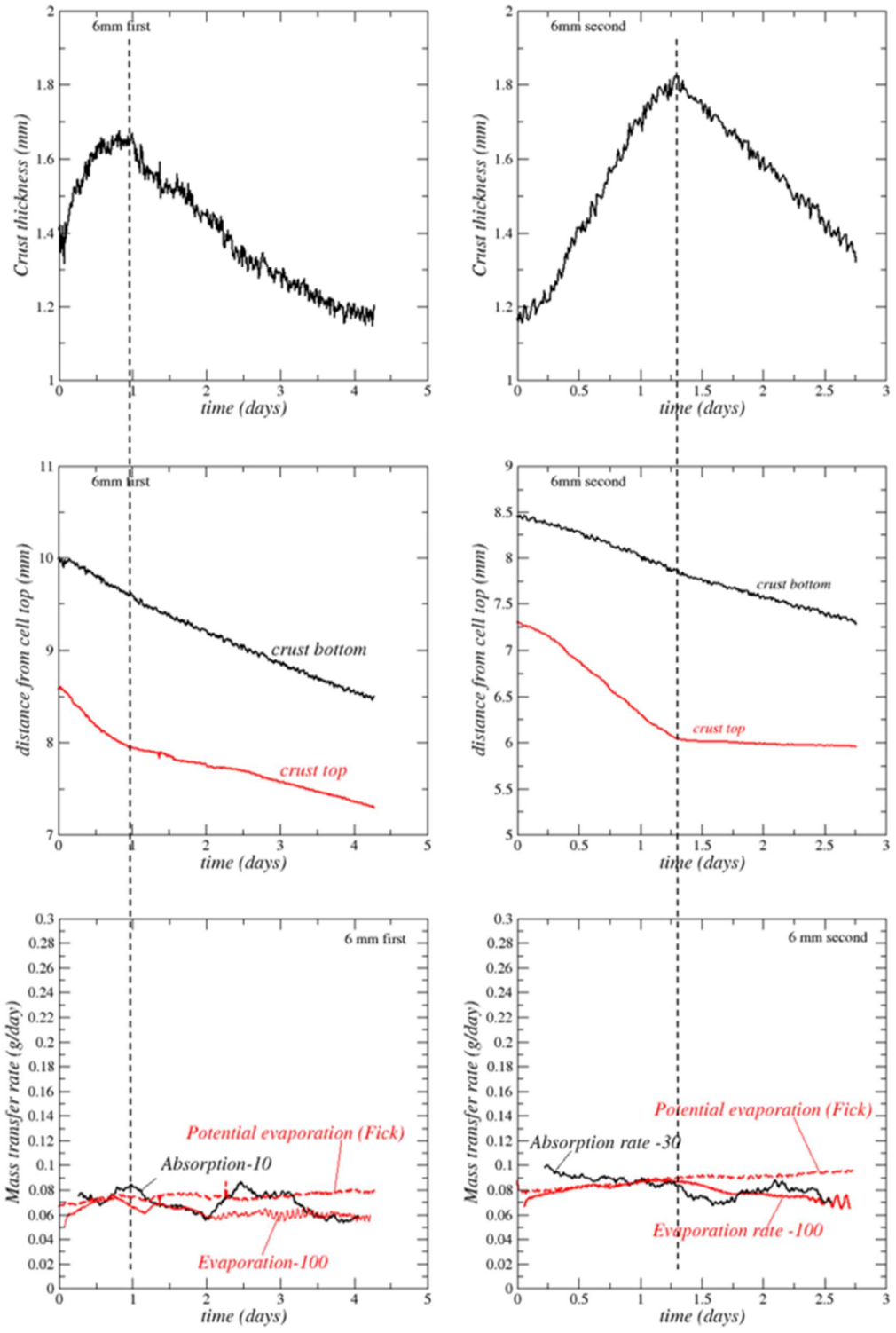


FIG. 10. Evolution of crust thickness, mean positions of crust top and bottom surface, potential evaporation and absorption and evaporation rate for the 6 mm experiments.

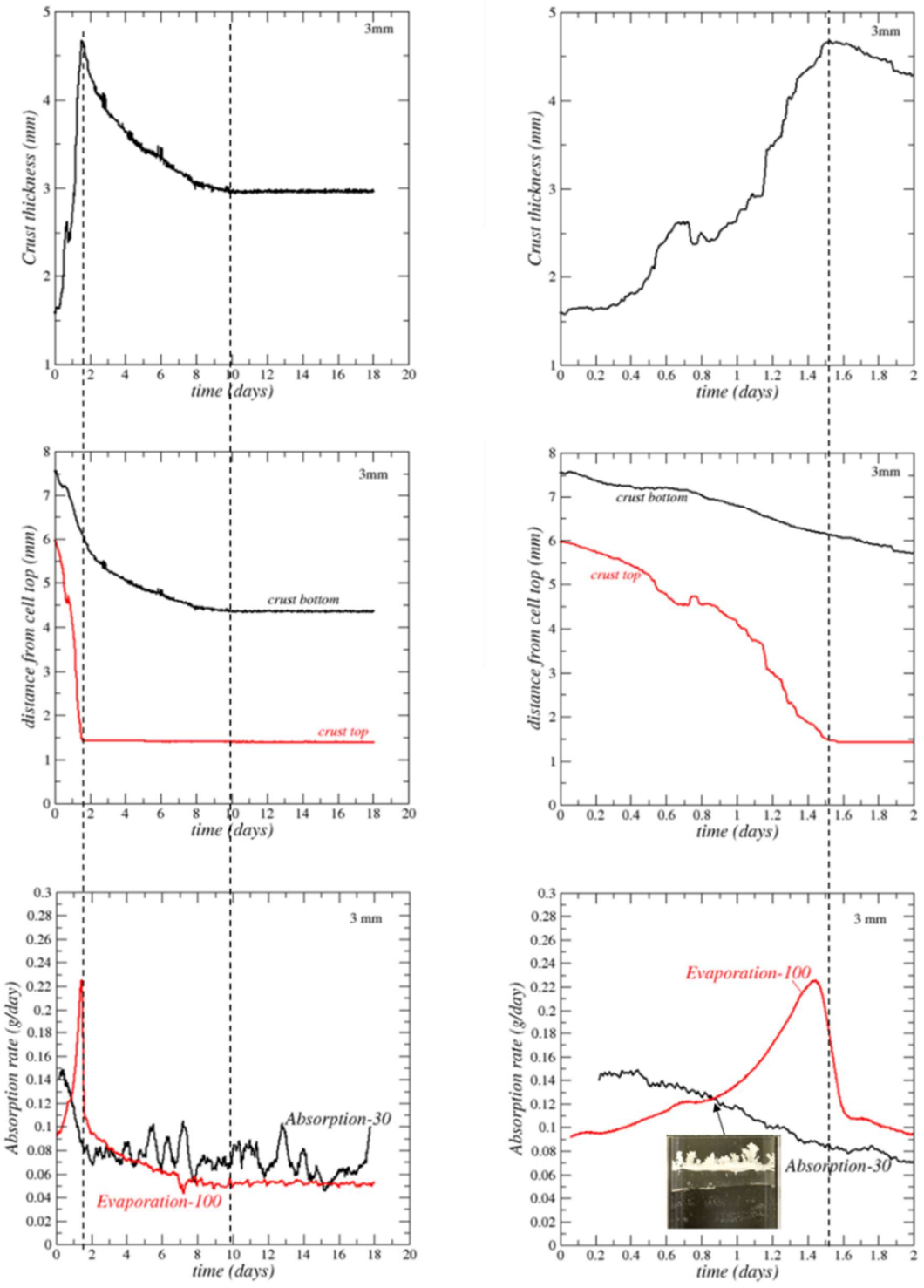


FIG. 11. Evolution of crust thickness, mean positions of crust top and bottom surface, potential evaporation and absorption and evaporation rates for the 3 mm experiment. The figures on the right are a zoom experiment over the first two days of the experiment.

$$\frac{dm_{water}}{dt} \approx A\rho_\ell(1-C_{sat})\left(\int_{z_b}^{z_t}\frac{\partial\varepsilon}{\partial t}dz + \varepsilon(z_t)\frac{dz_t}{dt} - \varepsilon(z_b)\frac{dz_b}{dt}\right) = J_{abs} - J_{evap.} \qquad (11)$$

The total mass of salt in the crust can be expressed as

$$m_{salt} \approx \int_{z_b}^{z_t} A(\varepsilon \rho_\ell C_{sat} + (1-\varepsilon)\rho_{cr})dz \quad (12)$$

where ρ_{cr} is the crystal density (ρ_{cr} = 2163 kg/m^3). The total mass of salt in the crust does not change during the crust displacement. Thus, $\frac{dm_{salt}}{dt} = 0$, which from Eq.(12) leads to

$$\int_{z_b}^{z_t} (\rho_\ell C_{sat} - \rho_{cr}) \frac{\partial \varepsilon}{\partial t} dz + (\rho_{cr} + \varepsilon(z_t)(\rho_\ell C_{sat} - \rho_{cr})) \frac{dz_t}{dt} - (\rho_{cr} + \varepsilon(z_b)(\rho_\ell C_{sat} - \rho_{cr})) \frac{dz_b}{dt} = 0 \quad (14)$$

Combining Eqs. (11) and (14) leads to

$$\frac{dh_c}{dt} = \frac{d(z_t - z_b)}{dt} = \frac{\left(1 - \frac{\rho_\ell C_{sat}}{\rho_{cr}}\right)}{A\rho_\ell(1-C_{sat})} \left(J_{abs} - J_{evap.}\right) \quad (15)$$

Where $h_c = z_t - z_b$ denotes the crust thickness. As can be seen, this simple derivation leads again to the naïve prediction $\frac{dh_c}{dt} \propto \left(J_{abs} - J_{evap.}\right)$, which is not in agreement with all the experimental results as pointed out previously.

The main assumptions leading to Eq. (15) can be summarized as: i) the crust pore space is occupied by an aqueous NaCl solution (no gas phase in the pore space), ii) the ion mass fraction in the crust pore space is everywhere equal to the solubility, iii) the crust top and bottom limiting surfaces are flat. As shown in Fig.11 (right column), the crust top surface is obviously not flat during the crust thickness growth period where $\frac{dh_c}{dt} > 0$ and $J_{abs} < J_{evap.}$ in the 3 mm experiment. However, the situation $\frac{dh_c}{dt} > 0$ together with $J_{abs} < J_{evap.}$, thus in contradiction with Eq.(15), is also observed in the experiments reported in [4] and [5]. Although not perfectly flat, the shape of the crust top surface in these experiments seems to be sufficiently close to a flat surface for considering that assumption "iii" is not the main problem, at least for all experiments where $\frac{dh_c}{dt} > 0$ with $J_{abs} < J_{evap.}$. For this reason, we rather explore the possible shortcomings associated with assumption "i". To this end, we rely on the analysis presented in [4], which leads to the following expression as regards the displacement velocity of the crust top and bottom surfaces,

$$\frac{dz_t}{dt} = \frac{C_{sat} j_{evap.}}{\rho_{cr}(1-\varepsilon_t)(1-C_{sat})} \left[\frac{Da_t}{1+Da_t}\right] \quad (16)$$

$$\frac{dz_b}{dt} = \frac{C_{sat} j_{abs.}}{\rho_{cr}(1-\varepsilon_b)(1-C_{sat})} \left[\frac{Da_b}{1+Da_b}\right] \quad (17)$$

where, $Da = \sqrt{\frac{(1-\varepsilon)^2(1-C_{sat})k_r}{\varepsilon D_s^* a_v}}$ is the Damkhöler number characterizing the competition between the precipitation – dissolution reaction and the diffusive ion transport [4], D_s^* is the effective diffusion of the ions, a_v is the pore wall surface area per unit volume, k_r is the reaction (dissolution or precipitation) coefficient, ε_t and ε_b are the porosity at the crust top and bottom respectively; $j_{evap.}$ and $j_{abs.}$ are the evaporation flux ($j_{evap.} = J_{evap.}/A$, $j_{abs.} = J_{abs.}/A$). Since the crust thickness is simply z_b - z_t , combining Eq.(16) and Eq.(17) leads to,

$$\frac{dh_c}{dt} = \frac{C_{sat} j_{evap.}}{\rho_{cr}(1-\varepsilon_t)(1-C_{sat})} \left[\frac{Da_t}{1+Da_t}\right] - \frac{C_{sat} j_{abs.}}{\rho_{cr}(1-\varepsilon_b)(1-C_{sat})} \left[\frac{Da_b}{1+Da_b}\right] \quad (18)$$

As described in [4], Eq. (18) takes into account the ion mass fraction positive gradient in

the vicinity of the top surface (where the ion mass fraction must be greater than the solubility since precipitation occurs in the crust top surface region) and the ion mass fraction positive gradient in the vicinity of the bottom surface (where the ion mass fraction must be lower than the solubility since dissolution occurs in the crust bottom surface region) (see Fig.5 in [4]). According to Eq. (18), we have

(19)

$$\frac{dh_c}{dt} > 0 \text{ if } \left(\frac{j_{evap.}}{j_{abs.}}\right) > \frac{(1-\varepsilon_t)}{(1-\varepsilon_b)}\left[\frac{Da_b}{Da_t}\right]\left[\frac{1+Da_t}{1+Da_b}\right] \quad (20)$$

$$\frac{dh_c}{dt} < 0 \text{ if } \left(\frac{j_{evap.}}{j_{abs.}}\right) < \frac{(1-\varepsilon_t)}{(1-\varepsilon_b)}\left[\frac{Da_b}{Da_t}\right]\left[\frac{1+Da_t}{1+Da_b}\right] \quad (21)$$

Eqs.(20) and (21) clearly indicate that the increase of the crust thickness as a function of time is not simply controlled by a criterion of the form $\left(\frac{j_{evap.}}{j_{abs.}}\right) > 1$ or $\left(\frac{j_{evap.}}{j_{abs.}}\right) < 1$. Actually, the criterion itself evolves with time, i.e. with the evolution of the crust properties in the top and bottom regions of the crust resulting from the precipitation and dissolution processes occurring in these regions. In other words, Eq.(20) is theoretically compatible with a situation where the ratio $\left(\frac{j_{evap.}}{j_{abs.}}\right)$ evolves from $\left(\frac{j_{evap.}}{j_{abs.}}\right) < 1$ to $\left(\frac{j_{evap.}}{j_{abs.}}\right) > 1$ with $\frac{dh_c}{dt}$ staying positive ($\frac{dh_c}{dt} > 0$) as this is the case during the crust thickness growth period in the 3mm experiment. Substituting the expression of the Damkhöler number in Eq. (20) one obtains

$$\frac{dh_c}{dt} > 0 \text{ if } \left(\frac{j_{evap.}}{j_{abs.}}\right) > \sqrt{\frac{\varepsilon_t D^*_{st} a_{vt}}{\varepsilon_b D^*_{sb} a_{vb}}}\left[\frac{1+\sqrt{\frac{(1-\varepsilon_t)^2(1-C_{sat})k_r}{\varepsilon_t D^*_{st} a_{vt}}}}{1+\sqrt{\frac{(1-\varepsilon_b)^2(1-C_{sat})k_r}{\varepsilon_b D^*_{sb} a_{vb}}}}\right] \quad (22)$$

As discussed in [4], how the specific surface area a_v and the effective diffusion coefficient D_S^* vary with the crust porosity is not documented in the literature. As in [4], classical expressions for random packings of particles are used, namely $a_v = \frac{3(1-\varepsilon)}{r}$ where r is a "grain" size and $D_S^*/D_s = \varepsilon^{0.4}$ where D_s is the molecular diffusion of ions in solution ($D_s \approx 1.3 \times 10^{-9}$ m^2/s). This leads to express Eq. (22) as

$$\frac{dh_c}{dt} > 0 \text{ if } \left(\frac{j_{evap.}}{j_{abs.}}\right) > \left(\frac{\varepsilon_t}{\varepsilon_b}\right)^{0.7} \sqrt{\frac{(1-\varepsilon_t)}{(1-\varepsilon_b)}}\left[\frac{1+\sqrt{\frac{(1-\varepsilon_t)^2(1-C_{sat})rk_r}{3{\varepsilon_t}^{1.4}D(1-\varepsilon_t)}}}{1+\sqrt{\frac{(1-\varepsilon_b)^2(1-C_{sat})rk_r}{3{\varepsilon_b}^{1.4}D(1-\varepsilon_b)}}}\right] \quad (23)$$

The expression $\left(\frac{\varepsilon_t}{\varepsilon_b}\right)^{0.7} \sqrt{\frac{(1-\varepsilon_t)}{(1-\varepsilon_b)}}\left[\frac{1+\sqrt{\frac{(1-\varepsilon_t)^2(1-C_{sat})rk_r}{3{\varepsilon_t}^{1.4}D(1-\varepsilon_t)}}}{1+\sqrt{\frac{(1-\varepsilon_b)^2(1-C_{sat})rk_r}{3{\varepsilon_b}^{1.4}D(1-\varepsilon_b)}}}\right]$ is referred to as the evaporation rate / absorption rate ratio threshold and is denoted by $R_{evap.-abs-th}$. Assuming $r \approx 1$ μ, i.e. on the same order of magnitude as in [4], $R_{evap.-abs-th}$ is plotted as a function of ε_t for three values of ε_b in Fig.12.

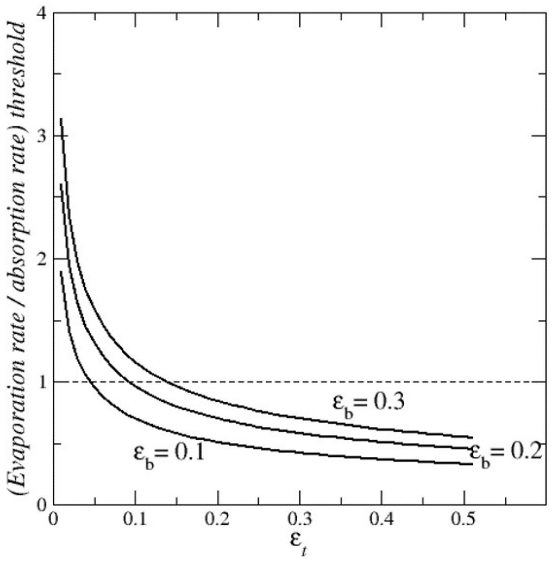


FIG. 12. Variation of evaporation rate / absorption rate ratio threshold controlling the crust thickness expansion as a function of crust top region porosity for three different values of the crust bottom porosity according to Eq. (23).

As can be seen from Fig.12, $R_{evap.-abs-th}$ varies with the porosities of the crust top and bottom regions. Consistently with the experimental results (Fig.10 right column and Fig.11 right column), the crust thickness can increase when $J_{abs} > J_{evap.}$ as well as for $J_{abs} < J_{evap.}$ depending on the values of the crust top and bottom region porosities. For instance, the fact that the crust thickness continues to increase for a while in the 3mm experiment after the period when $J_{abs} > J_{evap.}$ could be explained as follows according to the results plotted in Fig.12. Since the 3 mm experiment starts with the crust obtained at the end of the 6mm second experiment, i.e. after a period in which the crust becomes more compact and the evaporation rate and absorption rate are comparable and less than the potential evaporation (Fig.10 right column), it can be assumed that the situation at the beginning of the 3mm experiment is a relatively homogeneous crust of relatively low porosity. For illustration purposes, one can for instance consider the point $\varepsilon_b = \varepsilon_t$ = 0.1 in Fig.12 as the situation at the beginning of the 3mm experiment. This point corresponds $R_{evap.-abs-th}$ < 1 consistently with the experimental observation that $J_{abs} > J_{evap.}$ ($\frac{J_{evap.}}{J_{abs}} \approx 0.6$ at the beginning of the 3mm experiment). Since the evaporation rate is comparable to the potential evaporation at the beginning of the experiment whereas it is lower than the potential evaporation at the end of the 6mm second experiment, it is surmised some rapid pore declogging occurs when the liquid level is rise at the beginning of the 3mm experiment. Then, it is expected that ε_t decreases with time as the result of the precipitation process occurring in the crust top region whereas ε_b would tend to increase as the result of the dissolution process taking place in the crust bottom region. This porosity evolution would result in the increase in $R_{evap.-abs-th}$ up to values greater than one as shown in Fig.12 compatible with evolution of the ratio $\frac{J_{evap.}}{J_{abs}}$ depicted in Fig.11 (right bottom).

In summary the crust thickness can increase for both the cases when $\frac{J_{evap.}}{J_{abs}} < 1$ and when $\frac{J_{evap.}}{J_{abs}} > 1$ depending on the porosity distribution in the crust.

The next step is to explain why the crust thickness decreases after the first period of

continuous growth in each experiment. According to Eq. (21), the crust thickness contraction is expected when

$$\left(\frac{j_{evap.}}{j_{abs.}}\right) < R_{evap.-abs-} \tag{24}$$

Since the porosity is expected to continuously decrease at the crust top surface as the result of the precipitation process, $R_{evap.-abs-}$ is expected to continue increasing according to the results shown in Fig.12. It would increase to the point when Eq. (23) is verified, which would correspond to the transition between the crust expansion period and the crust shrinkage period.

This evolution of the porosity is also consistent with the relatively sudden decrease in the evaporation rate a little bit after the crust thickness peak in Fig.11 (right column). The porosity decrease at the surface should correspond to a decrease in the average pore opening at the surface. As discussed in [5], the Kelvin effect is expected to explain the reduction in the evaporation rate when the surface pore opening becomes sufficiently low, typically below 100 nm for the Kelvin effect to have an impact on the equilibrium vapor pressure at the top surface. This particular point is addressed in more details in the next subsection.

V.4.5. Evaporation rate, Kelvin effect

As shown in Fig.10, the evaporation rate is lower than the potential evaporation rate over a significant period in each experiment. For the particular experiment analyzed in [5], it was shown that assuming the crust fully wet, i.e. saturated by the solution, and considering the Kelvin effect, i.e. the existence of small pore openings at the surface in the sub-micrometer range, was consistent with the available data for explaining the evaporation rate lower than the potential evaporation. We begin by exploring whether this explanation can be also valid in the case of the three experiments considered in the present study. The Kelvin relationship expresses that the equilibrium vapor pressure at a curved meniscus depends on the meniscus curvature. For a hemispherical meniscus, Kelvin's relationship reads

$$RH_{r,eq} = \frac{p_{vequ.}}{p_{vs}} = \exp\left(-\frac{M_v}{RT}\frac{2\gamma cos\theta}{\rho_\ell r}\right) \tag{25}$$

where r is the meniscus curvature radius, γ is the surface tension and θ the contact angle $(\theta \sim 0)$, p_{vs} is the equilibrium vapor pressure over a flat meniscus for a NaCl saturated solution $(p_{vs} = 0.75\, p_{vsat})$.

$$r = -\frac{M_v}{RT}\frac{2\gamma cos}{\rho_\ell Log\left(\frac{p_{vequ.}}{p_{vs}}\right)} \tag{26}$$

To identify $RH_{r,eq}$, the evaporation rate is again expressed using Fick's law as,

$$J_{evap} = A\, D_v \frac{M_v}{RT} p_{vsat} \frac{\left(RH_{r,eq} - R_{\ inf}\right)}{\left(h_{crust-top-cell-top} + \delta\right)} \tag{27}$$

Using the values of J_{evap}determined from the mass variation measurements (Fig.9) and the measured values of RH_{inf} (Fig.8), $RH_{r,eq}$ is determined from Eq.(27) as

$$RH_{r,eq} = RH_{inf} + \frac{J_{evap}(h_{crust-top-cell-top}+\delta)RT}{A\, D_v M_v p_{vsat}} \tag{28}$$

and the corresponding curvature radius is determined from Eq. (26).

The corresponding results are shown in Fig.13.

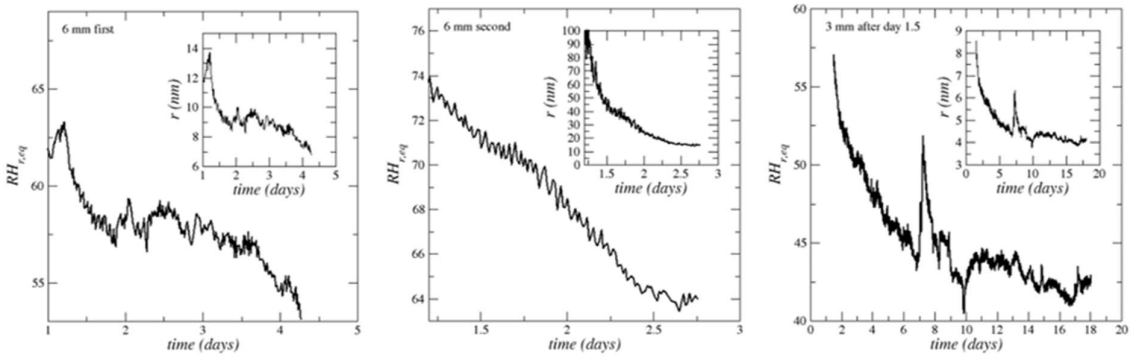


FIG. 13. Variation of relative humidity at crust top and equivalent curvature radius according to Eq. (27) and Kelvin relationship.

As can be seen, the low evaporation rate is compatible with the Kelvin's effect. The corresponding pore opening is found to be greater with the 6 mm second experiment compared to the 6 mm first experiment. As expressed by Eq. (27), the evaporation rate depends on both $RH_{r,eq}$ and $h_{crust-top-cell-top}$, i.e. the distance between the crust top surface and the cell top. Since the crust is higher in the cell in the 6mm experiment, i.e. $h_{crust-top-cell-top-6mm-secon} > h_{crust-top-cell-top-6mm-first}$, a comparatively greater $RH_{r,eq}$ is sufficient with the 6mm second experiment to transfer an evaporation rate comparable to the one in the 6 mm first experiment. Although the evaporation rate is slightly greater in the 6 mm first experiment (Fig.10), the results depicted in Fig.13 for the two 6 mm experiments are therefore considered as consistent.

However, the consideration of a wet crust with saturated pores at the crust top surface in the presence of non-negligible evaporation rate is consistent only if the crust top surface is moving upward since precipitation is expected to occur at the top of the crust top surface under these circumstances. Fig.10 suggests that this is indeed the case in the 6mm first experiment since the crust top surface average position is moving upward in the period after the crust thickness peak has been reached.

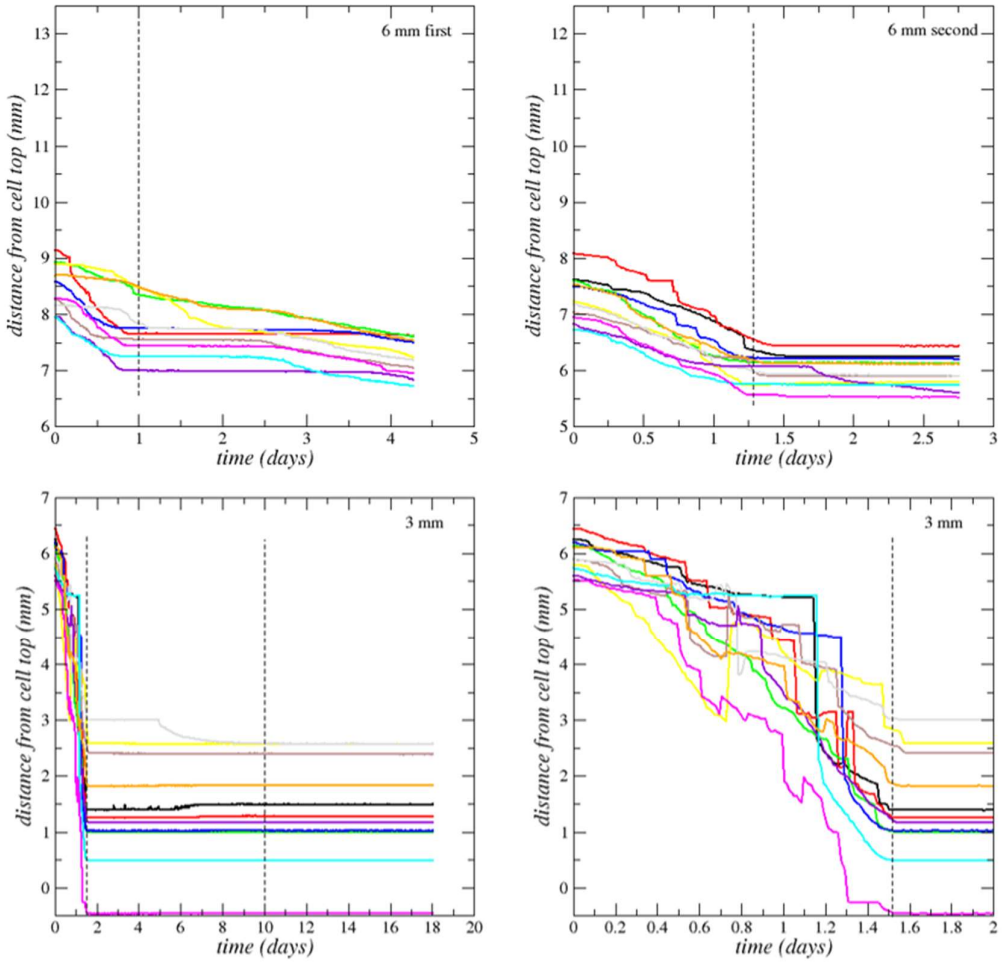


FIG.14. Variations of crust top surface positions along different vertical lines distributed in the cell (the considered lines are illustrated in Fig. 2). The vertical dashed lines correspond to the crust thickness peak whereas the second dashed line at day 10 for the 3 mm experiment corresponds to the crust frozen state (see section III.H).

However, the plot of the displacement of individual points belonging to the crust top surface in Fig.14 indicates a more complex situation. As can be seen some points are continuously moving upward whereas some others are not moving at all (horizontal lines after the vertical dashed line in Fig.14 (left column right top)). A first option would be full pore clogging at the crust top surface at the locations where the crust does not move anymore. However, full clogging means a gradual reduction in the surface pore openings until full clogging. According to Kelvin relationship the gradual closing of the pore would lead to a state where the evaporation flux would be extremely small before the full closing of the considered pore is reached. A related point is that evaporation is needed to induce the local slight supersaturation necessary for the precipitation process to occur [4]. In other words, it is argued that the locations where the crust top surface is not moving correspond to sufficiently small pore openings for the evaporation flux to become sufficiently small at these locations so that negligible precipitation occurs. It can be also noted that these considerations are consistent with the fact that some points resume moving upward after a relatively long period of stagnation (cyan line or brown line for instance in Fig.14 (top panel left column)). This indicates a local increase in the evaporation flux. According to Fig.13, the “active” pore

openings, where “active” means crust top surface pores forming in the regions where the crust top surface is moving, should decrease as these points are moving upward. This means a decrease in the vapor pressure at these moving locations and thus changes in the vapor pressure distribution elsewhere at the crust surface resulting from local water vapor absorption process and thus a possible increase of the vapor pressure due to the change in the menisci curvatures. In brief, the vapor pressure is not uniform at the surface due to Kelvin effect and the associated variation of the surface menisci curvatures and the vapor pressure distribution at the surface is continuously changing which makes possible the reactivation of some regions. In the present study, these considerations are speculative and more work is clearly needed for confirming (or not) the above explanations.

A similar evolution can be seen in Fig.14 with the 6 mm second experiment. The important difference is that the crust top surface moves only very little after the crust thickness peak. As can be seen, the crust top surface is moving upward only at one location among the ones shown in Fig.14 (right column top). Thus here, as can also be seen from the movie, a significant fraction of the crust top surface is “frozen”, i.e. is not moving upward, whereas upward local migration occurs in the complementary fraction.

Applying the Kelvin relationship for the external relative humidity, i.e. $r = -\frac{M_v}{RT}\frac{2\gamma cos}{\rho_\ell Log\left(\frac{RH_{inf}p_{vsat})}{p_{vs}}\right)}$ gives an indication on the menisci curvature radius corresponding to a zero evaporation flux. The obtained curvature radius is plotted in Fig.15.

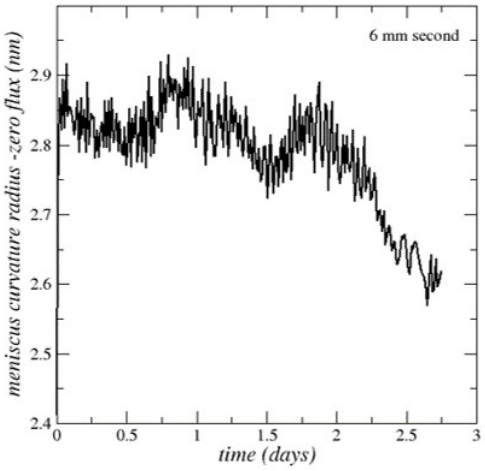


FIG.15. Meniscus curvature radius corresponding to a zero evaporation flux at the crust top surface according to Kelvin relationship.

According to Fig.13, the mean apparent curvature radius corresponding to the measured evaporation rate is much greater with a corresponding relative humidity not very different from 0.75. All this suggests that the vapor pressure is lower at the most advanced points of the crust top surface than in the least advanced points so that i) the net evaporation flux is zero at the most advanced points (stagnation points), ii) the evaporation rate is equal to the measured evaporation rate. A simplified version of the considered situation is schematically sketched in Fig.16.

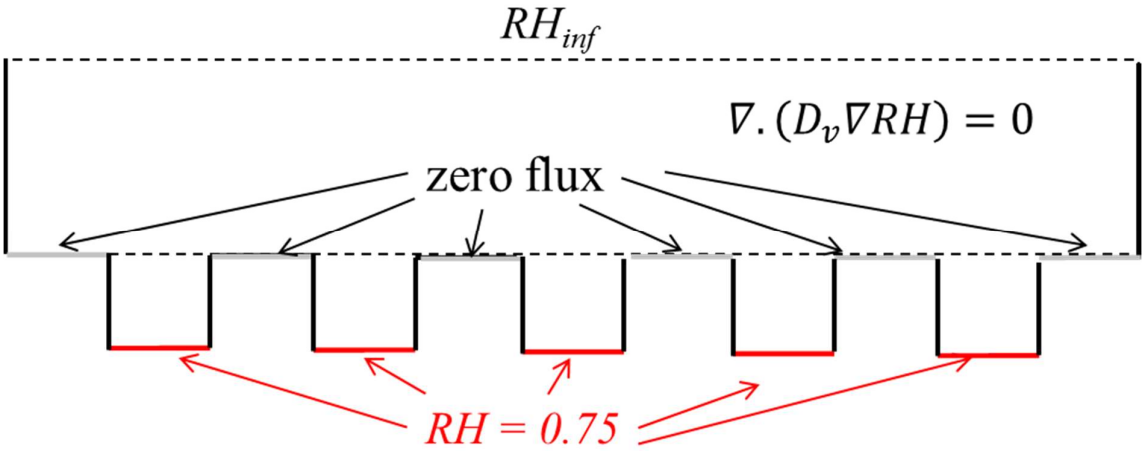


FIG.16. Model problem with heterogeneous distribution of vapor pressure at the crust top surface. The red portions of the crust surface are the evaporation active regions whereas the vapor pressure at the crust surface most advanced points is such that the net evaporation flux is zero at these locations.

The vapor pressure at the crust top surface most advanced points would be such that the "condensation flux" between the red segments and the grey segments is exactly compensated by the evaporation flux between the grey segments and the cell top (where $RH \approx RH_{inf}$).

As illustrated in Fig.14, the situation for the 3 mm experiments confirms the trend observed with the 6 mm second experiment. The crust top surface stops moving right after the crust thickness expansion period.

V.4.6. Crust shrinkage.

As depicted in Figs.10 and 11, the decrease in the crust thickness after the peak is due to the upward displacement of the crust bottom surface. This displacement is faster than the crust top surface displacement in the 6 mm first experiment whereas in the 6 mm second experiment and the 3 mm experiment the crust bottom surface moves upward while the top surface is immobile (3mm experiment) or almost immobile (6 mm second experiment). In the case of the 3 mm experiment the upward migration of the crust bottom surface eventually stops (around day 10) and there is no noticeable change in the crust during the last 8 days of the experiment after day 10.

These results are further illustrated in Fig. 17 which shows the crust bottom surface displacement along the selected vertical lines in the cell (Fig.2). Compared to the analogous results regarding the crust top surface shown in Fig. 14, Fig.17 illustrates that the crust bottom surface is much more uniform. This is also well illustrated with the pictures in Fig.3, especially in the case of the 3 mm experiment for which the crust top surface is branched whereas the crust bottom surface is approximately flat.

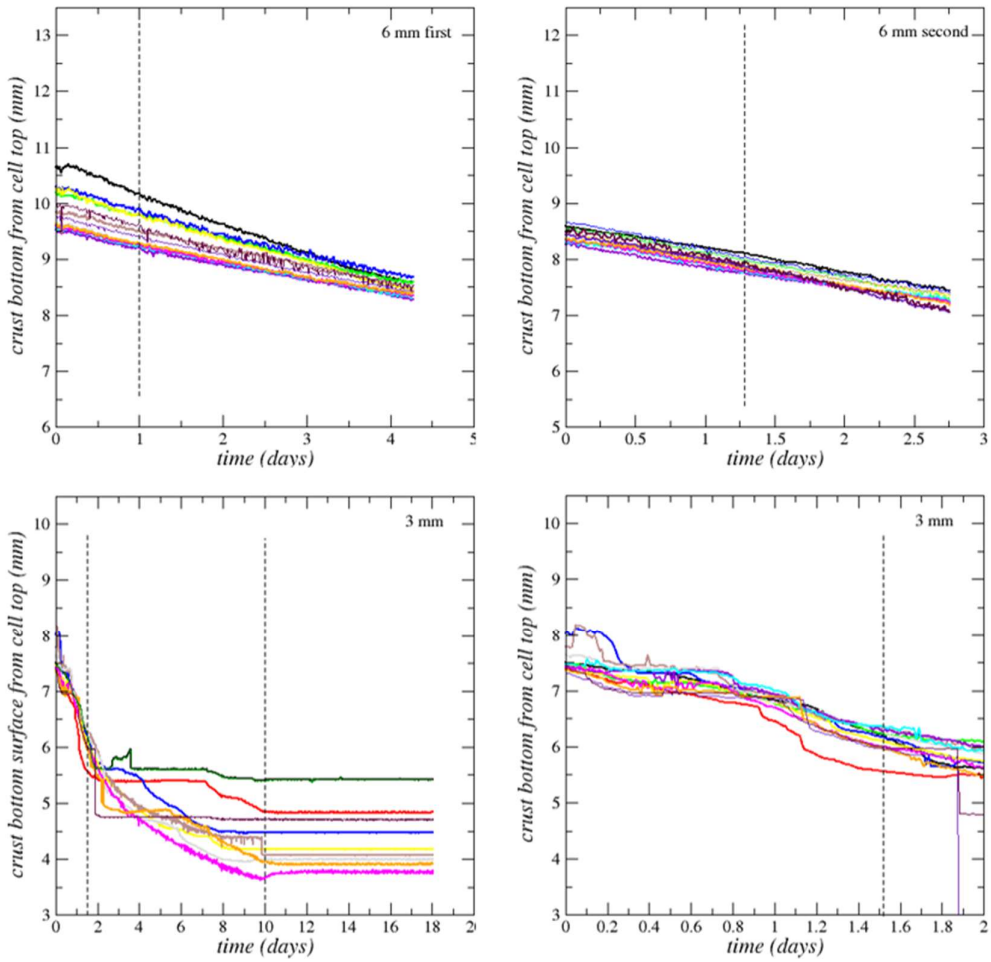


FIG.17 Variations of crust bottom surface positions along different vertical lines distributed in the cell (the considered lines are illustrated in Fig. 2) The vertical dashed lines correspond to the crust thickness peak whereas the second dashed line at day 10 for the 3 mm experiment correspond to the crust frozen state (see section III.H)

V.4.7. Stabilization, destabilization (branched morphology)

The most spectacular feature in the experiments is the branched morphology developing in the 3mm experiment at the crust top surface whereas the crust bottom surface remains essentially flat. Although much less spectacular a destabilization process also occurs in the 6 mm experiments with a clear increase in the roughness of the crust top surface in a first period (Fig.4). This first period corresponds in each experiment to a period of crust thickness expansion during which the evaporation rate is about equal to the potential evaporation. The destabilization process is explained as follows. Since the evaporation rate is very close to the potential evaporation the vapor pressure over the crust top surface must be equal to the equilibrium vapor pressure at the surface of a NaCl saturated solution, namely 0.75 p_{vsat}. Then, we rely on the crust surface local growth rate expression derived in [4], i.e. Eq. (16), which is expressed here as,

$$\frac{d\boldsymbol{X}_t}{dt} = \frac{C_{sat}}{\rho_{cr}(1-\varepsilon_t)(1-C_{sat})}\left[\frac{Da_t}{1+Da_t}\right]\boldsymbol{j}_{evap.}\cdot\mathbf{n} \quad (29)$$

where $\boldsymbol{X}_t$ is a position vector at the surface and $\mathbf{n}$ is a unit normal vector at the crust to surface. Thus $\frac{d\boldsymbol{X}_t}{dt} \propto \boldsymbol{j}_{evap.}$ with $\boldsymbol{j}_{evap.} \propto 1/h_{crust-top-ce}$ (the closer the considered point to the cell top, the greater is the evaporation flux according to Fick's law). Since the evaporation flux is greater at the most advanced points of the crust top surface, these points move faster than the points further away from the top cell. This effect is enhanced by the screening effect in the fjords which further reduce the evaporation flux. In other words, the destabilization is due to the dependence of the crust top surface local displacement speed and the local evaporation flux as schematically illustrated in Fig.18. A similar qualitative consideration explains why the crust bottom surface displacement is stable. Using again the expression derived in [4], the displacement of a point located at the crust bottom surface is expressed as

$$\frac{d\boldsymbol{X}_b}{dt} = \frac{C_{sat}j_{abs.}}{\rho_{cr}(1-\varepsilon_b)(1-C_{sat})}\left[\frac{Da_b}{1+Da_b}\right]\boldsymbol{j}_{abs.}\cdot\mathbf{n} \quad (30)$$

Thus, $\frac{d\boldsymbol{X}_b}{dt} \propto \boldsymbol{j}_{abs.}$ with $\boldsymbol{j}_{abs.} \propto 1 / h_{ll-c}$ (the smaller the distance between the liquid level in the cell and the crust bottom surface, the greater is the absorption flux). As a result, the absorption flux is greater at the least advanced points of the crust bottom surface (as schematically indicated in Fig. 18). The dissolution is therefore more effective at these points, which contributes to smooth out the bottom surface.

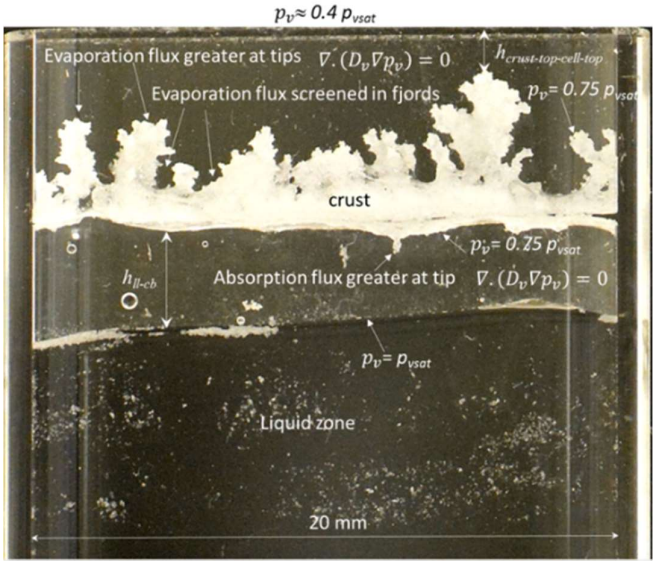


FIG.18. Schematic of absorption flux distribution at crust bottom surface and evaporation flux at crust top surface during the crust destabilization period.

As mentioned previously, the above applies to the situations where the vapor pressure is uniform over the considered surface. As illustrated in Fig.4, the crust top surface tends to become flatter during the period after the crust thickness peak has been reached in the 6 mm experiments. The main stabilization mechanism is attributed to the combined effect of the salt precipitation process taking place in the crust top region and the Kelvin effect which contributes to reduce the evaporation flux first at the most advanced points of the crust top surface since the precipitation process is expected to be more active there until the Kelvin effect becomes noticeable. The stabilization is therefore explained based on the same arguments as the ones already presented in section III.E. In summary, the destabilization

process occurs when the vapor pressure does not vary or varies little over the surface whereas the stabilization process is associated with the development of a non – uniform distribution of the vapor pressure at the surface as attributed to the Kelvin effect, which in turn is due to the gradual closing of the surface pores resulting from the precipitation process.

V.4.8. Crust frozen state – Crust apparent effective diffusion coefficient

As illustrated in Fig. 11 as well as in Fig. 14 and 17, no noticeable change is observed for the crust in the 3 mm experiment after day 10 during a relatively long period of about 8 days. The crust bottom and top surfaces do not move anymore and no noticeable modification of the crust morphology is observed within the crust between the two surfaces. For this reason, the crust state in this last period is referred to as a "frozen" state. However, as indicated in Fig.11, the evaporation rate is far from negligible in this period. It is about half the evaporation rate at the beginning of the 3mm experiment. This means that the crust is not clogged, or at least not fully clogged. Since no visible dissolution process at the bottom surface or precipitation process higher in the crust can be detected, it is tempting to consider the frozen crust as dry.

To further analyze the crust frozen state, we begin with a rough estimate of the crust effective diffusion coefficient assuming the crust fully dry. The latter can be obtained by expressing the evaporation rate in the cell as

$$J_{evap} = A\, D_v \frac{M_v}{RT} p_{vsat} \frac{(1-RH_{crust-bottom})}{h_{ll-c}} \tag{31}$$

$$J_{evap} = A\, \varepsilon D_{eff} \frac{M_v}{RT} p_{vsat} \frac{(RH_{crust-bottom}-RH_{crust-top})}{h_c} \tag{32}$$

$$J_{evap} = A\, D_v \frac{M_v}{RT} p_{vsat} \frac{(RH_{crust-top}-RH_{inf})}{(h_{crust-top-cell-t} \quad +\delta)} \tag{33}$$

Where Eq. (31) corresponds the vapor diffusive transport between the liquid level in the cell and the crust bottom surface, Eq. (32) to the diffusive transport within the crust and Eq.(33) to the diffusive transport between the crust top and the cell top.

Combining the above equations leads to

$$\frac{\varepsilon\, D_{eff}}{D_v} = h_c \left[\frac{A M_v\, D_v p_{vsat} (1-RH_{inf})}{J_{evap} RT} - (h_{ll-cb} + h_{crust-top-cell-top} + \delta) \right]^{-1} \tag{34}$$

Application of Eq. (34) leads to the results shown in Fig.19.

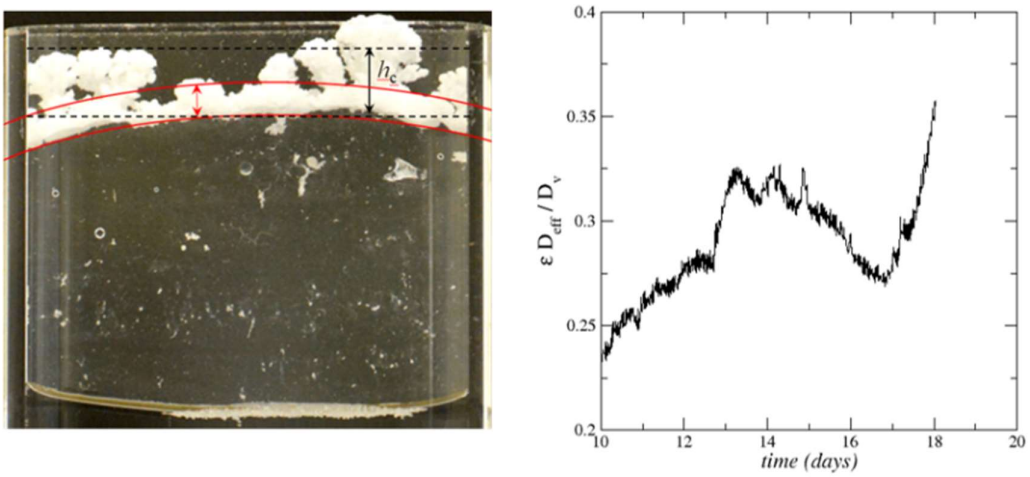


FIG.19 Crust apparent effective diffusion coefficient from 3 mm experiment after day 10. The image on the left is an image of the crust in the frozen state.

First, it can be noticed that $\frac{\varepsilon D_{eff}}{D_v} \approx 0.3$. Assuming a relatively low crust porosity, for instance $\varepsilon \approx 0.1$, leads to the unrealistic result $\frac{D_{eff}}{D_v} = 3$! It can then be argued that the crust effective thickness is less than determined from simply the average thickness from the considered vertical lines (Fig.2). As sketched in Fig. 19, a more representative thickness could correspond to the distance between the red curves in Fig.19. This distance is about 1.3 mm. Using this value of the thickness instead of the ones reported in Fig. 11 leads to $\frac{\varepsilon D_{ceff}}{D_v} \approx 0.15$, which is still quite high. In summary, assuming the crust in the frozen state as fully dry does not lead to a consistent result.

Therefore, the conclusion is that the frozen crust is actually wet, at least partially. Since the precipitation phenomenon at the crust top and the dissolution phenomenon at the crust bottom are negligible over the considered period whereas the absorption rate is noticeable (Fig. 11), the next step is therefore to consider that liquid clusters are present somewhere within the crust so as to explain the shortcut effect corresponding to the high apparent effective diffusion coefficient. Furthermore, the ion concentration in the liquid clusters can be expected to be very close to the solubility. It is tempting to conclude that the vapor pressure in the crust should be therefore close to 0.75 p_{vsat}. However, since the Kelvin effect has been invoked to analyze the experimental results in the periods prior to that considered, it is reasonable to consider it again. In other words, the situation would be isolated saturated clusters confined in sufficiently small pores for the Kelvin effect to have an impact. An estimate of the vapor pressure in the crust can be obtained from the liquid level variation absorption rate estimated (Figs.6 and 11) applying again Fick's law,

$$RH_{crust} = 1. - \frac{J_{abs.}\, h_{ll-c}\ RT}{A\, D_v M_v p_{vsat}} \tag{35}$$

This leads to the results shown in Fig.20 (right panel) where the results from the consideration of the evaporation rate (Fig. 13) are also reported (left panel).

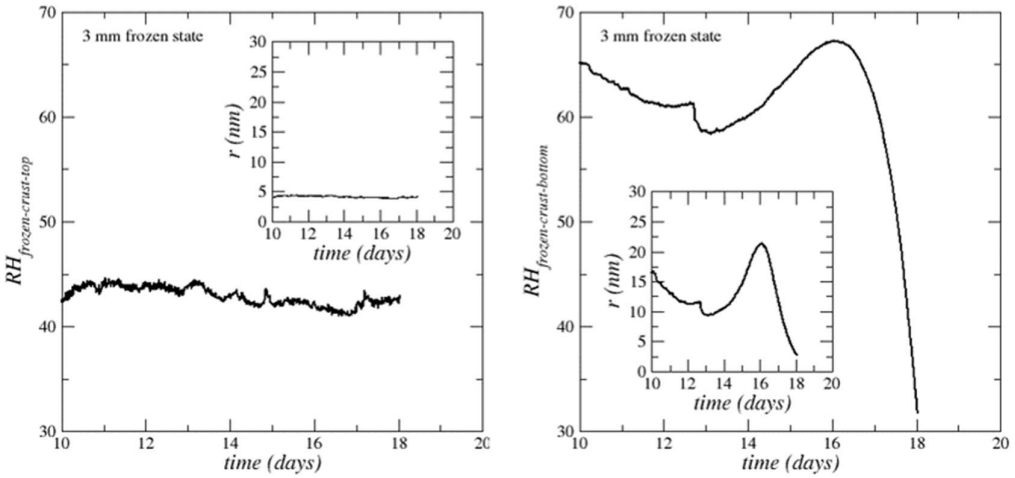


FIG. 20. Variation of relative humidity at crust top (left) and crust bottom (right) during the crust frozen state determined from Eqs. (28) and (35) and equivalent curvature radius according to Kelvin relationship.

The results shown in Fig.20 are compatible with a partially wet crust inside which trapped liquid clusters contribute to the enhanced vapor transport via condensation-evaporation mechanisms. The vapor partial pressure would decrease from crust bottom to crust top as reflected by the smaller menisci curvature radius in the top region (~ 4 nm) than in the crust bottom region (~10 – 20 nm).

In summary, the crust frozen state would correspond to a situation where the crust is partially wet with the liquid solution in the crust distributed under the form of isolated clusters (so that the ion transport from bottom to top is not possible). This liquid distribution is characterized by the existence of a meniscus curvature radius gradient (negative in the upward vertical direction) corresponding to a negative vapor pressure gradient. This gradient might correspond to a gradient in the pore size since the preferential precipitation on top favors the formation of pores smaller than in the crust bottom region. All this indicates that a crust drying process occurs during the experiment since the presented analysis suggests that the crust is fully wet during at least the crust thickness expansion period. The fact that the evaporation rate is significantly greater than the absorption rate at the end of the crust expansion period (Fig.11) could indicate that the drying process actually starts at the end of this period or just a little after.

V.4.9. Crust displacement regimes

Together with the experiments reported in [4] and [5], the experiments considered in the present study lead to identify different crust displacement regimes. For convenience, the crust top displacement at various locations at the crust top surface is shown in Fig.21 for all experiments, including the ones discussed in [4,5] whereas some characteristics of the experiments are reported in Table 2. A first regime corresponds to the one observed in [4]. As illustrated in Fig.21 (top left), the crust is moving upward continuously. Also, in this particular experiment, the evaporation rate was about equal to the potential evaporation, which indicates that the precipitation taking place in the crust top region during its displacement did not lead to a significant closing of the pore openings over the relatively long period of the experiment (18 days). The evaporation rate was about equal to the absorption rate.

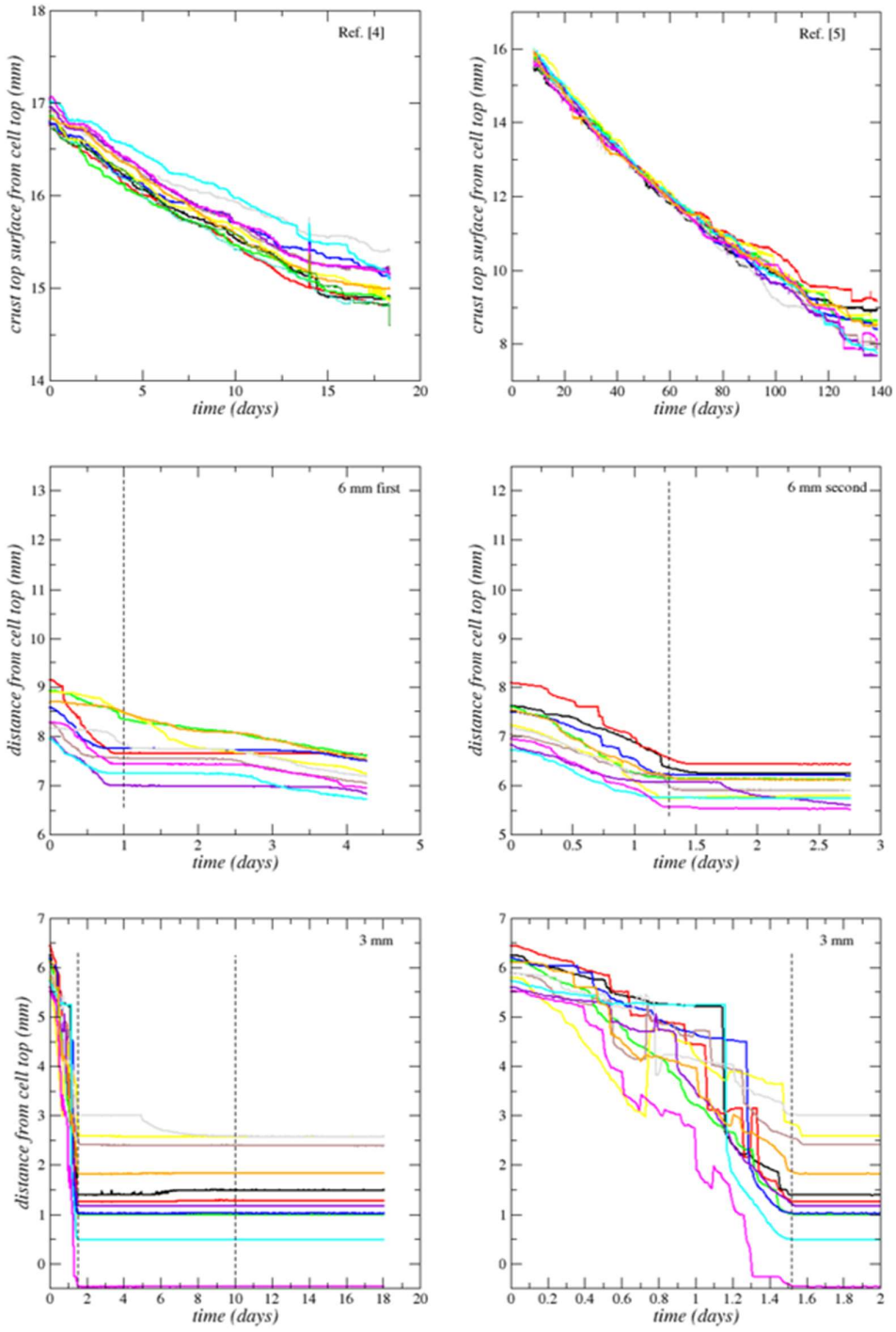


FIG. 21. Variations of crust top surface positions along different vertical lines distributed in the cell. Comparisons between the experiment analyzed in [4] (top left column), the experiment analyzed in [5] and the experiments considered in the present study.

TABLE 2. Some characteristics of the various experiments. $Pe \approx \frac{j_{evap} h_c}{\rho \varepsilon D_S^*}$ is computed assuming $\varepsilon = 0.1$ for all experiments.

	Experiment [4]	Experiment [5]	6 mm first experiment	6 mm second experiment	3mm experiment
Overall duration (days)	18	140	4	2.5	18
Overall duration of the crust top surface displacement period (days)	18	140	4	1.3	1.5
Potential Evaporation (g/day)	~ 0.04	~ 0.03	0.08	0.09	[0.1 - 0.2]
Evaporation rate (g/day)	~ 0.04	~ 0.015	[0.06 - 0.08]	[0.07 - 0.09]	[0.05 -0.23]
Evaporation rate /potential evaporation	~1	< 1	From ~1 to <1	From ~1 to <1	From ~1 to <1
Absorption rate	~ 0.04	~ 0.015	~ 0.07	~[0.07 -0.1]	~[0.08 - 0.15]
Crust top surface mean total displacement (mm)	~1.9	~ 8	~ 1.4	~ 1.25	~ 4.5
Crust top surface maximum velocity (mm/day)	0.14	0.07	0.6	1	3
Peclet number *Pe*	0,19	0.1	0.6	0.8	4.6
Initial crust thickness (mm)	0.8	1.2	1.4	1.2	1.6
Crust thickness variation (mm)	~ 0.2	~ 0.2	0.25	0.6	3
Branched morphology	No	No	No	No	Yes
Regime (continuous or with the crust surface displacement stop)	continuous	continuous	continuous / stopping	stopping	stopping

A somewhat similar regime was observed in the experiment considered in [5]. Here again, the upward displacement of the crust top surface is continuous over the experiment duration, noting that this duration is much longer with 140 days. However, contrary to the experiment in

[4], the evaporation was significantly lower than the potential evaporation, which would correspond to the formation of sufficiently small pores at the surface for the Kelvin effect to have an impact and explain the evaporation lower than the potential evaporation under the assumption of a fully wet crust. The absorption rate was again comparable to the evaporation rate. The analysis for these two experiments suggests that there is little change in the crust microstructure during its displacement. Also, it can be noticed that the Peclet number is rather small (Pe ~ 0,19 and Pe ~0.1 respectively). By contrast, the crust top surface eventually stops moving upward in the 6 mm second and 3 mm experiments. This regime is characterized by significantly higher evaporation rates, significantly higher crust displacement velocities and higher Peclet number in the period of crust top displacement (Pe ~ 0.8 and Pe ~4.6 respectively). It is thus considered that the precipitation process is more intense at the crust top leading to the formation of sufficiently small pores for the relative humidity at the crust top surface to become sufficiently close to the external relative humidity. Thus, this regime would be characterized by a significant variation in the crust pore size distribution as the crust moves upward.

V.4.10. Conclusion

In this chapter, we have studied the impact of the relative significance of the absorption rate ($J_{abs.}$) and the evaporation rate ($J_{evap.}$) on the upward displacement of a salt crust confined in a Hele-Shaw cell. The idea was to vary the relative significance of both rates by varying the initial position of the liquid level in the cell. In the three experiments considered in this study, the displacement of the crust is characterized by a first period of crust expansion followed by a period of a crust contraction. Since the absorption rate is clearly greater than the evaporation rate at the beginning of the experiment at least for two of the experiments, a naive view is to consider that the crust expansion period simply corresponds to $J_{abs.} / J_{evap.} > 1$. However, this simple view is not in agreement with the experimental results. A more refined analysis indicates that the transition from an expanding crust to a shrinking crust depends on the precipitation – dissolution processes taking place in the crust. Essentially, the transition depends on the precipitation phenomena taking place in the top region of the crust during its displacement. As the results, the condition $J_{abs.} / J_{evap.} > 1$ is not a discriminatory criterion. Crust expansion can be also observed when $J_{abs.} / J_{evap.} < 1$. A more refined criterion taking into account the dissolution – precipitation process within the crust was derived and leads to consistent qualitative results.

Two main crust morphologies can be identified from the experiments: compact and branched. The compact morphology is characterized by flat crust top and bottom surfaces whereas the branched morphology is characterized by a flat crust bottom surface and a branched crust top surface. The transition from compact to branched morphology is observed during the expanding crust period but is observed in only one of the three experiments. However, the crust top surface tends to be wavy in the two other experiments during the crust expansion period. The conditions leading to the crust top surface destabilization, i.e. the transition from compact to wavy or branched, have been identified. It is argued that the destabilization occurs when the partial vapor pressure is uniform along the crust. Since the crust top surface local growth is proportional to the local evaporation flux and the evaporation flux further increases at the crust most advanced top surface points, this situation leads, as observed, to the crust top surface destabilization. By contrast, the precipitation mechanisms in the top region of the crust are considered as a stabilizing mechanism as they can lead to sufficiently small pores for the Kelvin effect to be effective. Since the precipitation is expected to be more significant where the local evaporation flux is locally greater, this effect can counterbalance the destabilizing mechanism associated with the local heterogeneous

evaporation flux distribution. By contrast, the absorption / dissolution mechanisms at the crust bottom surface are stabilizing (the crust bottom surface stays essentially flat).

In conjunction with the experiments reported in [4,5], various crust displacement regimes can be distinguished. In [4], the displacement was essentially compact. The evaporation rate was on the order of the absorption rate and very close to the potential evaporation. In [5], the displacement was also compact but the evaporation rate was significantly lower than the potential evaporation. In the present study, the evaporation rate is close or equal to the potential evaporation rate in a first period corresponding to the crust expansion period. However, the precipitation mechanisms in the experiments of the present study eventually lead to pore clogging in the crust with the occurrence of dry/clogged regions in the top region of the crust. In addition to the branched morphology, this eventually leads to a regime where the crust does not change anymore within the cell while the evaporation rate is noticeable. This case begins with it the immobilization of the crust top region followed by a crust contraction period resulting from the upward displacement – rearrangement of the crust bottom surface until the crust morphology stops evolving. Assuming the crust fully dry in the period where the crust is not moving anymore within the cell, leads to an unrealistically high apparent effective diffusion coefficient. This suggests that the crust is actually partially wet in this period.

Several analyses presented in the study are speculative and need more work in order to be confirmed. Among the issues making the analyses difficult is the lack of information on the crust properties (porosity, pore size distribution, diffusion coefficient, etc). Furthermore, the study suggests that these properties evolve during the crust displacement, at least in the comparatively high Peclet number regimes considered in the present study.

Finally, the existence of the various displacement regimes and crust morphology evolutions is consistent with the variety of salt crust morphologies that can be observed in nature or in applications.

Bibliography

1. H. Eloukabi, Sghaier, N., Ben Nasrallah, S., Prat, M. Experimental study of the effect of sodium chloride on drying of porous media: the crusty-patchy efflorescence transition. Int. J. of Heat and Mass Tr. 56, 80–93 (2013).

2. U. Nachshon, N. Weisbrod, R. Katzir and A. Nasser, NaCl Crust Architecture and Its Impact on Evaporation: Three-Dimensional Insights, Geophys. Res. Lett. 45, 6100 (2018).

3. S. Dai, H.Shin, and J. C. Santamarina, Formation and development of salt crusts on soil surfaces, Acta Geotechnica, 11, 1103 (2016).

4. G. Licsandru, Noiriel, C., Duru, P., Geoffroy, S., Abou-Chakra, A., Prat, M. Dissolution-precipitation-driven upward migration of a salt crust. Physical Review E 100 (3), 032802 (2019).

5. G. Licsandru, G., Noiriel, C., Duru, P., Geoffroy, S., Abou-Chakra, A., Prat, M. Air gap formation between an efflorescence salt crust and the porous medium surface under deficit evaporation conditions. To be submitted (Chapter 4 of the present thesis).

6. F. Chauvet, P. Duru, S. Geoffroy, M. Prat, Three periods of drying of a single square capillary tube, Phys. Rev. Lett. 103, 124502 (2009).

General conclusions and perspectives

In the present work we have studied the evaporation of a sodium chloride solution in a porous medium and we have shown that this truly is a very rich and complex subject due to the multiple phenomenon couplings between evaporation, ion transport in solution and crystallized salt structure formations (efflorescence or subflorescence), not to mention the couplings with mechanical effects which have not even been discussed in this work. Although a lot of progress has been made in understanding and modelling these situations, especially over the past decade, many points remain to be clarified.

Here we have managed to bring forth new experimental techniques both in 2D (Hele-Shaw cells) as well as in 3D (PTFE containers) that allow new data to be collected in this vast domain and, as such, aid in developing new simple mathematical models regarding known salt crystallization problems.

For the first time -to the best of our knowledge- we have managed to create salt crust patterns in controlled laboratory conditions with two different recipes that have reproducibility, just by using simple concepts in order to control the flow and concentration gradients in a porous medium. These patterns have been named Grooved pattern and its counterpart Ridged pattern. The in depth study of the GP has produced a successful recipe which shows great potential. While its counterpart the RP, although still not stable enough, has been produced just by varying one factor of the GP recipe. However, in terms of patterning control we have just managed to show a clear direction. Thus, here there is a great need for more experimenting in terms of upscaling and a very important mathematical model to be related to the work done so far. As such we just scratched the surface of this completely new phenomenon.

In the present work we have shown that a normally considered static crust suspended in a 2D Hele-Shaw cell can transform into a dynamic crust through a self-propelled mechanism, just by exposing it to water vapor. Such a phenomenon has been explained in a simple way by a couple dissolution-transport-precipitation mechanisms with no need for any mechanical effects to be taken into account. This allows for a simple mathematical model to be created describing its behavior.

The concept of efflorescent and subflorescent crusts has been challenged with the aid of a very long experiment (280 days). This presented a new insight in terms of efflorescent salt crusts showing that the crusts are actually composed of two layers (cemented in halite porous media and halite). Such an experiment being able to bring forth new data on the detachment processes observed in the field of salt crust crystallization. Moreover, a mathematical model in good agreement with the phenomenology was tested with the aid of the data obtained.

The morphological destabilization of a salt crust has been shown to be directly related to its absorption/evaporation potential. This shows that a crust can go from a quasi-uniform morphology to a finger type structure and vice versa. Here a clear direction has been also established for a mathematical model. Thus, the need of more in depth studies to be done.

As we have just designed and tested these new techniques. There is a lot of room for improvement. Thus as a perspective in terms of the Hele-Show cells there is a clear need for more experiments in order to have multiple variations of environmental factors and, as such, to be able to fully predict the behavior of a salt crust. An also very important point would be that we have only tested in 2D cells these traits of salt crusts and as such a need for 3D type experiments and data would be the next step.

In conclusion in the present thesis salt crust behaviors such as patterning, dissolution-transport-precipitation mechanisms, detachment and very big morphological changes have been explored and discussed and as such showing that salt crusts are truly dynamical phenomena. However, there is still much more to explore and model in this vast scientific field.